Spectroscopy and Microscopy of Transition Metal Chalcogenide Nanomaterials

Martin O. King

Submitted in the fulfilment of the requirements for the
Degree of Doctor of Philosophy

School of Chemistry
College of Engineering and Physical Sciences
University of Glasgow

May 2013

Abstract

This thesis details the physical and electronic structure of several technologically important transition metal chalcogenides (TMCs) using a combination of transmission electron microscopy (TEM) and surface science experimental techniques. The materials studied include Cu_xTe and CdTe, which find application in high efficiency, low weight photovoltaic devices. Cu_xTe alloys are frequently used as an electrical back contact in high efficiency CdTe photovoltaics. Here, we examine the alloying of Te on the Cu(111), polycrystalline Cu and Cu(643) surfaces. Chapter 3 of this thesis shows that the alloying of Te and Cu(111) is facile at room temperature, contrary to previous reports. Two distinct surface phases exist, depending on Te surface concentration. Below a coverage of 0.33 monolayers (MLs) of Te a surface substitutional alloy (SSA) is found to exist, where a Te adatom substituted for a surface Cu atom. For Te coverages greater than 0.66 ML, an unusual Cu_3Te_2 alloy continually grows on the surface, stabilised by a good lattice match to the Cu(111) substrate. The surface alloying of the Cu-Te system displays an intriguing dependence on the surface termination of the Cu substrate. Of the three Cu substrates studied here, Cu(111), $Cu(643)^R$ and polycrystalline Cu, a 1 ML film of Te gave ordered alloy structures with stoichiometries of Cu_3Te_2, CuTe and Cu_2Te, respectively. In chapter 4, the study of thin film photovoltaics is extended to the deposition of CdTe onto Cu and Cu_xTe substrates. CdTe is observed to grow three dimensionally on Cu(111), Cu_3Te_2 and Cu_2Te. Cu^+ diffusion, crucial for photovoltaic performance, is detected for CdTe thicknesses greater than 2 ML and is assigned, predominately, to Cu_2Te crystallites forming within the CdTe layer, with a minor amount of Cu residing in interstitial sites in the host CdTe structure. Chapter 5 describes the alloying of Te with a intrinsically chiral surface, $Cu(643)^R$, the first study of its kind. The results of this study reveal that step mediated alloying occurs between Cu and Te with significant faceting of the surface. Two ordered CuTe alloy phases were observed for sub-monolayer Te coverages. The low coverage alloy exists for Te coverages between 0.18 ML and 0.45 ML and has a chiral unit cell. The high coverage alloy exists for Te coverages between 0.45 ML and 1.5 ML and has an achiral unit cell. The atomic positions of these surface alloys are tentatively interpreted from the scanning tunnelling microscopy (STM) images. In contrast to the thin film experiments in chapters 3-5, chapter 6 describes a study of TaS_3 nanoribbons. These studies reveal that the nanoribbons have a distinct core-shell type structure. Characterisation with surface science techniques shows that the shell is non-stoichiometric and amorphous while TEM shows a crystalline core to the material. Interestingly, the TaS_3 are observed to be unstable when interfaced on a Au substrate, with the shell persistently losing S to the substrate, which have potential implications in device integration.

Contents

List of Figures

List of Abbreviations

AFM	Atomic Force Microscopy
a.u.	Arbitrary Units
BA	Bulk Alloy
BF	Bright Field
BFP	Back Focal Plane
BSE	Back Scattered Electrons
CBED	Convergent Beam Electron Diffraction
CCD	Charge Coupled Device
CCS	Close Space Sublimation
CDW	Charge Density Wave
CIGS	Copper Indium Gallium Selenide
Cu_{poly}	Polycrystalline Copper
DFT	Density Functional Theory
DOS	Density of States
DS	Doniach-Sunjic
EDS	Energy Dispersive X-ray Spectroscopy
EELS	Electron Energy Loss Spectroscopy
EFTEM	Energy Filtered Transmission Electron Microscopy
eV	Electron Volt
E_F	Fermi Level
FCC	Face Centred Cubic
FEG	Field Emission Gun
FFT	Fast Fourier Transform
HRTEM	High Resolution Electron Microscopy
GIF	Gatan Imaging Filter
GL	Gaussian-Lorentzian
IMFP	Inelastic Mean Free Path
ITO	Indium Tin Oxide
LEED	Low Energy Electron Diffraction
MEIS	Medium Energy Ion Scattering
ML	Monolayer
PhD	Photoelectric Diffraction
PID	Proportional-Integral-Derivative
PXRD	Powder X-ray Diffraction
RGA	Residual Gas Analyser
RGB	Red-Green-Blue

RSF	Relative Sensitivity Factor
SAED	Selected Area Electron Diffraction
SE	Secondary Electrons
SEM	Scanning Electron Microscopy
SEXAFS	Surface X-ray Absorption Fine Structure
SIMS	Secondary Ion Mass Spectrometry
SSA	Surface Substitutional Alloy
STM	Scanning Tunnelling Microscopy
STS	Scanning Tunnelling Spectroscopy
TDMS	Thermal Desorption Mass Spectrometry
TEM	Transmission Electron Microscopy
TPD	Temperature Programmed Desorption
TMC	Transition Metal Chalcogenide
TSP	Titanium Sublimation Pump
UPS	Ultraviolet Photoelectron Spectroscopy
UV	Ultraviolet
XPS	X-ray Photoelectron Spectroscopy

List of Publications

- M.O. King, M. Popland, S.J. Denholme, D.H. Gregory, D.A. MacLaren, M. Kadodwala, *Nanoscale* **4** (2012) 607.
- M.O. King, I.M. McLeod, D. Hesp, V.R. Dhanak, M. Kadodwala, D.A. MacLaren, *Surf. Sci.* **606** (2012) 1353.
- M.O. King, I.M. McLeod, D. Hesp, V.R. Dhanak, C. Jack, D.A. MacLaren, M. Kadodwala, *invited paper for Surf. Sci.*, in preparation.

Acknowledgements

First and foremost, I would like to thank both of my supervisors, Dr. Donald MacLaren and Dr. Malcolm Kadodwala. I was in the rather fortunate position of having a supervisor from both the School of Physics and Astronomy and the School of Chemistry. I am indebted to both supervisors for their help, encouragement and expertise throughout this project. I would also like to thank my fellow Ph.D. student, Nadia Abdulrahman, for her help and words of advice throughout this project. I would also like to thank, the two project students I had the pleasure of working with, Michael Popland and Calum Jack. I must also thank the University of Glasgow for provision of a University Scholarship.

In addition, two weeks of this project was spent at the University of Liverpool. Although it was only a short period of time, I collected lots of useful STM data. I must thank Dr. Vin Dhanak, Ian McLeod and David Hesp for taking the time out of working on their own experiments, to let me use their system. It was a friendly and relaxed atmosphere and I gained crucial new insight into the systems in question. The TaS_3 chapter (chapter 6) of this thesis was only made possible by Dr. Saleem Denholme in Prof. Duncan Gregory's group. I thank him for synthesising the materials for me to study.

There have been times were things have failed and I am grateful for the technical assistance I have received from the Schools of Physics and Astronomy and Chemistry- Jim Gallagher, Jim Bannon, Stuart MacKay, Tony Ritchie, Brian Millar and many others. It is of great sadness that Brian passed away during the course of my time in the School of Physics and Astronomy. None of the electron microscopy would have been possible if it wasn’t for the help and expertise of William Smith, Colin How and Dr. Sam McFadzean.

Finally, I'd like to thank my parents (especially my dad!), for supporting me through my undergraduate and postgraduate studies.

Author's Declaration

I declare that, except where explicit reference is made to the contribution of others, that this thesis is the result of my own work and has not been submitted for any other degree at the University of Glasgow or any other institution.

1. Introduction

There are a number of themes running through this thesis. These include: the study of transition metal chalcogenides (TMCs), in particular fundamental studies into CdTe photovoltaic materials; the study of thin film alloys, deposited on flat and vicinal surfaces; the application of surface science and electron microscopy to both thin film systems and nanomaterials; and the comparison between bulk and surface structure.

TMCs are a large class of inorganic materials which display a wide variety of properties that lie at the forefront of modern solid state research, in terms of both technological applications and fundamental physics. In particular, they have several applications in renewable energy generation [1-3]; rechargeable batteries [4] and non volatile data storage [5]. In recent decades, there has been a substantial drive to increase renewable energy generation. Indeed, the Scottish government targeted, in 2005, that renewable energy should account for 40 % of total electrical power generated in Scotland by the year 2020 [6]. A significant and growing contribution to renewable energy generation is in photovoltaic devices, of which the thin film TMC, CdTe, is the second most widely used (behind polycrystalline Si) [7]. Due to increased costs of fossil fuels and a reduction in cost of photovoltaic modules, photovoltaic output has almost doubled every 2 years in the last decade [8]. A testament to the progress made in thin film photovoltaics is that the market share of thin film CdTe and CuInGaSe (CIGS) photovoltaic modules has grown from 0.6 % in 2001 [7] to over 10 % in 2011 [9]. The CdTe photovoltaic, (the composition of which is discussed in chapter 4 of this thesis) comprises a p-n heterojunction of CdTe (p type) and CdS (n type). The band gap of CdTe is ~1.5 eV, which almost perfectly matches the distribution of photons in the solar spectrum. When a photon is incident on the p-n heterojunction, it can promote an electron from the valence band to the conduction band, creating an electron-hole pair. In chapter 3, the crucial back contact of the CdTe photovoltaic is studied, which involves the alloying of Cu and Te. This study provides interesting new insight into the structure and thermal properties of the Cu-Te alloy structure. The study of CdTe photovoltaic materials is extended in chapter 4 to CdTe thin films, which are characterised on model, Cu single crystals and more realistic polycrystalline Cu (Cu_{poly}) specimens. The data presented reveals, for example, novel information on the nature of Cu diffusion.

A different aspect of power generation using TMCs is in thermoelectric devices (e.g. $CoSb_3$ [10] , Zn_4Sb_3 [10] and Ag_2Se [11]), which convert a thermal gradient into an electrical potential or vice versa and find application in areas as diverse as portable refrigerators to spacecraft [12,13]. TMCs are also used as a cathode in Li^+ ion batteries.

The layered nature of TaS_2 means that it is ideal for Li^+ insertion [14] and therefore acts as an effective cathode. TaS_2 is studied in chapter 6 of this thesis.

TMCs have also interested scientists for decades because of their fundamental properties. TMCs manifest a wide variety of fascinating physical phenomena, including: reduced dimensionality [15] (i.e. quasi one dimensional (1-D) and quasi two dimensional (2-D) solids); related to reduced dimensionality is the Peierls transition and charge density waves (CDWs) [16,17]; superconductivity [18-20] and more recently topological insulation [21-24]. In chapter 6, reduced dimensionality and CDWs are explicitly studied with TaS_3 and TaS_2 nanoribbons. The layered structure of TaS_2 means that electrons can only propagate along planes of Ta atoms, giving rise to its 2-D conductivity. TaS_3, on the other hand, can be thought of as having chains of Ta atoms meaning that electrons can only propagate in a single dimension (along the Ta chains). Hence TaS_3 is known as a 1-D conductor. With this reduced dimensionality, unusual physics are observed. For example, 1-D materials no longer obey the Fermi Liquid model for electronic conduction but instead are governed by the Luttinger Liquid model [15]. In addition, 1-D and 2-D materials can display a lattice instability, which is known as a Peierls distortion and is a periodic distortion of atoms from their equilibrium lattice position. The explanation of the Peierls distortion will be further developed in chapter 6. In addition to TaS_3 described in chapter 6, a wide range of other TMCs also display this reduced dimensionality, including: TaS_2, $TaSe_2$, $NbSe_2$, VSe_2, $TiSe_2$, TiS_2 and NbS_3 [16,17]. In general, the di-chalcogenides are 2-D while the tri-chalcogenides are 1-D.

The technological applications and fundamental properties of TMCs have generated a consistently high level of scientific interest over a period of several decades. Correspondingly there has been a great deal of scientific work devoted to the synthesis and preparation of TMCs. There are several comprehensive reviews available to the reader which deal with the structure, synthesis and properties of bulk TMCs (e.g. references [25-27]). Moreover, synthetic methodologies have also been developed to produce TMCs with dimensions on the nanoscale [5,28-30]. In this thesis, TMCs are studied with nanoscale morphologies, namely thin films of CdTe and Cu_xTe and nanoribbons of TaS_3. Although nanomaterials have been known for several decades (e.g. Au nanoparticles), the ability to characterise nanomaterials has only recently developed. In particular, it is the development of transmission electron microscopy (TEM), that has enabled researchers to visualise and characterise nanomaterials on the atomic scale. The high resolution nature of TEM is used extensively in this thesis. TMCs with nanoscale morphologies promise applications in areas such as electronics, whereby TMCs have been grown as conducting nanowires and transistors [31].

In some sense the concept of nanomaterials can be extended to include thin films as the normal definition of a nanomaterial is having at least one spatial dimension in the region of 1-500 nm. Thin films studied here have thicknesses of the order of 1 nm or less and no greater than 100 nm and hence fit into this categorisation. The study of metallic thin films has been at the heart of surface science and the wider condensed matter physics communities for several decades [32-35]. This thesis continues the investigation of metallic and poly-metallic thin films by studying three related systems of current scientific interest, namely materials used in thin film CdTe photovoltaics. These studies are performed with a range of well established experimental surface science techniques. Often in this thesis, surface science experiments are combined with TEM to provide a fuller understanding of the systems studied, a combination of techniques that is seldom used. The merits of each set of techniques are assessed and compared on a particular system. With the reduction in volume, the surface and near surface regions becomes an increasingly larger proportion of the entire material. Hence, the use of surface techniques is particularly important in determining structure and composition of nanomaterials.

The first two experimental chapters (chapters 3 and 4) describe studies of the interfaces and growth of components of high efficiency CdTe thin film photovoltaic devices. The first experimental chapter in this thesis, chapter 3, looks at the growth modes of Te on Cu(111) using XPS, UPS, LEED and STM. The Cu-Te system is of interest because of the role of Cu_xTe alloys in high efficiency CdTe photovoltaic devices. The Cu_xTe layer forms a pseudo-ohmic back contact to the CdTe layer, which is essential to achieve high efficiency [36]. Previous studies have tended to focus on the practical performance of the device and its phases [37,38]. Here, the structural and thermal properties of the model Te/Cu(111) system is studied and compared with Te on Cu_{poly}, the situation that is typical of practical CdTe photovoltaics. In chapter 4, the study of CdTe photovoltaics is extended to the CdTe layer. Although CdTe has been subject to intensive study due to its near ideal band gap for the absorption of solar radiation, to our knowledge no fundamental studies of the growth of CdTe on Cu and Cu_xTe surfaces have been published. Instead, studies have again been inclined to centre on practical aspects of polycrystalline cells (for reviews see, for example, references [9,39-41]). Sections 4.2.2 and 4.2.3 provide a surface science study of the growth of CdTe on model Cu(111) and Te/Cu(111) surfaces, respectively. The focus of the investigation in section 4.2.4 then turns to more realistic systems, in terms of the practical CdTe photovoltaic device: the deposition of CdTe onto Cu_{poly} and Cu_{poly} that has been pre-treated with Te to simulate practical back contact formation. This study uses both surface science and TEM techniques to give a unique picture into the heterogeneous nature of the CdTe film. The CdTe films studied in this section are quite thick (~50 nm) and

thus surface science and TEM allows us to compare the surface composition of the film with the structure deeper within the film, which surface science probes cannot reach. We believe that using a combination of surface science techniques and electron microscopy produces a more comprehensive picture of the Cu/CdTe system than has been previously published. For example, there is debate on where Cu resides when it diffuses into the CdTe host structure: it either substitutes for Cd (forming Cu_2Te) or is located in interstitial sites. Using TEM and XPS, it was shown that Cu diffusion predominantly leads to Cu_2Te crystallite formation in the CdTe film with a tendency for these Cu_2Te crystallites to segregate at the surface.

A feature of Cu-Te alloying developed in the course of this thesis is the effect of the "openness" of the Cu substrate in determining the thermal and structural properties of the particular Cu-Te alloy phase formed. Stepped or vicinal surfaces have long been of interest to surface science because of their increased reactivity due to reduced co-ordination of surface atoms. For example, stepped surfaces of Pt have been shown to enhance the reaction of CH_4O to CO_2 [42] and the Au(997) surface was shown to increase reactivity of NO decomposition [43]. As previously stated, chapter 3 deals with the deposition of Te onto Cu(111) and Cu_{poly} systems. The (111) substrate is a flat, closed packed arrangement of Cu atoms. At the other end of the scale in terms of the openness of the Cu substrate, is the deposition of Te onto the rough, Cu_{poly} substrate, which is also studied in chapter 3. The stepped nature of the Cu(643) surface was seen as an intermediate between the two extremes of Cu(111) and Cu_{poly}. Chapter 5 describes the deposition of Te onto the stepped and kinked Cu(643) surface, which was deemed worthy of a separate chapter as this chapter also deals extensively with surface chirality. The study of metallic growth on chiral surfaces is still a developing field and thus the chapter begins by summarising the previous work. Indeed, the deposition of thin metallic films onto chiral metallic surfaces is very limited, with only a few published studies [41,44]. Moreover, the growth of metals that alloy in the bulk (i.e. Cu and Te) has, to our knowledge, never been studied using a chiral substrate. Hence, Te/Cu(643) is the first example of such an alloy system. Interestingly, our work shows that chiral alloy structures form, in addition to significant faceting of the Cu(643) surface.

The systems studied in chapters 3, 4 and 5 are thin films and naturally lend themselves well to being studied with surface science measurements. In chapter 6 we extend our studies to a whole nanomaterial: TaS_3 nanoribbons. The application of surface science techniques to a nanomaterial of this kind is somewhat unusual, with researchers tending to study them with X-ray diffraction and electron microscopy as the morphology and bulk crystal structure of the nanomaterial is of upmost importance. Here, a combination of

surface science techniques, X-ray diffraction and electron microscopy are employed to provide insight into the differences between the core and the shell of the nanoribbon. The surface sensitivity of the photoemission spectroscopies allows for the shell of the material to be probed in detail, and revealed that the shell and core were structurally dissimilar. The core-shell structure of TaS_3 has perhaps been overlooked previously but would nevertheless be of crucial importance in device fabrication. For instance, if TaS_3 was used as a conducting wire, the additional interface between the core and shell would impede electron transport through the material.

1.2 References

[1] A. Shah, P. Torres, R. Tscharner, N. Wyrsch, H. Keppner, *Science* **285** (1999) 692.

[2] F.J. DiSalvo, *Science*, **285** (1999) 703.

[3] F. Britt, C. Ferekides, *Appl. Phys. Letts*, **62** (1993) 2851.

[4] S. Megahed, B. Scrosati, *J. Power Sources* **51** (1994) 79.

[5] C.N.R. Rao, F. Deepak, G. Gundiah and A. Govindaraj, *Prog. Sol. Stat. Chem*. **31** (2003) 5.

[6] *Scotland's Renewable Energy Potential: Realising the 2020 Target—Future Generation Group Report* (2005) Forum for Renewable Energy Development in Scotland (FREDS). Edinburgh. ISBN: 0-7559-4721-5.

[7] A. Goetzberger, C. Hebling, H.W. Schock, *Mater. Sci. Eng. R* **40** (2003) 1.

[8] M. Kaku, *Physics of the Future* (Penguin Books) 2012.

[9] A. Bosio, A. Romeo, D. Menossi, S. Mazzamuto, N. Romeo, *Cryst. Res. Technol*. **46** (2011) 857.

[10] J.R. Sootsman, D.Y. Chung, M.G. Kanatzidis, *Angew. Chem. Int. Ed.* **48** (2009) 8616.

[11] M. Ferhat, J. Nagao, *J. Appl. Phys.* **88** (2000) 813.

[12] G. Chen, M.S. Dresselhaus, G. Dresselhaus, J.P. Fleurial, T. Caillat, *Int. Mater. Rev.* **48** (2003) 45.

[13] T.M. Tritt, M.A. Subramanian, *MRS Bull.* **31** (2006) 188.

[14] J.B. Bates, G.R. Gruzalski, N.J. Dudney, C.F. Luck, X.H. Yu, *Solid State Ionics* **70** (1994) 619.

[15] T. Giamarch, *Quantum Physics in One Dimension* (Clarendon Press) 2004

[16] R.V. Coleman, B. Giambattista, P.K. Hansma, A. Johnson, W.W. McNairy, C.G. Slough, *Adv. Phys.* **37** (1988) 559.

[17] A. Meerschault, L. Guemas, J. Rouxel, *J. Sol. Stat. Chem.* **36** (1981) 118.

[18] W. Meissner, *Z. Phys.* **58** (1929) 570.

[19] J. Darby, J. Hatton, B.V. Rollin, *Proc. Phys. Soc. Lond. A*, **63** (1950) 1181.

[20] M.H. Fang, H.M. Pham, B. Qian, T.J. Liu, E.K. Vehstedt, Y. Liu, L. Spinu, Z.Q. Mao, *Phys. Rev. B* **78** (2008) 224503.

[21] H.J. Zhang, C.X. Liu, X.L. Qi, X. Dai, Z. Fang, S.C. Zhang, *Nature Phys.* **5** (2009) 438.

[22] Y. Tanaka, Z. Ren, T. Sato, K. Nakayama, S. Souma, T. Takahaski, K. Segawa, Y. Ando, *Nature Phys.* **8** (2012) 800.

[23] B.A. Bernevig, T.L. Hughes, S.C. Zhang, *Science*, **314** (2006) 1751.

[24] X. Dai, T.L. Hughes, X.L. Xi, Z. Fang, S.C. Zhang, *Phys. Rev. B* **77** (2008) 125319.

[25] J.A. Wilson, A.D. Yoffe, *Adv. Phys* **18** (1969) 193.

[26] F.K. McTaggart, *Aust. J. Chem* **11** (1958) 471.

[27] F. Jellinek, *React. Solid.* **5** (1988) 323.

[28] W. Shi, R. W. Hughes, S.J. Denholme, D.H. Gregory, *Cryst. Eng. Comm.* **12** (2010) 641.

[29] C.N.R. Rao, M. Nath, *Dalton Trans.*, **1** (2003) 1.

[30] C.N.R. Rao, S.R.C. Vivekchand, K. Biswas, A. Govindaraj, *Dalton Trans.* **34** (2007) 3728.

[31] Y. Xia, P. Yang, Y. Sun, Y. Wu, B. Mayers, B. Gates, Y. Yin, F. Kim,H. Yan, *Adv. Mater.* **15** (2003) 353.

[32] E. Bauer, *Z. Krist.* **110** (1958) 372.

[33] E. Bauer, *Appl. Surface Sci.* **11-12** (1982) 479.

[34] H. Lassen, L. Brück, *Ann. Physik* **22** (1935) 233.

[35] J.P. Biberian, G.A. Somorjai, *J. Vacuum Sci. Technol.* **16** (1979) 2973.

[36] X. Wu*, Sol. Energy* **77** (2004) 803.

[37] S.S. Hegedus, B.E. McCandless, *Sol. Energy Mater. Sol. Cells* **88** (2005) 75.

[38] K.D. Dobson, I. Visoly-Fisher, G. Hodes, D. Cahen, *Sol. Energy Mater. Sol. Cells* **62** (2000) 295.

[39] Z. Fang, X.C. Wang, H.C. Wu, C.Z. Zhao, *Int. J. Photoenergy* (2011) 297350.

[40] M.M. Aliyu, M.A. Islam, N.R. Hamzah, M.R. Karim, M.A. Matin, K. Sopian, N. Amin, *Int. J. Photoenergy*, (2012) 351381.

[41] A.J. Francis, A.J. Koritnik, A. Gellman, P.A. Salvador, *Surf. Sci.* **601** (2007) 1930.

[42] L.P. Ford, P. Blowers, R.I. Masel, *J. Vac. Sci. Technol. A* **17** (1999) 1705.

[43] Z. Wu, Y. Ma, Y. Zhang, L. Xu, B. Chen, Q. Yuan, W. Huang, *J. Phys. Chem. C* **116** (2012) 3608.

[44] O.A. Hazzazi, C.A. Harris, P.B. Wells, G.A. Attard, *Top. Catal.* **54** (2011) 1392.

2. Theory and Instrumentation

2.1 Introduction

This chapter gives a brief introduction into the experimental considerations and techniques encountered in this thesis and a description of the equipment employed to carry out experiments. Two different types of experiment were used extensively: transmission electron microscopy (TEM) and surface science. In a different sense, the techniques could also be split into spectroscopy and microscopy: the former being essential in understanding the chemistry and the latter in mapping the spatial variations that are inherent to nanomaterials. Throughout this thesis, the results obtained from these different types of experiments will compared and contrasted in the course of presenting the data. The chapter begins with a short discussion on the requirements of ultra high vacuum (UHV) and the surface and bulk sensitivity of electrons then describes the TEM and surface science based techniques used in this thesis. These techniques are X-ray photoelectron spectroscopy (XPS), ultraviolet photoelectron spectroscopy (UPS), low energy electron diffraction (LEED), scanning tunnelling microscopy (STM), TEM, energy dispersive X-ray spectroscopy, (EDS), electron energy loss spectroscopy (EELS), energy filtered transmission electron microscopy (EFTEM), and scanning electron microscopy (SEM). For a more detailed description of thin film growth, UHV and surface science techniques (XPS, UPS LEED, STM) see references [1-3]. For a more detailed description of EDS, EELS, EFTEM and TEM see references [4-6] (for EFTEM and EELS also see [7]). For more a more detailed description of SEM, see reference [8].

Two separate UHV chambers were used in the course of this project. The most extensively used UHV system was at the University of Glasgow and was used to acquire XPS, UPS and LEED data. The second UHV system was at the University of Liverpool and was primarily used to collect STM data. TEM was carried out either using FEI Tecnai TF20 or T20 microscopes. SEM was performed using a FEI Novobeam 200 SEM instrument. All SEM and TEM was carried out in the School of Physics and Astronomy at the University of Glasgow.

2.2 Ultra High Vacuum (UHV) Systems

In this thesis, the growth and structure of thin films and surfaces is studied on the atomic scale and it is therefore a necessity that the composition and structure of the surfaces do not change over the course of an experiment. This means that the rate of new chemical species being introduced to the surface by the surrounding gas phase molecules should

be low. In other words, we wish to minimise the amount of atomic and molecular adsorption. From the kinetic theory of gases it can be shown that [1]:

$$r = \frac{2.64\times10^{22}P}{(TM)^{0.5}} \qquad (2.1)$$

where r is the rate of arrival of atoms and/or molecules at the surface in units of $cm^{-2}s^{-1}$, P is the pressure in mbar, T is the temperature in Kelvin and M is the average molecular mass of the incident atoms and/or molecules. For the surface techniques used here (XPS, UPS, LEED and STM), acquisition times are approximately 2-3 hours per experiment. At 10^{-10} mbar, the time it would take for an entire monolayer (ML) to be incident on the film would be around 20 hours, for a close-packed Cu(111) lattice with ~2 x 10^{15} atoms per cm^2. Therefore achieving a base pressure in the region 10^{-10} mbar is required so that clean surfaces can be studied with confidence and reproducibility. At 10^{-10} mbar, the residual gases remaining in the chamber are H_2, CO and CO_2.

The two UHV chambers used in this thesis had base pressures of between 1 and 2 x 10^{-10} mbar. The SEM and TEM systems operate at high vacuum (10^{-6} - 10^{-8} mbar) rather than UHV and will be described separately in section 2.4.1. Figure 2.1 shows a labelled image of the XPS/UPS/LEED chamber located in the School of Chemistry at the University of Glasgow, which was the primary system used in this thesis. The main pumping of the XPS/UPS/LEED chamber was with a diffusion pump with a cryogenically cooled baffle, labelled in figure 2.1. Before pumping the chamber with the diffusion pump, the chamber was initially pumped to a rough vacuum (~10^{-3} mbar) with a rotary pump, shown at the bottom left hand corner of figure 2.1. At ~10^{-3} mbar, gas molecules have a mean free path length approaching the dimensions of the chamber and therefore do not constantly collide with each other. This means that the gas molecules no longer obey viscous flow dynamics and a simple displacement pump (the rotary pump here) cannot reduce the pressure further. Instead, gas molecules now follow molecular flow dynamics, whereby gas molecules can be thought of as of only colliding with the walls of the chamber. The diffusion pump works effectively in this flow regime and reduces the pressure further to ~10^{-7} mbar. At ~10^{-7} mbar, the pressure is limited by the slow desorption of water molecules from the chamber walls. To speed up this process, the chamber is baked at ~400 K for 48 hours. This rapidly increases the rate of water desorption and once cooled, improves the vacuum to 10^{-10} mbar. A titanium sublimation pump (TSP) provides additional pumping, especially of reactive species (e.g. CO, H_2).

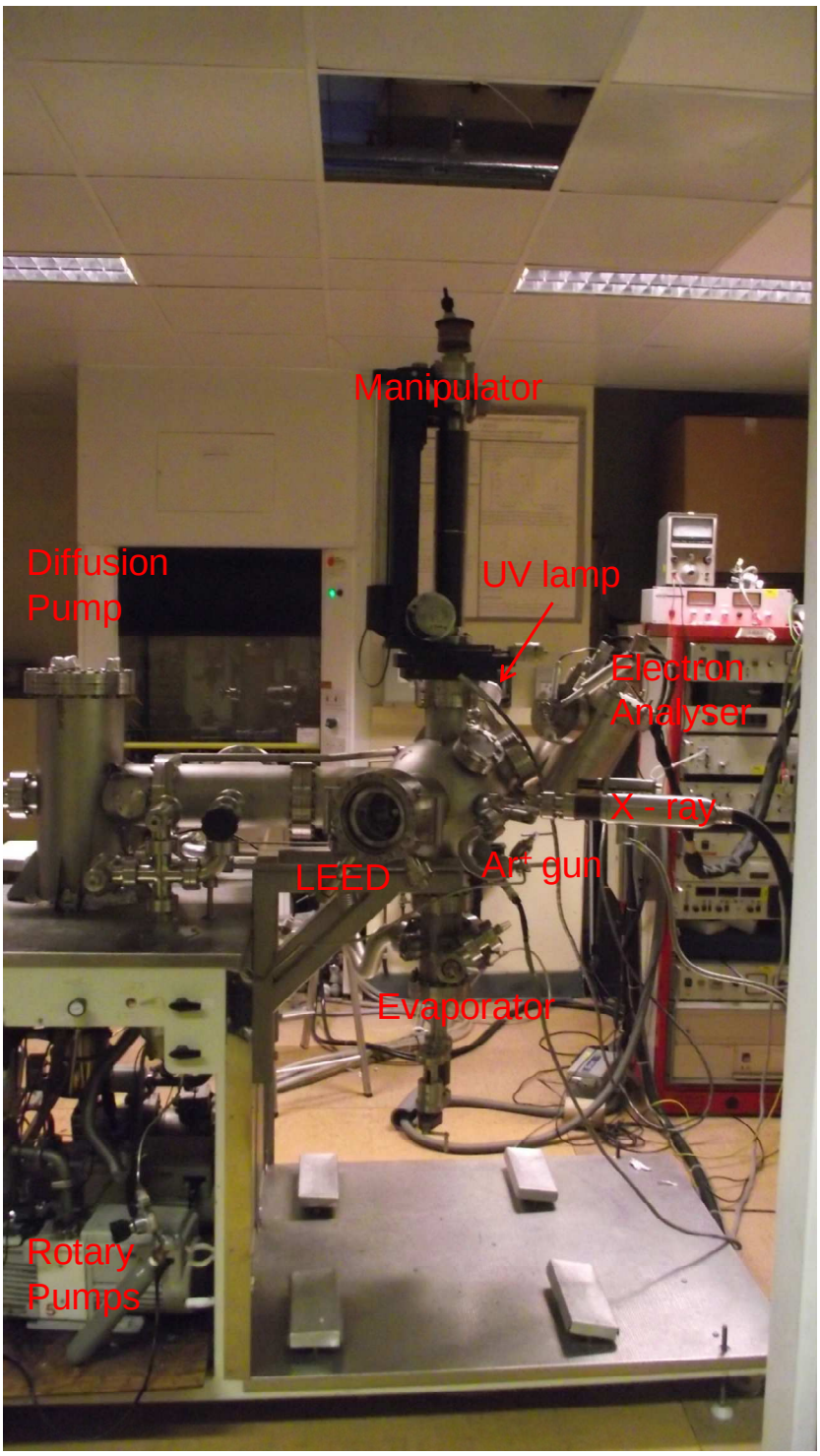

Figure 2.1. Labelled image of the XPS/UPS/LEED chamber. The diffusion pump, labelled, acted as the main pump for the chamber. Ar^+ gun was used to clean specimens *in situ*. The evaporator was used to deposit thin films on the clean specimen surface. The chamber also had a TSP and mass spectrometer (out of view). A mass spectrometer was used for residual gas analysis (RGA).

In the XPS/UPS/LEED UHV chamber, figure 2.1, samples were mounted onto a VG SH2 sample holder. The sample holder assembly was attached to a Omnimax Translator manipulator which had the capability for linear motion in the x, y and z directions. The manipulator could also be precisely moved angularly in polar and azimuthal directions.

The sample holder was also fitted with liquid nitrogen cooling. Liquid nitrogen cooling was achieved through a flow of N_2 gas that was condensed by dewar of liquid N_2. The flow of gas from the cylinder ensured that the condensed N_2 passed through the capillaries attached to the manipulator, which meant that the sample could be cooled to 110 K. Heating of the sample was provided by an electron beam heater [9]. The electron beam heater could be operated with or without biasing the thoriated W filament and cathode tray to 650 V DC, relative to the sample plate, which acts as an anode. Without biasing the filament, the sample can only achieve temperatures up to approximately 450 K by radiative heating. Applying the 650 V to the filament and cathode accelerates thermionically emitted electrons towards the sample plate. This process increases the power input (~100 W) into the specimen, which means that temperatures in excess of 1100 K were achieved using a filament current of ~2.5 A. Temperature was measured using a chromel/alumel (K type) thermocouple. The control unit was a proportional-integral-derivative (PID) controller which only requires the user to set a maximum current to accurately heat the sample.

A simple, resistively heated, evaporator was constructed to deposit metals onto a particular substrate for the XPS/UPS/LEED chamber at the University of Glasgow. Figure 2.2 shows an image of the final assembly of the evaporator before it was installed. The feedthrough was attached to a T-piece so that a thermocouple could be mounted to give accurate temperature measurements, figure 2.2 (a). Two Mo crucibles were wrapped in 1 mm diameter W wire and a thermocouple attached to each crucible. The W wire was spot-welded to the steel support rods, as shown in figure 2.2 (b). Mo crucibles were chosen because they do not react with any of the materials deposited (Te, CdTe). The disadvantage of using Mo (or any conductive crucible) is that it will short circuit through the crucible body and thus the heating will come from the heating wires not in contact with the crucible and will therefore take longer to achieve a uniform temperature distribution in crucible.

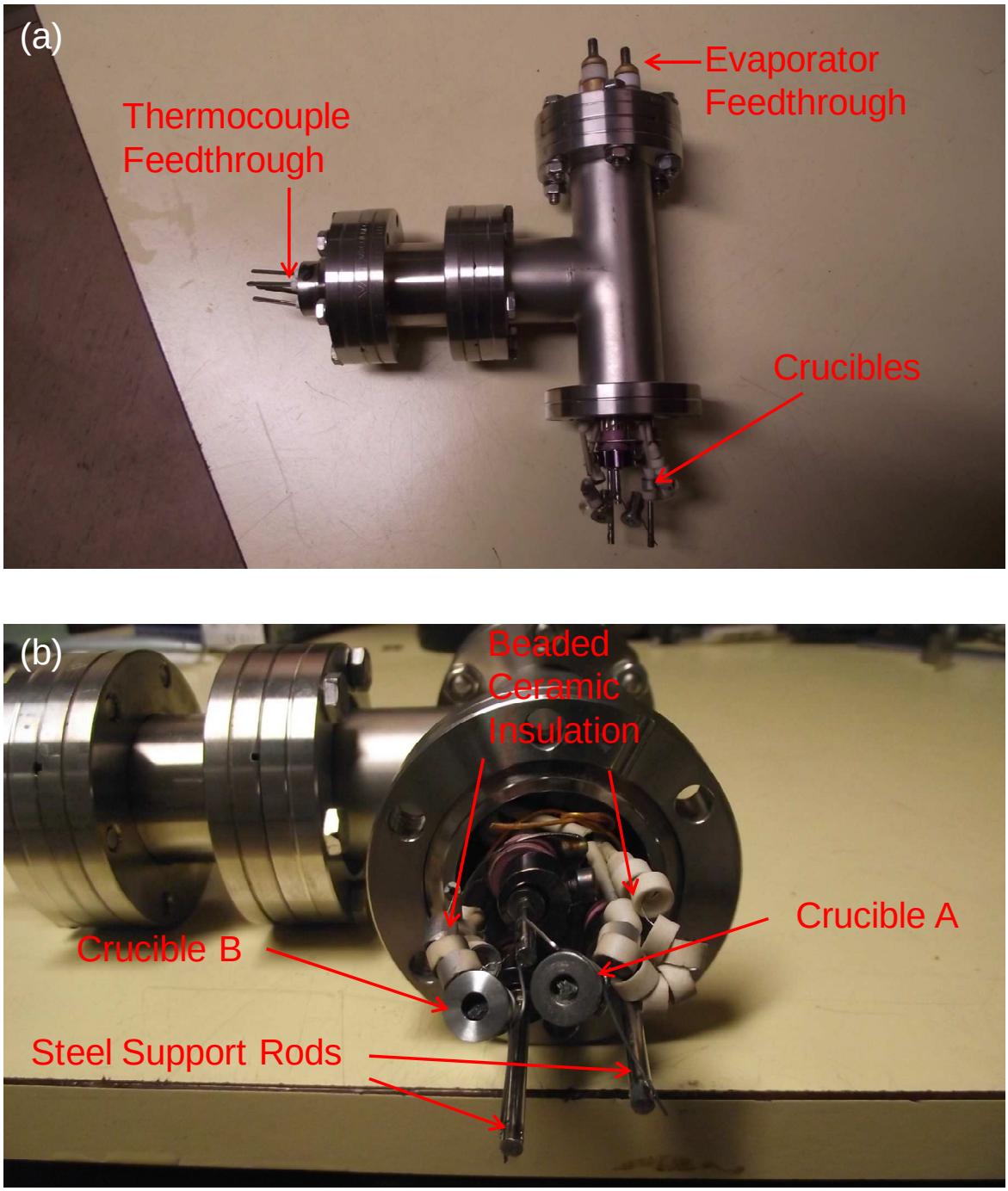

Figure 2.2. (a) Labelled image of the home-built evaporator mounted in the T-piece, before installing. The labels in (a) show the position of the dual evaporators and the thermocouple and power supply feedthroughs. (b) Close up of the crucible end of the evaporator. Beaded ceramic insulation was used to isolate the thermocouple wires from the rest of the evaporator assembly.

Vapour pressure (as a function of temperature) of Te and CdTe was obtained from a database [10]. Several trial runs of heating of the crucible were performed to ascertain the optimum crucible temperature for deposition. The crucible was thoroughly degassed at a temperature ~10-15 K above the desired deposition temperature for 4-6 hours after each bake. The pressure in the chamber did not exceed 2 x 10^{-9} mbar during a Te or CdTe deposition. A shutter was added just in front of the crucible to improve reproducibility of deposition thickness.

Figure 2.3 shows a labelled image of the STM chamber. The STM chamber was housed in the Chadwick Building at the University of Liverpool. An identical procedure was required to achieve UHV conditions (bake at 400 K for 48 hours), except the main pumping of this system was performed with a turbomolecular pump. During acquisition of STM data, the chamber was pumped with an ion pump (labelled on figure 2.3) which eliminated the effects of vibrations from the turbomolecular pump. The sample holder on the STM chamber was a Ta tab that Cu(111) or Cu(643) crystals were spot welded onto. Heating was provided through resistive heating using Ta wires. A ~5 A current was required for the sample to reach 723 K. The temperature of the sample was measured with a pyrometer, with the control of the temperature performed manually by adjusting the current thorough the Ta wires. No cooling experiments were performed on this system. On this system, Te was evaporated from a Ta pouch constructed by Mr. Ian McLeod. The STM chamber had equipment for XPS, UPS and LEED, (not in view in figure 2.3) which were used simply to verify sample preparation and composition as the XPS, UPS and LEED data had already been taken and analysed on the UHV system at the University of Glasgow. The mass spectrometer, labelled in figure 2.3, was used as a RGA.

There were several different methods used to prepare samples for study. Cu single crystals [Cu(111) and Cu(643)] were cleaned by multiple cycles of Ar^+ ion sputtering (10-12 μA, 30 minutes) and annealing (823 K, 30 minutes for Cu(111) and 773 K, 30 minutes for Cu(643). The cleanliness and crystallinity of the Cu surfaces were verified with XPS and LEED. Samples were declared clean when they showed no O 1s, C 1s and S 2s peaks in XPS and a sharp (111) or (643) pattern was observable with LEED. Polycrystalline Cu samples of chapters 4 and 5 were prepared by evaporating Cu from a W basket onto the surface of an oxidised Si wafer. This was done in a standalone evaporation system. The thickness of the Cu film was checked with AFM and confirmed by TEM. The TaS_3 specimens used in chapter 6 were dispersed in ethanol and spotted on a Si or Au substrate for study in UHV. The substrate was then mounted on the VG SH2 holder and inserted into the UHV chamber, shown in figure 2.1. TaS_3 nanoribbons were prepared for study in the TEM by dispersing them in ethanol and spotting on a holey

carbon grid. TEM cross-sections of CdTe thin films were prepared using a focussed ion beam (FIB) system. The focussed beam (Ga^+ ions accelerated through 30 kV) was used to mill a well defined section of the specimen. The section was then lifted out and welded to a Cu grid. The specimen was then thinned to less than 100 nm using the FIB (so that it was transparent to electrons), ready for insertion into the microscope.

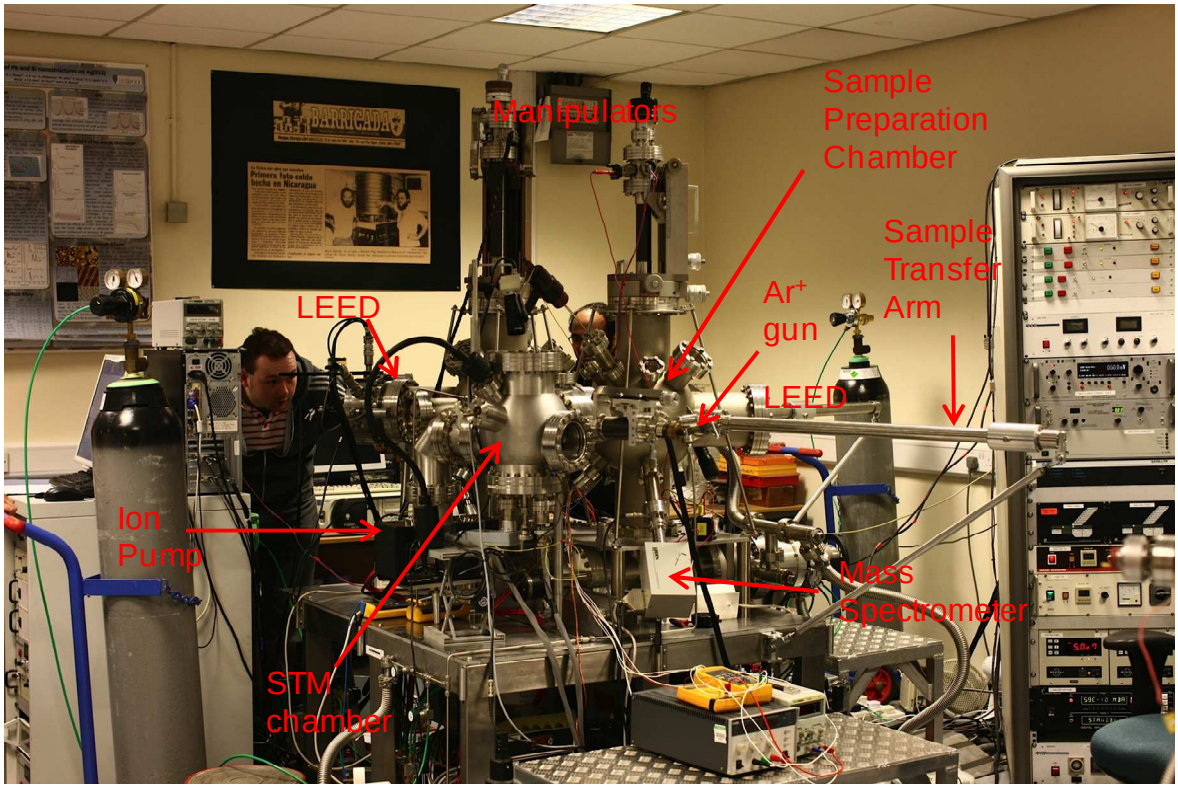

Figure 2.3. Labelled image of the STM chamber at the University of Liverpool. The STM chamber contains 3 interlinked chambers: a sample preparation chamber equipped with an Ar^+ sputter gun and LEED optic; an analysis chamber with XPS, UPS and LEED and the dedicated STM chamber.

2.3 Surface and Bulk Sensitivity of Electrons

Electrons are commonly used as a probe of the structure of solid materials. In this thesis, we use different energies of electrons to selectively probe the bulk and the surface of a material. The length that an electron can travel in a solid before it is inelastically scattered is dependent on the kinetic energy of the electron and the material in which it is travelling, as shown in figure 2.4. This distance is termed the inelastic mean free path (IMFP) length and can be thought of as an attenuation length (although the they are not strictly speaking

interchangeable) in that it is the thickness of a material required to reduce the number of unscattered electrons by a factor of 1/e.

The electrons that are typically detected in XPS and LEED have kinetic energies of 30-1000 eV. The IMFP of electrons in this energy range has been well documented and leads to the so called universal curve, shown in figure 2.4. Thus in XPS and LEED, electrons have an IMFP length of only a 0.5-2 nm and therefore, the useful information gleaned from these techniques originates from the top few nanometres of a sample, giving these techniques their surface sensitivity [2]. Electrons with a kinetic energy of less than ~20 eV cannot excite plasmon resonances and hence have a longer mean free path, as shown in figure 2.4. Consequently, electrons detected in UPS are less surface sensitive and information comes from the uppermost 1-10 nm [2]. In contrast, electrons in TEM have kinetic energies of 200 keV and have IMFP of 10-100 nm and thus can be thought of as passing through the entire thickness of a thin specimen [4], where typical TEM specimens are less than 100 nm thick.

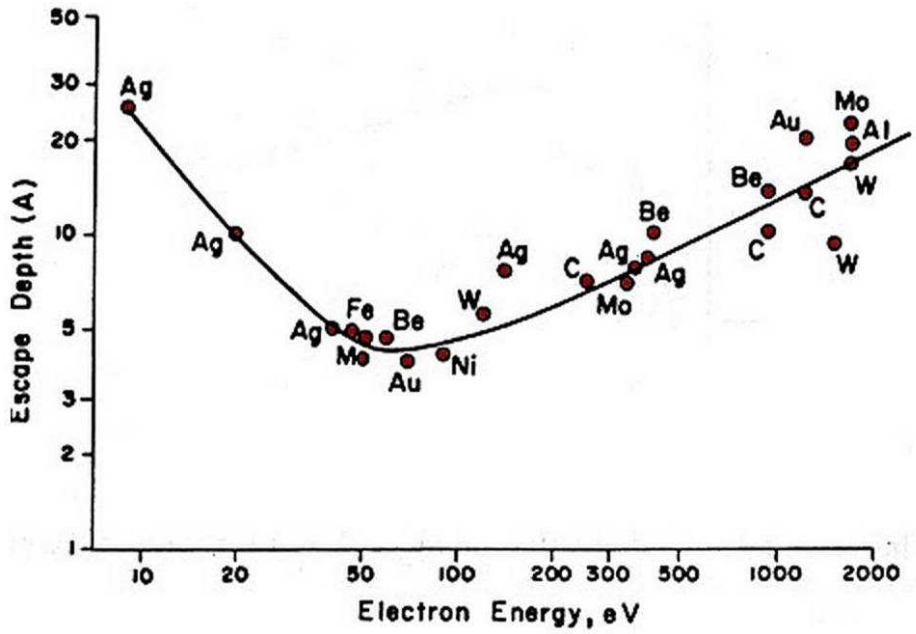

Figure 2.4. Mean free path length of an electron in a given solid derived from experiment and the comparison with theory. The red dots are measured from experiment and the black line is theoretical model. The figure is extracted from [2].

2.4 Techniques

2.4.1 Microscopy

Microscopy is an especially large field and encompasses such techniques as: optical, atomic, scanning probe and electron microscopes. In all cases, microscopy yields local, real space information about a specimen. In this thesis, we used a scanning probe microscope - the scanning tunnelling microscope (STM) - and two different electron microscopes - the scanning electron microscope (SEM) and the transmission electron microscope (TEM). As each technique is distinct, this section will describe each in turn.

2.4.1.1 Scanning Tunnelling Microscope (STM)

The STM provides high resolution images of a surface. For well defined single crystal surfaces, it can be used for imaging individual atoms. The STM operates by scanning an atomically sharp tip across the surface of a sample, shown in figure 2.5 as a pyramid of atoms transversing across an atomically flat surface. A voltage is applied between the tip and the sample, causing electrons to quantum mechanically tunnel in or out of the tip, depending on the bias applied between tip and sample. The tunnelling current is a result of the quantum mechanical electron wavefunction leaking out of its confining potential well which occurs for all finite potential wells. It can be shown that the tunnelling current (at low voltages) is proportional to the exponential of the distance between sample and tip [1]:

$$I \propto \exp(-2Kd). \tag{2.2}$$

K is given by:

$$K = h^{-1}(2m\phi)^{1/2}, \tag{2.3}$$

where d is the distance between the sample and the tip, h is Plank's constant, m is the mass of the electron and ϕ is the effective local work function.

A negative tip voltage will cause electrons to tunnel out of the tip into the sample, effectively probing the sample's electronic unoccupied density of states (DOS). A positive tip voltage causes electrons to tunnel from the sample into the tip, effectively probing the sample's occupied DOS. The STM can provide very accurate measurements of height above a surface because the tunnelling current drops off exponentially with sample tip

distance. For example, if the value of ϕ = 4 eV is inserted into equation 2.3, then K = 10 nm^{-1}. If one then sets up a feedback loop to maintain the current to within a few percent, then the gap, d, remains constant to 0.001 nm. In practice, vibrations mean that the working vertical resolution of the STM is around 0.01 nm. The lateral resolution is governed by the precision of which the piezoelectric scanners can be positioned and the lateral confinement of the tunnelling current, which is typically around 0.1 nm. A schematic of a STM is shown in figure 2.5, describing, in general terms, how STM images are acquired.

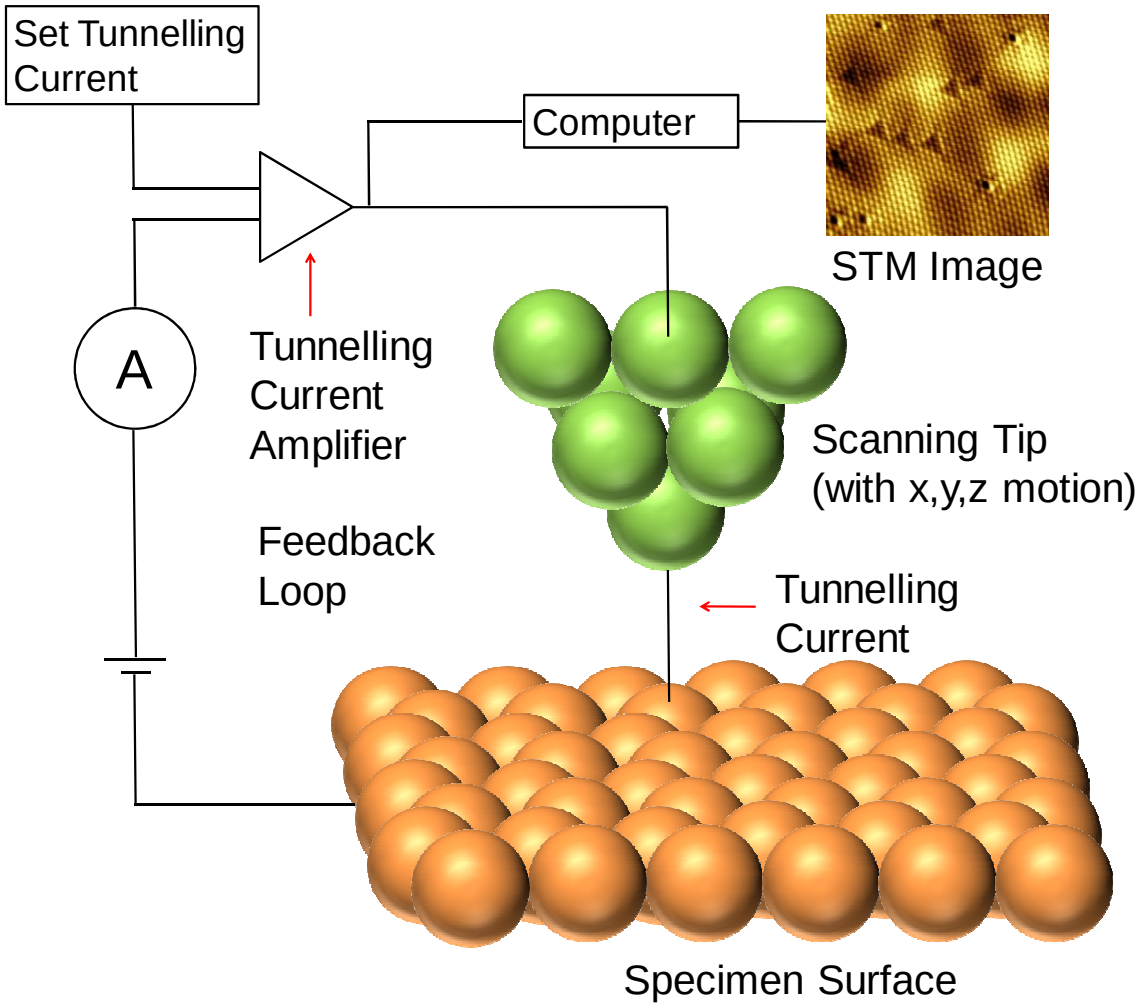

Figure 2.5. Schematic diagram showing the operation of the STM. The tip, shown in green, is scanned across the surface, and the image built up point by point. In constant current mode the image contrast is derived from variations in z, the height of tip above the surface. The feedback loop adjusts the height to maintain a constant tunnelling current. Figure is based on schematic in [1].

The STM can operate in two different modes: constant height and constant current. In constant current mode, used in this thesis, a tunnelling current and applied voltage is set by the user (typically 100-1000 pA and 1-2 V) and the tip brought close to the surface so that a user defined tunnelling current can be measured. Constant height mode was preferred because it measures height changes on surfaces well, which was of importance on the stepped Cu(643) surface, described in chapter 5. When the tip is scanned across the surface (the x-y direction), it encounters variations in height, composition, structure etc., causing an instantaneous change in current. An electronic feedback loop corrects the change in voltage by changing the sample-tip distance (d). This variation of d as a function of the x and y positions of the piezoelectric (i.e. $d(x,y)$) gives rise to contrast in an image. In constant height mode, the user sets a working height, typically a few nm, and an applied voltage. As the tip is scanned the tunnelling current changes (in constant height mode) with position due to changes in topography and composition. STM is sensitive to topography because, by equation 2.34, tunnelling current is proportional to sample tip distance. STM is also sensitive to composition because different atoms have different electronic DOS close to the Fermi level (E_F), and hence the tunnelling current will be different even though there is no (or virtually no) height difference. Examples of composition dependent tunnelling currents will be discussed in the following paragraph.

Bimetallic or alloyed surfaces often show interesting changes in apparent height which have been in fact ascribed to changes in composition. These studies are of relevance because this thesis is also concerned with alloyed surfaces. As the STM probes the local electronic structure of the surface, extra care must be taken when more than one atomic species is present on the surface. One might naively think that adsorbate atoms would be visualised in the STM images as new protrusions on the surface [11]. This simple model is often incorrect, as demonstrated by studies of the O/V(100) [12] and Br/Cu(100) [13] systems. In O/V(100), dips in STM images were assigned to O adatoms and bright protrusions were assigned to unoccupied four hold hollow sites on the surface. In the Br/Cu(100) system, Cu atoms were imaged as bright protrusions while dips were Br adatoms occupying the fourfold hollow sites, illustrating that adatoms, although sitting physically closer to the tip, may be imaged as hollows. For alloyed surfaces, the situation is also complex. The substitutional nature of some surface alloys means that often the substrate is imaged as protrusions even though the adatom may be physically closer to the tip. An example of this is the Au/Ni(110) system [14]. The STM images show the substituted Au as shallow vacancies, even though Au is a larger atom than Ni and thus should protrude further from the surface. These examples illustrate that extra care must be taken when deducing the atomic structure of overlayers from STM images, which is appropriate for this thesis as Te is deposited on Cu. Often STM and microscopy in general

is used in conjunction with another structural or chemical probe (e.g. LEED, XPS), to correlate the observed structure. Here, STM acts an invaluable probe of local, real space structure.

The STM was housed within the UHV system at the University of Liverpool. It was a commercially available Omicron STM-1 instrument [15], capable of operating only at room temperature. The instrument was computer controlled with the MATRIX software provided by Omicron. The STM tips were made of W and were produced "in house" by electrochemical etching in concentrated nitric acid. To reduce vibrations, the sample holder was magnetically levitated. The STM was operated by manually bringing the tip close to the surface by eye. When sufficiently close to the surface, the user applied a tunnelling voltage (typically ~1 V) and initiated a computer controlled routine. This moved the tip close enough so that a measurable tunnelling current (typically 500-700 pA) could be achieved. The system was then ready to collect data. The scanning tip was cleaned by applying a voltage pulse of ~5 V. During operation, the user could define the scan area (both in terms of position on the surface and magnification), scan acquisition time and the tip tunnelling parameters (tunnelling current, tunnelling voltage and feedback loop gain) using the MATRIX software. When the scan area and acquisition time were defined by the user, the computer physically changes the voltages applied to the (x, y) piezoelectric drives (the scan area) and at which rate the voltages are changed (scan time). The tunnelling parameters determine how the local DOS are probed. The acquisition time was kept short (< 10 s per image) to limit drift.

2.4.1.2 Transmission Electron Microscope (TEM)

As described above, STM provides atomic imaging of surfaces. By preparing cross sections of specimens, TEM can provide high resolution imaging and structural and elemental analysis of bulk specimens. The bulk specimens must be thinned so that they are transparent to electrons, which is normally less than 100 nm thick. Nanomaterials (e.g. the TaS_3 nanoribbons described in chapter 6) are often of the order of 100 nm thick so are therefore convenient to study with TEM without further preparation. Electrons in the TEM are accelerated through much higher potentials than in LEED (100-300 kV in TEM as opposed to 30-300 V in LEED). This means that electrons are travelling a significant proportion of the speed of light, which make relativistic effects a factor in calculating the de Broglie wavelength. Therefore, equation 2.4 must be used:

$$\lambda = \frac{h}{[2m_0 eV(1+\frac{eV}{2m_0 c^2}]^{1/2}} \quad (2.4)$$

where λ is the de Broglie wavelength of the electron, h is Plank's constant, e is the fundamental charge, V is the accelerating voltage, c is the speed of light and m_0 is the rest mass of the electron. Using 100-300 kV, a value of λ = 3.7-1.9 pm is achieved. The actual resolution of the microscope is much less than this due to aberrations and limitations in the imaging system [16]. However, significant work has been done in correcting aberrations [17] and new aberration corrected microscopes are now commercially available. TEM was performed on a combination of FEI Tecnai T20 and Tecnai TF20 instruments. The T20 instrument had a thermionic LaB_6 source and was capable of performing BF imaging; HRTEM, CBED, SAED and EFTEM. The TF20 had a thermally assisted Schottky field emission gun (FEG) and in addition to the functionalities of the T20, it had added EELS and EDS capabilities, offering high spatial and energy resolution studies.

To illuminate the sample in TEM, a source of electrons is required, of which, there are two general types [4]. The first of which is a thermionic source, which in the case of the T20, was a LaB_6 filament. The source was heated to 1700 K, which gives electrons sufficient energy to overcome the work function of the material and be thermionically emitted. Once free of the filament, electrons were accelerated to the operating voltage of the microscope, in the T20 and TF20 microscopes, V = 200 kV. The second type is the FEG. A fine W crystal is placed close to an extraction anode. A high voltage (typically a few kV), is placed on the anode, producing a very high electric field at the tip. The key aspect of this design is the fine tip of the W crystal, which accentuates the electric field and allows for greater electron extraction. The anode voltage effectively reduces the potential barrier and allows electrons to tunnel through. The electron source on the TF20 was a thermally assisted Schottky FEG. The W filament was coated in a thin film of ZrO_2 which reduces the work function and thus allows a greater flux of electrons leaving the filament. The thermionic source was more robust than the FEG as the FEG requires higher vacuum conditions to prevent contamination. However, FEGs produce more intense beams of electrons and have a narrower spread of energies than thermionic sources (0.7 eV spread in energy for a Schottky FEG compared to 1.5 eV for a LaB_6 filament).

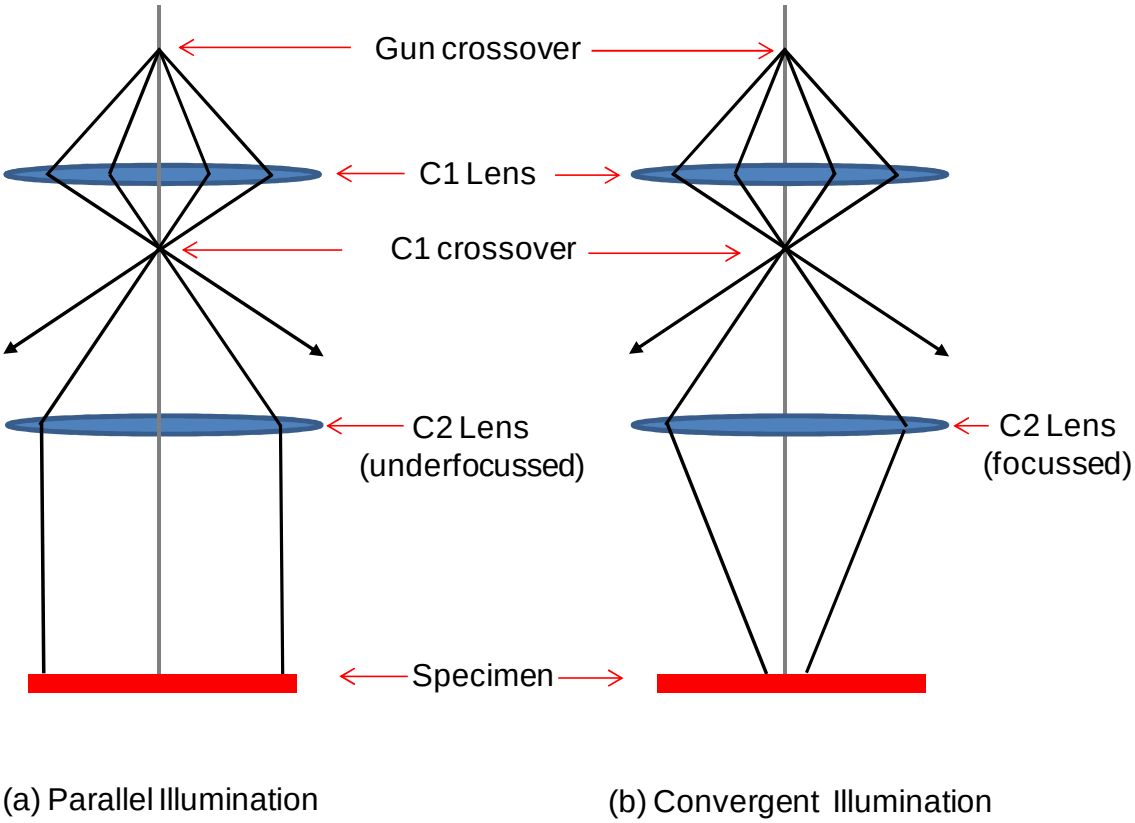

Figure 2.6. Schematic ray diagrams illustrating (a) parallel and (b) convergent illumination of the specimen. Figure is based on diagram in [4].

The T20 used multiple magnetic condenser lens to form the incident beam onto the specimen. There were two modes of operation: the beam of electrons could be spread to make illumination parallel (e.g. for BF, SAED, EFTEM) and illuminate a wide area (up to 100 µm) of the specimen, figure 2.6 (a). Alternatively, the electron beam could be focussed down to a fine probe (e.g. for CBED) to investigate small particles (~30 nm), figure 2.6 (b). Note that parallel illumination was never truly parallel but is far from convergent.

The beam then strikes the specimen. Figure 2.7 shows the interactions that a high energy beam of electrons can have with a thin sample and the possible signals that can be detected. These include, for example, X-rays and Bremsstrahlung for EDS, which will be discussed in section 2.4.2. Inelastically scattered electrons are also produced that are transmitted through the specimen and can be used to form EELS or EFTEM data sets. Electrons incident on a thin specimen can also be elastically scattered, figure 2.8, when passing through the sample, whereby they lose no (or virtually no) energy. The angle of scattering is dependent on how close the incident electron passes to the nucleus. If the

electron passes particularly close it may be elastically backscattered which gives rises to Rutherford Backscattering Spectroscopy. However, as we are dealing with TEM, we are interested in transmitted signals. When an electron passes close to the nucleus, the interaction is strong and the electron is scattered through a high angle. When the electron passes some distance from the nucleus, the electrons effectively screen the incident electron and it is scattered through a small angle. This effect is shown in figure 2.8.

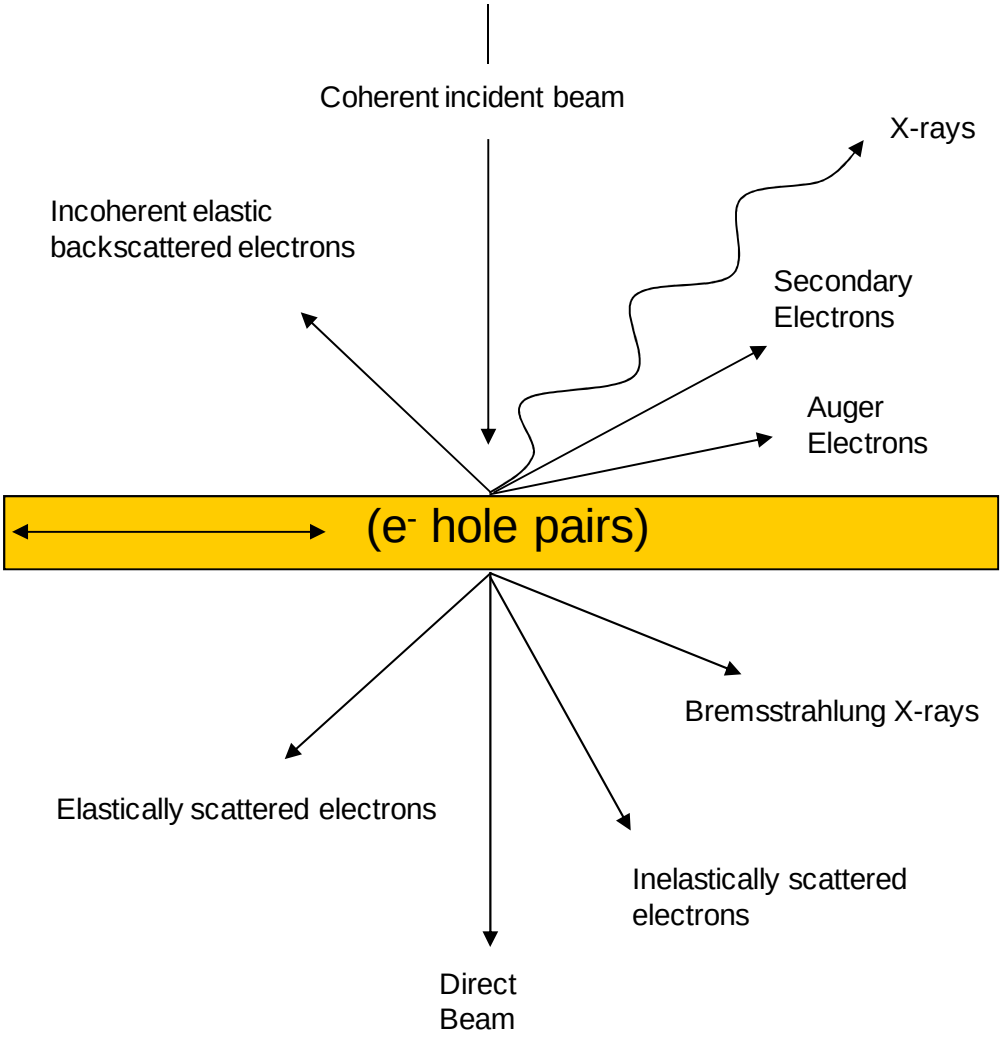

Figure 2.7. Schematic showing the interactions of a focussed electron beam with a specimen, showing the underlying processes occurring in SEM and TEM. Note that for TEM, a thin specimen is required, with thickness less than 100 nm. Whilst in SEM there is no transmitted beam detected.

A scattering factor, $f(\theta)$, can be derived to quantify the interaction of the electron beam with a lone atom, that takes into account the wave nature of the electron [4]:

$$f(\theta) = \frac{\left(1+\frac{E_0}{m_0 c^2}\right)}{8\pi a_0}\left(\frac{\lambda}{\sin\frac{\theta}{2}}\right)^2 (Z - f_x), \tag{2.5}$$

where a_0 is the Bohr radius, λ is the wavelength of the incident electron, E_0 is the incident beam energy, θ is the scattering semi angle, m_0 is the rest mass of the electron, Z is the atomic number of the scattering atom and f_x is the scattering factor for X-rays.

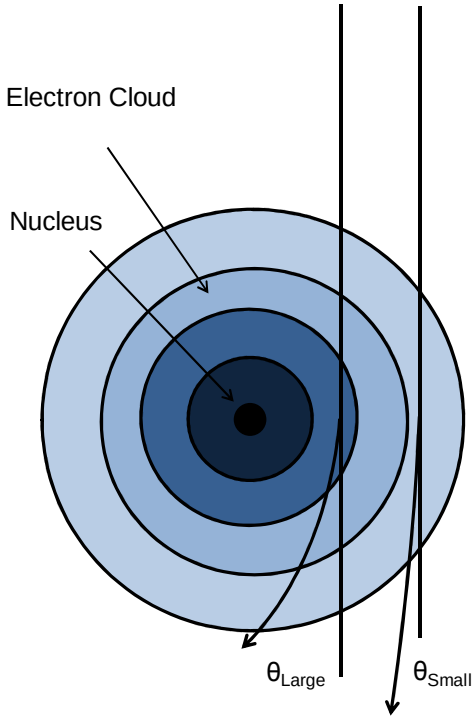

Figure 2.8. A schematic diagram illustrating the difference in high and low angle scattering. Scattering from the electron cloud dominates low angle scattering, while scattering from the nucleus dominates high angle scattering. Figure is based on figure in [4].

The scattering factor defines the angular variation in scattering from an isolated atom. Equation 2.5 indicates that scattering intensity is lower for larger scattering angles. It also indicates that scattering increases for larger values of Z. Specimen thickness (t) also has an effect on scattering because, in a thicker specimen, there are more atoms to scatter from. Hence, a thick specimen containing a high atomic number element will scatter a lot more than a thin, low atomic number specimen and as a result will appear darker on the detector.

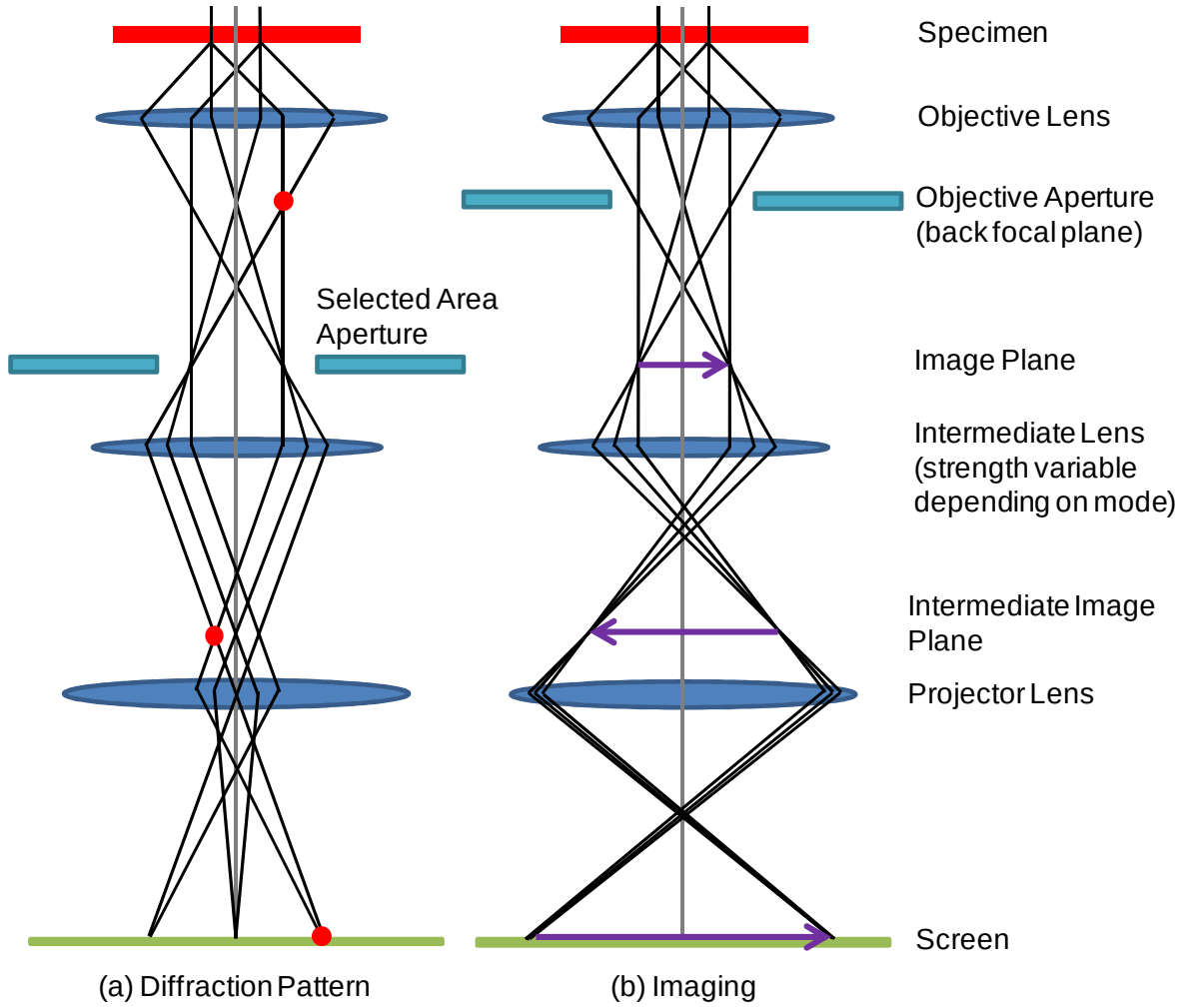

Figure 2.9. Ray diagrams showing how (a) diffraction patterns and (b) images are formed in the TEM. The red dot in (a) shows on which diffraction patterns are formed. The purple arrow in (b) shows on which planes images are formed. Figure is based on figure in [4].

This is called amplitude contrast or Z-t contrast and is a contrast mechanism frequently seen in BF images. Figure 2.9 shows how diffraction patterns and images were formed in the microscope. Electrons exit the back surface of the specimen, as shown in figure 2.9, and propagate down the column. Diffraction patterns and images of the specimen are formed on different planes and thus to view both of them on a static viewing screen additional intermediate and projector lenses were required. On figure 2.9 (a), the red dot represents the plane on which the diffraction pattern was formed, which is initially the back focal plane (BFP). To form the diffraction pattern on the viewing screen, the strength of the intermediate lens was adjusted appropriately. Figure 2.9 (b) shows how a BF image was formed. It is common practice to introduce an objective aperture into the BFP, figure 2.9

(b). The aperture will physically block electrons that have been scattered through wide angles and will therefore improve the contrast. The images were constructed from the electrons that had been either unscattered or only scattered through a small angle, which were normally a significant portion of the incident beam. Therefore these images appeared bright, hence the term BF. The BF image, denoted by a purple arrow on figure 2.9 (b), was formed on the image plane. To view this image on the screen the strength of the intermediate lens was adjusted appropriately to project the image onto the viewing screen.

The diffraction pattern comes from the entire portion of specimen illuminated by the electron beam. In this thesis, nanoribbons have width of the order of 100-500 nm, which is typically smaller than the area illuminated by the beam. In order to reduce the size of the area probed with diffraction, the selected area aperture was inserted. It was inserted into the image plane which is conjugate to the specimen, which is shown in figure 2.9 (a). This gives rises to the term SAED. Alternatively, to reduce the size of the area probed, the incident electron beam could be focussed down to a fine point (the T20 can produce a beam of width ~30 nm). Figure 2.8 (b) illustrates how a fine probe was produced. The CBED technique operates with a fine probe. The ray diagram for CBED is the same as in figure 2.9 (a) except the selected area aperture is removed. The applicability of SAED or CBED depends largely on the size of the particles or grains under study. SAED uses a parallel beam of electrons, but by inserting an aperture, a desired area could be selected. These areas were of the order of 1 µm. Whereas in CBED, the diameter of the incident electron beam could be made as small as ~30 nm which can be used to study small grains or particles. CBED typically contain more information than SAED, for example information about thickness and coherent inelastically scattered electrons (Kikuchi diffraction). CBED patterns were collected from a single crystal Si wafer substrate to act as a calibration for the system. The theory of diffraction will be presented in section 2.4.3.

Images were collected on a Gatan Image Filter (GIF) camera, located beyond the viewing screen (the viewing screen was withdrawn for acquisition with the GIF). Figure 2.10 shows a schematic of the GIF camera set up, consisting of a magnetic sector prism, quadrupole, sextupole lenses and a slow scan charge coupled device (CCD), consisting of 1024 x 1024 pixels. The magnetic prism was a homogeneous magnetic field that is perpendicular to the direction of the electron beam. For ease of design of a microscope, the magnetic field bends the electron beam by 90° and hence the equation for the Lorentz force becomes [4]:

$$\boldsymbol{F} = e(\boldsymbol{v} \times \boldsymbol{B}) = evB, \tag{2.6}$$

where F is the force on the electron, e is the elementary charge, v is the velocity and B is the magnetic field. Equation 2.6 shows that electrons of different velocity (and hence different kinetic energy and different energy loss), will experience a different bend radius and thus emerge from the magnetic sector spatially dispersed.

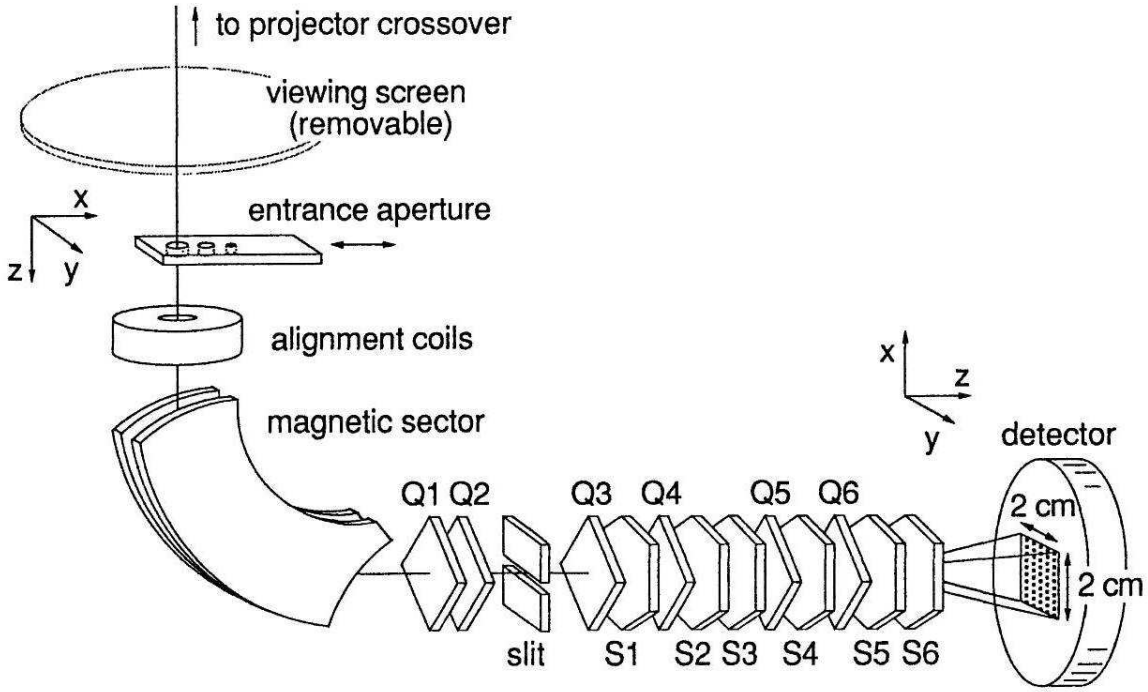

Figure 2.10. Schematic of the GIF camera. The figure is extracted from [18]. Q1-Q6 are quadrupole lenses and S1-S6 are sextupole lenses. The viewing screen in this figure is equivalent to the screen in figure 2.9.

The GIF, shown in figure 2.10, can be used to acquire an EELS spectrum or record a magnified image. The magnitude of excitation of the magnetic prism can be set to form a BF (zero loss) image or it can be used to probe a broad region of the EELS spectrum at relatively low resolution or a smaller region at higher resolution. The energy resolution of the resultant EELS spectrum is determined by the energy spread of the electron source (for LaB_6 filament, the energy spread is 1.5 eV and 0.7 eV for a FEG [4]), the resolution of the magnetic sector and the resolution of the detection system, a CCD. Typical resolution of an EFTEM data set was ~2 eV primarily because the electron source was a LaB_6

filament.

4.2.1.3 Scanning Electron Microscope (SEM)

In addition to the high resolution TEM studies in this thesis, SEM was also used to provide imaging and chemical analysis of surfaces of nanomaterials. SEM only formed a minor component of this thesis and hence the discussion here will be brief. The SEM work and TEM cross section preparation work (section 2.2) was performed with a FEI Nova 200 DualBeam FIB. This system had two columns: one an electron beam and the other a Ga ion beam. The Ga beam was primarily used to remove material (milling) from a specimen to create cross sections but can also be used to image. The electron beam was used to form high resolution SEM images of specimen surfaces. The electron source on the SEM component of the Dualbeam FIB was a FEG, as described for the electron source on the TF20 TEM. After electrons were generated, they were then accelerated through a voltage of, typically, 30 kV. They then passed through a condenser lens that focused the beam down to less than 10 nm. The beam was then rastered across the surface using scanning coils to deflect the beam. Figure 2.11 shows a schematic ray diagram of the electron column [8]. The image was built point-by-point from the detected signal at a given point at which the electron beam was on the surface. The resolution was therefore not governed by the strength of an objective lens but by how small the electron beam can be made, how small the area that was scanned over was and the extent of the interaction volume. The interaction volume is the finite volume over which these interactions take place and is a function of beam energy, atomic number and sample density and is of the order of 1-20 nm, which is the limiting factor for resolution in SEM.

The relatively low beam energy (30 keV), with respect to the TEM beam energy (200 keV), is the reason why the interaction volume is large. This is too large to image atoms and hence the SEM is used to probe features such as morphology and topography. Magnification was determined by the scanned area and hence the voltages applied to the scanning coils.

When an electron beam strikes the sample, electrons interact and lose energy due to inelastic scattering from atoms in the sample. Figure 2.7 lists the interactions that an incident electron beam can have with a specimen. The material must be conductive to dissipate the charging effects generated from the incident electron beam. In SEM, it is normal to image with secondary electrons (SEs) or back scattered electrons (BSEs).

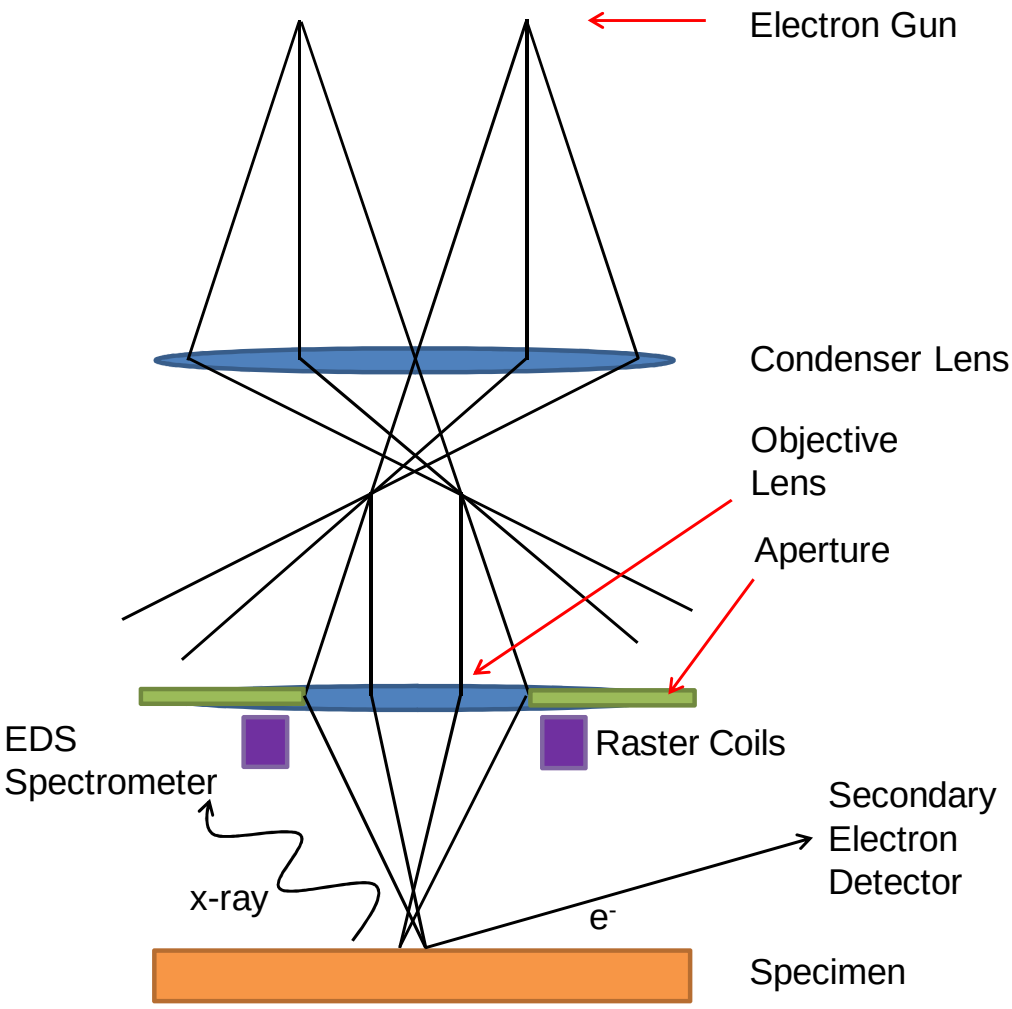

Figure 2.11. Ray diagram for the illumination of a specimen under the SEM electron column. The diagram shows how the spot is formed on the specimen surface and the resulting signals that are detected. Secondary electrons are used for imaging while X-rays are analysed to provide compositional information. The figure is based on a figure in [8].

We do not detect the transmitted signals in the SEM. SEs are generated from the electron beam ejecting loosely bound outer shell electrons via inelastic scattering. SEs undergo multiple scattering events and are therefore of low kinetic energy, normally less than 50 eV. The low energy of SEs distinguishes them from BSEs, which have a substantial proportion of the incident beam energy. The contrast in SE images is generated by different amounts of electrons reaching the detector as the scanning coils raster the beam across the surface. Differences in detected SE signal is primarily a result of the topography of a surface and is insensitive to composition. This is a result of the fact that the emitted secondary electron flux is maximal normal to the surface and drops off as a

cosine function. This makes the SEM particularly adept at determining the morphology of specimens.

2.4.2 Electron and X-ray Spectroscopies

This section will deal with the spectroscopies that involve the interactions of photons or a beam of electrons with bound electrons in a solid material. It is therefore convenient to discuss them in a single section and make explicit comparisons between each technique. Specifically, the techniques used in this thesis, that fall under this category are XPS, UPS, AES, EDS and EELS/EFTEM. EELS and EFTEM have been touched upon in the previous section and will be developed further here. This section is divided in sub sections detailing closely related techniques. Within each sub-section, the fundamental processes of each technique will be discussed, stressing the applicability of the particular technique. Then the experimental steps taken to record the data, including the equipment used will be described. Finally, the methods used to analyse the data will be discussed.

2.4.2.1 X-ray Photoelectron Spectroscopy (XPS) and Ultraviolet Photoelectron Spectroscopy (UPS)

A photon can eject an electron it encounters from a material if the energy of the photon is greater than the binding energy of the electron. The excess energy of the photon is passed to the kinetic energy of the outgoing electron. The process is shown in figure 2.12 and can be neatly summarised by the equation [1]:

$$E_K = h\nu - E_B - \phi, \tag{2.7}$$

where E_K is the kinetic energy of the emitted electron, h is Plank's constant, ν is the frequency of the photon, E_B is the binding energy of the electron and ϕ is the work function of the detector.

X-rays have enough energy to probe core level electronic states in solids (figure 2.12) and hence the spectroscopy is called X-ray photoelectron spectroscopy (XPS). The typical excitation energy used in XPS ranges from 1-2 keV. For example, in this thesis, Mg K_α and Al K_α X-rays were used, which have energies of 1253 and 1485 eV, respectively. The kinetic energy of the emitted photoelectron is limited only by the excitation source.

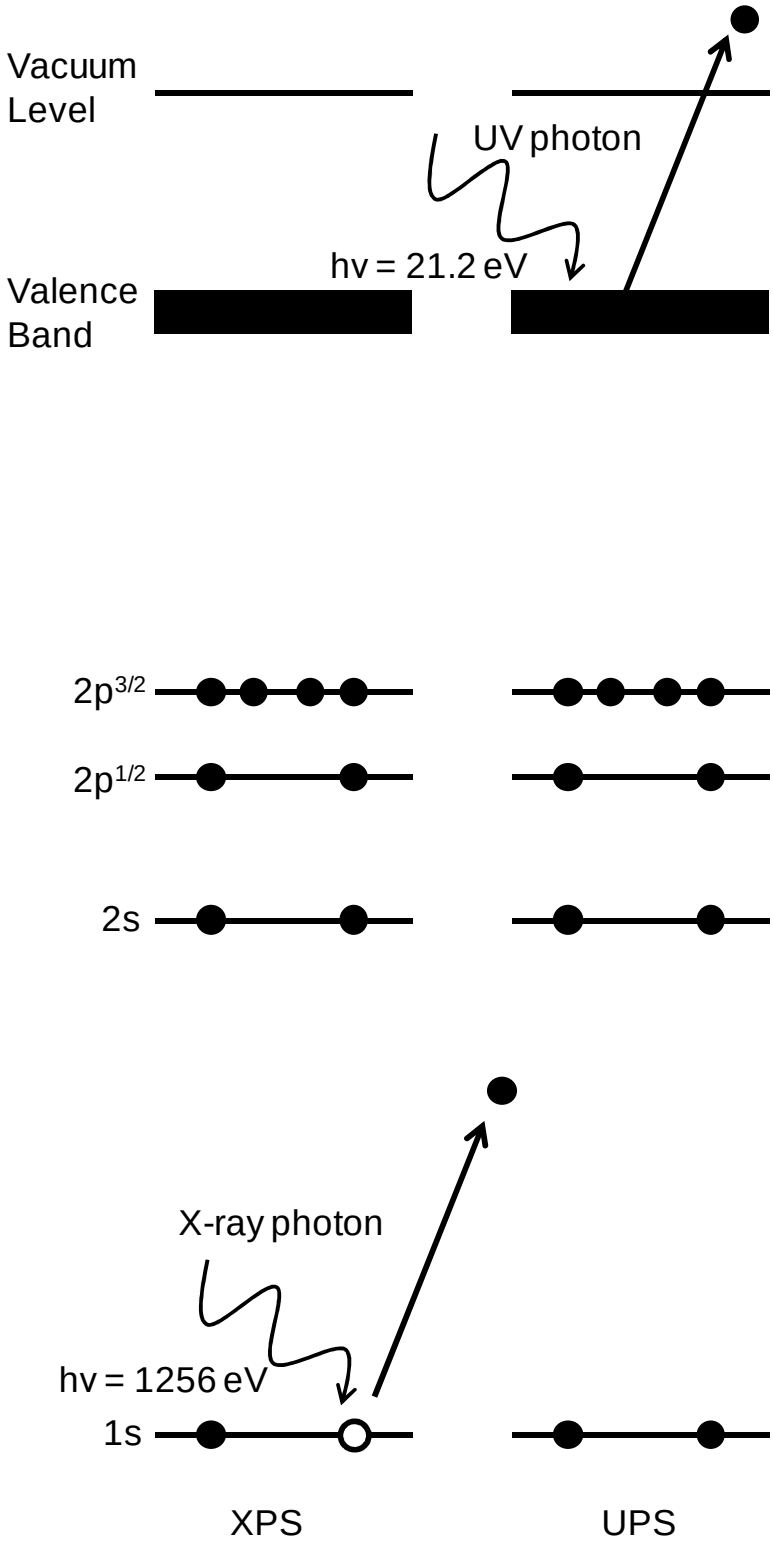

Figure 2.12. Photoemission process shown for both XPS and UPS. An incoming photon transfers its energy to a bound electron. The excess energy of the photon is converted to the kinetic energy of the outgoing electron.

Typical kinetic energies range from 100-1000 eV which means XPS is a surface sensitive technique because the photoelectrons produced have IMFP in solids of < 1 nm, as shown in figure 2.4.

XPS is sensitive to the chemical environment of a particular atom because the binding energy of a core electron is dependent on the local electron density. For example, the creation of a chemical bond causes a redistribution in electron density and thus causes a shift in the binding energy of a given electron, which can be measured and are typically of the order of 1 eV. An increase in binding energy suggests that the atom has become positively charged because the removal of electron density from the atom implies that the core level electron will feel the pull of the nucleus more (less shielding). The converse is true for a decrease in binding energy. Spin orbit coupling influences XPS spectra as splitting in energy of core level peaks. For example, the 2p orbital splits into two discrete energy states, $2p^{1/2}$ and $2p^{3/2}$. The spin orbit interaction occurs because the electron spin interacts with the magnetic field generated by the motion of the electron around the nucleus (the electron's angular momentum).

The simple picture presented in equation 2.7 is complicated by other factors. Equation 2.7 requires Koopman's theorem to be valid [1]. That is, the binding energy felt by the electron when it leaves the material is the same before the interaction with the photon. In practice, Koopman's theorem is never observed because the hole created by the photoionisation event causes other electrons in the atom to partially screen the nuclear potential, resulting in an apparent increase in the kinetic energy available to the outgoing electron. This is called an intra-atomic relaxation shift. In a solid material, the situation is further complicated. Weakly bound valence electrons can be very mobile (especially in metals) and can efficiently screen the hole created by photoionisation. This is called an inter-atomic relaxation shift and is observed in chapter 4 for Cd $3d^{5/2}$ core levels when Cd is present on a Cu(111) surface. There are other physical phenomena that manifest in a XPS spectrum. The above description of the relaxation effect is described if photoionisation was a slow process. In reality, this is not the case and the assumption of the "sudden" approximation is usually made. The result of considering the process like this is that the final state of the atom may be one which has an electron in an previously unoccupied bound state. This leads to less kinetic energy being passed to the emitted electron and appears on the XPS spectrum as a satellite feature known as a "shake up". In a solid material, the picture of the final state being in discrete excited states is not appropriate as solid materials normally have a band structure (a continuum). This means that electron-hole pairs in the vicinity of E_F can be excited, resulting in the low kinetic energy tail being observed for a particular core level XPS peak. The tail on the peak leads to the

characteristic asymmetry of certain XPS peaks. When analysing asymmetric XPS peaks, we use the Doniach-Sunjic (DS) function [19], which models the electron-hole excitation discussed above. The functional form of the DS function is discussed later in this section when the analysis procedures are considered.

In principle, XPS can be used to probe the electronic structure of the valence band. However, the cross section for photoionisation of the valence band is much higher with ultraviolet (UV) radiation (He (I) $h\nu$ = 21.2 eV) than with X-rays and hence UV radiation is favoured when it comes to analysing the valence region. Also the line width of UV light is less than typical X-ray line widths and hence higher resolution spectra are obtainable. Hence, we use UPS to probe the band structure and the vicinity of E_F. Perhaps the most important use of UPS is in the elucidation of the full band structure both in energy and momentum of electrons. In this case, it is termed angle resolved photoemission spectroscopy (ARPES) and is often performed with synchrotron radiation. The importance of ARPES is highlighted by the fact that it was used experimentally, to verify the existence of topological insulators as briefly described in chapter 1.

In this thesis, X-rays were produced for XPS using a conventional laboratory X-ray tube. Specifically the model used here was a twin anode (Mg K_α, Al K_α) unmonochromated source, as shown schematically in figure 2.13 [20]. X-rays were generated in the following process. Thermionically emitted electrons from a thoriated Ir filament are accelerated across a +15 kV potential where they strike either a Mg or Al target. These high energy electrons ionise the core electrons of the target leaving the atom in an excited state. Weaker bound electrons fill these holes and emit a photon in the X-ray portion of the electromagnetic spectrum. The resulting X-ray spectrum shows emission lines that are characteristic of the element they originated from, superimposed upon a continuum background called Bremsstrahlung. The K_α lines are the most intense from Mg and Al. They originate from the transition of an electron from the L shell (n = 2) to the K shell (n = 1). Other lines are generated (e.g. K_β) but they account for less than 1 % of the total emission. In the experiments here the Mg line was used for all photoemission experiments except Cd 3d because Cd 3d line lies on top of a Cu Auger line using Mg K_α. XPS spectra of the Cd 3d orbitals were obtained using Al K_α X-rays.

The source had a thin Al window that acts to filter unwanted X-rays and to prevent the anode potential affecting the electrons emitted from the sample during photoemission. The anode was cooled through a flow of water and was connected to an interlock mechanism so that if, for whatever reason, the passage of water through the cooling pipes was impeded, the high voltage supply would automatically trip. This feature was designed to

prevent damage to the anode coating through overheating. The source was mounted on a linear drive that gave ~30 mm movement. This meant that the source could be positioned close to the sample during an experiment, increasing the incident X-ray flux on the sample. The unmonochromated source means that the FWHM of the K_α lines are ~1.5 eV. The spot size of the X-ray beam was estimated to be ~1 cm^2.

The UV source in the system used a gas discharge lamp, a schematic of which is shown in figure 2.14 [21]. A UV discharge was produced from He gas that was admitted into the chamber at a high pressure (10^{-2} mbar) from the inlet valve, also shown in figure 2.14. He purity was checked with a RGA, which indicated that impurity levels were of the order of 0.001 %. At the end of the capillary tube, a voltage of 1 kV is applied between two plates (cathode and anode). The applied voltage ionises gas molecules and the liberated electrons, accelerated by the electric potential, collide with further gas atoms, leaving them in an excited state.

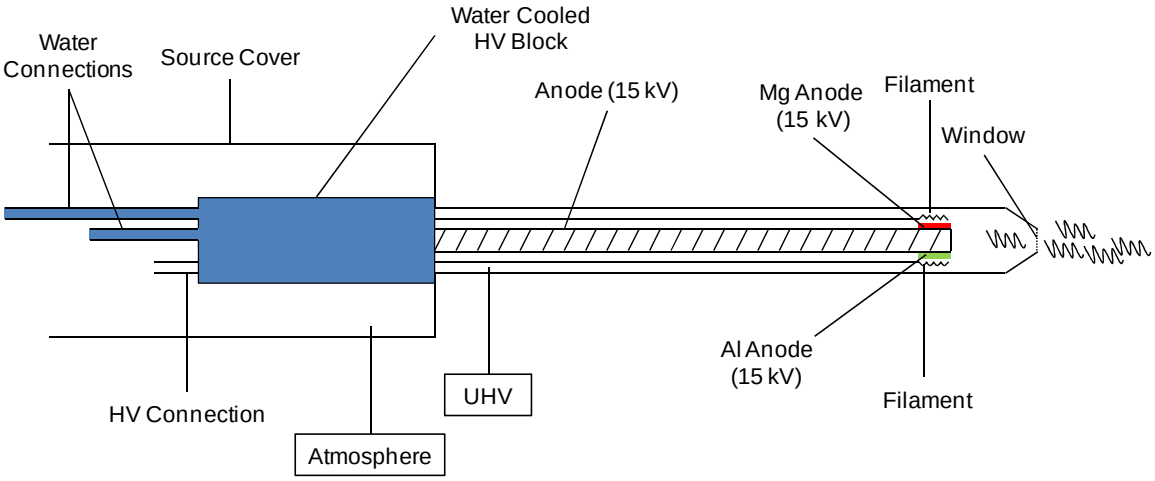

Figure 2.13. Schematic labelled diagram of the X-ray source. The figure is adapted from [20]. The electrical feedthrough connections of the filaments have been omitted for clarity.

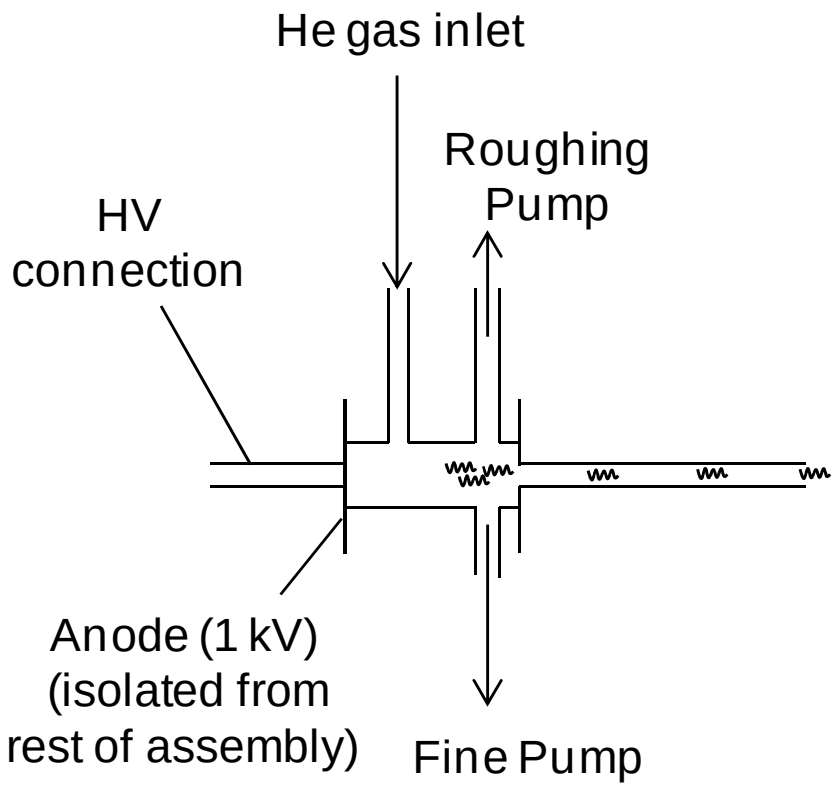

Figure 2.14. Schematic labelled diagram of the UV discharge lamp. The figure is based on figure in [21].

When the electrons of the excited gas atoms de-excite, they emit a photon of characteristic energy, which in the case of He is 21.2 eV. He gas was differentially pumped by a roughing pump (rotary pump) and a fine pump (turbomolecular pump), as shown in figure 2.14. Differential pumping meant that the pressure between the cathode and anode could be as high as 10^{-2} mbar while 10^{-8} mbar is maintained in the chamber. In a typical experiment, a 1 kV potential was applied between cathode and anode. The He line leak valve was then opened so that the pressure in the chamber reached 10^{-7} mbar, initiating a discharge. At this point the leak valve was slowly closed to reduce the pressure in the chamber to 10^{-8} mbar, which was normal operating pressure for a UPS experiment. Unwanted He(II) lines are generated when the pressure is reduced to ~5 x 10^{-9} mbar, so it was important to monitor the pressure during an experiment.

Electrons were detected in XPS, UPS and AES using a concentric hemispherical analyser (CHA), illustrated schematically in figure 2.15 [22]. The purpose of the CHA was to filter electrons so that only electrons that have a narrow range of kinetic energies were passed to the electron multiplier. For the CHA used in this thesis, energy filtering was done

through the retarding potentials of the R and N lens, which also acted to focus electrons into the hemisphere. To select an electron of a particular energy, the R and N lens were set so that the retardation of the incident electron allowed it to pass through the electric field of the hemisphere. The hemisphere was fixed at a particular "pass energy", determined by the user. Electrons that had two much energy collide with the outer wall of the hemisphere, while electrons with too little energy collided with the inner wall and were lost. The resolving power of the CHA is related to the geometry, physical size and pass energy [14]. The geometry and physical size are set by the manufacturer, so resolution can be user controlled using the pass energy. The pass energy was set as 50 eV for XPS and 10 eV for UPS. It can be shown that the pass energy is inversely proportional to the resolution. However, lowering the pass energy reduces the electron flux reaching the detector. Lowering the pass energy did not adversely affect the signal to noise ratio in UPS spectra because of their high spectral intensity and hence UPS spectra could be obtained at a higher energy resolution than XPS.

When electrons successfully travelled through the CHA, they were detected by the channeltron. The channeltron acted as an electron amplifier. The channeltron was a spiral glass tube coated in a material with a high secondary electron coefficient. When an electron struck this material more electrons were produced and by applying a voltage, a cascade of electrons was generated. A single electron can generate 10^8 electrons [22] which can then be detected after passing through a pre-amp and is displayed on a ratemeter. Data were collected with the VGX900 software and exported to Microcal Origin for analysis. In all experiments here, the R and N lens were operated in 1:1 mode which meant they were held at the same potential. In effect, this means that the area analysed by the detector is the same width as the physical entry slit to the detector, 4 mm^2. In both XPS and UPS experiments, the sample was orientated normal to the analyser.

The CHA can be thought of as recording spectra in serial mode as the energy of electrons detected by the channeltron at a given time is a very narrow range. Thus, to record a spectrum, the CHA has to step through a series of energies. This is in contrast to the magnetic sector in the TEM which can produce an entire spectrum simultaneously. Hence recording XPS and UPS spectra with the CHA takes significantly longer than recording an EELS spectrum or an EFTEM image with the magnetic sector analyser.

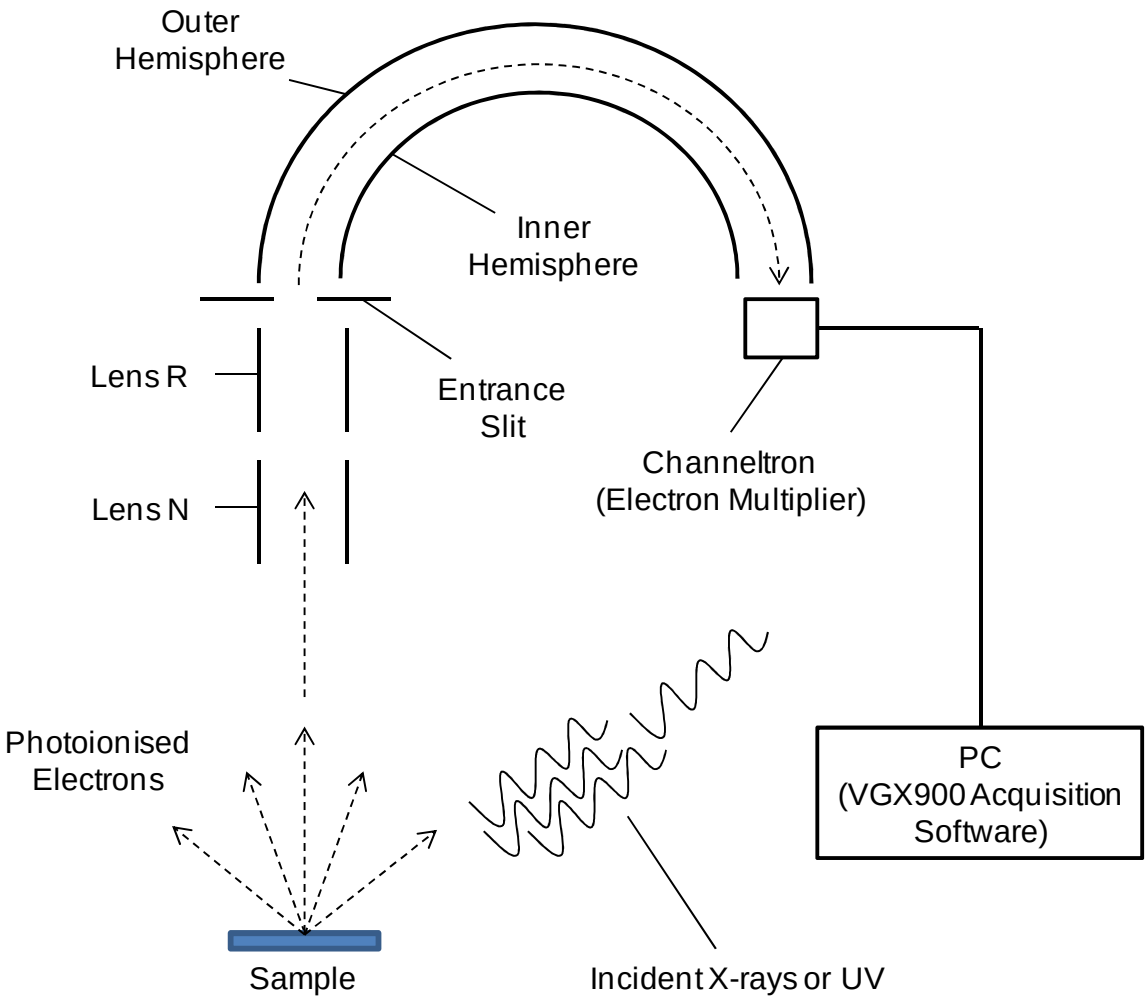

Figure 2.15. Schematic labelled diagram of the CHA electron analyser. The figure is adapted from a figure in [22].

In addition to probing the core and valence band electronic structure, the CHA was also able to measure the work function of a sample. The determination of the work function means detecting secondary electrons with relatively low energies (1-5 eV). The detection efficiency of these electrons in the CHA is low; so to get a more reliable measure of the position of the secondary electron peak and hence the work function, the sample was biased with 9 V. This shifted the entire spectrum up 9 eV in energy and pushes the secondary electron tail into a more reliable region of energy determination of the CHA, making work function determination less ambiguous. The method of measuring the work function with UPS is described later in this section when analysis methods are presented.

The methods employed to analyse XPS and UPS spectra will now be discussed. XPS is used for quantitative surface analysis and therefore necessitates the fitting of peaks. The

shape and width of a XPS peak is influenced by a number of factors and therefore simple Gaussian and Lorentzian profiles are seldom adequate. For example, the electronic transition in producing the X-ray line and the lifetime width of core level hole state is well approximated by a Lorentzian curve, while the slit positioned on exit of the X-ray source is assumed to be Gaussian [15]. Ideally, one would perform a convolution of a Gaussian and Lorentzian (also called a Voigt function) to model the effects described above. However, it is common that a simpler sum of a Gaussian and a Lorentzian (GL) is used to model the behaviour contained within an XPS core level peak [15]. This is termed a pseudo-Voigt function. The pseudo-Voigt or GL peak is defined as:

$$V(x) = y_0 + A\left[\mu\frac{2}{\pi}\frac{w}{4(x-x_c)^2+w^2} + (1-\mu)\frac{\sqrt{4\ln 2}}{\sqrt{\pi}w}e^{-\frac{4\ln 2}{w^2}(x-x_c)^2}\right], \qquad (2.8)$$

where y_0 is the offset from y = 0 (i.e. the background), A is the area, w is the FWHM, μ is the mixing factor or the profile shape factor and is limited to the range 0 → 1, and x_c is the centre of the peak. The first term inside the bracket is the Lorentzian contribution and the second term is the Gaussian contribution. For μ = 0 we recover a Gaussian curve and for μ = 1 we recover a Lorentzian curve.

As described above, symmetric peaks are rarely observed from metals, due to the excitation of electron-hole pairs around E_F. This intrinsic asymmetry has to be accounted for if quantification of the XPS peaks is to be performed. The model normally used to fit asymmetric metallic XPS peaks is the DS function [19]:

$$DS(x) = y_0 + \frac{H\cos\left(\frac{\alpha\pi}{2}+(1-\alpha)\arctan\left(\frac{x-x_c}{w}\right)\right)}{\sqrt{(w^2+(x-x_c)^2)^{1-\alpha}}}. \qquad (2.9)$$

where y_0 is the vertical offset, H is the height of the peak, α is an asymmetry factor, w is the FWHM and x_c is the centre of the peak. In the limit $\alpha \rightarrow 0$, the DS function reduces to a Lorentzian function. Hence the Lorentzian in the pseudo-Voigt peak is replaced by a DS function when deemed appropriate. For example, the Te $3d^{5/2}$ core level in chapters 3-5 is strongly asymmetric and clearly requires a DS function. In the case of multiple chemical species on the surface, each XPS spectrum was fitted to a combination of peaks, with each peak representing a particular chemical species. The best fit was found after minimising the difference between the data set and the sum of the fitted functions (i.e. the χ^2 value was minimised). To aid the fitting of multiple peaks, the width (w) and asymmetry (α) of each peak was set to the value of the fitted elemental XPS spectrum. For example,

the values of w and α in Te $3d^{5/2}$ spectra of Cu-Te alloys were set to the value obtained for the elemental Te species.

Once the appropriate functions have been fitted to a XPS spectrum, quantitative analysis can proceed and is be used here to measure thickness and composition. To measure thickness, one needs to appreciate that photoelectrons are attenuated by the bulk solid and thus for a particular electron energy and solid, an inelastic mean free path (IMFP) length of an electron can be measured or calculated. Figure 2.16 shows a schematic of an overlayer A deposited onto a substrate B. The electron flux emitted by the substrate of element B will be attenuated by the overlayer of element A; the magnitude of attenuation is related to the thickness of the overlayer and its scattering cross section (i.e. its composition), as shown in figure 2.16. The photoelectron intensity of the overlayer, A, can be written as [23]:

$$I_A = I_A^{\infty}\left\{1 - \exp\left(\frac{-d\cos\theta}{\lambda_A}\right)\right\}, \tag{2.10}$$

where I_A is the photoelectron intensity of overlayer peak, I_A^{∞} is the photoelectron intensity of an infinitely thick layer of element A, d is the overlayer thickness, λ_A is the IMFP of electrons in element A and $\cos\theta$ is the takeoff angle, with respect to the surface normal.

Equation 2.10 is easily rearranged, in terms of d as:

$$d = \frac{\lambda_A}{\cos\theta}\ln\left(\frac{I_A^{\infty} - I_A}{I_A^{\infty}}\right). \tag{2.11}$$

The unknowns in equation 2.11 are easily obtained. λ_A is measurable through calculations or experiment, $\cos\theta$ = 1 for normal emission and I_A^{∞} is measurable by depositing a very thick film (possibly at low temperatures) so that the substrate XPS peaks are completely attenuated. I_A is the measured peak intensity for a thickness, d, of element A. A similar expression can be obtained for the substrate, B, covered by a certain thickness, d, of element A:

$$I_B = I_B^{\infty}\left\{\exp\left(\frac{-d\cos\theta}{\lambda_A}\right)\right\}. \tag{2.12}$$

Equation 2.12 uses the same variables as 2.10 and 2.11. Again this can be easily rearranged to give a thickness d:

$$d = \frac{\lambda_A}{\cos\theta} \ln\left(\frac{I_B^{\infty}}{I_B}\right). \quad (2.13)$$

The only difference in the unknowns in this equation is the fact that we are measuring the attenuation of the substrate XPS signal as opposed to the overlayer signal. I_B^{∞} is measured from the clean substrate and I_B is the measured XPS intensity for an overlayer of element A with thickness d.

To convert thickness to coverage, we can estimate the unit cell parameter, a in the growth direction and thus the coverage in ML is given as:

$$\theta = \frac{d}{a}. \quad (2.14)$$

The models presented here for overlayer thickness are based on several key assumptions [23-25]. The model assumes that the surface is flat, there are no significant angular anisotropies (such as diffraction effects) and X-ray reflection is negligible (i.e. X-rays are not at a near grazing angle of incidence). It also assumes that the X-ray beam is larger than the spot viewed by the analyser, the X-rays themselves are not attenuated significantly within the material and that elastic scattering of photoelectrons is negligible.

In addition to measuring overlayer thickness, one can estimate stoichiometry from the relative intensities of photoelectron peaks. In addition to the assumptions made for measuring thickness, to estimate stoichiometry the following model assumes that the sample is homogeneous. In chapter 4, TEM data shows that the sample is inhomogeneous and has a degree of roughness. Therefore, chapter 4 discusses the limitations of this model in accurately determining composition. The general formula for obtaining a fractional atomic composition is through the following equation [23-25]:

$$\chi_A = \frac{\frac{I_A}{S_A}}{\sum_i \frac{I_i}{S_i}}, \quad (2.15)$$

where χ_A is the fractional composition of element A, I_A is the photoelectron peak intensity from element A, S_A is the sensitivity factor for element A, I_i is the photoelectron peak intensity from element I, S_i is the sensitivity factor for element i.

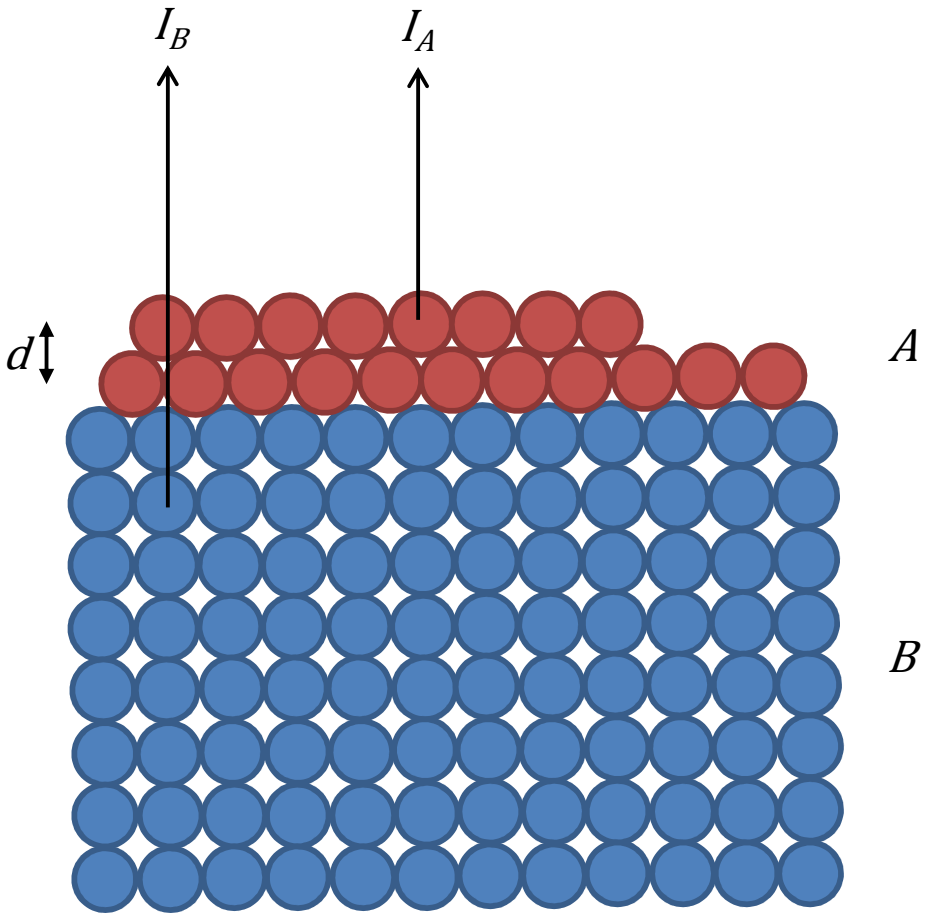

Figure 2.16. Cross sectional view of an overlayer, A, deposited onto a substrate, B, illustrating how thickness calculations are made in XPS: equations 2.10-2.14. The thickness of A is d. I_B is the XPS intensity from element B, the substrate. I_A is the XPS intensity from element A, the overlayer.

The sensitivity factor, S, is a measure of the photoionisation cross section for a particular core level in a given atom. This equation arises from the fact that the ratio of XPS signals, adequately normalised, is proportional to atomic ratio of the constituents in a homogeneous sample. According to Seah et al. [26], there are three choices available to measure the value of S. Firstly, one can use calculations, but these are only truly valid with the same experimental set up as the calculations, which is difficult to reproduce. Secondly, one can use an externally compiled database, such as that of Wagner [27]. The problem with using an external database is that it is only valid using the same experimental set up as the compiler, which again, in practice, is difficult to achieve. Thirdly, it is recommended by Seah et al. [28] that sensitivity factors be measured on individual systems. The user can compile their own database using their own experimental set-up and standardised materials, where available. In chapters 4 to 6, we make use of the third method described

here as we have access to two known standards to calibrate our system - Cu_2Te and CdTe. As Te is common to both Cu_2Te and CdTe we measure the sensitivity factors relative to S_{Te}= 1. To measure S_{Cd} we rearrange equation 2.15 to be:

$$S_{Cd} = S_{Te}(1 - \chi_{Cd})\frac{I_{Cd}}{I_{Te}}. \quad (2.16)$$

Then substituting S_{Te} = 1 and χ_{Cd} = 0.5 gives:

$$S_{Cd} = \frac{I_{Cd}}{2I_{Te}}. \quad (2.17)$$

For S_{Cu} equation 2.15 is rearranged as

$$S_{Cu} = S_{Te}(1 - \chi_{Cu})\frac{I_{Cu}}{I_{Te}}. \quad (2.18)$$

Then substituting S_{Te} = 1 and χ_{Cu}= 0.67 gives:

$$S_{Cu} = \frac{I_{Cu}}{3I_{Te}}\ . \quad (2.19)$$

These standards give relative sensitivity factors (RSFs) of S_{Cu} = 0.39 and S_{Cd} = 0.60, relative to S_{Te} = 1. For comparison, values S_{Cu} = 0.77 and S_{Cd} = 0.64 relative to S_{Te} = 1 have been measured by Wagner et al. [27]. The value of S_{Cd} has also been summarised by Christie et al. [29] and was found to lie in the range 0.58-0.73, relative to S_{Te} = 1. It is also noted by Wagner that the chemical state of Cu can cause a large variability in the sensitivity factor, which may explain the discrepancy in the value of S_{Cu} measured here. Also Seah [26,28] commented that some of the data obtained by Wagner et al. [27], probably suffered from contamination. The values of S are used extensively in chapters 3, 4 and 5.

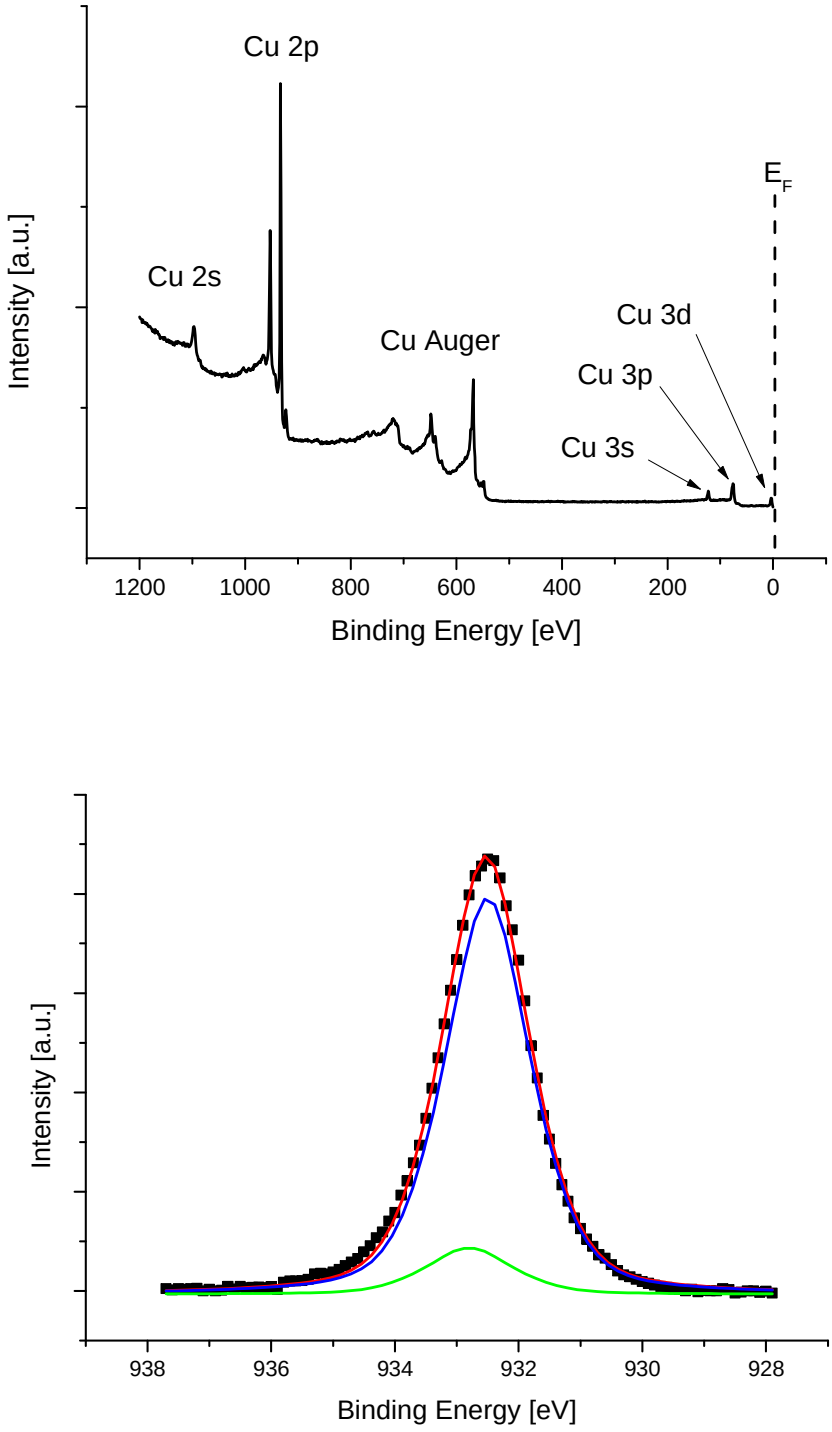

Figure 2.17. (a) Typical survey XPS spectrum from clean Cu(111), with individual core levels labelled. Only Cu components are identifiable on the surface. (b) High resolution XPS spectrum from the Cu $2p^{3/2}$ core level of a partially tellurided Cu(111) surface. The blue and green line represent different chemical species on the surface and the red line represents the overall fit of the model to the experimental data.

We shall now discuss the features present on XPS and UPS data sets. A sample XPS spectrum, from the clean Cu(111) surface, is shown in figure 2.17 (a) and shows how a broad scan, covering a large number of core levels. It shows that qualitative elemental identification is readily available. Figure 2.17 (b) shows a high resolution XPS spectrum of the Cu $2p^{3/2}$ orbital intended to illustrate how the fitting procedure was performed and shows that quantitative compositional information can be extracted. As shown in figure 2.12, UPS data probes the valence band of the material and hence can be used to investigate the electronic states that are directly involved in bonding. In this thesis, UPS data are used qualitatively to compare different alloy compositions. An example, annotated UPS spectrum from the clean Cu(111) surface is shown on figure 2.18. The process in qualitatively analysing UPS spectra involves comparing the ideal spectrum from clean surfaces (either obtained explicitly from our experiments or if acquisition is not possible, then from the published literature). For example, in chapter 4, comparison of UPS spectra is very useful in probing the nature of Cu diffusion into CdTe. The XPS data only show that Cu exists as Cu^+, and it is known that Cu^+ can exist in CdTe both interstitial sites or as a Cu_2Te alloy. By comparing valence band spectra with the valence band spectra of Cu_2Te, it was determined that Cu_2Te was present.

UPS is also an effective way of measuring the work function of a material. There is a high binding energy "edge" or "cutoff" at the end of the secondary electron peak. At the secondary electron edge, the electrons (which have been initially emitted by the valence band and have undergone inelastic scattering events) have the minimum energy required to escape the metal surface. This is equivalent to the work function and hence the work function is measured by simply subtracting the photon energy by the width of the UPS spectrum:

$$\Phi = h\nu - w, \tag{2.20}$$

where $h\nu$ = 21.2 eV (He(I) line) and w is the width of the UPS spectrum, as shown in figure 2.18. Changes in the work function, caused by the deposition of another element or compound onto a surface manifests in the UPS spectrum as changes in the low energy tail of the secondary electron peak. The example UPS spectrum displayed in figure 2.18, shows that the secondary electron tail (at ~15 eV), is not straight. As stated in the description of the CHA electron analyser, the biasing of the sample with 9 V, moves the spectrum into a more reliable energy region so that the work function can be accurately measured.

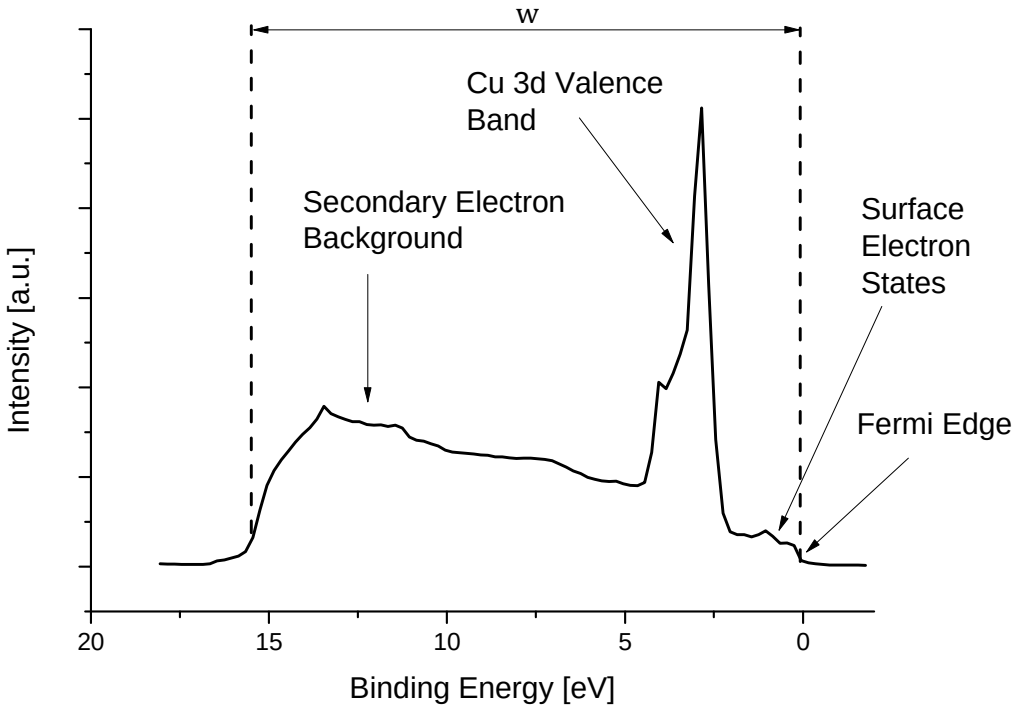

Figure 2.18. Typical UPS spectrum from the clean Cu(111) surface, with annotations showing the features of the spectrum. The width of the UPS spectrum is labelled w, which is used to calculate the work function as described by equation 2.20.

2.4.2.2 Auger Electron Spectroscopy (AES) and Energy Dispersive X-ray Spectroscopy (EDS)

Figure 2.19 shows the process involved in generating EDS and AES signals. In EDS and AES it is convention to use K, L_I, L_{II}, L_{III}, M_I... to represent the 1s, 2s, $2p^{1/2}$, $2p^{3/2}$, 3s... core levels. Both AES and EDS are two step processes. Firstly, there has to be a core level ionisation event, normally achieved with high energy electron bombardment or (less commonly) X-ray irradiation. This leaves the atom in an excited state, as shown in figure 2.19 (a). The modes of de-excitation give rise to AES and EDS signals. The atom can de-excite by a weaker bound electron falling into the hole, with the release of energy in the form of a photon. For the transition shown in figure 2.19 (b), between the L (n = 2) → K (n = 1) levels, the emitted photon will have energy $h\nu$ [1-4]:

$$h\nu = E_K - E_{L_I}, \tag{2.21}$$

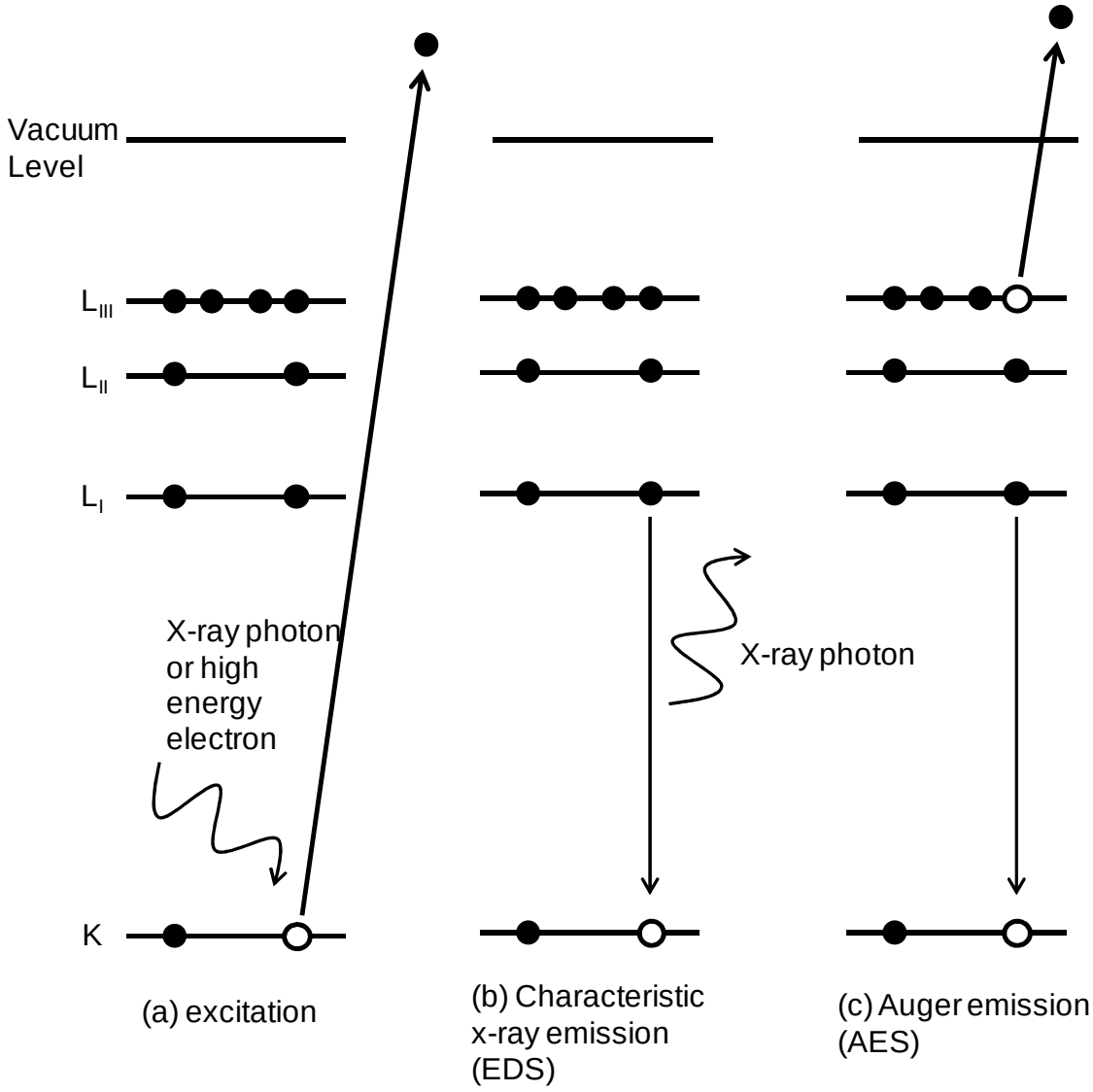

Figure 2.19. Pictorial representation of the production of characteristic X-rays and Auger electrons. AES and EDS use a different notation to XPS and UPS to describe electronic states in the atom (see text for further details). Specifically, K, L_I, L_{II} and L_{III} states are equivalent to the 1s, 2s, $2p^{1/2}$ and $2p^{3/2}$ atomic orbitals, respectively.

where E_K is the binding energy of the K level electron, E_{L_I} is the binding energy of the L_I electron. The X-ray emitted from this transition is labelled K_α. The M (n = 3) → K (n = 1) transition is called K_β. The energy difference in the electronic transition means that the photon will be from the X-ray portion of the electromagnetic spectrum. As the binding energies of electrons are dependent on the particular atom, the energy of the emitted X-ray is characteristic of the atom it has originated from and thus gives us information about elemental composition. In this thesis, we use the production of X-rays to characterise our specimens with the technique known as EDS. The term “energy dispersive” refers to the method in which the X-rays are detected. EDS sit on top of a background because electrons travelling through a specimen will be decelerated and emit energy in the form of X-rays. This additional interaction is not quantised and thus the X-rays produced are a continuous background called Bremsstrahlung ("braking radiation"). The maximum X-ray energy is limited to the incident beam energy.

EDS spectra were collected on the TEM and SEM which have already been described in the microscopy section, sections 2.4.1.2 and 2.4.1.3, respectively. The EDS spectrometer consisted of a reverse biased p-i-n diode [4] (Li doped Si is used here as a diode). When an X-ray transfers energy to the semiconductor, it promotes electrons from the valence band to the conduction band. In case of Si, this transition is 3.8 eV at 77 K. X-rays have energies between 1-10 keV and hence a single X-ray will form many thousands of electron-hole pairs. The energy of the X-ray is directly proportional to the number of electron-hole pairs created and hence the energy of the X-ray is proportional to magnitude of the detected current. The diode was biased to separated electrons and holes. The detector must be cooled to 77 K (with liquid N_2) to reduce thermal noise that would mask the X-ray signal.

A typical EDS spectrum is shown in figure 2.20. The energy resolution of EDS is significantly lower than XPS primarily because of Gaussian broadening of the detector meaning that FWHM of the EDS peaks are ~100 eV. Therefore EDS is not suitable for measuring chemical shifts and hence deriving information on chemical bonding or oxidation states. In chapter 6, EDS is used for an initial assessment of TaS_3 nanoribbons. The spatial resolution of EDS is ~1 μm which is a result of the X-rays being generated deep within the interaction volume. In contrast, the FWHM of XPS peaks are of the order of 1 eV and are therefore appropriate for identifying chemical shifts. However, EDS can be used to provide quantitative information on the relative abundance of particular elements in a specimen, using the Cliff-Lorimer method. The weight percentage of each element, C_A

and C_B can be related to the measured X-ray intensity of I_A and I_B by the equation [4]:

$$\frac{C_A}{C_B} = k_{AB}\frac{I_A}{I_B}, \tag{2.22}$$

where k_{AB} is the Cliff-Lorimer sensitivity factor for elements A and B. Similar to XPS and EFTEM quantification, equation 2.22 essentially states that the ratio of EDS peaks for to particular elements is proportional to the atomic ratio. The value of k_{AB} is dependent on a number of factors that can be related in an equation, derived from the physics of X-ray generation:

$$k_{AB} = \frac{Q_A\omega_A\tau_A}{Q_B\omega_B\tau_B}\frac{M_B}{M_A}\frac{\varepsilon_A}{\varepsilon_B}, \tag{2.23}$$

where Q is the ionisation cross section, ω is the fluorescence yield, τ is the relative transition probability, M is the atomic mass and ε is the detector efficiency.

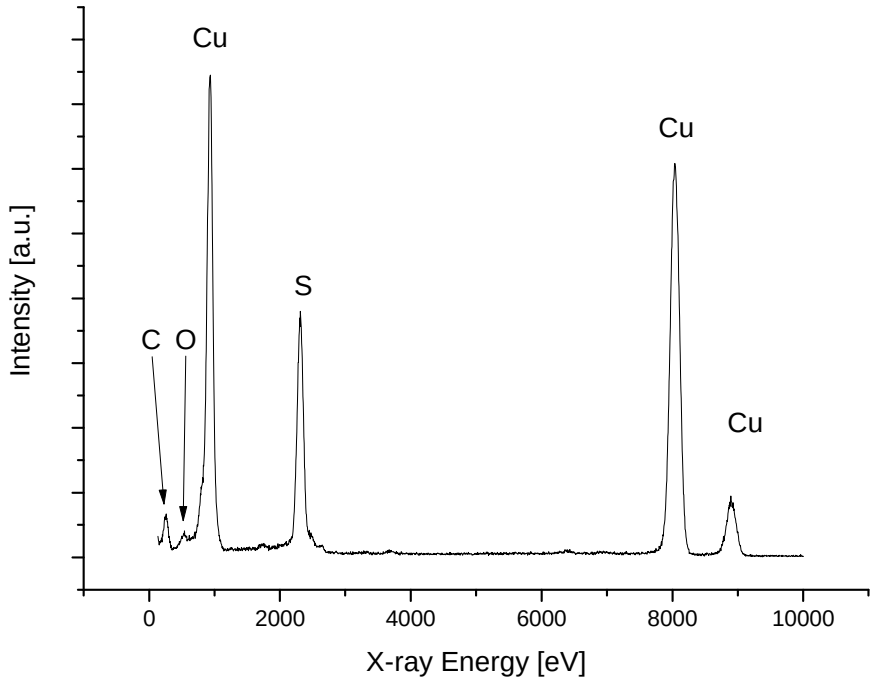

Figure 2.20. A typical EDS spectrum. Peaks are labelled according to their element of origin. FWHM of EDS peaks are of the order of 100 eV.

Alternatively, an electron can be emitted when the atom de-excites, with a characteristic kinetic energy, known as the Auger process. Figure 2.19 (c) shows the emission of the KLL Auger electron and shows that the Auger electron will have a kinetic energy of [1-4]:

$$E_{Kin} = E_K - E_{L_I} - E_{L_{III}}, \quad (2.24)$$

where E_{Kin} is the kinetic energy of the Auger electron, E_K is the binding energy of the K level electron, E_{L_I} is the binding energy of the L_I electron and $E_{L_{III}}$ is the binding energy of the L_{III} electron. Equation 2.22 shows that the kinetic energy of the Auger electron is independent of the excitation energy. X-ray induced AES data were collected with the CHA analyser and using the X-ray source described above as the excitation.

Unlike XPS and UPS, which are extensively used in this thesis, AES only forms a minor component, only appearing in chapter 3, and therefore the analysis of the data will only be briefly discussed. AES can be used in a similar fashion to XPS. The intensity of the AES signal can be used, with appropriate normalisation, to quantify the relative abundance of a particular element, analogous to equation 2.15 which was given for XPS. As the binding energy of electronic states are sensitive to the chemical environment, the kinetic energy of the Auger electron will also be sensitive to the chemical state. For example, chemically specific X-ray induced AES is used to corroborate the assignment of Cu_3Te_2 in chapter 3. However, due to the complex nature of the observed spectra, AES was only used qualitatively to corroborate quantitative XPS analysis.

2.4.2.3 Electron Energy Loss Spectroscopy (EELS) and Energy Filtered Transmission Electron Microscopy (EFTEM)

XPS, UPS, EDS and AES all have in common the fact that the detected particle (either photon or electron) originates from the atom under investigation. EELS and EFTEM are different in the sense that the atoms in question are probed indirectly. A high energy beam of electrons (e.g. the electron beam in the TEM) can interact with a specimen and lose a quanta of energy, through a number of different interactions with the solid, a list of which are shown in figure 2.7. These interactions include the production of electron-hole pairs, single electrons, Bremsstrahlung X-rays, the production of characteristic X-rays (EDS) and Auger electrons; the unscattered beam and the beam that has been inelastically scattered through an interaction with the specimen.

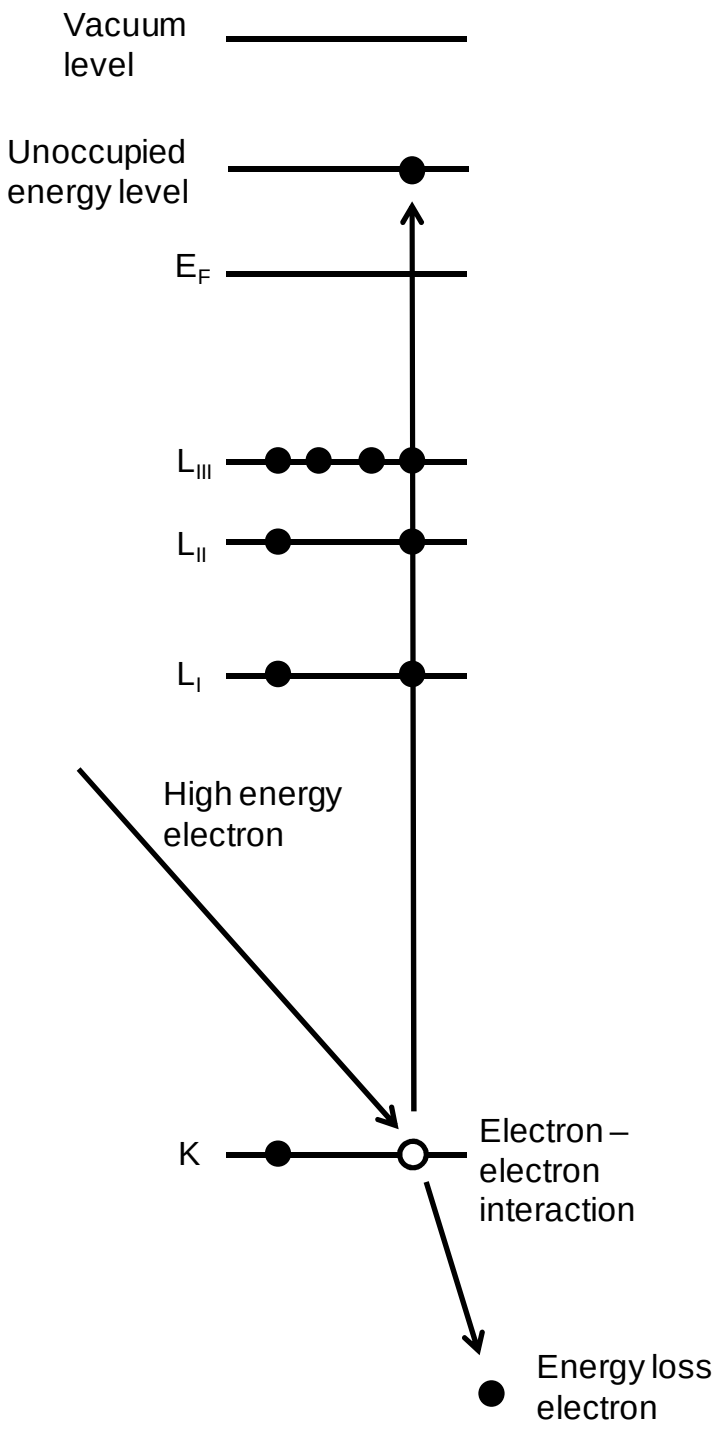

Figure 2.21. Pictorial representation of the process occurring in EELS or EFTEM for a core loss K edge. The K electron is transferred to an unoccupied energy level above E_F. In EELS and EFTEM, the energy of the "energy loss electron" is analysed.

The processes that give rise to inelastically scattered electrons will now be discussed as these electrons form EELS and EFTEM spectra. The difference between EELS and EFTEM is in the nature of the incident electron beam. An EELS spectrum is normally obtained from a scanning transmission electron microscope (STEM) while an EFTEM spectrum is obtained from a conventional TEM. There are several processes that can lead to the electron beam losing energy. These processes include: exciting collective vibrational modes (phonons) in the sample; exciting collective electronic modes of the sample (plasmons) and interactions with single bound electrons of the sample. The plasmon peak has the largest cross section of all inelastic processes and can be used to measure specimen thickness. The interaction of the beam with a single bound electron of a sample is called core loss edge and is used in this thesis for EFTEM elemental mapping. The highly energetic electron beam promotes a core level electron to an occupied energy level above E_F, as shown in figure 2.21. Electrons can be ionised but the cross section for this process is very low. The interaction transfers energy from the electron in the electron beam to the core level electron, resulting in a quantum of energy being lost by a high energy electron in the electron beam. As the core level electron is excited to a state above E_F, the energy loss electron contains information about the unoccupied density of states of the atom and hence gives information on chemical bonding. There is also fine structure after a core level edge which is the result of multiple scattering events in its local environment giving information on the local geometry of the atom it has encountered. Similar to XPS, the position of the core level edge is dependent on the chemical environment of the atom in question and hence chemical shifts can be used to gain information on oxidation state and chemistry. The resolution is of the order of 1 eV and is therefore sufficient to identify chemical shifts. In addition, the magnitude of the core level edge is proportional to the quantity of atoms present and hence can be used for elemental quantification. EELS and EFTEM spectra were collected using the TEM column, which was described in section 2.4.1.

A typical EELS spectrum is shown in figure 2.22. The EELS spectrum is roughly divided into two sections: the low loss and the high loss regions. The low loss region contains the zero loss peak, which is the part of the electron beam that has passed through the specimen without interacting. It also contains electrons from the incident beam that have excited a plasmon resonance. The high loss region contains electrons that have lost energy through interaction with core level electrons in the specimen. As stated above, these "edges" are used to fingerprint elements, quantify composition, identify oxidation state and probe the local geometry of an atom [4].

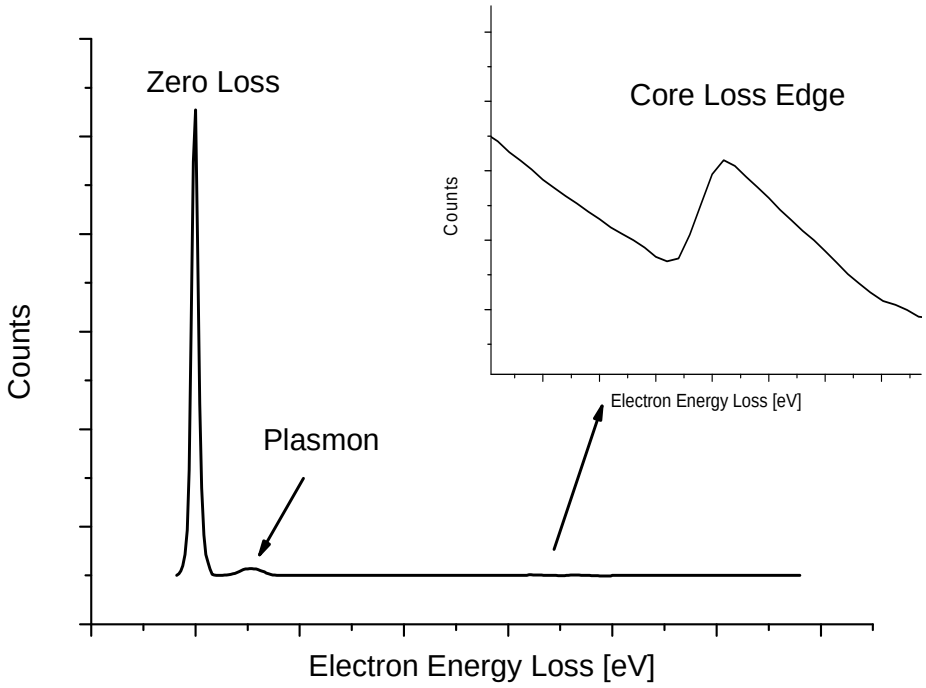

Figure 2.22. Structure of a typical EELS spectrum. Note that zero loss and plasmon peaks are many orders of magnitude more intense than the core loss peaks and fine structure.

An EFTEM image can be thought of as an image collected from a specific core energy loss. The energy loss of the image can be positioned over a core loss edge of an element of interest and the image will therefore contain information on the relative abundance of the element in question (i.e. an elemental map). Experimentally, an elemental map from an EFTEM image is extracted by first assuming a power law background and using the so called "three window method" [6,7], shown in figure 2.23. In the "three window method" two pre edge windows (labelled I_1 and I_2 on figure 2.23) and one post edge window (labelled I_3 on figure 2.23) are collected. The two pre-edge windows are used to produce an extrapolated background image. As there is an approximately linear relationship between the logarithm of intensity and the logarithm of energy loss, the background, $B(E)$ is an exponential with the form [6,7]:

$$B(E) = AE^{-r}, \tag{2.25}$$

where E is the electron energy loss and A and r are defined by:

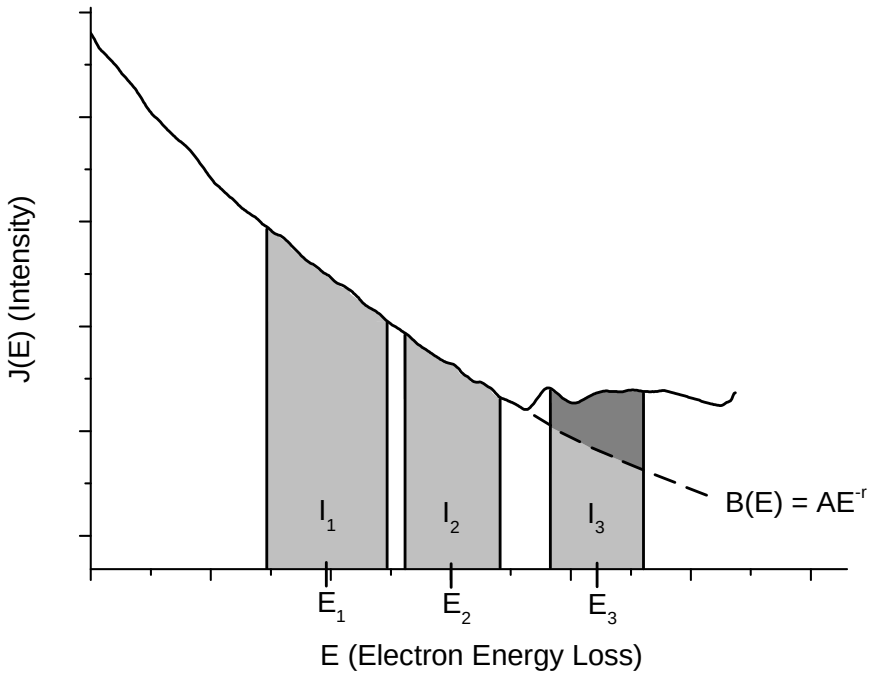

Figure 2.23. EELS spectrum from the Cu $L_{2,3}$ edge, with added boxes illustrating the "three window method" of performing EFTEM. Windows 1 and 2 are the pre edge windows that are used to calculate the power law background. Window 3 is the post edge window. The net signal is the region shade dark in region 3.

$$\ln A = \frac{1}{2}\left[\ln\left(\frac{I_1}{I_2}\right) + ln\left(\frac{E_2}{E_1}\right)\right], \tag{2.26}$$

$$r = \frac{\ln\left(\frac{I_1}{I_2}\right)}{\ln\left(\frac{E_1}{E_2}\right)}, \tag{2.27}$$

where I_1 and I_2 are pre-ionisation edge integrals, and E_1 and $E_2$are the mid points of the of the pre ionisation edge windows, as defined in figure 2.23. This extrapolated background image is subtracted from the post-edge image to give the elemental map. Acquisition times are normally kept short (less than 10 s) to prevent drift. To ensure the two pre-edge images are properly aligned, a spatial cross-correlation algorithm is performed to accurately align these two images. Once the net ionisation signal intensity has been obtained, quantification can be performed. Relative quantification of two elements (A and B) can be obtained from the normalisation of the net signal intensity by

the appropriate cross section:

$$\frac{n_A}{n_B} = \frac{I_A(\beta,\Delta)}{I_B(\beta,\Delta)} \frac{\sigma_B(\beta,\Delta)}{\sigma_A(\beta,\Delta)}, \quad (2.28)$$

where I_A and I_B are the net ionisation intensities for two different elements, σ_A and σ_B are the appropriate cross sections, β is the collection semi angle, defined by the microscope set up and Δ is the energy window. Equation 2.28 is analogous to the equation for compositional quantification in XPS (equation 2.15) and EDS (equation 2.23), in that the ratio of the intensity of core loss edges is proportional to the ratio of atomic constituents. EFTEM elemental maps will therefore give relative elemental concentrations at high spatial resolutions. The EFTEM elemental maps obtained here had a spatial resolution of ~1-10 nm.

2.4.3 Diffraction

This section describes the phenomenon of diffraction from both surfaces and bulk materials. Diffraction is a structural probe and is used here to measure lattice parameters and verify crystal structure. This section will be divided into two parts: the first will describe the theory of diffraction and the second will describe the equipment used to study diffraction. In this thesis, we use three different diffraction methods. Firstly, LEED, which was used to study surface structure. Secondly, electron diffraction in the TEM was used to probe the crystallography of thin specimens (thickness less than 100 nm). Diffraction in the TEM can also be sub divided into SAED and CBED, which will be subsequently discussed. Thirdly, PXRD was used to probe the crystallography of bulk materials.

Diffraction from crystals occurs when electrons or photons (X-rays) are elastically scattered. It was noticed by Bragg that it is convenient to consider the crystal as a series of planes, as illustrated in figure 2.24, when explaining diffraction by crystals. The condition for constructive interference, also known as the Bragg condition, is given by the equation [30]:

$$n\lambda = 2a \sin\theta \quad (2.29)$$

where n is an integer (i.e. n = 0, ±1, ±2, ±3...) and λ is the wavelength of the electron or photon.

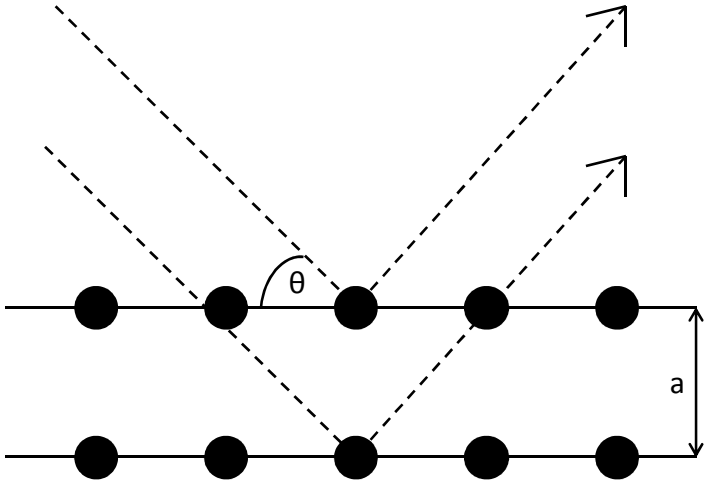

Figure 2.24. The geometric representation of Bragg's Law. θ is the angle of incidence of the X-rays, and a is the lattice plane separation.

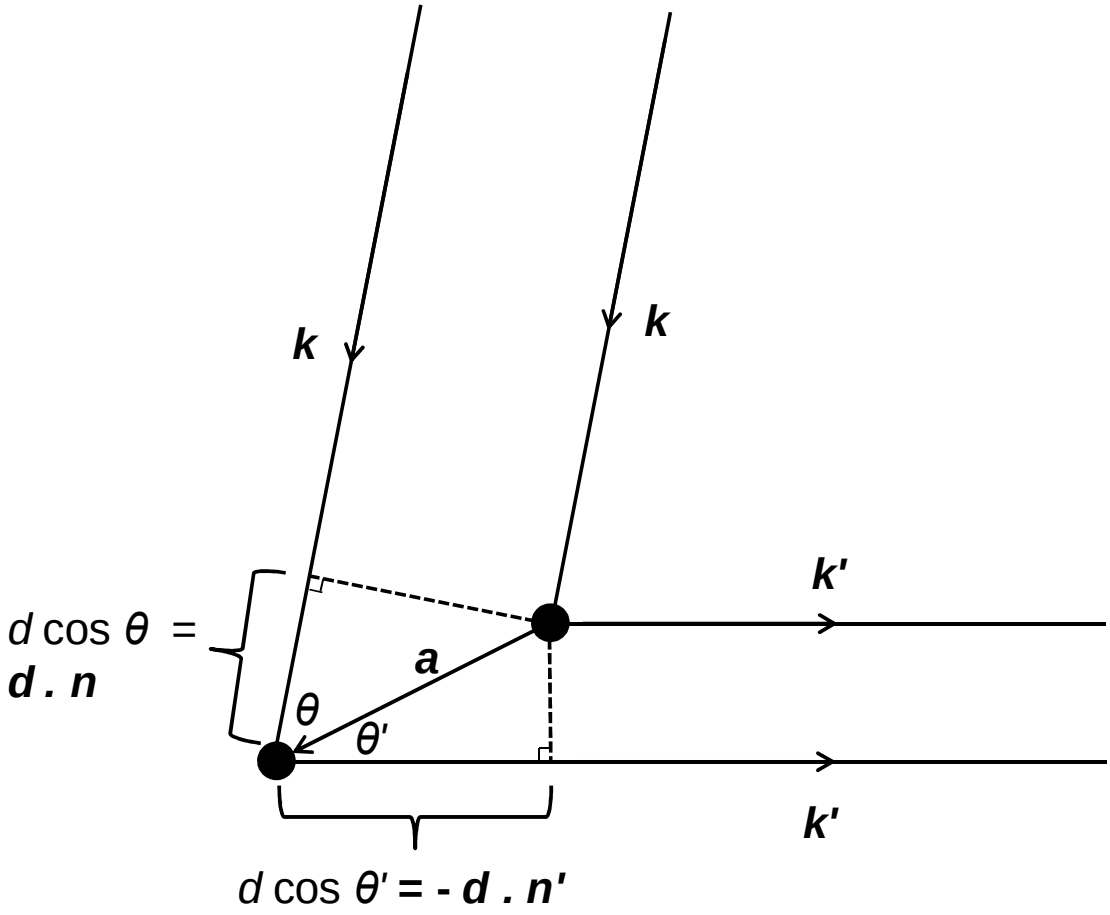

Figure 2.25. Geometric representation of the Laue formulation of diffraction. $\boldsymbol{d}$ is the separation of the two scattering points. $\boldsymbol{k}$ is the unscattered wavevector, $\boldsymbol{k'}$ is the scattered wavevector, θ is the angle of incidence and θ' is the angle of scattering. The figure is based on figure from [30].

It is derived geometrically from figure 2.24. An equivalent way of formulating diffraction from crystals was given by von Laue [30]. To formulate the Laue condition we consider just two points of scattering, a distance d apart, shown in figure 2.25. The path difference is then:

$$d\cos\theta - d\cos\theta' = \boldsymbol{d}.(\boldsymbol{n} - \boldsymbol{n'}), \tag{2.30}$$

so the condition for constructive interference is (in terms of a wavevector):

$$\boldsymbol{d}.(\boldsymbol{k} - \boldsymbol{k'}) = 2\pi m. \tag{2.31}$$

Instead of a single pair of scattering points, the separation vector, $\boldsymbol{d}$, is replaced with the Bravais lattice vector, $\boldsymbol{R}$. Rearranging gives:

$$(\boldsymbol{k} - \boldsymbol{k'}) = \frac{2\pi m}{\boldsymbol{R}}, \tag{2.32}$$

This is can be written in terms of lattice parameters:

$$(\boldsymbol{k} - \boldsymbol{k'}) = \frac{2\pi l}{\boldsymbol{a}} + \frac{2\pi m}{\boldsymbol{b}} + \frac{2\pi n}{\boldsymbol{c}} \tag{2.33}$$

The right hand side of equation 2.33 is equal to the reciprocal lattice vector,

$$\boldsymbol{G} = l\boldsymbol{a}^* + m\boldsymbol{b}^* + n\boldsymbol{c}^* \tag{2.34}$$

where $\boldsymbol{a}^* = \frac{2\pi}{\boldsymbol{a}}$, $\boldsymbol{b}^* = \frac{2\pi}{\boldsymbol{b}}$ and $\boldsymbol{c}^* = \frac{2\pi}{\boldsymbol{c}}$. The parameters $\boldsymbol{a}^*$, $\boldsymbol{b}^*$ and $\boldsymbol{c}^*$ are termed the reciprocal lattice vectors. This gives the Laue condition:

$$\boldsymbol{G} = \boldsymbol{k} - \boldsymbol{k'}, \tag{2.35}$$

i.e. for constructive interference, the change in the wavevector, $\boldsymbol{k} - \boldsymbol{k'}$ must be equal to a vector of the reciprocal lattice.

A way to visualise diffraction and the Laue condition from a periodic crystal is by using the

Ewald sphere construction, shown in figure 2.26. Figure 2.26 (a) shows a rectangular reciprocal lattice but is equally applicable to other lattices. To satisfy the Laue condition, the scattered wavevector, $\boldsymbol{k}'$, must be equal to a reciprocal lattice vector. This means that if a circle of radius $\boldsymbol{k}$ is drawn (i.e. the incoming wavevector) then the intersections between the reciprocal lattice and the circle defined by $\boldsymbol{k}'$ (i.e. the scattered wavevector) will give the condition for diffraction. In three dimensions (i.e. for PXRD) the reciprocal lattice is a series of points as defined, for example, in figure 2.26 (a) [30]. For thin specimens (i.e. diffraction with SAED and CBED), the conditions for diffraction are relaxed, which means that the series of points become a series of ellipses [4]. This partially relaxes the conditions for Bragg diffraction and, as is shown in figure 2.26 (b), allows for more diffracted beams to be excited. The situation is substantially modified in two dimensions, (i.e. for surface diffraction measured with LEED) as the system is now only symmetric in two directions. To account for this the reciprocal lattice is replaced by infinite reciprocal lattice rods, perpendicular to the surface, as shown in figure 2.26 (c) [1]. This greatly relaxes the conditions for the formation of diffracted beams. In the three dimensional case, a small change in the $\boldsymbol{k}$ wavevector will result in the loss of many diffracted beams or the emergence of different beams. However, in the case of the two dimensional surface, a change in $\boldsymbol{k}$ will only cause a slight change in the position of the diffracted beams.

The different diffraction techniques used will now be discussed, as will the equipment used to obtain the diffraction data. X-rays are not surface sensitive and hence the diffraction of X-rays by crystals can be used as a probe of bulk structure. The PXRD method (also called the Debye-Scherrer method) was used in this thesis, which involves a finely powdered specimen which is exposed to X-rays while being rotated. This isotropic averaging means that all possible orientations are available for scattering. PXRD was performed using a PANalytical Xpert PRO MPD powder diffractometer with Cu K_α source (λ = 0.154056 nm) with a flat plate geometry where powdered samples were loaded into the recess of a flat glass holder. Diffraction data were typically collected for $5° \leq 2\theta \leq 85°$ with a 0.017° step size with scan times from 1-12 h .

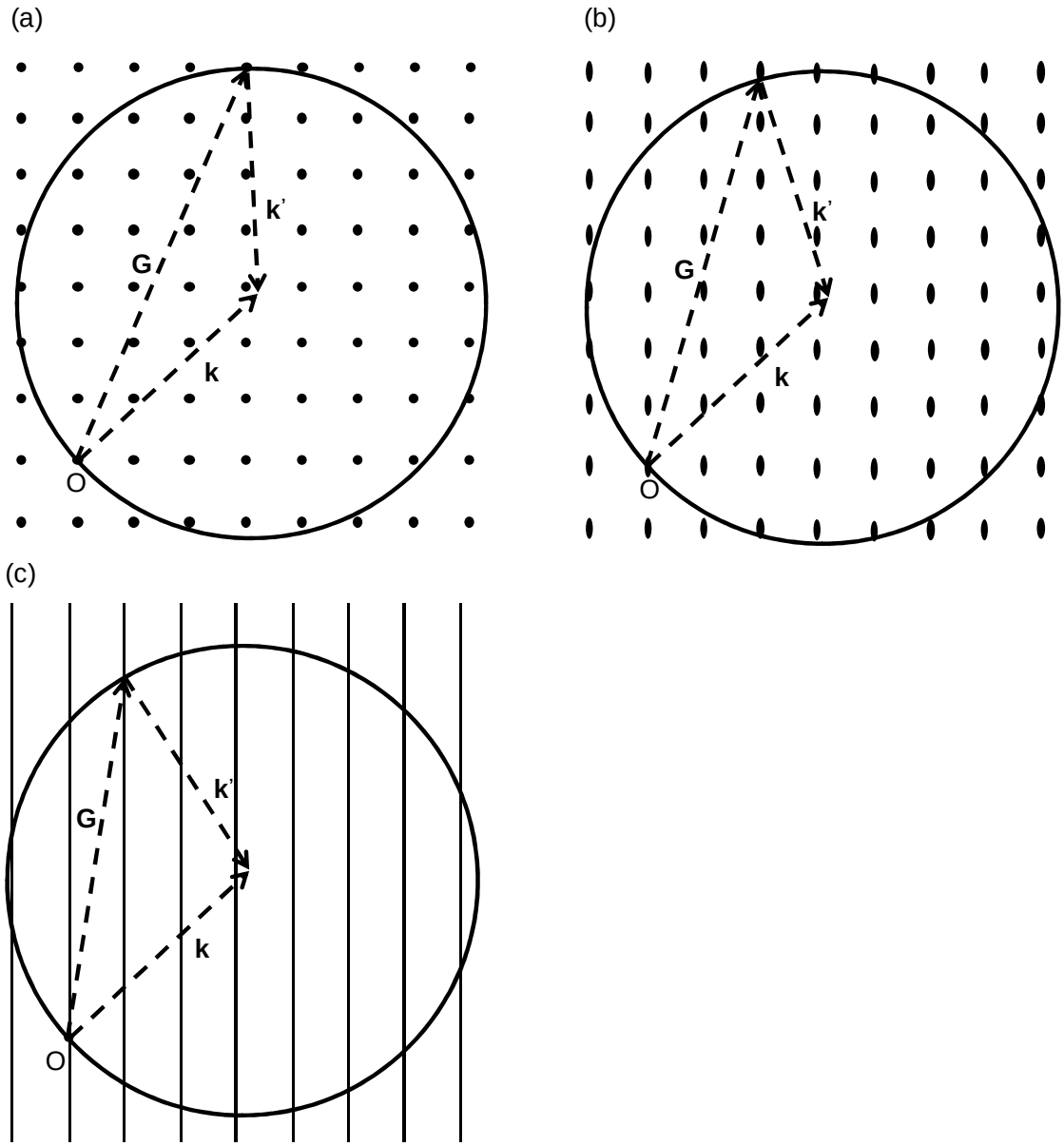

Figure 2.26. Ewald sphere construction showing the Bragg condition for different types of specimen. (a) for the 3-D case (i.e. bulk specimen), applicable to PXRD. (b) the thin specimen case, applicable to CBED and SAED, (c) for the 2-D case (i.e. surface), applicable to LEED.

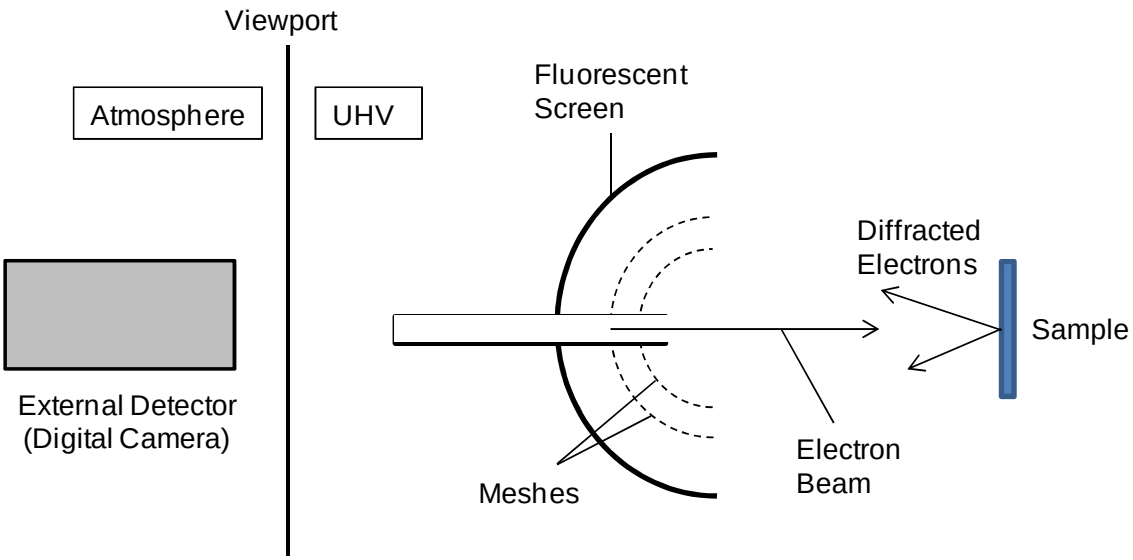

Figure 2.27. Labelled schematic diagram of the rear view LEED apparatus. This figure has been adapted from [31].

Diffraction from electrons with kinetic energy of between 30-300 eV is surface sensitive because, as shown in section 2.2, the IMFP length of an electron in solids is dependent on the kinetic energy of the electron. Electrons that have kinetic energy of 30-300 eV have an IMFP length of the order of 1 nm and hence are surface sensitive. Diffraction with low energy electrons is termed LEED, which was acquired with a rear view LEED optic, a schematic of which is shown in figure 2.27 [31]. The source of electrons on the LEED optic was from a heated thoriated W filament. A constant potential of 600 V was applied to the extraction plate to ensure sufficient electron emission from the filament, even with a low beam energy. The beam energy was controlled using a user variable voltage. The shape and focus of the electron beam was controlled using voltages applied to appropriate focussing elements. Elastically backscattered electrons were used for diffraction and were filtered through a series of meshes. A negative potential was applied to the meshes which reduced the flux of inelastically scattered electrons being incident on the viewing screen. The viewing screen was coated in a fluorescent phosphor, allowing electrons to be detected. In operation, the earthed sample was orientated normal to the incoming electron beam. The resultant LEED pattern was visible in the centre of the phosphor screen. Finally images were recorded using a flange mounted digital camera.

The electrons propagating in the LEED optic will have a wavelength given by the de Broglie relation:

$$\lambda = \frac{h}{p}. \quad (2.36)$$

As shown in figure 2.27, electrons in LEED are accelerated through an electrostatic potential and therefore equation 2.36 is rewritten in terms of the accelerating voltage, V

$$\lambda = \frac{h}{\sqrt{2m_e eV}}, \quad (2.37)$$

where h is the Plank constant, e is the elementary charge and m_e is the mass of the electron. At low energy, relativistic effects can be ignored. Using, for example, V = 300 V, gives λ = 71 pm, which is of the order of the atomic dimensions and hence diffraction is obtainable.

For electrons in the TEM (E_K = 200 keV), the IMFP is of the order of 10-100s of nm. This means that electron diffraction can occur for specimens that are up to ~100 nm thick. At these kinetic energies (200 keV), relativistic effects can no longer be ignored hence the expression for the wavelength is [4]:

$$\lambda = \frac{h}{[2m_0 eV(1+\frac{eV}{2m_0 c^2}]^{1/2}}. \quad (2.4)$$

The parameters in equation 2.4 are the same as in equation 2.37. Except m_o is the rest mass of the electron and c is the speed of light in vacuum. Setting V = 200 kV, in equation 2.33, yields λ = 2.7 pm. The method for obtaining CBED and SAED patterns from the TEM have already been discussed in the microscopy section (section 2.4.1).

2.5 Conclusions

This chapter has shown that a wide range of experimental techniques are at our disposal, each with different sensitivities and spatial resolution. These techniques can be broken down into whether or not the technique is surface sensitive or not; or if a technique is spatially resolving (on the atomic scale) or not. Table 2.1 summarises this information. We use the properties of the techniques described in table 2.1 extensively in the experimental chapters, which are presented in chapters 3-6.

	Surface Sensitive	Not Explicitly Surface Sensitive	Spatially Integrating	Spatially Resolving
Technique	XPS, UPS, AES, LEED, STM, SEM	PXRD, TEM (EDS, EELS, EFTEM, SAED, CBED)	XPS, UPS, LEED, PXRD	SEM, TEM (EDS, EELS, EFTEM, SAED, CBED), STM

Table 2.1. Categorisation of experimental techniques used in this thesis by surface sensitivity and spatial resolution.

2.6. References

[1] D.P. Woodruff, T.A. Delchar, *Modern Techniques of Surface Science*, 2nd edition (Cambridge University Press) 1994.

[2] A. Zangwill, *Physics at Surfaces* (Cambridge University Press) 1992.

[3] G. Attard, C. Barnes, *Surfaces* (Oxford University Press) 1998.

[4] D.B. Williams, C.B. Carter, *Transmission Electron Microscopy: A Textbook for Materials Science*, 2nd edition (Springer) 2009.

[5] M.H. Loretto *Electron Beam Analysis of Materials*, 2nd edition (Chapman and Hall) 1993

[6] J. W. Steeds *Introduction to analytical electron microscopy* (Plenum)1979.

[7] R. Brydson, *Electron Energy Loss Spectroscopy* (Taylor and Francis) 2001.

[8] J. Goldstein, D. Newbury, D. Joy, C. Lyman, P. Echlin, E. Lifshin, L. Sawyer, J. Michael, *Scanning Electron Microscopy and X-ray Microanalysis*, 3rd edition (Springer) 2003.

[9] VG, SH2 sample holder instruction manual, UI428 94U.

[10] W.M. Haynes, *CRC Handbook of Chemistry and Physics*, 93rd edition (Taylor & Francis) 2012.

[11] D.P. Woodruff, *Curr. Opin. Solid State Mater. Sci*. **7** (2003) 75.

[12] R. Koller, W. Bergermayer, G. Kresse, E.L.D. Hebenstreit, C. Konvicka, M.Schmid, R. Podloucky, P. Varga, *Surf. Sci.* **480** (2001) 11.

[13] S.D. Kenny, J.B. Pethica, R.G. Edgell, *Surf. Sci.* **524** (2003) 141.

[14] L.P. Nielsen, F. Besenbacher, I. Stensgaard, E Lægsgaard, C. Engdahl, P. Stoltze, K.W. Jacobsen, J.K. Nørskov, *Phys. Rev. Lett*. **71** (1993) 754.

[15] Omicron, UHV STM 1manual, 1_210V03/Mar12.

[16] P. Grivet, *Electron Optics* (Pergamon Press) 1972.

[17] O.L. Krivanek, N. Dellby, A.R. Lupini, *Ultramicroscopy* **78** (1999) 1.

[18] O.L. Krivanek, A.J. Gubbens, N. Dellby, *Microsc. Microanal. Microstruct.* **2** (1991) 315-332.

[19] S. Doniach, M. Sunjic, *J. Phys. C* **3** (1970) 285.

[20] VG, X-ray instruction manual, HA030001.

[21] VG, UV instruction manual, HA030005.

[22] VG, CLAM 2 instruction manual, HA010001.

[23] S. Evans, *Surf. Interface Anal.* **17** (1991) 85.

[24] P.J. Cumpson, M.P. Seah, *Surf. Interface. Anal.* **25** (1997) 430.

[25] C.J. Powell, A. Jablonski, *J. Electron Spectrosc.* **178-179** (2010) 331.

[26] M.P. Seah, *J. Electron Spectrosc. Relat. Phenom.* **71** (1995) 191.

[27] C. Wagner, L. Davis, M. Zeller, J. Taylor, R. Raymond, L. Gale, *Surf*. *Interface Anal*. **3** (1981) 211.

[28] M.P. Seah, I.S. Gilmore, S.J. Spencer, *J. Electron Spectrosc. Relat. Phenom.* **120** (2001) 93.

[29] A.B. Christie, I. Sutherland, J.M. Wallis, *Surf*. *Sci*. **135** (1983) 225.

[30] N.W. Ashcroft, N.D. Mermin, *Solid State Physics*, 1st ed. (Brooks/Cole) 1976, p725.

[31] VG, LEED instruction manual, HA020010.

3. Growth and Alloying of Thin Film Te on Cu(111) and Polycrystalline Cu

3.1 Introduction

Copper telluride finds technological application as a component of several high efficiency CdTe thin film photovoltaics: either explicitly or as a consequence of interfacial reactions between the active layer and underlying Cu-based contacts [1-6]. A critical aspect of the photovoltaic device is the reliable formation of a pseudo-ohmic back contact [7,8] that integrates the photovoltaic into an electric circuit. CdTe has a high work function so metals commonly used by the electronic industry, such as Au or Cu, do not explicitly form ohmic electrical contacts with CdTe, instead forming Schottky barriers that have a much higher electrical resistance. This problem can be overcome by electrochemically etching the CdTe surface so that it is Te rich [3]. On the application of Cu, the Cu and Te react to form a $Cu_{2-x}Te$ alloy. $Cu_{2-x}Te$ alloys readily allow Cu to diffuse into CdTe, effectively reducing the work function in the surface region, allowing pseudo ohmic contacts to form. However, the situation is complicated by the fact that copper telluride exists in a multitude of phases, all of which are crystallographically distinct (e.g. Cu_2Te [9], Cu_7Te_4 [10], $Cu_{3.18}Te_2$ [11], Cu_3Te_2 [12], $Cu_{2.8}Te_2$ [11], CuTe [13] and $CuTe_2$ [14]). Indeed, Cu-Te system has the most complicated phase diagram of all the copper chalcogenides [15,16]. Each alloy has a different resistance, giving rise to substantial variability in device performance and stability [4]. This problem has motivated several recent applied studies [17-20] of typically polycrystalline systems. Studies [17-20] give good insight into the physical structure of Cu-Te alloying and will now be briefly discussed. Teeter [17] studied the deposition of Te onto polycrystalline Cu with AES and thermal desorption mass spectrometry (TDMS), concluding that Cu_2Te was formed below 373 K. Interestingly, we will show that Te/Cu(111) results in the formation of Cu_3Te_2, driven by the good lattice match between substrate and overlayer alloy. Zhou et al. [18], studied the growth of Cu_xTe alloys by evaporating a thin film of Cu onto a Te rich surface of CdTe. Using XRD, it was found that the deposition of Cu onto the enriched Te surface created a variety of alloys, including Cu_2Te, $Cu_{2.8}Te_2$, $Cu_{3.18}Te_2$, Cu_4Te_3 and CuTe. The Cu_2Te alloy was most prevalent at room temperature, with the other alloys tending to exist after annealing to temperatures up to 673 K. This study highlights the fact that the formation and interconversion of Cu_xTe alloys is facile. Spath et al. [19] used XRD and photoemission to study the deposition of Cu onto a Te enriched polycrystalline CdTe substrate. XRD results showed that $Cu_{2-x}Te$ formed with x between 0.1 and 0.5. The Cu $2p^{3/2}$ XPS spectra showed shifts with respect to elemental Cu of 0.4-0.6 eV, similar to the shift described here. Also, the structure of the valence band of $Cu_{2-x}Te$ was similar to that observed in this chapter. A further study by Teeter [20]

studied the deposition of Cu onto CdTe(111) with XPS and UPS. It was concluded that the deposition of Cu onto CdTe(111) reduced the work function and led to the precipitation of Cu_2Te by the substitution of Cd by Cu.

This chapter describes the growth, alloying and thermal properties of the model Te/Cu(111) system. Despite its obvious technological importance, the Te/Cu(111) system and indeed the deposition of Te on other Cu single crystals has not been studied in great detail. There are only two reports of the Te/Cu(111) system [21,22] and four other reports of Te on other low miller index Cu surfaces [22-25]. An early LEED study [21] assessed the sub-monolayer growth of Te/Cu(111). The data were interpreted as showing unalloyed ($2\sqrt{3}$ x $2\sqrt{3}$) R30° and ($\sqrt{3}$ x $\sqrt{3}$) R30° domains for Te coverages of 0.08 ML and 0.3 3 ML, respectively. The LEED study also suggested that for thicker Te films, epitaxial growth occurred at room temperature, along the [0001] direction, although alloying would be expected thermodynamically. The other study of Te/Cu(111) [22], used surface extended X-ray absorption fine structure (SEXAFS) to probe the geometry of 0.33 ML overlayer of Te and showed that Te substituted for a Cu atom in the outermost Cu layer, residing 0.084 nm above the Cu nuclear plane. The other studies of Te deposited onto Cu single crystals involve the sub-monolayer growth of Te on Cu(100) [22-25] and act as a good comparison to the Te/Cu(111) system. Two early LEED studies [23,24] showed that Te forms a c(2 x 2) overlayer with Te occupying the fourfold hollow sites for a coverage less than 0.25 ML. Above this coverage, a structure forms that is incommensurate with the substrate. This assignment was confirmed by both photoelectron diffraction (PhD) [25] and SEXAFS [22]. Interestingly, the SEXAFS studied showed that Te did not substitute for a Cu atom and form a substitutional alloy, as in Te/Cu(111), but instead Te occupied the fourfold hollow sites. To our knowledge, the alloying and thermal properties of thicker Te films on Cu(111) has never been studied. We address this issue here. In contrast to Te/Cu(111), preliminarily studies into the alloying of thicker Te films on Cu(100) [26] have shown that bulk alloying is inhibited at room temperature.

We present a detailed characterisation of the initial growth of Te on single-crystal Cu(111) and show immediate surface alloying at temperatures above 275 K. Continued Te deposition leads to the formation of a stable alloy phase that is consistent with a relatively unusual bulk Cu_3Te_2-like alloy with $F\bar{4}3m$ symmetry. Our study provides insight into the fundamentals of Te/Cu(111) growth and alloying, thereby aiding the interpretation of device performance in more applied studies. The work presented in this chapter has been published: M.O. King et al., *Surf. Sci.* **606** (2012) 1353.

3.2 Results and Discussion

3.2.1 Room Temperature Deposition of Te on Cu(111)

3.2.1.1 Low Coverage Growth Modes (0 < θ_{Te} < 0.33 ML)

The deposition of Te on Cu(111) at 300 K was monitored with LEED, XPS and UPS at the University of Glasgow. Further studies of the system were performed at the University of Liverpool with STM. Te was deposited from the homemade thermal evaporator described in section 2.2. The evaporator was held at 610 K during deposition, which led to an approximate growth rate for Te of 0.5 MLmin^{-1}. Coverage was calculated using equations 2.11, 2.13 and 2.14 and is quoted to an error of ± 0.05 ML, where 1 ML refers to the number of atoms in the ideal Cu(111) surface plane. The stoichiometry calculations were performed using the integrated intensities of Cu 2p$^{3/2}$ and Te 3d$^{5/2}$ XPS data with equation 2.15 and using the sensitivity factors derived in section 2.4.2.1.

Te was deposited onto Cu(111) at 300 K and studied first with LEED. The LEED data are shown in figure 3.1 and are in good agreement with the literature [21]. The dashed lines in figure 3.1 demarcate the unit mesh of the clean Cu(111) surface with all LEED patterns collected at the same energy to aid comparison. The first ordered pattern has (2√3 × 2√3) R30° symmetry and appears at 0.08 ML but is sharpest around θ_{Te} = 0.17 ML, then becomes progressively more diffuse up to 0.33 ML. Sketched in figure 3.2 (a) is the (2√3 × 2√3) R30° structure and is used to illustrate how the overlayer structure is defined. Vectors a and b define the substrate surface lattice and are related to the overlayer structure by a length factor and a rotational operation. a' and b' are 2√3 times larger than a and b, respectively. The angle at which a' and b' are rotated with respect to the substrate surface lattice vectors is 30°, hence the description of the overlayer is (2√3 × 2√3) R30°. A sketch of the (2√3 × 2√3) R30° LEED pattern is shown in figure 3.2 (b) and illustrates how the symmetry of LEED patterns are related to the real space structure. Since we are now in diffraction space the overlayer lattice vectors are 2√3 times shorter than the substrate lattice vectors. Figures 3.2 (c) and (d) illustrate the same LEED analysis process except for the higher coverage (√3 × √3) R30° SSA phase.

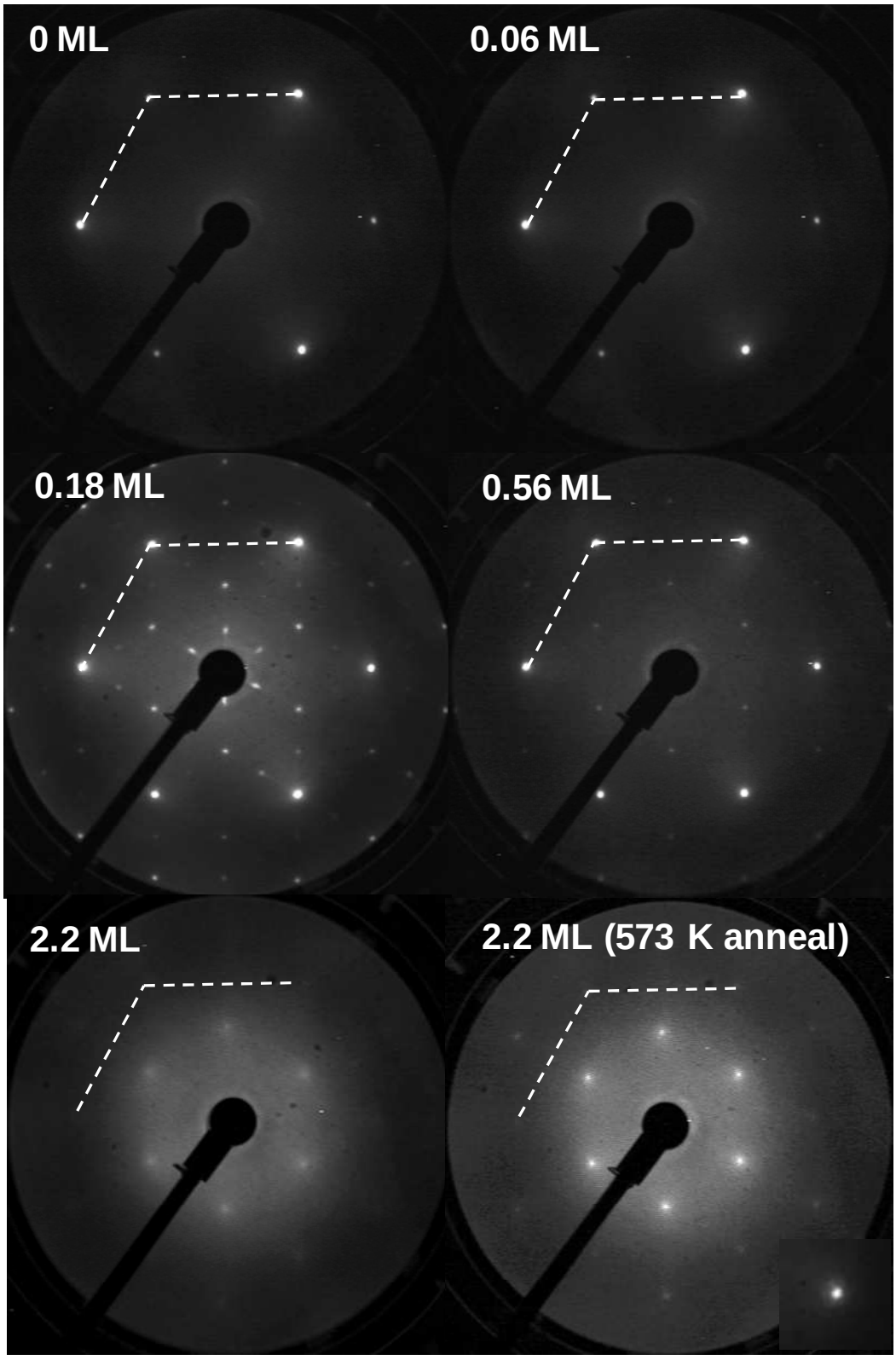

Figure 3.1. LEED patterns of room temperature deposition of Te onto Cu(111), collected at 111 eV and at a sample temperature of 300 K. The dashed lines show the part of the unit mesh of the Cu(111) substrate. The inset of the bottom right panel shows an expanded view of a single diffraction spot, where the contrast has been adjusted to pick out weak six-fold satellite spots.

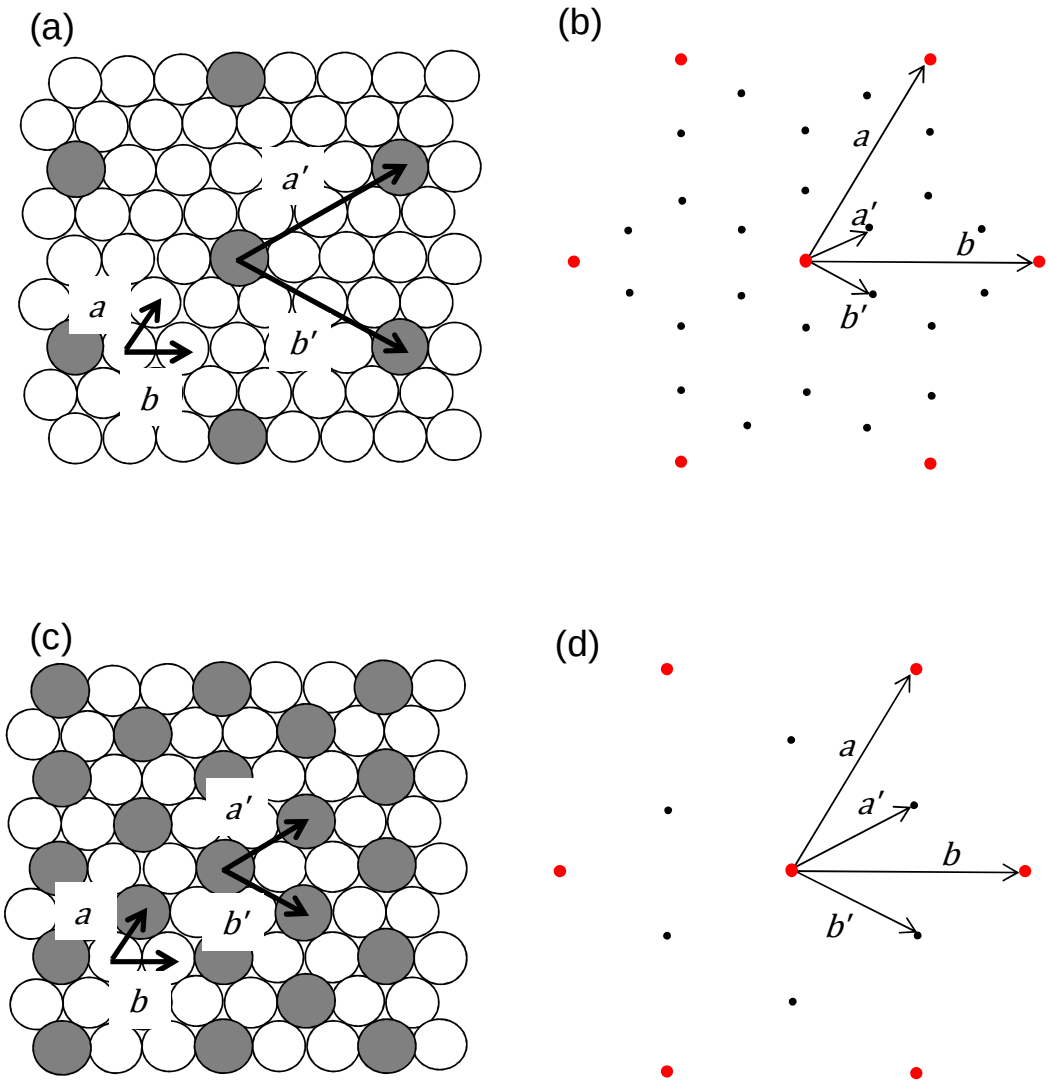

Figure 3.2. (a) Real space structure of the (2√3 × 2√3) R30° overlayer on Cu(111), with corresponding LEED pattern sketched in figure (b), which is identical to what was observed for θ_{Te} = 0.08 - 0.33 ML in figure 3.1. (c) Real space structure of the (√3 × √3) R30° overlayer on Cu(111), with the corresponding LEED pattern given in figure (d), which is identical to what was observed for θ_{Te} = 0.33 - 0.66 ML in figure 3.1. The white circles are Cu atoms, the grey circles are Te atoms. The red dots are the substrate LEED spots while the black dots are the overlayer spots. The lattice vectors describing the surface are given by *a* and *b*, while the lattice vectors for the overlayer are given by *a'* and *b'*. The angle between *a* and *a'* is 30°.

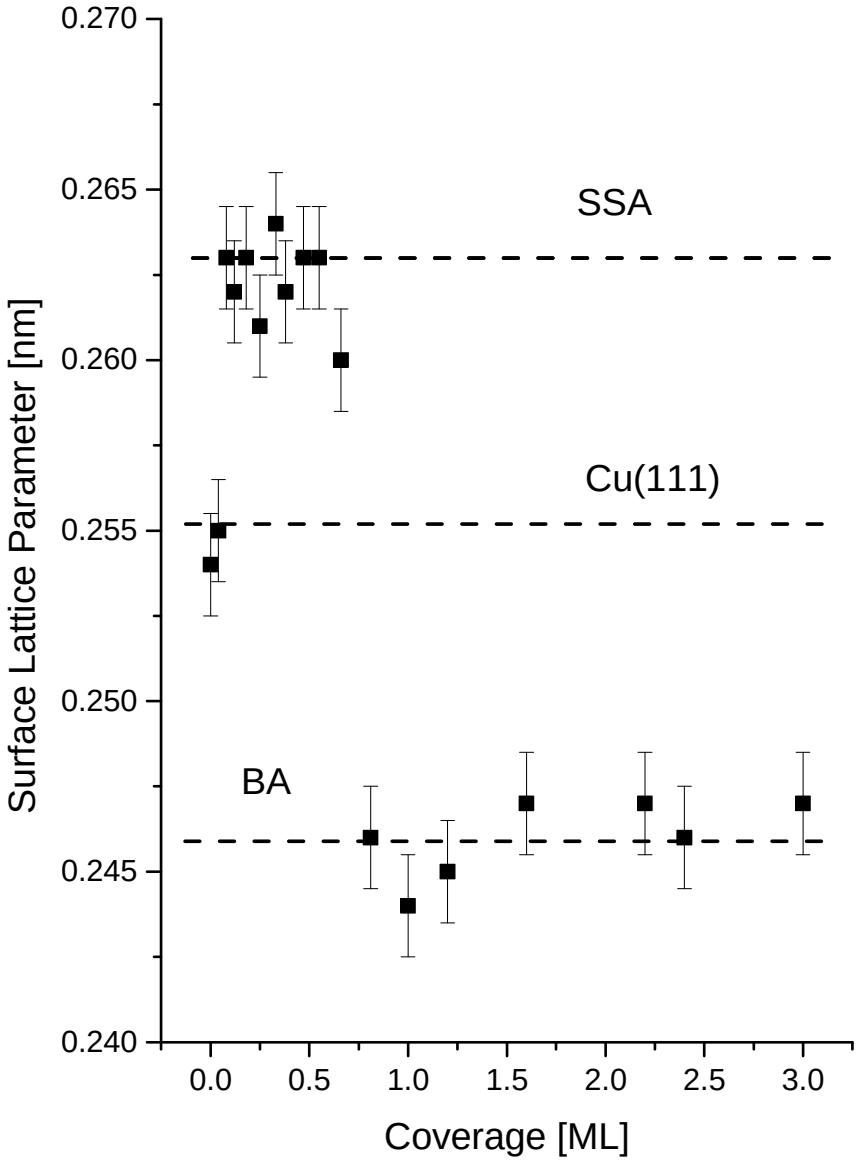

Figure 3.3. Measured surface lattice parameter for increasing coverage of Te on Cu(111). Values have been measured from the LEED patterns obtained at the designated coverages shown. Annotated on the figure are dashed lines showing the surface lattice parameters for Cu(111) (0.254 nm) and the average values obtained for the surface substitutional alloy (SSA) (0.263 nm) and the bulk alloy (BA) (0.246 nm).

A surface lattice parameter is derived from the measurement of diffraction spot positions and is shown as a function of coverage in figure 3.3. The separation of diffraction spots indicate that the surface lattice vector has expanded by ~2.8% with respect to the clean Cu(111) surface (i.e. to 0.263 nm), which could indicate strain arising from direct incorporation of Te into the surface plane, consistent with the SEXAFS study [22]. Interestingly, and in spite of the increased Te incorporation, the apparent lattice constant, shown in figure 3.3, is invariant between Te coverages of 0.08 ML and 0.33 ML.

Surface alloying was confirmed by complementary Te $3d^{5/2}$ and Cu $2p^{3/2}$ XPS data, collected immediately after LEED analysis and presented in the first panels of figure 3.4. Alloying involves the formation of chemical bonds and the redistribution of charge, which is detectable as shifts in binding energy in XPS spectra (chemical shifts). Each spectrum was fitted to the sum of a Gaussian and DS function and the fitted binding energies, presented in table 3.1, are in agreement with previous studies of copper and tellurium systems [27-30]. Reference spectra were collected from the clean Cu(111) surface (upper right panel of figure 3.4) and a thick, 22 ML Te film that was deposited below the alloying transition temperature (upper left panel of figure 3.4). For each fit, peak widths were fixed to those of the reference spectra (w_{Cu} = 1.8 eV, w_{Te} = 1.6 eV) whilst the asymmetries were free parameters and were fitted to yield results that are consistent with previous observations of Cu and other p-block semi-metals (e.g. Sn [30]). Specifically, we obtain asymmetry values of α_{Cu} = 0.02 and α_{Te} = 0.12, using the definitions of equation 2.9. For a coverage of 0.18 ML, the Te $3d^{5/2}$ data are well fitted by a single component of 572.3 eV binding energy, which is 0.8 eV lower than the value we measured for elemental Te. The Cu $2p^{3/2}$ data can be fitted by two components: the largest is elemental Cu, at 932.4 eV; a smaller component, shifted by 0.2 eV to higher binding energy, indicates slight charge transfer away from the surface Cu atoms. Thus, the data suggest that the (2√3 × 2√3) R30° surface contains a single $Te^{\delta-}$ species and a minority $Cu^{\delta+}$ species and so are consistent with the formation of a surface substitutional alloy (SSA), in agreement with both an earlier SEXAFS study [22] and the lattice expansion noted above, but different to the adsorbed overlayer implied by reference [21]. Indeed, although no ordered Te structures are observed by LEED for coverages below 0.08 ML, XPS show similar chemical shifts, indicating that Te is incorporated within the surface layer immediately upon deposition.

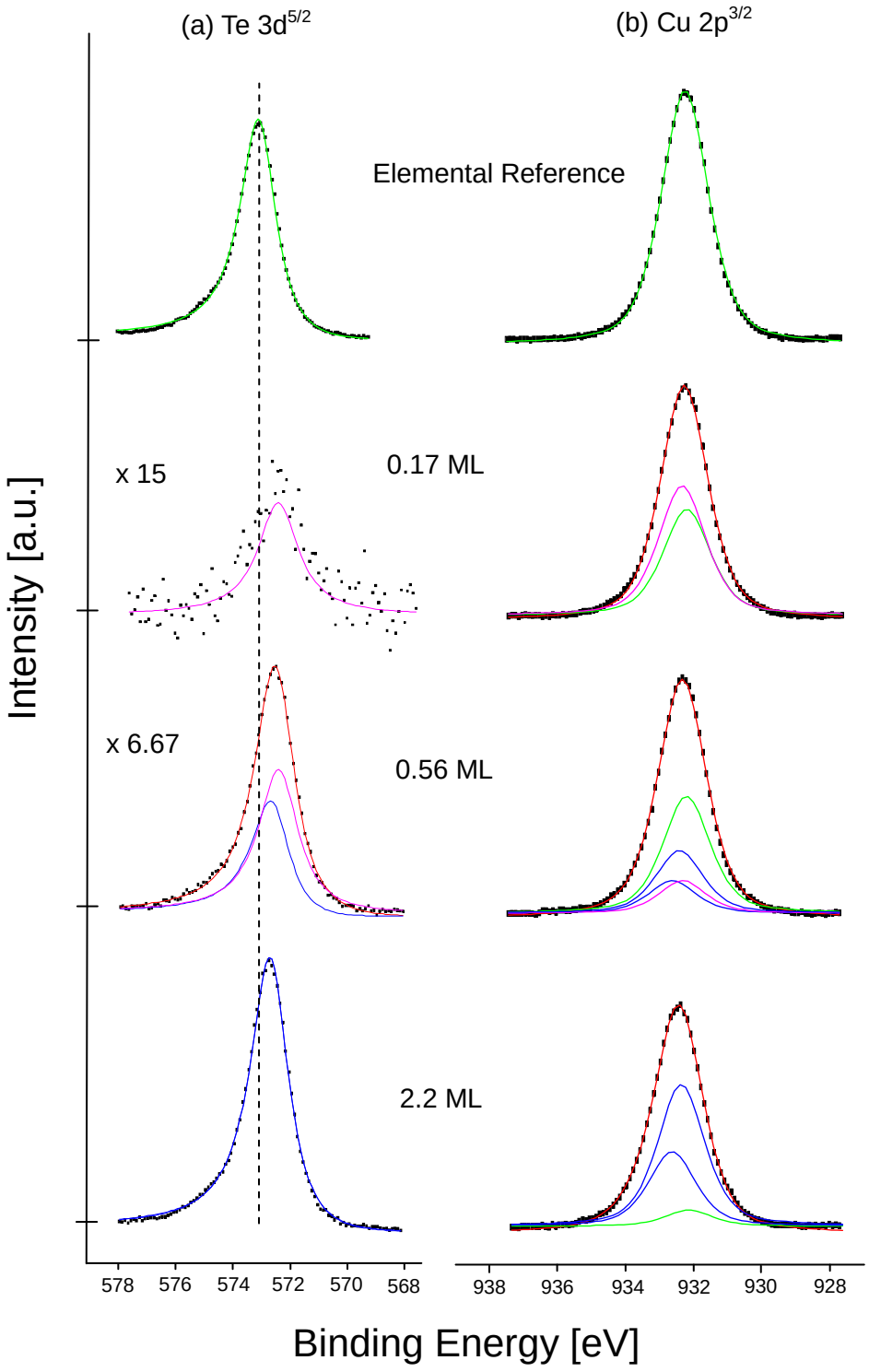

Figure 3.4. XPS spectra for (a) Te $3d^{5/2}$ and (b) Cu $2p^{3/2}$ core levels. The upper panels show elemental (a) Te $3d^{5/2}$ and (b) Cu $2p^{3/2}$ reference spectra. The lower panels show Te $3d^{5/2}$ and Cu $2p^{3/2}$ core levels as a function of Te coverage on Cu(111). The fitted spectra are in red whilst green indicates elemental Cu or Te components; magenta represents the surface substitutional alloy (SSA) contribution and blue is the bulk alloy (BA).

	Cu $2p^{3/2}$				Te $3d^{5/2}$		
	Cu	$Cu^{\delta+}$	Cu^{+}	Cu^{2+}	Te	$Te^{\delta-}$	Te^{2-}
Binding Energy [eV]	932.4	932.6	932.7	933.0	573.1	572.3	572.7
FWHM [eV]	1.8	1.8	1.8	1.8	1.6	1.6	1.6
asymmetry	0.02	0.02	0.02	0.02	0.12	0.12	0.12

Table 3.1. Parameters used to fit Cu $2p^{3/2}$ and Te $3d^{5/2}$ XPS spectra.

UPS spectra collected from clean Cu(111) and the surface alloy are presented as the upper three traces of figure 3.5. The Cu(111) spectrum is identical to those previously reported [30], with sharp 3d bands between 2 and 4 eV and surface states located within 1 eV of the Fermi edge. The only significant spectral difference between the clean surface and the SSA is that the presence of Te gradually quenches the surface states of Cu(111), which is typical of chemisorbed species [31].

A representative STM image of the low coverage surface is presented in figure 3.6 (a) and was collected at room temperature from a 0.18 ML surface displaying a sharp ($2\sqrt{3} \times 2\sqrt{3}$) R30° LEED pattern. The STM image is in agreement with the LEED data, being dominated by one of two possible ($2\sqrt{3} \times \sqrt{3}$) R30° domains. It is likely that distinct ($2\sqrt{3} \times 2\sqrt{3}$) R30° domains form at coverages below 0.18 ML; however we did not image at low enough coverage to observe them. The overlayer unit cell dimensions are measured to be 0.45 ± 0.05 nm and 0.91 ± 0.05 nm using the FFT shown in the inset of figure 3.6 (a), which compare favourably to the expanded lattice constant of 0.456 nm (i.e. $\sqrt{3} \times$ 0.263 nm) that was determined by LEED. Rectangular ($2 \times 2\sqrt{3}$) domains (not shown) are also occasionally observed in STM, but these must be relatively minor since they are not evident by LEED; similar rectangular overlayers have been observed previously for low coverages of Te/Pt(111) [32], in which a ($2 \times \sqrt{3}$) structure was observed.

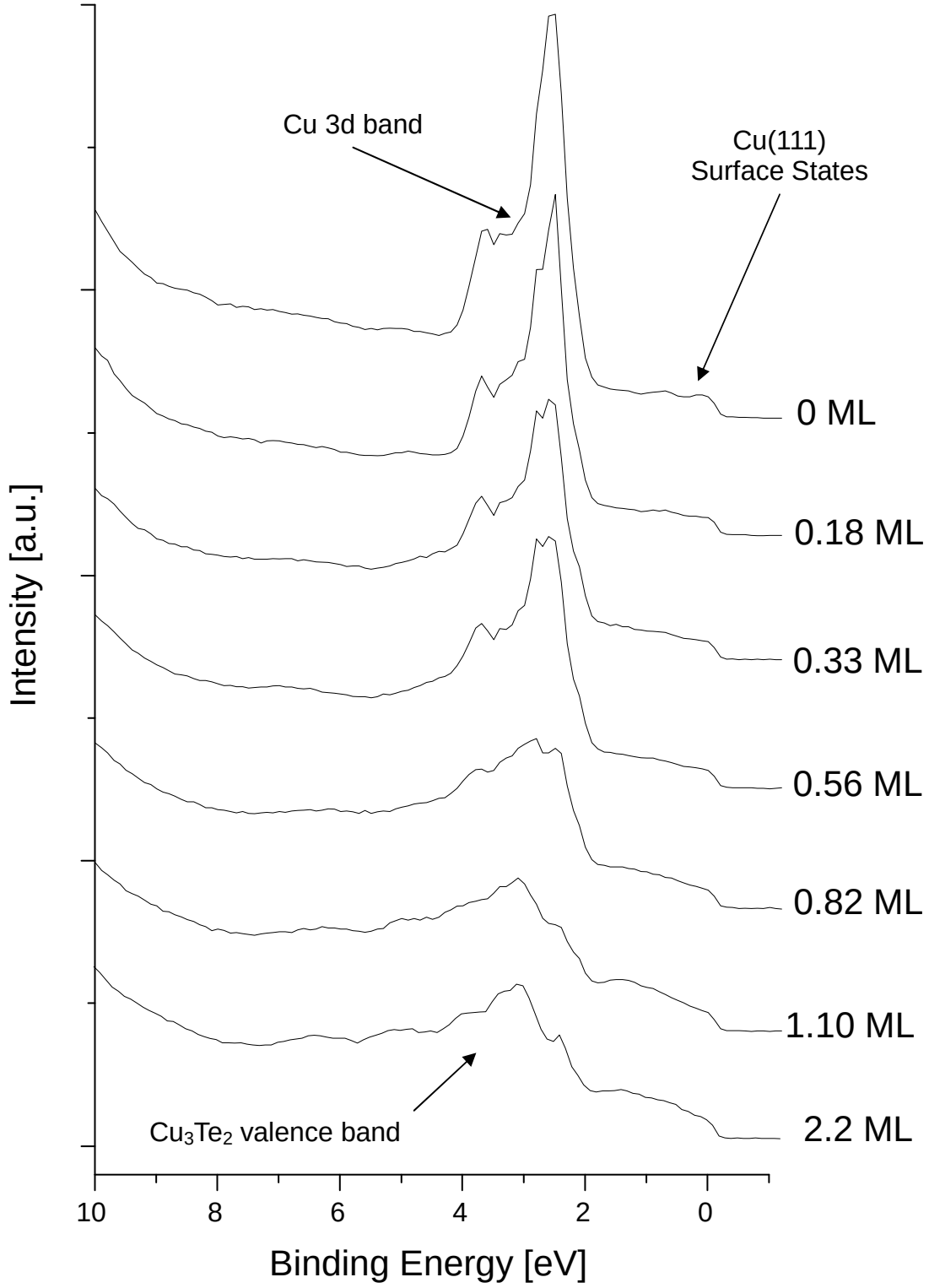

Figure 3.5. Series of UPS spectra for increasing coverages of room temperature Te deposition onto Cu(111).

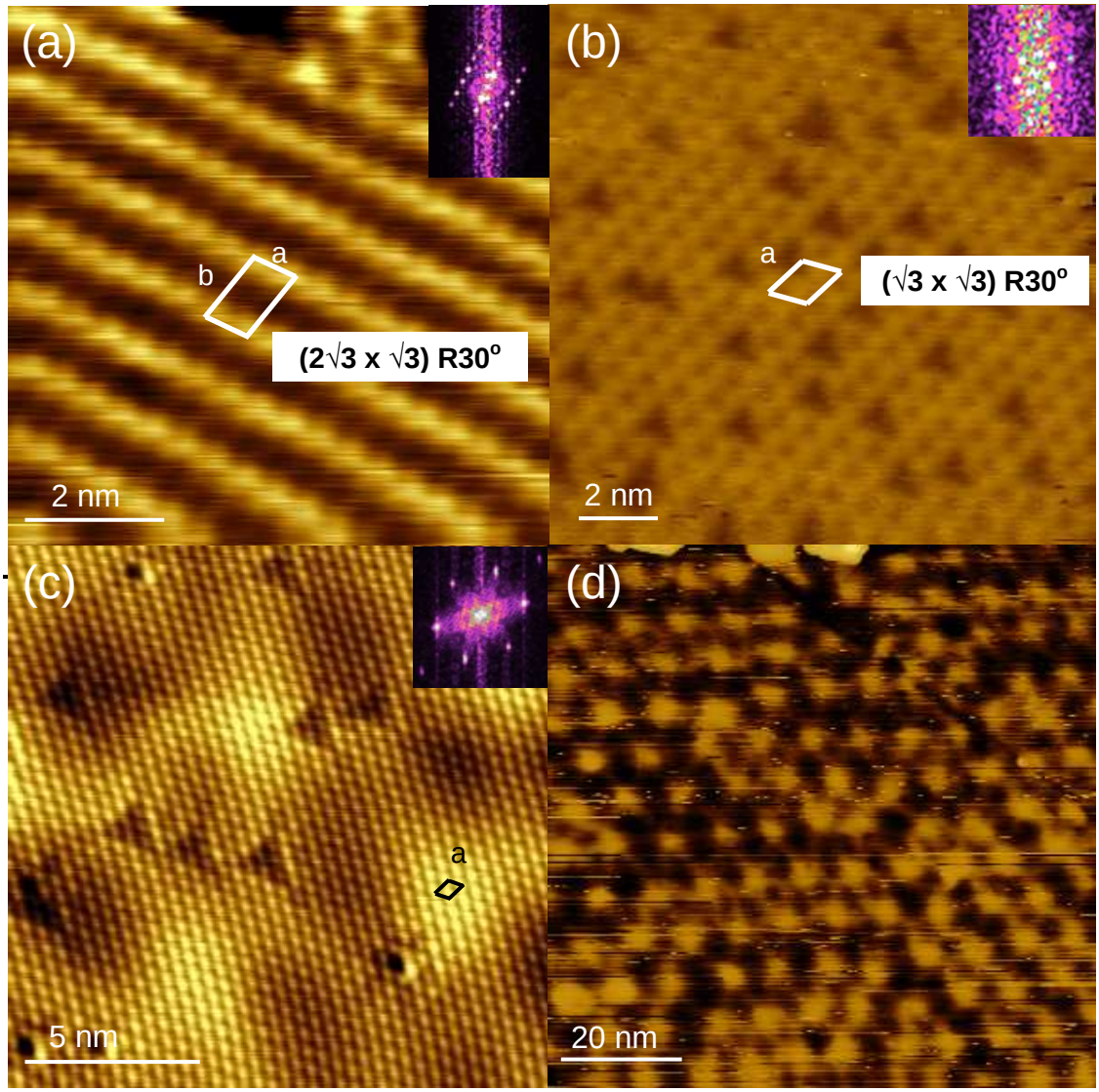

Figure 3.6. STM images for Te coverages of (a) 0.18 ML, (b) 0.38 ML, and (c-d) 2.2 ML at 300 K. (a) is obtained from a surface that produced a sharp (2√3 × √3) R30° LEED pattern. The tunnelling parameters were V_{gap} = 1.8 V, I_t = 800 pA. Inset is the FFT of the image. The surface unit cell dimensions are measured to be a = 0.45 ± 0.05 nm and b = 0.91 ± 0.05 nm. (b) is obtained from a surface that produced a sharp (√3 × √3) R30° LEED pattern. The tunnelling parameters were V_{gap} = 1.7 V, I_t = 1.9 nA. Inset is the FFT, yielding a surface unit cell dimension of a = 0.45 ± 0.05 nm. (c) is an STM image of the Cu_3Te_2 alloy generated by room temperature deposition of 2.2 ML Te on Cu(111). The tunnelling parameters were V_{gap} = 1.8 V, I_t = 800 pA. The inset is the FFT yielding a surface unit cell dimension of a = 0.43 ± 0.05 nm. (d) is a wider, 90×90 nm^2 image, taken at the same tunnelling parameters as (c).

Together, the LEED, XPS and STM data indicate the gradual incorporation of Te into an expanded Cu surface lattice with increasing coverage. The simplest structure that is consistent with the data is sketched in the first panel of figure 3.9 (b), which shows a strained domain of a (2√3 × 2√3) surface substitutional alloy that should be complete at a coverage of 0.08 ML. Between 0.08 ML and 0.17 ML, Te adatoms are incorporated within growing domains of (2√3 × √3), as shown in the second panel of figure 3.9 (b). Te atoms are incorporated directly within the Cu surface, causing a 2.8% lattice expansion and - as revealed by previous SEXAFS data [22] - sitting slightly above the Cu plane. Lines of Te atoms (along the short axis of the (2√3 × √3) R30° unit cell) are in good agreement with the dominant striped structure observed by STM, taking the bright features to correspond to Te atoms. Te has been previously imaged as bright protrusions in other systems, such as Te/Pt(111) [32,33]. Above a coverage of 0.17 ML, the surface morphology is only slightly modified. Te $3d^{5/2}$ XPS data, shown in figure 3.4, indicate that Te atoms continue to be incorporated into the surface layer and the LEED data show that there is no further expansion until a coverage of 0.33 ML, when LEED shows that a (√3 × √3) R30° structure is formed. Figures 3.2 (c) and (d) show how the LEED pattern is interpreted as a real space structural model. As sketched in figure 3.9 (b), there is a natural progression from the (2√3 × √3) R30° SSA to a related (√3 × √3) R30° SSA by the incorporation of additional Te between the Te lines of the (2√3 × √3) R30° overlayer. Our LEED patterns show a gradual extinction of the extra LEED spots associated with the (2√3 × √3) R30° SSA, in agreement with this process. As XPS does not indicate any more than one Te species, alloying is restricted to the uppermost (111) layer.

3.2.1.2 Intermediate Coverage Growth Modes (0.33 < θ_{Te} < 0.66 ML)

Clearly, Te atoms deposited beyond 0.33 ML cannot be incorporated within the simple (√3 × √3) R30° structure sketched in figure 3.9 (b). Never theless, the strained (√3 × √3) R30° LEED pattern first observed at 0.33 ML was found to persist up to 0.66 ML, albeit rapidly becoming weak and diffuse with increased coverage and therefore accounting for an increasingly small fraction of the surface. Figure 3.6 (b) presents a typical STM image of the residual (√3 × √3) R30° structure, collected at a coverage of 0.38 ML, only slightly beyond where LEED intensity starts to diminish. A brief anneal to 423 K was required prior to imaging to improve surface ordering but did not change the XPS or UPS spectra. The measured lattice parameter, using the Fourier Transform shown in the inset of figure 3.6 (b), is 0.45 ± 0.05 nm, which is within error of that measured with LEED. The STM image is therefore in good agreement with the (√3 × √3) R30° structure sketched in figure 3.9. There is also a significant density of triangular surface defects that have a size and shape

that is consistent with Te vacancies. Such vacancies were found to be commonplace across the surface alloy surface and may act as a strain-relief mechanism. In contrast to the LEED data, XPS indicates substantial differences above 0.34 ML since additional components are required to fit both the Te $3d^{5/2}$ and Cu $2p^{3/2}$ XPS spectra. The Te spectra, shown in figure 3.4, are best-fitted using an additional component, 0.6 eV higher than that of elemental Te and consistent with Te^{2-} [26-29]. The Cu $2p^{3/2}$ XPS spectra collected for Te coverages above 0.33 ML also require additional components, representing formal Cu oxidation states.

The discrimination between different Cu oxidation states is a common issue throughout this thesis. The binding energy of Cu^{+} and Cu^{2+} in different Cu_xTe alloys has been measured by references [19,20] to be 932.7 eV and 932.9 eV, respectively, and is measured here to be 932.7 eV and 933.0 eV. This reasonably small variation in binding energy, coupled with the fact that there are a wide range of possible stoichiometric and non-stoichiometric Cu_xTe alloys (e.g. Cu_2Te [9], Cu_7Te_4 [10], $Cu_{3.18}Te_2$ [11], Cu_3Te_2 [12], $Cu_{2.8}Te_2$ [11], CuTe [13] and $CuTe_2$ [14]), means that unambiguously determining the Cu_xTe phase from the relative ratio of Cu^{+} : Cu^{2+} XPS signal is difficult. We therefore discuss the fitting details below, starting with the higher Te coverage since increasing the Te coverage extinguishes the SSA component that is still evident at 0.56 ML (figure 3.4), simplifying the fitting.

To summarise the intermediate regime, LEED and XPS data imply a broad surface phase transition between a SSA and a bulk-like alloy compound, with the fraction of (√3×√3) R30° SSA gradually diminishing as coverage exceeds 0.33 ML, as additional Te atoms are incorporated into a growing bulk alloy. The former is characterised by a slight shift of charge towards Te whilst the latter is better characterised by formal changes in oxidation states and therefore in bond formation. The spot spacing in the LEED patterns indicates that the ordered areas of the surface retain the SSA form and we did not discern diffraction from the bulk-like alloy, indicating a degree of rough, or disordered, growth at room temperature. Good quality STM images could not be obtained from this surface without further annealing.

3.2.1.3 High Coverage Growth Modes (θ_{Te} > 0.66 ML)

For θ_{Te} > 0.66 ± 0.05 ML, the LEED pattern retained its (√3 × √3) R30° symmetry but measurement of the lattice spacing, (after a brief anneal to 573 K to improve surface ordering) indicated a ~3.2% in plane lattice *contraction* with respect to Cu(111) (i.e. to

0.248 nm), shown in figure 3.3. We will show that this rather subtle LEED transition actually marks the complete formation of an ordered Cu_3Te_2-like alloy, which we will refer to as a bulk alloy (BA) since it is consistent with a known bulk alloy phase and appears to persist up to at least 100 ML. Within the discrete coverages studied, the sharpest LEED pattern obtained was at θ_{Te} = 2.2 ML and it became progressively more diffuse with increasing Te coverage, most likely because of a degree of surface roughening and the onset of a three-dimensional growth mode. Annealing a 2.2 ML film (573 K, 10 min) reduced the background LEED intensity and sharpened the diffraction spots, consistent with surface smoothing without a further change in alloy phase. The fitting of the 2.2 ML film is shown in the bottom panel of figure 3.4. The XPS features attributed to the SSA (i.e. components at 572.3 eV and 932.6 eV for Te $3d^{5/2}$ and Cu $2p^{3/2}$, respectively) are absent and only those components attributed to bulk alloy formation in the previous section are observed.

As it remains difficult to discriminate between the binding energies of Cu^+ and Cu^{2+} states, we start by considering the Cu : Te stoichiometry alone and find that the ratio of integrated intensities of ionic Cu to Te yields a value of 1.4 ± 0.1, using equation 2.17 and the appropriate sensitivity factors, as defined in section 2.4.1. We therefore fit the data assuming a Cu_3Te_2-like composition, fixing the peak widths and asymmetries for all components to those determined from elemental Cu, then fixing the binding energies of 932.7 and 933.0 eV for the Cu^+ and Cu^{2+} oxidation states (as found, for example, in bulk copper telluride and copper sulphides [34]). When analysed in this way, the best-fit yields a ratio of Cu^+ : Cu^{2+} = 1.9 : 1, within error of the 2 : 1 ratio expected for Cu_3Te_2 but also encompassing other non-stoichiometric phases (e.g. $Cu_{2.8}Te_2$). The fitted parameters are given in table 3.1.

We note that the X-ray induced Cu LMM Auger feature of the BA also differed from that of Cu(111) [35]. The peak separation between Cu^+ and Cu^{2+} has been reported to be 0.7 eV in CuS and Cu_2S [36]; and 1.4 eV in CuO and Cu_2O [37], which is a larger separation than measured here for the Cu $2p^{3/2}$ XPS data, 0.3 eV. However, quantitative analysis of Cu(I) and Cu(II) components was less precise than the XPS discussed above due to the intricate nature of the peak shape which meant that without a standard sample, analysis with the Cu LMM data are ambiguous.

STM of the BA, figure 3.6 (c), shows a hexagonal surface unit cell which is consistent with the hexagonal LEED symmetry observed in figure 3.1. In the right hand inset of figure 3.6 (c) is the FFT of the STM image, which has sharp spots similar to the LEED pattern and

relates to a spacing in real space of 0.43 ± 0.05 nm, compressed with respect to sub-monolayer SSA. There is also a long range, 8.5-10 nm, periodicity in the BA STM images which is corrugated by ~0.05 nm. Figure 3.6 (d) shows a lower magnification image, showing this long range periodicity. This is attributed to a Moiré effect, producing a superlattice similar to that observed in a wide variety of systems [38-44] and originating from the mismatch of the underlying substrate lattice with the overlayer structure. Such superlattices tend to imply that epitaxial strain in the overlayer is slight, the overlayer adopting an incommensurate relationship to the substrate. One can calculate the expected long range periodicity using [45]:

$$D = \sqrt{\frac{a_1 a_2}{(a_1^2 + a_2^2 - 2a_1 a_2 \cos\alpha)}}, \tag{3.1}$$

where D is the long range periodicity and α is the angle of rotation between an overlayer and substrate of lattice parameters a_1 and a_2, respectively. To calculate D, the following values were used: a_1 was set to the measured BA Te-Te separation (0.428 nm); a_2 was set as √3 × the Cu-Cu separation in Cu(111) (i.e. 0.440 nm); and α was taken to be the experimentally measured rotation angle of 2 ± 2°. U sing equation 3.1, we obtain values of D of between 8.2 nm to 10.4 nm for α in the range 2.6° to 1.6°. This is in good agreemen t with the observed value of D = 8.5-10 nm. Conversely, taking the strained SSA surface lattice vector for a_2 yields a far smaller Moiré periodicity that is inconsistent with the STM data and indicates that the SSA structure is not retained following alloy overgrowth. Figure 3.6 (d) shows that the Moiré structure is faulted, with poor translational symmetry. Moiré superlattices can also give rise to sharp satellite spots in LEED, as observed in the FeO/Pt(111) [38] and Ag/Cu(111) [44] systems. In the present case, weak satellite spots were observed about the principal diffraction spots, as indicated in the final inset panel of figure 3.1. Their diffuse nature is ascribed to the faulted nature of the extended periodicity observed by STM, as shown in figure 3.6 (d). We also note a large number of triangular defects on the surface. Their size and shape suggest that they are Te vacancies.

The formation of Cu_3Te_2 is interesting since Cu_2Te is more typically suggested in Cu_xTe back contact studies. In bulk systems, a number of different Cu_xTe phases have been described, including Cu_2Te [9], Cu_7Te_4 [10], $Cu_{3.18}Te_2$ [11], Cu_3Te_2 [12], $Cu_{2.8}Te_2$ [11], CuTe [13] and $CuTe_2$ [14], of which Cu_2Te is perhaps the most common. Of these, only the $P6/mmm$-Cu_2Te [9] and a relatively unusual $F\bar{4}3m$-Cu_3Te_2 [12] alloys have low-index planes with hexagonal symmetry and a surface lattice vector that would be consistent with our measured LEED and STM data. However, XPS is only consistent with a Cu_3Te_2-like

alloy. Indeed, artificially fixing the Cu^+ : Cu^{2+} ratio to that required for other known alloy phases significantly worsens the fit, as shown in table 3.2.

Figure 3.7 shows the (111)-oriented, Te-terminated $F\bar{4}3m$-Cu_3Te_2 structure that was described by a previous bulk XRD study [12]. The unit cell is cubic with lattice constant of a = 0.603 nm. It has a face centred cubic arrangement of Te atoms that are extremely well lattice-matched to the Cu(111) surface if the (110) lattice vectors of the BA - i.e. the close-packed lines - lie at 30º to the (110) vectors of the Cu(111) substrate, so that the interfacial layer between Cu and Cu_3Te_2 alloy mimics the symmetry (but not the strain) of the (√3 × √3) R30°SSA.

Alloy	Cu^+ : Cu^{2+}	Goodness of Fit (χ^2/DoF) (x 10^6)
Cu_2Te	1 : 0	1.81
CuTe	0 : 1	5.49
$CuTe_2$	0	n/a
$Cu_{2.8}Te_2$	4 : 3	0.44
Cu_3Te_2	**2 : 1**	**0.37**
$Cu_{3.18}Te_2$	3 : 1	0.61
Cu_7Te_4	6 : 1	1.05
(Best Fit)	**1.9 ± 0.1 : 1**	**0.36**

Table 3.2. The goodness of fit for fixed various Cu_xTe alloys for the deposition of Te/Cu(111) at 300 K. In each case, the ratio of Cu^+ : Cu^{2+} has been fixed to the value shown. With the ratio of Cu^+ to Cu^{2+} a free parameter, the best fit is for Cu^+ : Cu^{2+} = 1 : 1.9.

In fact, in-plane epitaxial strain of the alloy is minimal, in agreement with the observation of a Moiré pattern, since the Te-Te separation of the literature unit cell is within error of that measured by STM here. Cu atoms in the proposed $F\bar{4}3m$ BA are distributed statistically over a number of different sites: they fill all the tetrahedral holes [e.g. at (1/4, 1/4, 1/4)], 20% of the octahedral holes [e.g. at (1/2, 1/2, 1/2)] and 7.5% of tetrahedral sites

that are displaced from the tetrahedron centre to one of the cell faces [e.g. at (0.71, 0.71, 0.71)]. Such a multiplicity of Cu sites may well facilitate the alloying described in the following section and Cu diffusion into CdTe, as will be described in chapter 4.

Further evidence for a Cu_3Te_2 alloy rather than the more common Cu_2Te alloy is provided by the surface step heights measured by STM, since the step heights expected for the (001) step of the $P6/mmm$-Cu_2Te structure and the (111) step of $F\bar{4}3m$-Cu_3Te_2 structure are significantly different. The step height was measured by integrating across the length of the step, indicated in figure 3.8, and the measurement of several similar steps gave a range of heights of 0.32 ± 0.02 nm.

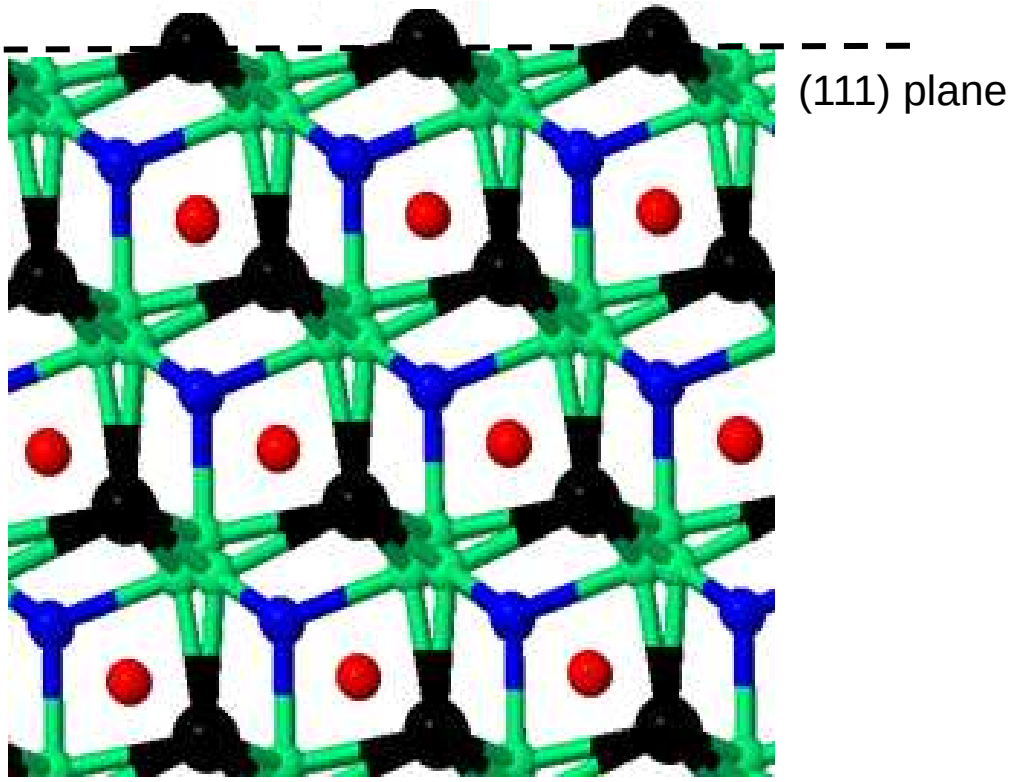

Figure 3.7. Schematic side-on representation of the (111)-terminated $F\bar{4}3m$ Cu_3Te_2 structure, derived from reference [12]. Black spheres are Te atoms, in a face-centred-cubic arrangement. Blue spheres are Cu atoms located in octahedral sites, 20% of which are occupied. Green spheres show Cu atoms in distorted tetrahedral sites, 7.5% of which are occupied. Red spheres show Te atoms in tetrahedral sites, all of which are occupied. Bonding is schematic and to aid visualisation only.

This result compares poorly with the height of steps separating (001) planes of Cu_2Te, which are 0.424 nm high, but is in reasonable agreement with the (111) steps of $F\bar{4}3m$-Cu_3Te_2, which are 0.349 nm high for the full stoichiometric alloy described in reference [12]. We suggest that such a contraction of the bulk alloy lattice constant could be accounted for by a slight nonstoichiometric composition, particularly since non-stoichiometric $Cu_{3-x}Te_2$ alloys are well-known. These non-stoichiometric Cu-Te alloys usually adopt $Pmmn$ or $P4/nmm$ symmetry and the $F\bar{4}3m$ structure is relatively rare in the literature. We conclude that it is stabilised in this case as a surface phase, facilitated by the good lattice match outlined above.

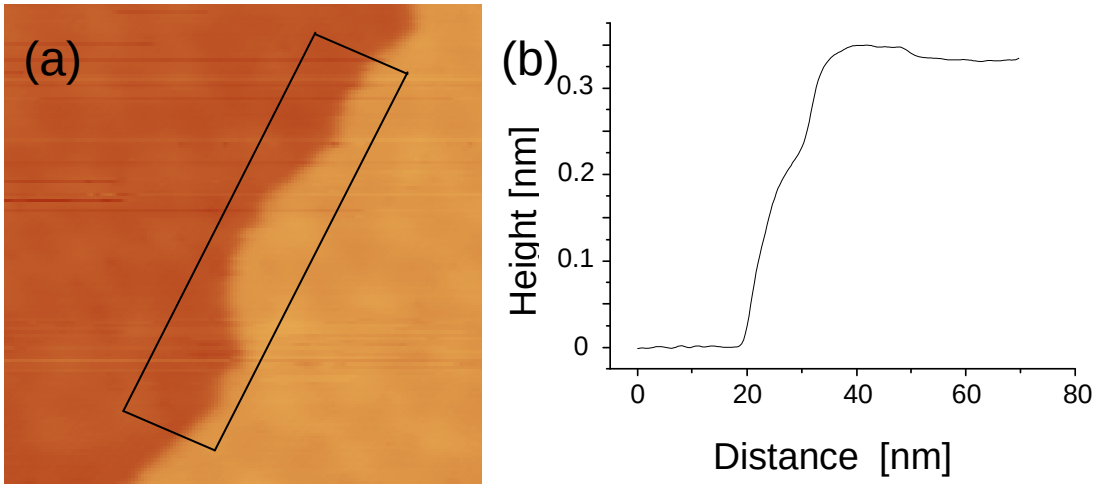

Figure 3.8. An STM image showing a typical step between two terraces of the Cu_3Te_2 alloy. The image size is 100×100 nm^2 and tunnelling parameters were V_{gap} = 1.6 V, I_t = 800 pA. (b) The step height was integrated over the boxed region and measured to be 0.32 ± 0.01 nm high.

Finally, we note that the UPS data, shown in figure 3.5, are also in agreement with a stoichiometry of Cu_3Te_2 rather than Cu_2Te. The data are similar to spectra previously reported for glassy copper telluride alloys with a Cu_xTe_{1-x} composition, where x ~0.58 [46], which show a step at the Fermi level. In contrast, a separate study of Cu_2Te valence band spectra [47] showed no step at the Fermi level. As our data show a strong step at Fermi level, it is more consistent with Cu_3Te_2 than Cu_2Te.

In addition to the studies presented here, IV curves has been extracted from the LEED patterns in figure 3.1 and compared to density functional theory (DFT) calculations by K.

Pussi's group at the Lappeenranta University of Technology, Finland. The preliminary results of the (√3 x √3) R30° and Cu_3Te_2 phases [48] show a poor match between experiment and calculation. We suggest that the discrepancy between calculation may be a result of the (√3 x √3) R30° or Cu_3Te_2 layer being laterally displaced so that all the Cu and Te atoms occupy HCP hollow sites, in essence a stacking fault. This effect has been observed on a similar system - Sb/Cu(111) [49].

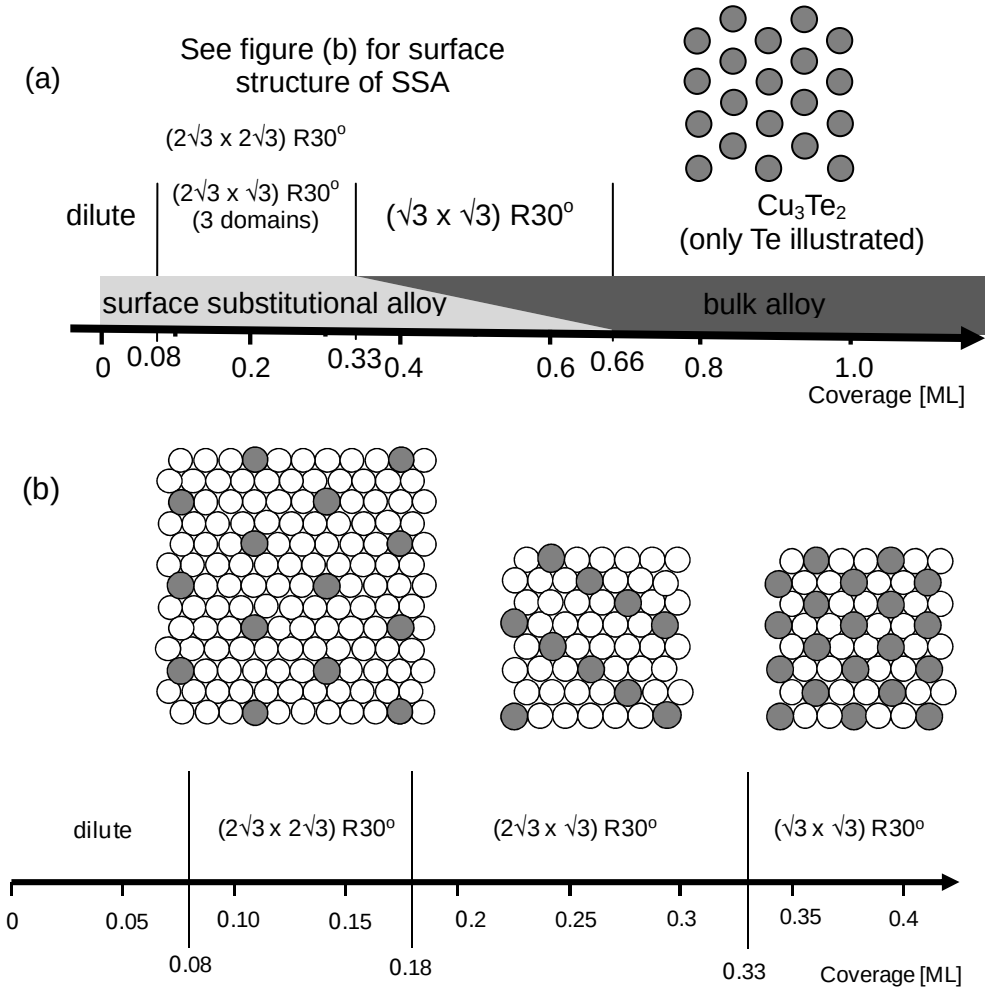

Figure 3.9. Schematic surface phase diagram for Te/Cu(111) at room temperature. Grey circles represent Te atoms and white circles represent Cu. (a) covers a broad range of Te coverages while (b) shows the different surface structures of the SSA. There were no further detectable phase changes up to the maximum coverage examined (~100 ML).

We summarise the data for Te/Cu(111) in figure 3.9. Upon deposition, Te was immediately incorporated into a SSA, the structure of which goes from a (2√3 x 2√3) R30° overlayer → (2√3 x √3) R30° overlayer → (√3 x √3) R30° overlayer with increasing Te coverage. Above 0.33 ML, a bulk like Cu_3Te_2 alloy increasingly grows at the expense of the SSA. For Te coverages greater than 0.66 ML, only the Cu_3Te_2 alloy was observed.

The above results provide an interesting comparison to a previous XRD study [18], where Cu was deposited onto a Te rich CdTe substrate at room temperature to form a surface Cu_xTe film. The study showed that 10-100 nm thick Cu_2Te films were observed at room temperature and only transformed into $Cu_{2.8}Te_2$ by annealing at 523 K. The XRD patterns shown in reference [18] clearly indicate that the structure is not the $F\bar{4}3m$ form that we propose here. Another previous study of 5 nm Te deposition on polycrystalline (and presumably predominantly (111)-terminated) Cu [17] used AES to again identify the formation of a Cu_2Te surface alloy. In contrast, our own data show the immediate formation of a Cu_3Te_2-like alloy at room temperature. XPS and UPS measurements (not shown) at 300 K and 573 K are identical, indicating no further transitions in this temperature range. Whether differences in film thickness alone can account for this difference in alloying is unclear but it is certainly the case that no change in alloying behaviour across the thickness range studied here (up to ~100 ML thickness) is observed and that $F\bar{4}3m$ alloy formation in even 30 ML thick films on Cu(111) is facile. It is possible that the presence of grain boundaries in polycrystalline systems act as a strain relief mechanism that promotes the Cu_2Te formation. Conversely, and as seen in many single crystal systems, it may be the case that the single crystal substrate and good lattice matching stabilise the unusual Cu_3Te_2-like alloy phase that we observe. To rationalise the observations made for Te/Cu(111) compared to Te/Cu_{poly}, a study of the alloying of thick Te film on Cu_{poly} was made and described in the following section.

3.2.2 Room Temperature Deposition of Te on Polycrystalline Cu

Practical CdTe photovoltaic cells are typically formed with polycrystalline Cu back contacts [1-6]. For comparison with the extensive study of the model Te/Cu(111) presented in section 3.2.1, we now deposit Te onto a thermal evaporated, polycrystalline Cu surface. Furthermore, we use a polycrystalline Cu substrate in chapter 4, when we study the deposition of CdTe on Cu, so it was important to understand the differences in terms of alloying with Te between the single crystal and polycrystalline Cu substrates.

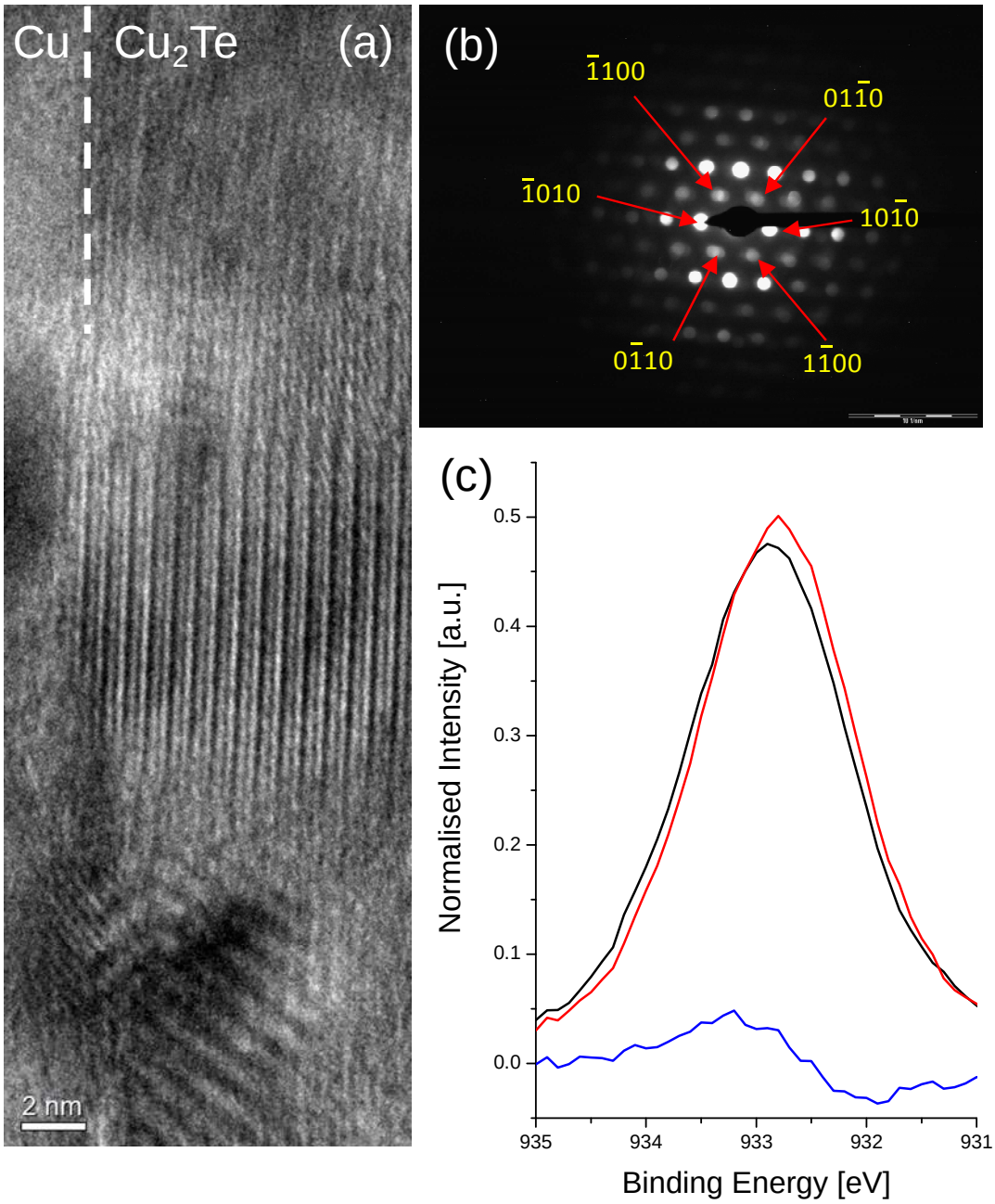

Figure 3.10. (a) BF image of the interface between Cu_{poly} and Cu_2Te. (b) CBED pattern of a crystallite in Te/Cu_{poly} film. The CBED pattern can only be indexed to that of $P6/mmm$-Cu_2Te, with lattice parameters of a = 0.457 nm, c = 0.750 nm and γ = 120°. (c) Normalised Cu $2p^{3/2}$ XPS spectra showing the difference in peak shape and binding energy between 10 ML Te/Cu(111) (i.e. Cu_3Te_2), shown in black and 10 ML of Te/Cu_{poly} (i.e. Cu_2Te), shown in red. The difference spectrum is shown as the blue line and shows a shift in the peak position of the Cu $2p^{3/2}$ spectra.

As discussed in the section 3.2.1, there are a number of different possible Cu-Te alloys. In the case of Te/Cu(111), we have shown that this gives a Cu_3Te_2-like alloy for Te coverages exceeding 0.66 ML, due to the good lattice match with the substrate. Previous studies of Te deposited onto polycrystalline Cu (or vice versa) have been performed with the consensus being that Cu_2Te is the predominant alloy phase formed [17-20]. In this study, Te deposited onto polycrystalline Cu also led to the Cu_2Te phase. As LEED can only give information on smooth, ordered surfaces, it is therefore not appropriate to use in the case of rough, polycrystalline Cu substrates. Indeed all observed LEED patterns were diffuse with no observable spots. Electron diffraction techniques in TEM, described in section 2.4.3, are more applicable to polycrystalline materials. As the grain size of Cu is quite small (less than 100 nm), CBED was the appropriate electron diffraction technique to use (as opposed to SAED).

The structure of a 10 ML thick Te/Cu_{poly} was unambiguously identified using BF imaging, as shown in figure 3.10 (a) and CBED, figure 3.10 (b); and confirmed by XPS, figure 3.10 (c). A TEM cross section for the Te/Cu_{poly} was prepared with the standard lift out procedure, described in chapter 2.2. BF and CBED patterns were obtained using the T20 microscope.

The CBED patterns in figure 3.10 (b) could only be indexed to hexagonal $P6/mmm$-Cu_2Te (a = 0.457 nm, c = 0.750 nm, γ = 120°). BF imaging, shown in figure 3.10 (a), shows Cu on the left hand side of the image and Cu_2Te grains on the right. The image shows that Cu_2Te is polycrystalline with layers arranged vertically. The lattice spacing obtained from these layers in figure 3.10 (a) is consistent with Cu_2Te. Grains of Cu_2Te were observed to be up to 30 nm in length (the vertical direction of figure 3.10 (a)).

Cu $2p^{3/2}$ XPS data are displayed in figure 3.10 (c) and supports the assignment of Cu_2Te. The Cu $2p^{3/2}$ spectrum collected from 10 ML Te/Cu_{poly} shows a slightly different peak shape and binding energy to that of Cu_3Te_2. The binding energy is shifted towards lower binding energy, strongly suggesting that the oxidation state of Cu was lower than in the Cu_3Te_2 alloy. Indeed, the spectra could be fitted to a single function, corresponding to the Cu^+ oxidation state, with a slightly larger width (0.2 eV or ~15 % wider) than the elemental Cu spectra. The assignment of the Cu $2p^{3/2}$ XPS spectrum to Cu_2Te is a useful indicator for the formation of Cu_2Te in other systems, especially the CdTe/Cu and Te/Cu(643) systems which will be described in chapters 4 and 5. The polycrystalline Cu substrate is likely terminated in (111) facets so it is likely that the grain boundaries of the polycrystalline substrate play a significant role in favouring the growth of the Cu_2Te alloy.

We suggested that the Cu_3Te_2-like alloy forms because of good match between the substrate and overlayer. The polycrystalline Cu surface is naturally more disordered and hence the affinity for the growth of Cu_3Te_2 will be diminished.

3.2.3 Thermal Processing

The interdiffusion of p-block metals and metalloids with Cu(111) has been studied previously. For example: Ge/Cu(111) has been shown to alloy above 375 K [50]; Sb/Cu(111) has been shown to form the alloy Cu_3Sb at room temperature and above [49]; the growth of In/Cu(111) has been revealed to form a Cu_3In alloy above room temperature [51]; and Si/Cu(111) has been shown to form a Cu rich Cu_2Si alloy above 400 K [52]. Although Te has previously been shown to alloy with polycrystalline Cu below 373 K, no detailed work was done below this temperature [17] and, to our knowledge, the temperature dependent interdiffusion of Te on Cu(111) has never been studied previously.

To probe the nature of Cu-Te interdiffusion, we deposited a thick layer of Te (θ_{Te} ~30 ML) on Cu(111) at 110 K and followed its structural transitions as it was annealed. Photoemission data are summarised in figure 3.11 and LEED and broad-range temperature dependence data are summarised in figure 3.12. The starting temperature was too low for alloying to occur and the film was sufficiently thick to completely attenuate core level photoemission from the underlying Cu substrate, as indicated in figure 3.11 (a). The initial Te film did not display an ordered LEED pattern, figure 3.12 (b), indicative of three dimensional Te growth; it was then sequentially annealed to higher temperatures, held for 10 min and allowed to cool before XPS spectra and LEED patterns were collected. Only one, sharp transition was observed and lies between 265 K and 280 K, figure 3.12 (a). Between these temperatures, the Cu $2p^{3/2}$ peak reappeared and the Te $3d^{5/2}$ peak shifted from a binding energy characteristic of elemental Te, 573.1 eV, to that of Te in the BA, 572.7 eV, clearly indicating alloying. Figure 3.12 (c) shows that the alloyed film displayed a high background and diffuse LEED pattern with a surface that matched the (111) termination of the bulk Cu_3Te_2 alloy described in the section 3.2.1. In contrast to Ge/Cu(111) [47], we find that the interdiffusion process is independent of film thickness for 10 minute anneals and θ_{Te} < 100 ML. This experiment was repeated 8 times in total with the same findings each time. In principle, alloying of Cu and Te is thermodynamically favourable even at 120 K [15,16,53] but we find it to be kinetically limited in thin films below ~275 K. This alloying phase transition observed here is close to a known amorphous to crystalline phase transition in elemental Te, which occurs at 283 K [53], suggesting that Te adatom mobility is a limiting factor.

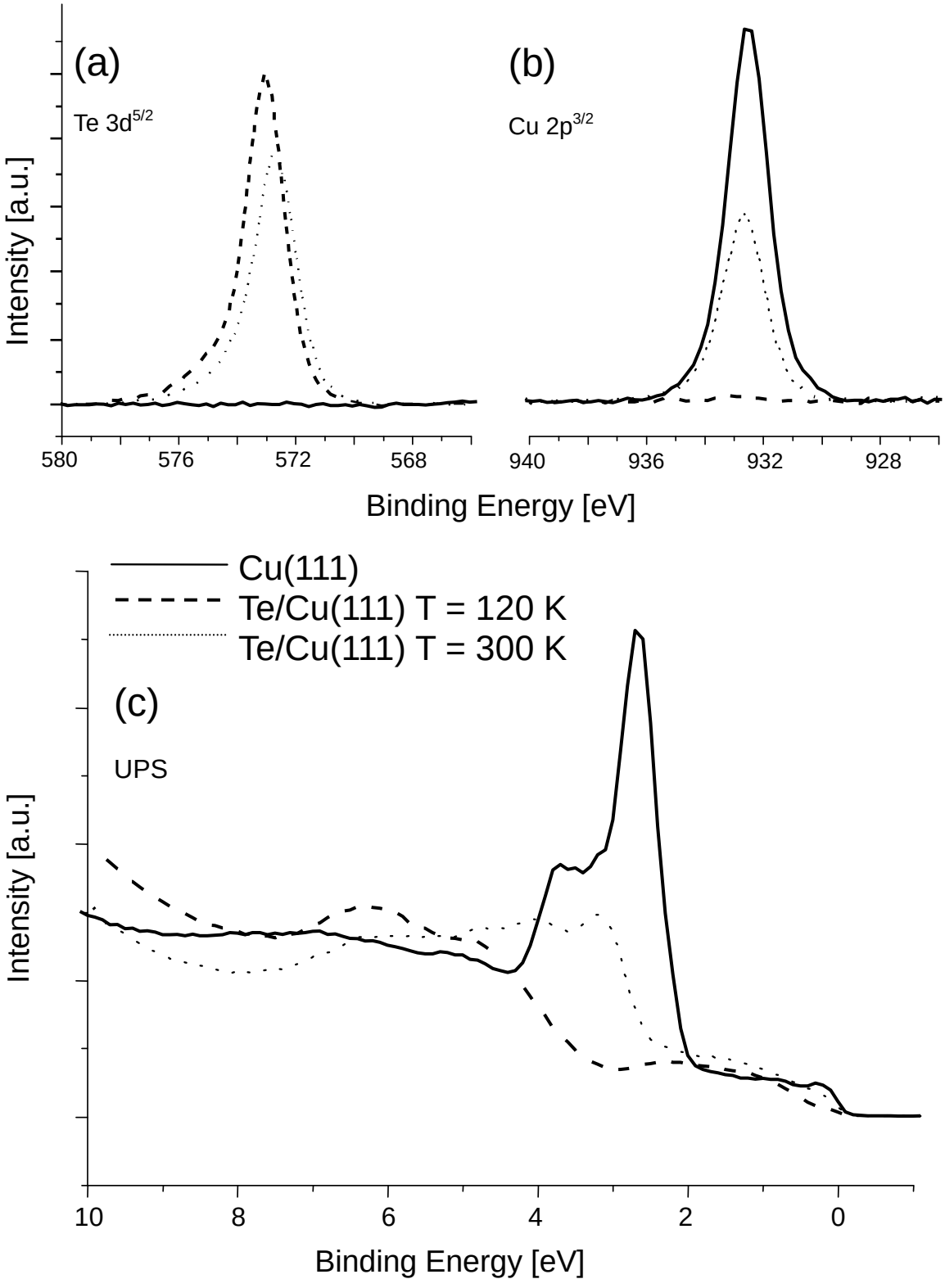

Figure 3.11. The alloying of Te/Cu(111) studied by (a) Te $3d^{5/2}$ XPS, (b) Cu $2p^{3/2}$ XPS and (c) UPS. The legend in the lower panel is common to all three data sets.

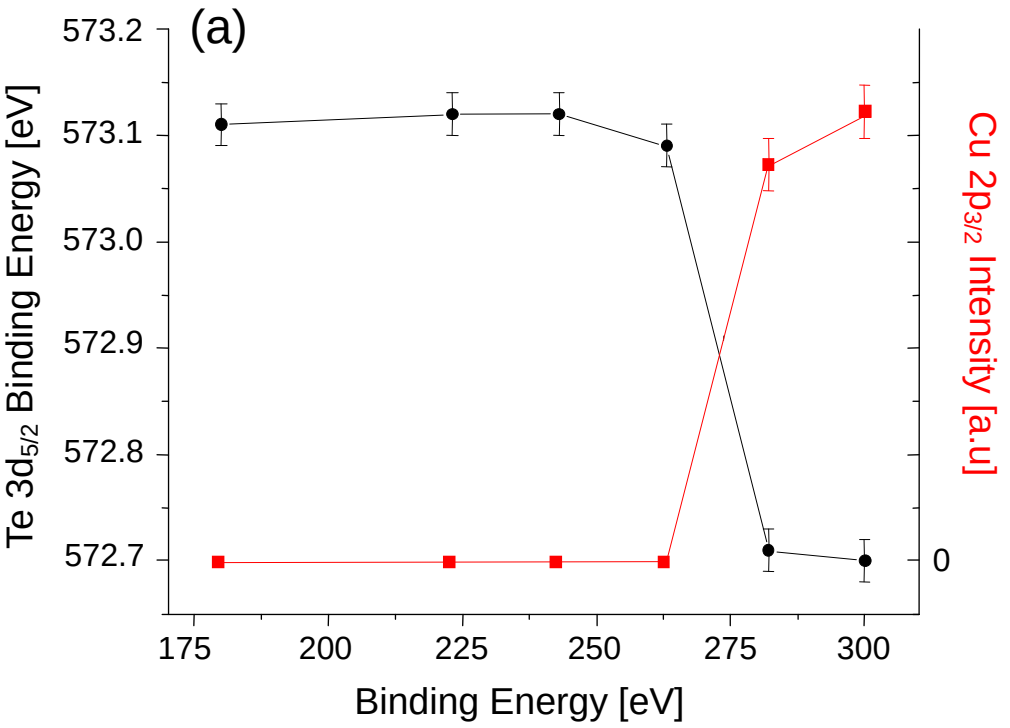

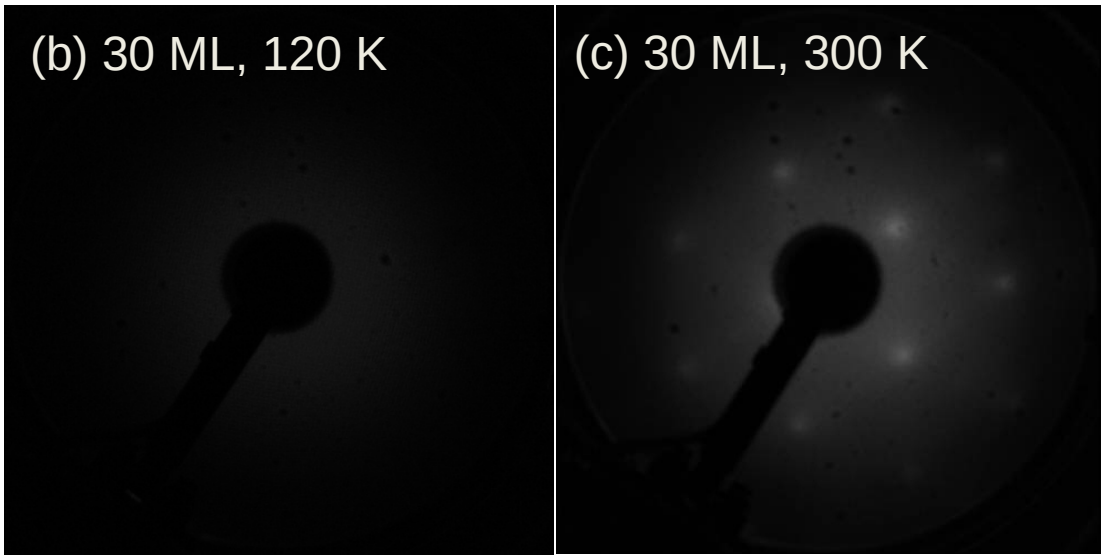

Figure 3.12. (a) Changes in Te $3d^{5/2}$ binding energy and Cu $2p^{3/2}$ intensity as a function of temperature for a Te coverage of 30 ML initially deposited at 120 K. The 105 eV LEED patterns from the surface, (b) at 120 K and (c) after annealing to 300 K.

Further investigations into the thermal properties of Te/Cu(111) were performed by annealing the 30 ML film above room temperature. The Te/Cu(111) film was annealed in 25 K increments for 10 minutes each with XPS, UPS and LEED data collected after each anneal. Figure 3.13 shows the integrated intensity of the Cu $2p^{3/2}$ and Te $3d^{5/2}$ XPS peaks and shows no change up to 800 K, indicating no further phase transitions. Above 800 K, the Cu_3Te_2 alloy began to decompose, as indicated by the rapid loss in intensity of the Te $3d^{5/2}$ signal. The intensity of the Cu $2p^{3/2}$ XPS peak began to increase which indicated that Te was either subliming into the vacuum or diffusing into the bulk Cu crystal. After annealing to 873 K, the LEED and XPS data indicated that the SSA alloy was recovered on the surface: the LEED pattern showed a sharp ($2\sqrt{3}$ x $2\sqrt{3}$) R30° pattern (with an expanded Cu lattice parameter of 0.263 nm); the Te $3d^{5/2}$ XPS could be well fitted to a single function, centred at 572.3 eV, representing $Te^{\delta-}$ from the SSA; and the Cu $2p^{3/2}$ XPS could we well fitted to two functions: one representing elemental Cu and the other $Cu^{\delta+}$ from the SSA. The coverage, after annealing to 873 K, was measured to 0.17 ML, in agreement with the coverage expected from the SSA.

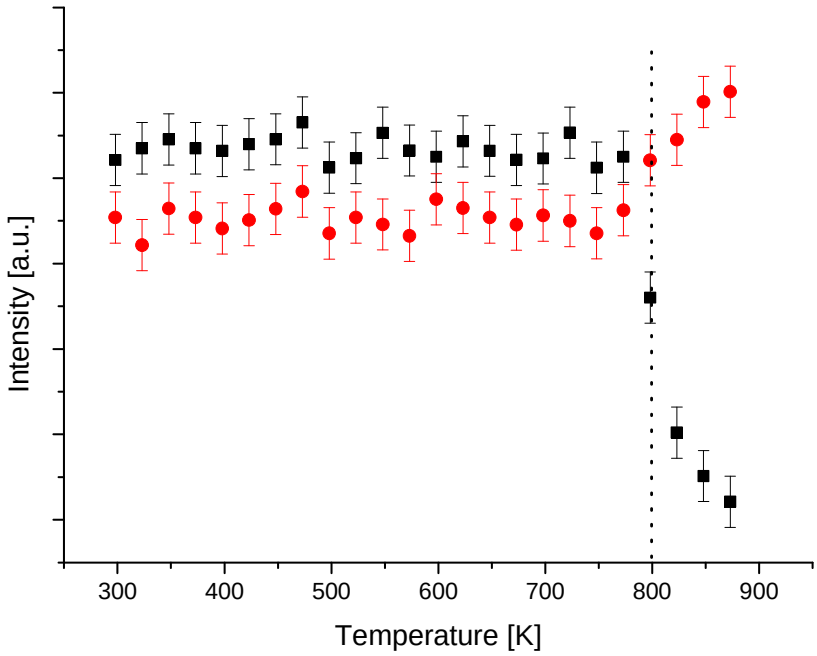

Figure 3.13. The intensity of the Te $3d^{5/2}$ signal (black squares) and Cu $2p^{3/2}$ signal (red circles) as a function of temperature. The vertical dotted black line indicates the point at which there is a rapid reduction in Te signal intensity.

An additional phase change was observed for a 30 ML Te deposition on the Cu(111) substrate, with the substrate held at 673 K during deposition. Once cooled to room temperature the observed LEED pattern, shown in figure 3.14 (a), showed greater ordering than a film of the same thickness, deposited at 300 K. Interestingly, when cooled below 228 K, extra spots were observed in the LEED pattern, shown in figure 3.14 (b), indicating a phase transition. The transition was reversible. The spots lie at the midpoint between the spots observed at 300 K, and hence it is a (2 x 2) reconstruction. The lattice parameter extracted from the LEED patterns both at 300 K (figure 3.14 (a)) and 110 K (figure 3.14 (b)) measures 0.426 nm (i.e. $\sqrt{3}$ x 0.246 nm), which is consistent with Cu_3Te_2 at both temperatures. The assignment of a bulk like alloy is reinforced by the Te $3d^{5/2}$ XPS spectrum obtained at 110 K, which is well fitted to a single component at 572.7 eV, representing the bulk Te^{2-} state. Hence the LEED and XPS data are consistent with the bulk alloy described in section 3.2.1.3.

There are several examples in the literature of cooling induced surface phase transition identified by LEED. These include α-Ga(010) [55-57], Sn/Ge(111) [58,59] and Pb/Ge(111) [60]. The transition in α-Ga(010) is a result of surface Ga atoms dimerising with subsurface atoms. In the Sn/Ge(111) [58,59] or Pb/Ge(111) [60] bimetallic films, the phase transition has been determined to be a transition from a flat surface at high temperature to a corrugated surface at low temperature driven by two non-equivalent adsorption sites by Sn or Pb. It was suggested that the switching between these two non-equivalent sites is too fast to observe at 300 K and by reducing the temperature these fluctuations are frozen out. Ultimately, we cannot elucidate the structural phase transition observed here without further structural probes (such as LEED IV analysis as used for Ga(010) [55] or cryo-STM). However, given the similarities between the Te/Cu(111) and Sn/Ge(111) system, (both form substitutional alloys and rapid interdiffusion occurs at room temperature) it is plausible that the same effect observed in detail on Sn/Ge(111) occurs in the Te/Cu(111) system, i.e. there is a corrugation of the surface below a transition temperature.

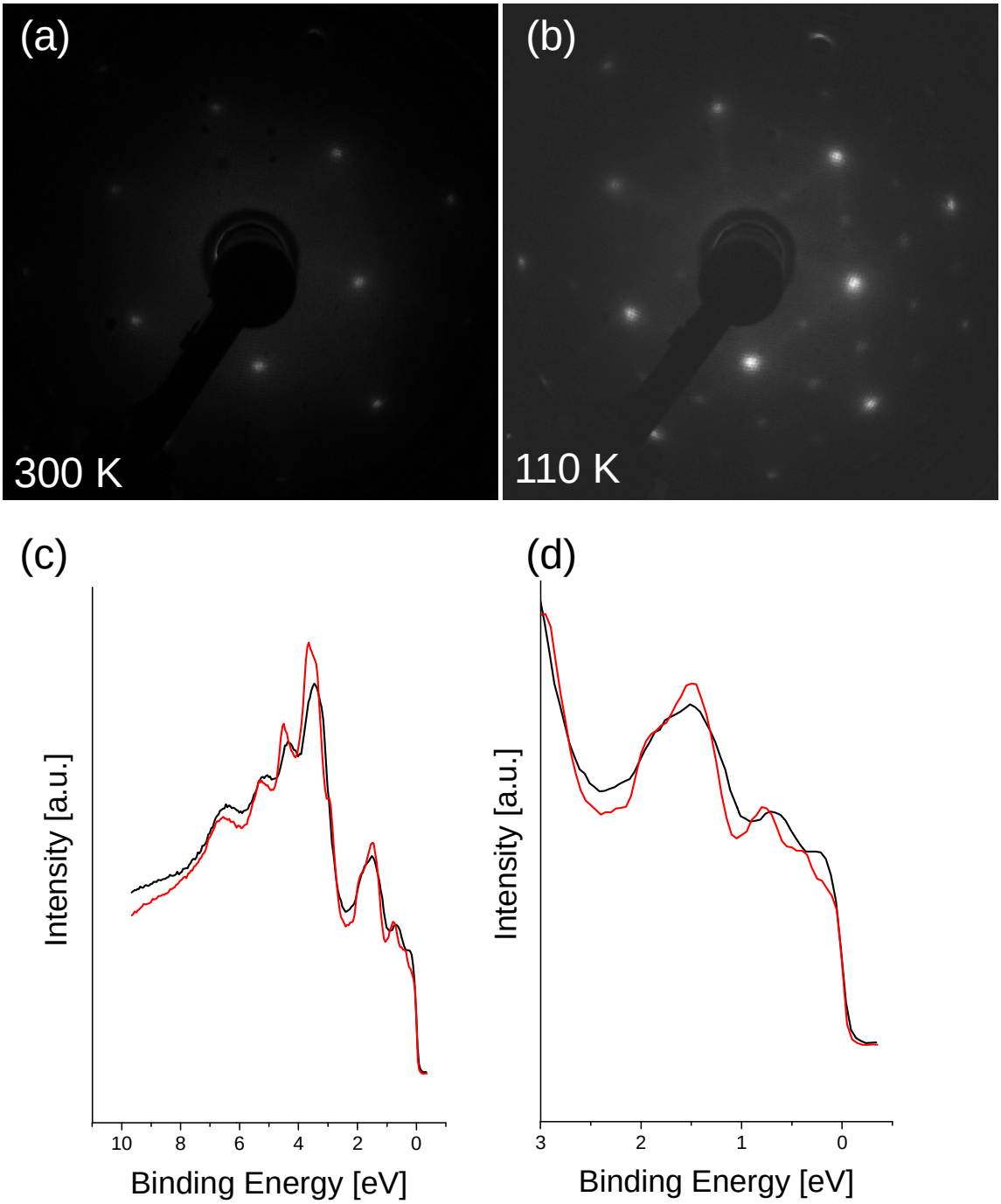

Figure 3.14. (a) LEED pattern obtained from depositing 10 ML of Te on Cu(111) with the substrate held at 675 K during deposition. The pattern was acquired at 300 K. (b) LEED pattern obtained after cooling to 110 K. The contrast has been boosted to accentuate the (2 x 2) spots. LEED patterns in (a) and (b) were acquired at 105 eV beam energy. (c) UPS spectra covering the valence band of Cu_3Te_2 at 300 K (black line) and 110 K (red line). (d) is an expanded view of (c) up to 3 eV below E_F.

The UPS data, displayed in figures 3.14 (c) and (d), indicate the surface electronic states change upon cooling. Figure 3.14 (d) is an expanded view of the UPS spectra within 3 eV of E_F and shows that by depositing Te at 673 K, previously absent surface states from the Cu_3Te_2 film, shown in figure 3.5, were now visible on the UPS spectrum (black line of figure 3.14 (d). The sharper LEED pattern indicates a greater degree of surface ordering, which is naturally a contributing factor in the formation of surface electronic states. Upon cooling below 228 K, the valance band (between 3 eV and 8 eV) of the Cu_3Te_2 alloy is slightly perturbed, with a shift in peaks of ~0.5 eV. In addition, the features within 1 eV of E_F also show a ~0.5 eV shift in peak position, consistent with a surface phase transition.

3.3 Conclusions

We have presented the structural phases of the Te/Cu(111) system as a function of both Te coverage and temperature. At room temperature Te/Cu(111) exists entirely as a surface substitutional alloy for coverages below 0.33 ML and has an ordered (2√3 x 2√3) R30° structure for 0.08 < θ_{Te} < 0.17 ML. For 0.17 ML < θ_{Te} < 0.33 ML, a (2√3 x √3) R30° structure exists. For 0.33 < θ_{Te} < 0.66 ML, a mixture of disordered bulk alloy and (√3 x √3) R30° surface substitutional alloy coexist. Above 0. 66 ML and up to at least 100 ML only the bulk alloy phase exists, with the data for the bulk alloy best fitting an $F\bar{4}3m$ Cu_3Te_2-like structure; a structure that may have been overlooked in previous studies that are unable to quantify alloy stoichiometry explicitly. For comparison, we have also described the deposition of a 10 ML Te film on polycrystalline Cu. The results being a polycrystalline alloy with the Cu_2Te structure. We suggest that the relatively unusual $F\bar{4}3m$ Cu_3Te_2 alloy is stabilised by a good lattice-match to the Cu(111) substrate. A (2 x 2) reconstruction is observed for a well ordered Cu_3Te_2 alloy deposited at 623 K and cooled below 228 K, which we suggest may be surface corrugation. Below 275 K alloying between a Te overlayer and Cu(111) is kinetically limited. Above 800 K Cu_3Te_2 decomposes leaving the Cu-Te SSA, which persists up to at least 873 K.

In this chapter we touched on the combination of electron microscopy and traditional surface science techniques, an idea which will be developed further when we discuss the growth of CdTe on Cu and Cu_xTe substrates in chapter 4. It is clear that the surface science structural probes (STM and LEED) are well suited to growth studies of Te on single crystal Cu and readily give atomic scale information about the surface. However, when looking at a polycrystalline Cu surface, LEED and STM do not give any useful information about structure, due to the roughness of the surface and its polycrystalline nature. The versatility of TEM means that, with a little preparatory work, crystallographic

and chemical information are readily available. However, TEM is not surface specific and the entire film can be probed, which means it cannot rival the surface sensitivity of STM and LEED. Hence, depending on the system in question and if surface structure was of importance to the study, the experimentalist would normally choose between TEM and surface science structural probes, such as STM and LEED. We were in the fortunate position that both were available for this project. Photoemission, however, retains the surface sensitivity of LEED and STM but is more flexible and can be used to study the composition (and possibly infer the structure) of polycrystalline and amorphous materials, provided that they are good conductors.

3.4 References

[1] H. Uda, S. Ikegami, H. Sonomura, *Sol. Energy Mater. Sol. Cells* **50** (1998) 141.

[2] J.H. Yun, K.H. Kim, D.Y. Lee, B.T. Ahn, *Sol. Energy Mater. Sol. Cells* **75** (2003) 203.

[3] S.S. Hegedus, B.E. McCandless, Sol. Energy Mater. *Sol. Cells* **88** (2005) 75.

[4] X. Wu, J. Zhou, A. Duda, Y. Yan, G. Teeter, S. Asher, W.K. Metzger, S. Demtsu, S. Wei, R. Noufi, *Thin Solid Films* **515** (2006) 5798.

[5] K. Neyvasagam, N. Soundararajan, V. Venkatraman, V. Ganesan, Vacuum **82** (2008) 72.

[6] X. Wu, *Sol. Energy* **77** (2004) 803.

[7] H.C. Chou, A. Rohatgi, E.W. Thomas, S. Kamra, A.K. Bhat, *J. Electrochem. Soc*. **142** (1995) 254.

[8] D. Grecu, A.D. Compaan, *Appl. Phys. Lett*. **75** (1999) 361.

[9] H.N. Nowotny, *Z. Metallk*. **37** (1946) 409.

[10] R.V. Baranova, *Kristallografiya* **12** (1967) 266.

[11] R.V. Baranova, Z.G. Pinsker, *Kristallografiya* **14** (1969) 274.

[12] A.L.N. Stevels, G.A. Wiegers, *Recl. Trav. Chim. Pays-Bas* **90** (1971) 352.

[13] F. Pertlik, *Mineral. Petrol.* **71** (2001) 149.

[14] T.A. Bither, R.J. Bouchard, W.H. Cloud, P.C. Donohue, W.J. Siemons, *Inorg. Chem*. **7** (1968) 2208.

[15] A.S. Pashinkin, L.M. Pavlova, *Inorg. Mater*. **41** (2005) 939.

[16] A.S. Pashinkin, V.A. Fedorov, *Inorg. Mater*. **39** (2003) 539.

[17] G. Teeter, *Thin Solid Films* **515** (2007) 7886.

[18] J. Zhou, X. Wu, A. Duda, G. Teeter, S.H. Demtsu, *Thin Solid Films* **515** (2007) 7364.

[19] B. Spath, K. Lakus-Wollny, J. Fritsche, C.S. Ferekides, A. Klein, W. Jaegermann, *Thin Solid Films* **515** (2007) 6172.

[20] G. Teeter, *J. Appl. Phys*. **102** (2007) 034504.

[21] S. Andersson, I. Marklund, J. Martinson, *Surf. Sci*. **12** (1968) 269.

[22] F. Comin, P. Citrin, P. Eisenberger, J. Rowe, *Phys. Rev. B* **26** (1982) 7060.

[23] D.E. Andersson, S. Andersson, *Surf. Sci.* **23** (1970) 311.

[24] A. Salwén, J. Rundgren, *Surf. Sci.* **53** (1975) 523.

[25] P.D. Johnson, D.P. Woodruff, H.H. Farrell, N.V. Smith, M.M. Traum, *Surf. Sci.* **129** (1983) 366.

[26] D. Hesp, Private Communication.

[27] H. Neumann, M. Mast, J. Enderlein, R.D. Tomlinson, M.V. Yakushev, *Cryst. Res.*

Technol. **31** (1996) 75.

[28] A.J. Ricco, H.S. White, M.S. Wrighton, *J. Vac. Sci. Technol*. **2** (1984) 910.

[29] F. Debbagh, E.L. Ameziane, M. Azizan, M. Brunel, T.T.A. Nguyen, *Mater. Sci. Eng*. **38** (1996) 223.

[30] S. Hufner, G.K. Wertheim, J.H. Wernick, *Solid State Commun*. **17** (1975) 417.

[31] D. Westphal, A. Goldmann, *Surf. Sci*. **131** (1983) 113.

[32] C.K. Rhee, C. Jung, B. Ku, *J. Solid State Electrochem*. **9** (2005) 247.

[33] P. Rodriguez, E. Herrero, A. Aldaz, J.M. Feliu, *Langmuir* **22** (2006) 10329.

[34] D.L. Perry, J.A. Taylor, *J. Mater. Sci. Lett*. **5** (1986) 384.

[35] M. Lampimäki, K. Lahtonen, M. Hirsimäki, M. Valden, *Surf. Interface Anal.* **39** (2007) 359.

[36] D. Brion, *Appl. Surf. Sci* **5** (1980) 133.

[37] F.M. Capece, V. Dicastro, C. Furlani, G. Mattogno, C. Fragale, M. Gargano, M. Rossi, *J. Electron Spectrosc, Relat. Phenom.* **27** (1982) 119.

[38] H.C. Galloway, J.J. Benitez, M. Salmeron, *Surf. Sci*. **298** (1993) 127.

[39] Y.C. Kim, C. Westphal, R.X. Ynzunza, Z. Wang, H.C. Galloway, M. Salmeron, M.A. Van Hove, C.S. Fadley, *Surf. Sci.* **416** (1998) 68.

[40] E. Lundgren, B. Stanka, M. Schmid, P. Varga, *Phys. Rev. B* **62** (2000) 2843.

[41] T.A. Land, T. Michely, R.J. Behm, J.C. Hemminger, G. Comsa, *Surf. Sci.* **264** (1992) 261.

[42] J.A. Meyer, P. Schmid, R.J. Behm, *Phys. Rev. Lett.* **74** (1995) 3864.

[43] J. Jacobsen, L. Pleth Nielsen, F. Besenbacher, I. Stensgaard, E. Lægsgaard, T. Rasmussen, K.W. Jacobsen, J.K. Nørskov, *Phys. Rev. Lett.* **75** (1995) 489.

[44] E. Bauer, *Surf. Sci.* **7** (1967) 351.

[45] M. Stecher, *Am. J. Phys*. **32** (1964) 247.

[46] A.J. Brunner, H. Bretscher, R. Lapka, P. Oelhafen, R. Schögl, H.J. Güntherodt, *J. Phys. C*. **20** (1987) 5233.

[47] S. Kashida, W. Shimosaka, M. Mori, D. Yoshimura, *J. Phys. Chem. Solids* **64** (2003) 2357.

[48] K. Pussi, Presented at *European Conference in Surface Science*, Edinburgh, September 2012.

[49] P. Bailey, T.C.Q. Noakes, D.P. Woodruff*, Surf. Sci.* **426** (1999) 358.

[50] J.S. Tsay, L.W. Chang, A.B. Yang, *J. Vac. Sci. Technol. A* **21** (2003) 1892.

[51] H. Wider, V. Gimple, W. Evenson, G. Schatz, J. Jaworski, J. Prokop, M. Marszalek, *J. Phys.: Condens. Matter* **15** (2003) 1909.

[52] J.S. Tsay, A.B. Yang, C.N. Wu, F.S. Shiu, *Surf. Sci.* **601** (2007) 4265.

[53] B. Eichler, H. Rossbach, H. Gaggeler, *J. Less-Common Met.* **163** (1990) 297.

[54] H. Keller, J. Stuke, *Phys. Status Solidi (a)* **8** (1965) 831.

[55] S. Moré, E.A. Soares, M.A. Van Hove, S. Lizzit, A. Baraldi, Ch. Grütter, J.H. Bilgram, Ph. Hofmann, *Phys. Rev. B* **68** (2003) 075414.

[56] Ch. Søndergaard, Ch. Schultz, S. Agergaard, S.V. Hoffmann, Z. Li, Ph. Hofmann, H. Li, Ch. Grütter, J.H. Bilgram, *Phys. Rev. B* **67** (2003) 165422.

[57] S. Lizzit, A. Baraldi, Ch. Grütter, J.H. Bilgram, Ph. Hofmann, *Surf. Sci.* **603** (2009) 3222.

[58] J. Avila, Y. Huttel, G. Le Lay, M.C. Asensio, *Appl. Surf. Sci.* **162-163** (2000) 48.

[59] M.E. Dávila, J. Avilaa, H. Ascolani, G. Le Lay, M. Göthelid, U.O. Karlsson, M.C. Asensio, *Appl. Surf. Sci.* **234** (2004) 274.

[60] J.P. Carpinelli, H.H. Weitering, E.W. Plummer, R. Stumpf, *Nature* **381** (1996) 398.

4. Growth of CdTe Thin Films on Cu and Cu_xTe Alloys

4.1 Introduction

In chapter 3, we examined the alloying of thin film Te with Cu(111) - a model system for the back contact interface of CdTe photovoltaics - and showed that alloying occurred when the Cu substrate was annealed above 275 K. Here, we extend this work by depositing CdTe onto a range of polycrystalline Cu and Cu_xTe surfaces, which are more representative of real photovoltaic devices. Thin film CdTe has shown promise in high efficiency photovoltaic devices. It has a near ideal bandgap for absorption of solar radiation (~1.5 eV) and a high absorption coefficient [1-7]. It is theoretically possible to achieve energy conversion efficiencies of almost 30 % [6], although 16.5 % is maximum efficiency demonstrated in a real device [3] because of limiting factors such as the difficulties in forming a reliable ohmic back contact. A schematic of a typical CdTe photovoltaic is shown in figure 4.1 (a) [7].

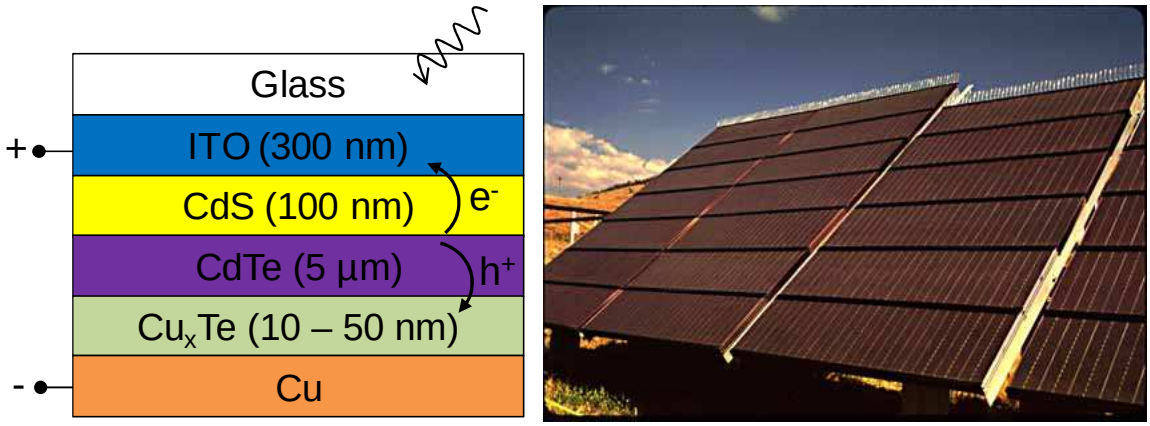

Figure 4.1. (a) Schematic of CdTe photovoltaic cell using a metallic (Cu) substrate. The approximate thickness of each layer is indicated on the cartoon. ITO is indium tin oxide, used as a transparent conductor. (a) is based on figure in reference [7]. (b) Example of a commercially available CdTe photovoltaic array [8].

In this chapter, we study the deposition of CdTe onto Cu or Cu_xTe substrates. Metal substrate based CdTe photovoltaics have several advantages over their glass substrate counterparts. In general, they are lighter, more flexible and more robust [9]. However, glass substrate based cells have tended to attract more attention because of their higher conversion efficiency. A key stage in the fabrication process is the deposition of a 5 µm

thick CdTe layer onto a metal substrate. The metal substrate acts as a back contact, which is typically Cu or a Cu_xTe alloy and has motivated various studies investigating the nature of the back contact and its effect on the cell [10-15]. Cu or a Cu_xTe alloy has been used as the back contact because Cu readily diffuses into CdTe. CdTe has a high work function (measured in this chapter to be 5.6 eV and in [16] to be 5.7 eV) and thus ohmic contacts with most metals are not possible [17]. Cu diffusion into the CdTe film reduces the work function of CdTe at the interface and allows a pseudo ohmic contact to form. However, Cu diffusion can lead to adverse side-effects, such as accumulation at the CdTe/CdS junction leading to stability problems [10,11,18,19]. These studies [10-15] have shown that the structure of the Cu_xTe back contact is of crucial importance. For example, the resistance of Cu_xTe, with x =1.4, is 3 orders of magnitude greater than Cu_xTe with x = 2 [10]. Hence in this chapter, we chose to deposit CdTe onto a range of different Cu and Cu_xTe compounds.

Despite the obvious technological importance of the deposition process, to our knowledge, no fundamental studies of the growth of CdTe on Cu have been undertaken. Work on the interaction of Cu and CdTe has instead tended to focus on studies relevant to the glass substrate configuration, whereby CdTe crystals were doped with small amounts of Cu. These studies are still relevant because they show that Cu can exist in the CdTe film in a variety of different forms: in interstitial sites of the host CdTe structure (equation 4.1) [20-24], as phase segregated Cu_2Te (equation 4.2) [16, 25-27], or as a ternary alloy, $Cu_xCd_{1-x}Te$ (equation 4.3) [28] (equation 4.3). The chemical equations can be written as:

$$Cu^0 + CdTe \rightarrow Cu^0_{(i)} + CdTe \quad (4.1)$$

$$2\,Cu^0 + Cd^{2+}Te^{2-} \rightarrow Cu_2^{+}\,Te^{2-} + Cd^0 \quad (4.2)$$

$$Cu^{2+}_{x} + Cd^{2+}_{1-x} + Te^{2-} \rightarrow Cu_x^{2+}Cd_{1-x}^{\ 2+}Te^{2-} \quad (4.3)$$

The studies which lead to equations 4.1 to 4.3 will now be described in turn. Interstitial Cu was observed by Dzhafarov et al. [17] when Cu films of thickness 6 to 70 nm were deposited on polycrystalline CdTe. They found no evidence of the Cu_2Te phase - or any other Cu_xTe phase - from the observed XRD pattern. By using spatially resolved photoluminescence measurements, Feldman et al. [28] showed that the differences in the observed spectra were due to Cu substituting for Cd in the CdTe layer, implying that Cu_2Te would form if the Cu concentration was high enough. This conclusion was supported by Teeter in two separate surface science studies [16,25]. Using TDMS and AES, he studied the deposition of Cu onto CdTe(111). By comparing the AES spectra obtained after depositing 15 nm of Cu on to CdTe(111) with a reference Cu_2Te spectrum, a qualitative

assignment of Cu existing as Cu_2Te was made. This led the author to propose that Cu displaced Cd in the CdTe structure, as in equation 4.1. TDMS data showed a single broad peak for Cd desorption from a pure CdTe(111) substrate when the temperature was greater than 650 K. When a 0.3 nm thick Cu film was deposited, a second peak in the TDMS profile of Cd was observed, centred at 550 K. The second desorption peak was assigned to the Cd metal that had been formed through the reduction with Cu. Cd^0 metal has a much higher vapour pressure than Cd^{2+} in CdTe and thus desorbs at a lower temperature. Späth and co-workers [26] also performed XPS and UPS of Cu and $Cu_{2-x}Te$ deposited onto close spaced sublimation (CSS) prepared CdTe films. This work looked at different thickness of Cu and $Cu_{2-x}Te$ and also concluded that segregated domains of Cu_2Te and CdTe were formed. In this chapter, we find that Cd $3d^{5/2}$ XPS is inconclusive in accurately assigning Cd oxidation state but additional measurements made with EFTEM allowed us to show that there was $Cd^{(0)}$, Cu_2Te and CdTe present on the surface. Indeed, this chapter is first such EFTEM study of the CdTe-Cu interface. The $Cd_{1-x}Cu_xTe$ ternary alloy [28] was formed through sputtering elemental powders of Cu, Te and Cd onto a glass slide and then annealing. EDS measurements showed that a $Cu_xCd_{1-x}Te$ compound was found to have been synthesised, corresponding to equation 4.3.

We can rewrite equations 4.1-4.3 to account for different compositions of surface Cu_2Te, $Cu_{(i)}$ and CdTe. Therefore they can be modified to include a compositional parameter, x (x will be determined by the magnitude of Cu diffusion):

$$x\ Cu + CdTe \rightarrow x\ Cu_{(i)} + CdTe \quad (4.4)$$

$$x\ Cu + CdTe \rightarrow (CdTe)_{1-x/2} + (Cu_2Te)_{x/2} + Cd_{x/2} \quad (4.5)$$

$$x\ Cu + CdTe \rightarrow Cd_{1-x/2}Cu_{x/2}Te \quad (4.6)$$

The implication of equations 4.2 and 4.5 is that Cu and Cd undergo a redox reaction:

$$2\ Cu^0 + Cd^{2+} \rightarrow Cd^0 + 2\ Cu^+ \quad (4.7)$$

In this study, we also look at growth of CdTe on a Cu(111) single crystal and Cu_3Te_2 surfaces. To our knowledge, layer by layer growth of CdTe has not been studied on Cu(111), nor any other single crystal of Cu or Cu_xTe. However the growth of CdTe has been studied on semiconductor surfaces, for example Si(100) [30-33], GaSb(111) [34] and GaAs(100) [35-37]. Ordered, epitaxial growth was observed on GaAs(100) and GaSb(111), up to a thickness of several monolayers, but on Si(100) [30] the growth was described as being rough or polycrystalline, which we also find to be the case on Cu(111)

and Cu_3Te_2.

To summarise, the literature suggests that there are three different possible outcomes when Cu diffuses into CdTe: Cu resides in an interstitial site (Cu_i^+); Cu reduces Cd, either displacing Cd or occupying a vacancy; or a ternary Cu-Cd-Te alloy is formed. A mixture of these structures is also conceivable.

The strategy adopted in this chapter was to first look at the deposition of CdTe onto the single crystal Cu(111) substrate, described in section 4.2.2. The CdTe/Cu(111) system is a rather idealised system, but nevertheless important information was obtained from it, which will be presented subsequently. Section 4.2.3 details the deposition of CdTe on Cu that had been pre-treated with Te, i.e. Te/Cu(111), using traditional surface science techniques (XPS, UPS and LEED). Film thicknesses studied were between 0.1 and 50 ML. We then extend our studies to more realistic substrates: vapour-deposited polycrystalline Cu (Cu_{poly}) and Te/Cu_{poly} (section 4.2.3), where we deposit thicker CdTe films, 10s of nm thick and study them using a combination of surface science and TEM techniques. The TEM data obtained from the polycrystalline specimens provide a statistical description of thin film structure and composition, while the surface science studies of single crystal surfaces naturally gives an understanding into the growth modes at the atomic level. We compare the data from the single crystal and polycrystalline experiments and, for example, show that Cu diffuses into the CdTe layer from all Cu containing substrates, reacting and displacing Cd. The products formed are predominantly Cu_2Te and CdTe and the TEM data demonstrate that they segregate within the film and at the surface. A small amount of interstitial Cu is also suggested, as described by equation 4.1, by CBED. We also show that the quantity of surface Cu_2Te produced depends on (1) the substrate used - the largest amount is formed on a Cu_3Te_2 surface - and (2) the substrate temperature during deposition. An increase in substrate temperature during deposition temperature results in an increase in surface Cu_2Te content. This study provides insight into the fundamentals of CdTe growth on Cu and $Cu_{2-x}Te$ alloys and its effects on Cu diffusion which may help understanding device related experiments.

4.2 Results

4.2.1 Deposition of CdTe

Since CdTe was evaporated from a single evaporator, it was important to ascertain the stoichiometry of the deposited compound as Cd and Te have significantly different vapour

pressure diagrams. With the techniques at our disposal, this is most easily done with XPS and UPS. The CdTe evaporator was held at 823 K during deposition and to eliminate Cu diffusion into the CdTe film, the Cu(111) substrate was held at 110 K during deposition and analysis. The resulting film produced a Te $3d^{5/2}$ XPS peak, shown in figure 4.2 (a), centred at 572.7 eV, indicating Te^{2-} and no elemental Te which would be centred at 573.1 eV. This indicates that there was no excess elemental Te on the surface for a film thickness of ~10 ML.

The Cd $3d^{5/2}$ XPS spectra are ambiguous for distinguishing between Cd oxidation states because the chemical shifts between Cd^0 and CdTe, is less than 0.1 eV. Cd 4d states have a binding energy of 10-12 eV and therefore photoionisation is possible with He(I) UV radiation ($h\nu = 21.2$ eV). The narrow linewidth of He(I) radiation would mean that high resolution spectra would be obtainable, leading to the possibility of identification of different chemical species in the Cd 4d peaks. However, the picture is complicated substantially by the presence of the broad Te 5s band which lies 9-11 eV below E_F. A detailed ARPES and UPS study by Hochst et al. [38] and a DFT calculation by Zhang et al. [39] showed that not only does the Te 5s band overlap with Cd 4d core levels, intra-band transitions occur in the Te 5s band. There is also a degree of hybridisation of 4d and 5s states. These features mean that the assignment of chemical states is not straightforward. The Cd 4d photoemission data will be discussed in section 4.2.2, when describing the evolution of Cd 4d peaks for increasing CdTe thickness.

Further evidence for the deposition of a stoichiometric CdTe compound is found in the valence band region of the UPS data, shown in figure 4.2 (b). The data show two features at 2.2 eV and 5.4 eV, marked by dashed lines in figure 4.2 (b). Two ARPES studies [38,40] showed that the valence band data of CdTe(111) display two broad bands at ~2.2 eV and ~5.4 eV, which is consistent with our data. The relative intensities of these peaks are different, which is probably a result of polycrystalline CdTe growth on Cu(111) (no LEED pattern is visible). ARPES of Cd(0001) has been reported [41] and shows a small feature at ~3.3 eV in normal emission, which we do not see in the UPS from this deposition. The work function of this CdTe layer was measured to be 5.6 eV, in good agreement with the value measured in reference [16].

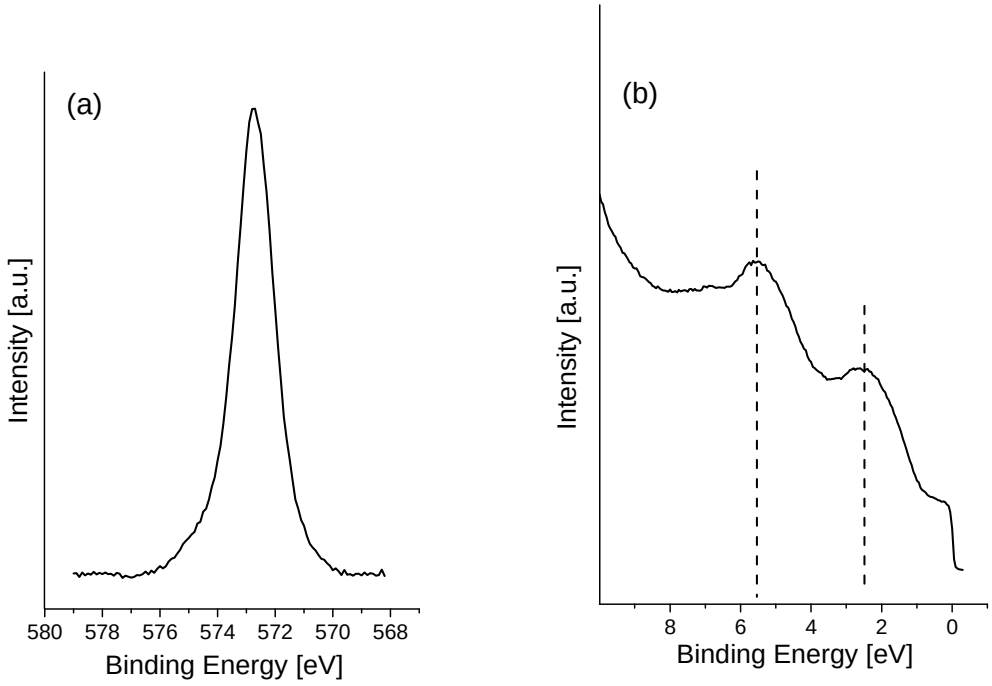

Figure 4.2. (a) Te $3d^{5/2}$ XPS spectrum from 50 ML CdTe deposited onto Cu(111) at 110 K. The binding energy of the peak is 572.7 eV. (b) UPS data of the valence band for 50 ML CdTe deposited onto Cu(111) at 110 K. The dashed lines indicate the strong features on the UPS spectrum, at 2.2 eV and 5.5 eV.

4.2.2 Growth of CdTe on Cu(111)

4.2.2.1 Low Coverage Growth Modes (θ_{CdTe} < 0.66 ML)

The deposition of CdTe onto Cu(111) at 300 K was examined firstly using LEED patterns for CdTe coverages of 0, 0.33, 0.66 and 1.1 ML which are shown in figure 4.3. No ordered LEED patterns were observed above 1.1 ML. The definition of a 1 ML is a complete layer of Cu(111), hence 1 ML of CdTe ≡ 0.5 ML of Cd and 0.5 ML of Te. Complementary Cu $2p^{3/2}$, Te $3d^{5/2}$ and Cd $3d^{5/2}$ XPS spectra were recorded immediately after acquisition of the LEED pattern and are shown in figures 4.4, 4.5 and 4.6, respectively. Additional XPS spectra are shown at 2.5, 3.8 and 10 ML where no LEED pattern was visible. Coverage was again calculated using equations 2.11, 2.13 and 2.14 and using the appropriate sensitivity factors as listed in section 2.4.2.

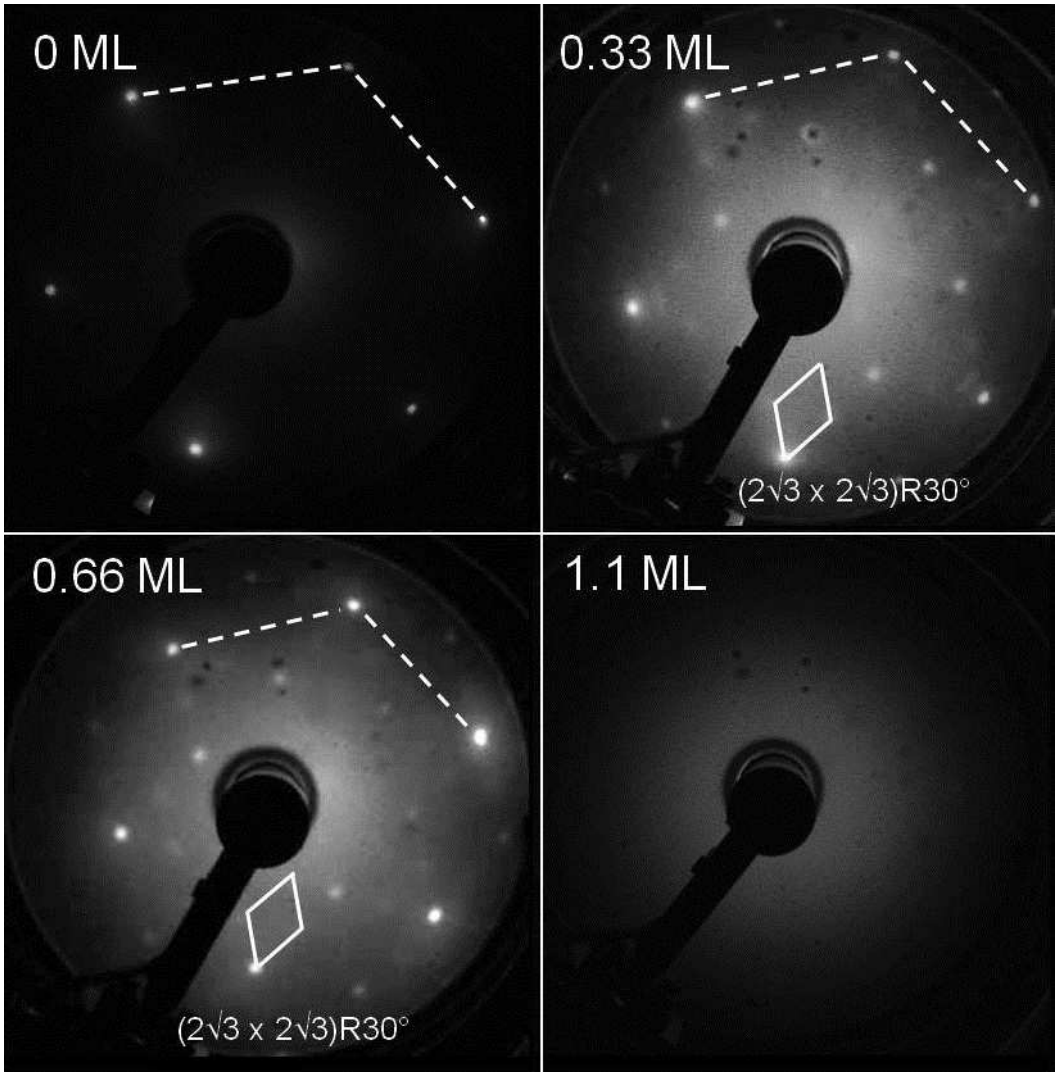

Figure 4.3. LEED patterns of the 300 K deposition of CdTe/Cu(111), collected at 150 eV and at a sample temperature of 300 K. The dashed lines show the unit mesh of the Cu(111) surface. The Cu(111) substrate spots in the 0.33 ML and 0.66 ML coverage show an expansion of 2.8% with respect to the 0 ML.

The coverages obtained were in good agreement with coverages derived from calculated cross sections, as given by references [42,43]. In all cases coverage is quoted with an error of ± 0.05 ML. Each component of the fitted Cu $2p^{3/2}$ and Te $3d^{5/2}$ XPS spectra comprised the sum of a Gaussian and a DS function. Each component had its width (w) and asymmetry factor (α) set to that of the elemental species. These are w_{Cu} = 1.6 eV, w_{Te} = 1.8 eV, α_{Cu} = 0.02 and α_{Te} = 0.12, which are the same as in chapter 3. Figure 4.7 summarises the evolution of the component of the Cu $2p^{3/2}$ XPS spectra as a function of coverage. Cd 4d peaks were also recorded with UV irradiation and collected in the same spectrum as the valence band. However, UPS spectra collected from the Cd 4d and the valence band regions are displayed in separate figures: figures 4.8 (a) and 4.8 (b), respectively. Figure 4.9 shows the work function for increasing CdTe thickness.

Between 0.15 ML and 0.33 ML, the LEED patterns, displayed in figure 4.3, show a (2√3 x 2√3) R30° pattern that matches the dimensions and sym metry of the Te/Cu(111) LEED pattern for 0.17 ML of Te, shown in chapter 3, albeit with spots that are more diffuse and on a higher background. The Cu(111) surface lattice parameter derived from the 0.33 ML LEED pattern, shown in figure 4.3, confirmed that the Cu(111) lattice had expanded by ~2.8% (i.e. to 0.263 nm), implying that the Te atoms were again forming a SSA in the Cu(111) surface plane, identical to the behaviour of Te/Cu(111), described in chapter 3. The view that Te forms a SSA is supported by the Te $3d^{5/2}$ XPS, shown in figure 4.5, which is well fitted to a single function centred at 572.3 eV, indicative of $Te^{\delta-}$ in the Cu-Te SSA. The Cu $2p^{3/2}$ XPS, shown in figure 4.4, is also in agreement with the SSA as it is well fitted to two peaks, one of which represents metallic Cu and the other $Cu^{\delta+}$ in the SSA. The assignment of Cu-Te SSA is interesting because it shows that the interfacial layer between Cu and vapour deposited CdTe will be between Cu and Te.

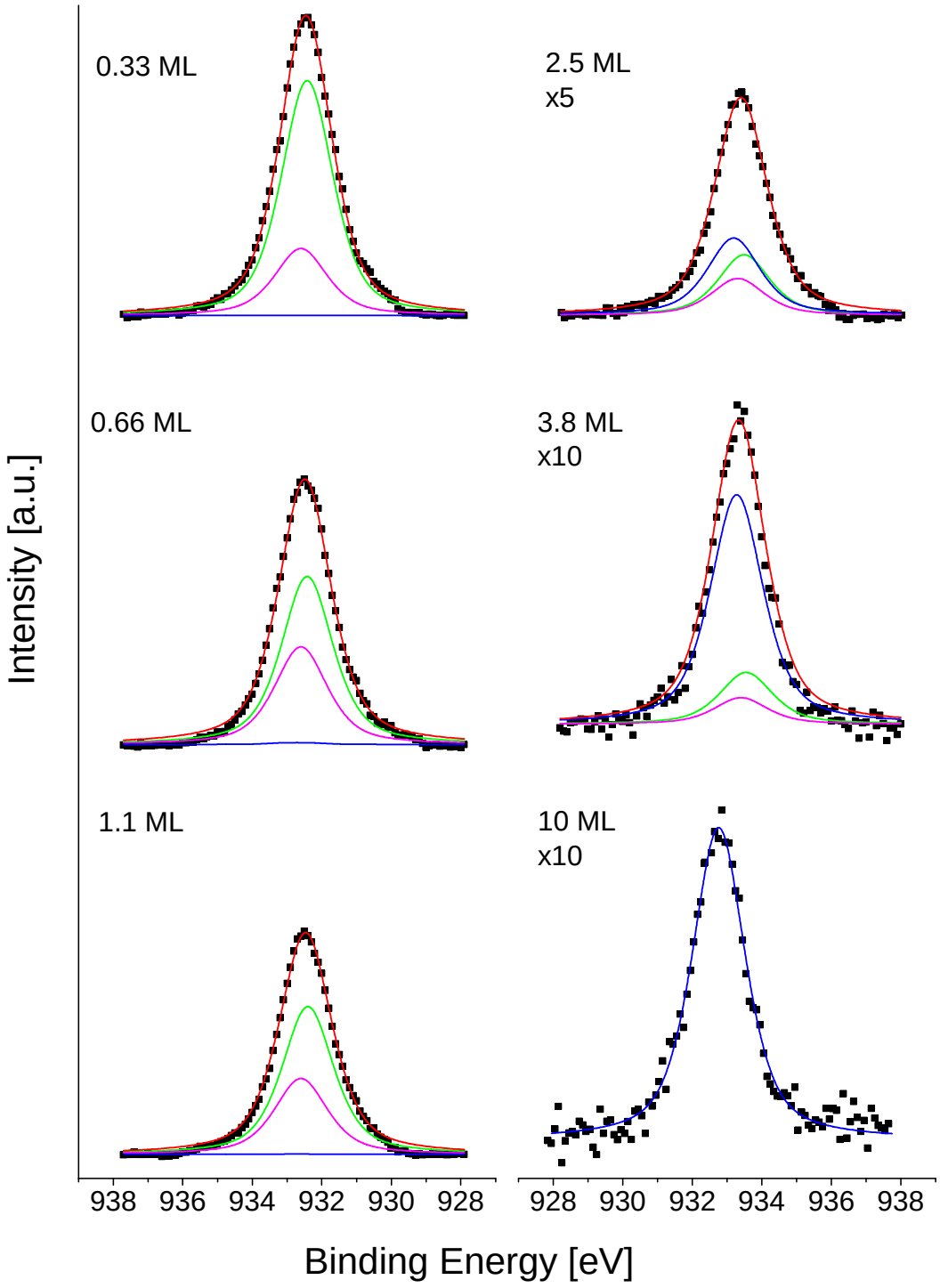

Figure 4.4. Cu $2p^{3/2}$ XPS spectra for increasingly thick CdTe films on Cu(111) at 300 K. The fitted spectra are in red whilst the green line indicates elemental Cu, the magenta line the SSA and the blue line the Cu^{+}.

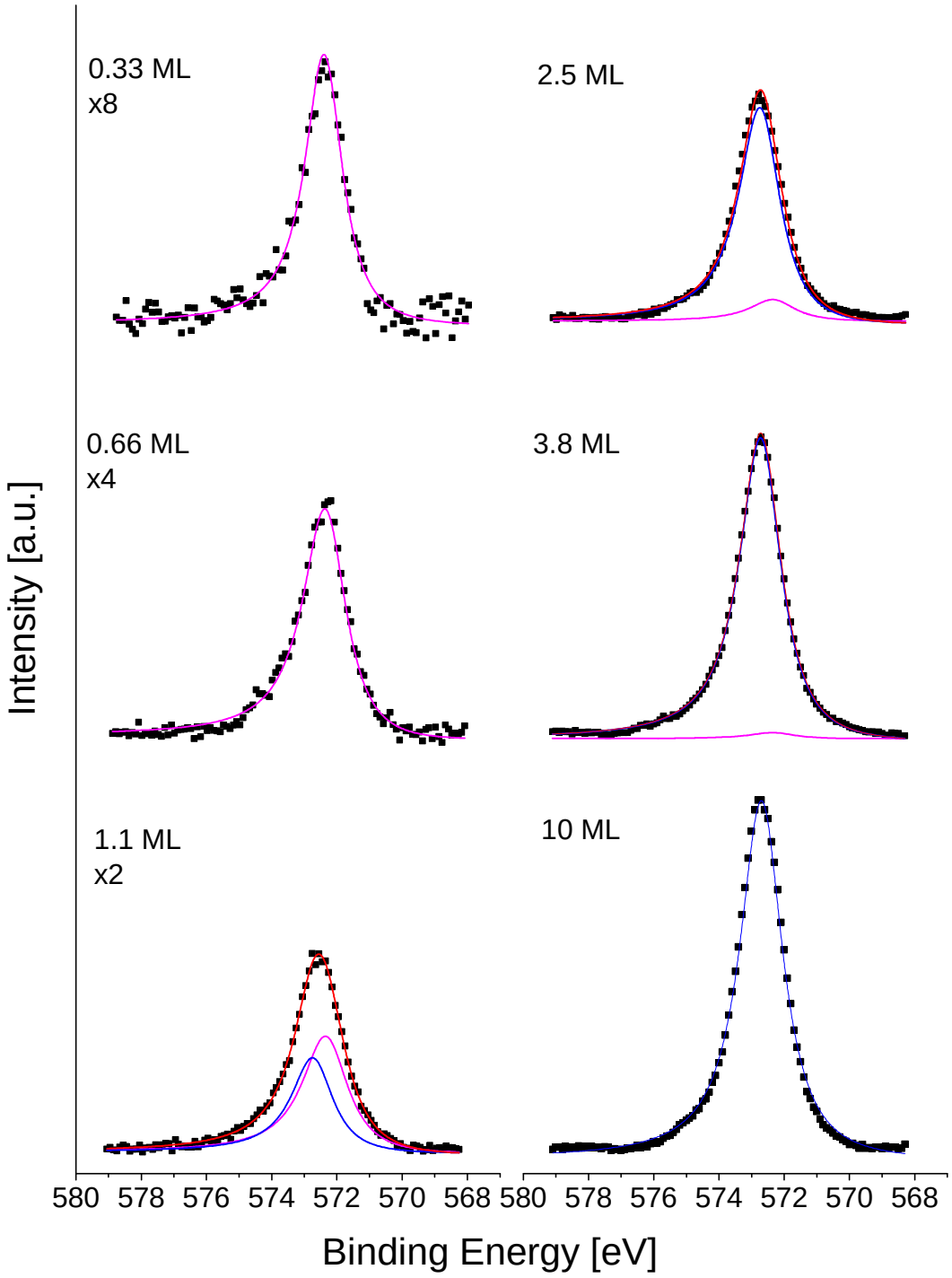

Figure 4.5. Te $3d^{5/2}$ XPS spectra for increasingly thick CdTe films on Cu(111) at 300 K. The fitted spectra are in red, whilst the magenta line indicates the SSA and the blue line the Te^{2-}.

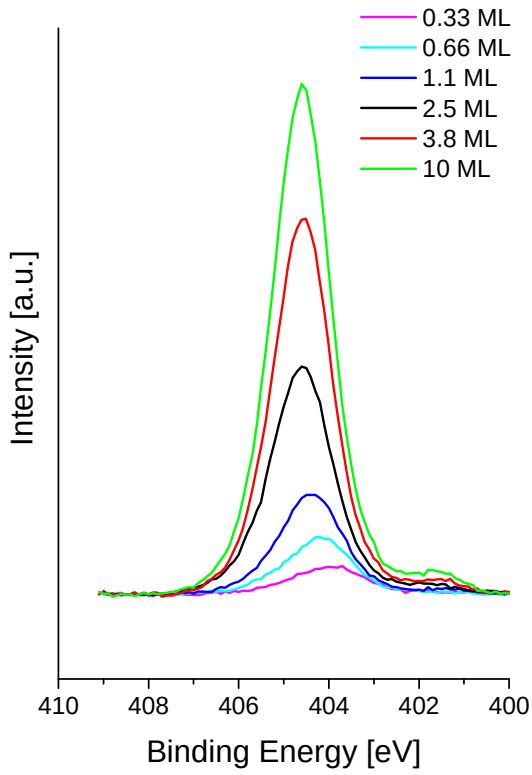

Figure 4.6. Cd $3d^{5/2}$ XPS spectra for increasingly thicker CdTe films on Cu(111). Spectra shift in binding energy from 404.2 eV for 0.33 ML to 405.1 eV for 10 ML.

The Cd $3d^{5/2}$ signal for a coverage of 0.33 ML displays a single peak at 404.2 eV which is ~0.8 eV lower than what is expected for Cd metal [44] or Cd^{2-} in CdTe [44-47]. Other plausible chemical environments for Cd would be CdO or Cd-Cu. The reported values for the binding energy of the Cd $3d^{5/2}$ state in Cd metal [44] is 404.9 to 405.0 eV; in CdTe [44-47] it is 405.0 to 405.1 eV; in alloyed Cu-Cd it is 405.0 eV [47]; and in CdO it is 404.2 eV [44,48]. However, no O 1s signal is detected from this surface and we therefore discount the CdO chemical shift. We attribute the apparent shift in binding energy to a relaxation shift as described in section 2.4.2.1. The conduction electrons in Cu are highly mobile [49], so when a hole is formed from the ionisation event, the high mobility of the electrons in the Cu substrate can effectively screen the nuclear potential, giving rise in an apparent increase in outgoing electron kinetic energy. No previous studies of Cd deposition onto metals could be found to either support or contradict the assignment of Cd $3d^{5/2}$.

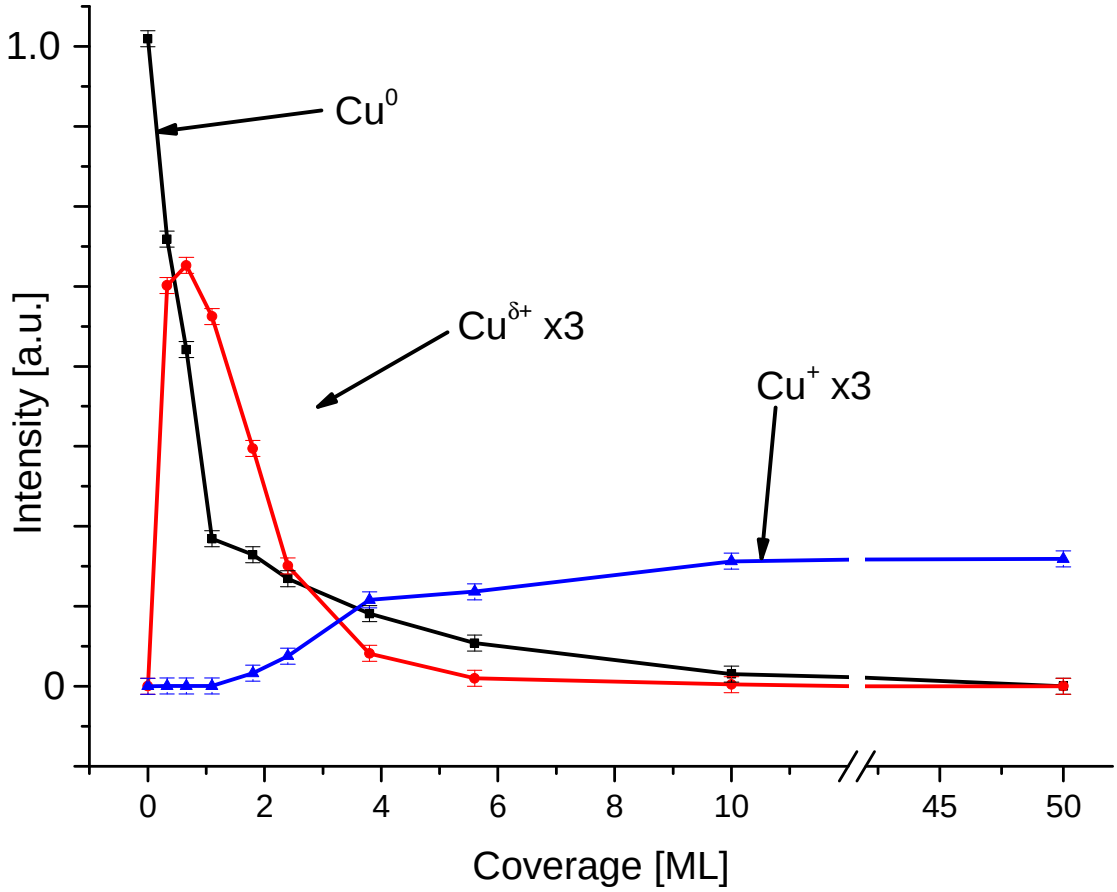

Figure 4.7. Summary of the intensities of Cu $2p^{3/2}$ XPS spectra as a function of CdTe coverage on Cu(111). The $Cu^{\delta+}$ (from the Cu-Te SSA) and Cu^{+} (from diffused Cu) signals have been multiplied by 3 for ease of comparison. Above 1 ML, the $Cu^{\delta+}$ component decreases with increasing CdTe coverage. The Cu^{+} component is undetectable below ~2 ML. Above ~3 ML the SSA is not visible. Lines are added to guide the eye.

We can use our experimentally determined RSFs to measure the ratio of Cd:Te, and hence check stoichiometry. Using equation 2.15, S_{Cd} = 0.60 and S_{Te} = 1 we measure the Cd:Te = 0.9 ± 0.1, which is in good agreement with a stoichiometric deposition for a coverage between 0.15 ML and 0.33 ML. The similarities in the binding energy of the Cd $3d^{5/2}$ state in the Cu-Te-Cd system mean that Cd $3d^{5/2}$ XPS spectra cannot differentiate between a Cd-Te bond and metallic Cd on the Cu(111) surface. The LEED pattern, for 0.33 ML CdTe/Cu(111) is a more diffuse version of the 0.18 ML Te/Cu(111) LEED pattern. The increase in diffusivity must be a result of the additional Cd atoms on the surface. However, the symmetry of a LEED pattern can only give information on the lattice and not the basis (i.e. atomic positions). To obtain information on the basis (which in this case

would show where Cd atoms were located), LEED I-V analysis is required, and is beyond the scope of the presented study. However, we suggest likely sites for Cd atoms that are consistent with the observed LEED pattern symmetry. Cd atoms are likely bonded directly to the Te atom, which is embedded in the surface layer, either atop or to the side. Both positions would increase the surface corrugation, which is consistent with an increase in the background of the LEED pattern. In addition, it is likely that there would be disorder in the Cd position which would also lead to an increase in the background observed in LEED patterns. Full decomposition of Cd and Te into their elemental constituents is unlikely because this would suggest that a bulk Cu_xTe alloy would form (see Te/Cu(111), chapter 3), which we do not observe in this system. Further deposition of CdTe leads to the formation of a rough or polycrystalline CdTe layer which we will discuss in subsequent paragraphs.

As the coverage was increased from 0.33 ML to 0.66 ML, the spots associated with the (2√3 x 2√3) R30° LEED pattern became increasingly weak with the LEED pattern gradually changing to that of a (√3 x √3) R30°. The Cu(111) spacing remained elongated by ~2.8 %, consistent with the Cu-Te SSA. The gradual change in LEED pattern indicates that vacant sites on the Cu(111) surface are being filled. Interestingly the (2√3 x 2√3) R30° spots are not fully attenuated at this coverage, which one would expect from the Te/Cu(111) system, described in chapter 3. This implies that the Cd atoms must inhibit Te filling all of the vacant SSA sites on the Cu surface. The measured surface lattice parameters from the LEED patterns and Te $3d^{5/2}$ XPS data, show that between 0.33 ML and 0.66 ML, the SSA is retained. Between 0.66 ML and 1.1 ML the LEED pattern becomes increasingly diffuse and is fully attenuated above 1.1 ML, indicating a three dimensional growth mode.

4.2.2.2 High Coverage Growth Modes (θ_{CdTe} > 0.66 ML)

For 0.66 ML of CdTe/Cu(111) (≡ 0.33 ML of Te), the (√3 x √3) R30° SSA alloy sites are fully saturated. In the Te/Cu(111) system, a bulk like Cu_3Te_2 alloy begins to grow when the (√3 x √3) R30° SSA alloy sites are full. In contrast, the CdTe/Cu(111) system displays three dimensional overlayer growth of CdTe, as will now be shown with XPS, UPS and LEED, indicating that the Cd must inhibit further alloying between Cu and Te. Between 0.66 ML and 1.1 ML the intensity of the Cu $2p^{3/2}$ XPS peak, shown in figure 4.3, becomes increasingly attenuated but remains at the same binding energy and hence is fitted to the same peaks as in 0.33 ML - a metallic Cu and SSA Cu component, only with reduced peak intensity.

Above 0.66 ML, the peak in the Te $3d^{5/2}$ XPS spectrum, shown in figure 4.4, begins to shift towards the bulk alloy component at 572.7 eV. The Te $3d^{5/2}$ XPS spectra are now fitted using two components: one representing the Cu-Te SSA, at 572.3 eV and the other a formal Te^{2-} species, at 572.7 eV. With increasing CdTe coverage, the SSA component is attenuated and the bulk alloy component increases in intensity. The lack of a formal Cu^{n+} species below ~2 ML indicates that Te must be bound to Cd and hence that CdTe is forming an overlayer. A binding energy of 572.7 eV is at the high end of values reported for the binding energy of Te in CdTe [45,50,51], which is in the range 572.5 to 572.7 eV. Between 0.66 ML and 1.1 ML, the Cd $3d^{5/2}$ XPS and Cd 4d UPS peaks increase in intensity and shift to higher binding energy. A satellite peak also emerges in the Cd $3d^{5/2}$ spectra at 402.0 eV. This apparent change in binding energy of Cd $3d^{5/2}$ is attributed to a decrease in the effect of the relaxation shift on the Cd 3d and 4d states. As the thickness of the CdTe film is increased, the Cu surface is increasingly distant from the Cd metal and therefore would have less influence on the screening of the Cd $3d^{5/2}$ hole.

The gradual attenuation of the LEED pattern, a measured Cd:Te ratio of ~1 and the attenuation of the Cu $2p^{3/2}$ XPS peak is consistent with a polycrystalline or three dimensional overlayer of CdTe growing on Cu. The SSA component of Cu $2p^{3/2}$ XPS spectra only decays slowly and is observable up to coverages of 3 ML, indicating that the growth of CdTe was three dimensional (c.f. Te/Cu(111), where the SSA was lost on completion of a single monolayer of Cu_3Te_2, θ_{Te} = 0.66 ML). The intensity of the Te^{2-} component of the XPS signal is too large to originate from a subsurface Cu-Te bulk alloy and therefore must come from a CdTe overlayer. Furthermore, we use equation 2.15 to quantify the relative composition of Cd:Te for these intermediate coverages and we calculate that the ratio of Cd:Te = 1.1 ± 0.1 : 1, consistent with stoichiometric CdTe.

Further deposition of CdTe/Cu(111) was probed up to 50 ML. Figure 4.7 shows the relative intensities of the Cu components in the Cu $2p^{3/2}$ XPS spectra. It shows that Cu^+ becomes detectable in the CdTe/Cu(111) system for CdTe thickness greater than ~2 ML, which is attributed to Cu diffusion into the CdTe layer. There are two further aspects of the XPS data that led to this assignment. Firstly, for a 50 ML CdTe film, it is surprising that we see any Cu $2p^{3/2}$ XPS signal at all. The 50 ML CdTe film is approximately 25 to 30 nm thick, which vastly exceeds the information depth of XPS (0.5-2 nm) and island growth for such thick films is unlikely. Indeed, the TEM images (figure 4.23) show that the variation in film thickness on the Cu_{poly} substrate is of the order of 1 nm. Therefore, Cu must diffuse through the CdTe layer to the near surface region, in agreement with previous studies [20-

28]. Secondly, above ~2 ML, the Cu $2p^{3/2}$ XPS spectra shown in figure 4.3 display a measurable shift in binding energy. We therefore we fit the spectra with an additional component to represent $Cu^{+,}$ at 932.7 eV. We do not include a component to model the Cu^{2+} state because, at 50 ML, the Cu $2p^{3/2}$ spectrum is well fitted to a single function with the same binding energy, asymmetry and width as the Te/Cu_{poly} deposition (i.e. Cu_2Te, figure 3.10 (c)), which only contains Cu^+. For the intermediate coverages we fit to a combination of functions representing metallic Cu, $Cu^{\delta+}$ and Cu^+. The Cu $2p^{3/2}$ XPS spectra show a gradual attenuation of the metallic Cu and $Cu^{\delta+}$ peak and growth of the Cu^+ peak. At a coverage of 10 ML, the Cu^+ reaches a maximum in intensity and remains constant to 50 ML, indicating a constant surface Cu^+ concentration in this coverage regime. Cu^+ implies that Cu_2Te may exist, the concentration of which will be discussed when describing thicker CdTe films in section 4.2.3.

In the Te/Cu(111) system described in chapter 3 the Cu-Te SSA is not retained when the bulk Cu_3Te_2 alloy is formed. In contrast, for the CdTe/Cu(111) system, the SSA is still observable when CdTe forms, which is consistent with a surface containing three dimensional islands of CdTe and areas of SSA. With increasing coverage, the three dimensional CdTe islands coalesce forming continuous films such as what was observed with TEM for 50 ML of CdTe on Cu_{poly} (figure 4.23). The SSA component of fitted Te $3d^{5/2}$ XPS spectra, shown in figure 4.5, is present up to ~3 ML. In comparison, the SSA component of the Te $3d^{5/2}$ spectra for the Te/Cu(111) system is extinguished after just a Te coverage of 0.66 ML (figure 3.4), which corresponds to a single atomic layer of the Cu_3Te_2 alloy.

The UPS data covering the Cd 4d peaks is shown in figure 4.8 (a). The Cd 4d peaks display the same relaxation shift as in the Cd $3d^{5/2}$ XPS data due to the close proximity of the Cu(111) surface. Also, the Te 5s state overlap with the Cd 4d states, the result of which is the smearing out of the Cd 4d peaks, especially for intermediate coverages. At higher coverages, 10 and 50 ML, the Cd $4d^{3/2}$ and Cd $4d^{5/2}$ peaks are clearly identifiable at 10.9 eV and 11.6 eV, respectively. These binding energies match that of previous studies for CdTe [34,38].

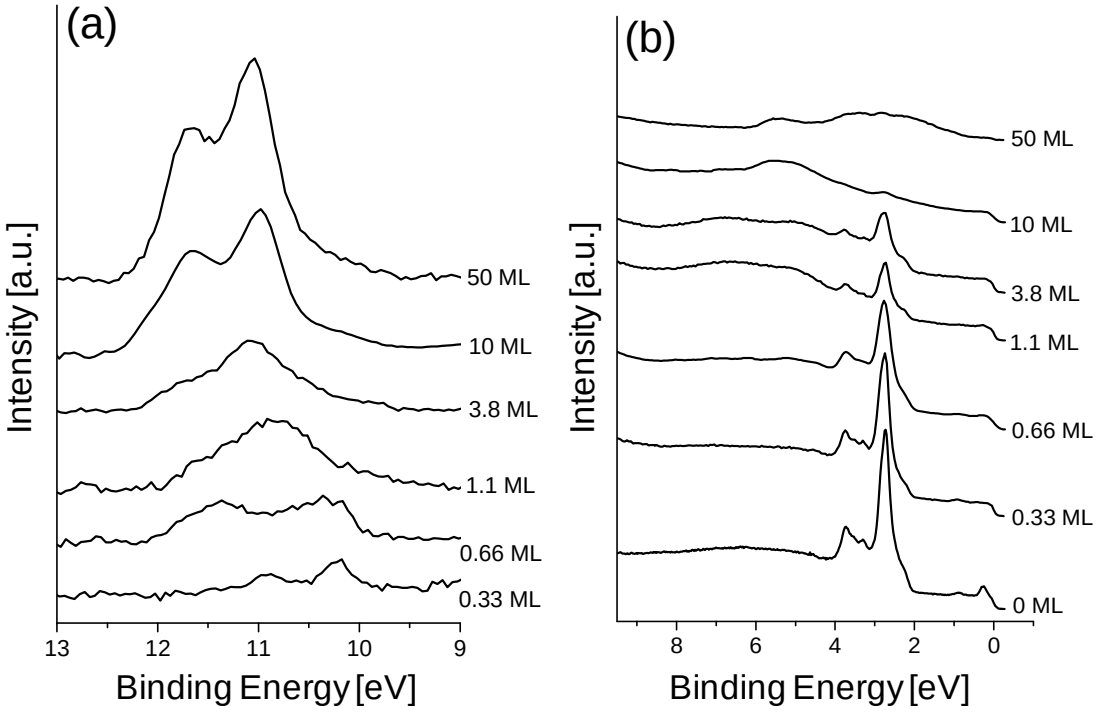

Figure 4.8. UPS spectra spanning (a) the Cd 4d states and (b) the valence band for increasingly larger doses of CdTe on Cu(111), deposited with the substrate temperature held at 300 K. Cd 4d states shift by 0.9 eV from 0.33 ML to 50 ML coverage.

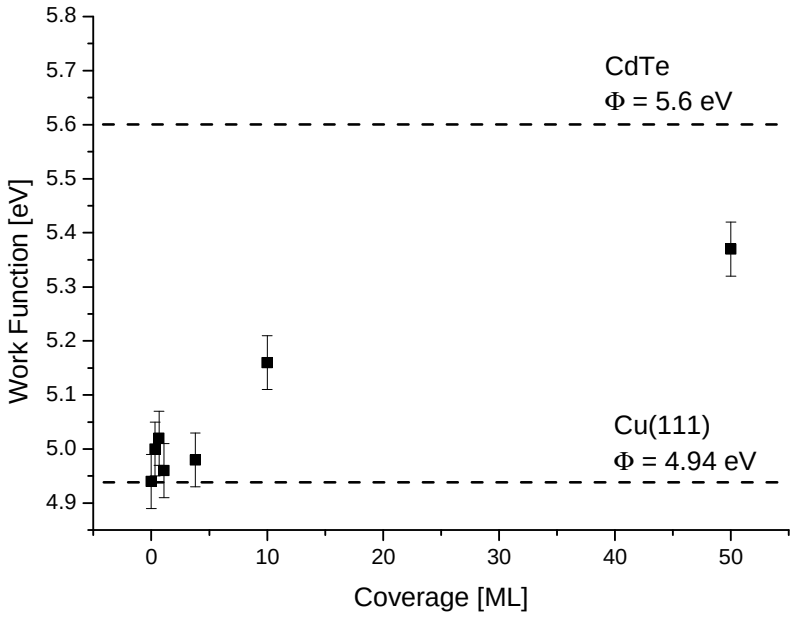

Figure 4.9. The measured work function as a function of increasing CdTe coverage on Cu(111) at 300 K.

The UPS spectra of the valence band, shown in figure 4.8 (b), indicate that the surface states are immediately quenched on deposition of CdTe, similar to Te/Cu(111) and other chemisorbed species on Cu(111) [52]. The Cu 3d peaks, between 2 and 4 eV, are progressively attenuated consistent with a growing overlayer of CdTe. A new feature at ~5.3 eV emerges and grows with CdTe coverage. Another new feature arises at ~2.2 eV, which is more clearly seen once the Cu 3d peaks have been attenuated. These two peaks are consistent with the valence band of CdTe [38]. In this work, the valence band shows a small feature at ~3 eV, at higher coverages, which is ascribed to Cu_2Te. This assignment is consistent with the TEM data, which will be described in detail in section 4.2.4. and suggest that discrete units of metallic Cd and Cu_2Te coexist. The measured work function is shown as a function of coverage in figure 4.9. Interestingly, it shows that for even the thickest CdTe films studied here, the work function does not approach the value known for the bulk crystal, 5.7 eV [16], or what was measured for a pure CdTe deposition (i.e. CdTe deposition with the Cu substrate held at 110 K), 5.6 eV, described in section 4.2.1. A reduction in the work function has been observed before for Cu doped CdTe films [16] and is consistent with Cu diffusing into the CdTe layer.

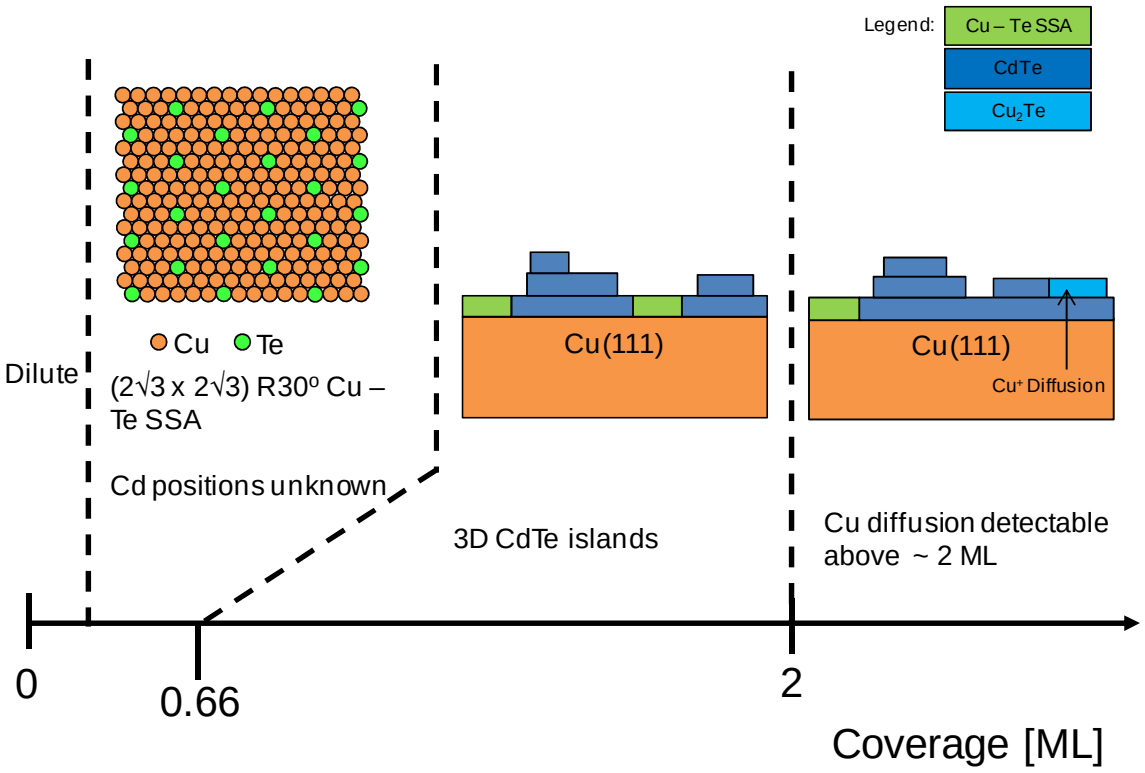

Figure 4.10. Schematic detailing the growth of CdTe/Cu(111) at 300 K. Cd is omitted from the schematic in the coverage regime 0 to 0.66 ML because the positions are undetermined.

The proposed model for the growth of CdTe/Cu(111) at 300 K is summarised in figure 4.10. CdTe/Cu(111) initially forms a Cu-Te SSA, with Cd atoms orientated in an unknown position around the Te atom. Above 0.66 ML coverage, a three dimensional or polycrystalline CdTe overlayer is formed. Above ~2 ML, Cu diffusion is detectable and has stoichiometry consistent with Cu_2Te.

4.2.3 Growth of CdTe/Cu_3Te_2

The growth of CdTe/Te/Cu(111) was also studied with XPS, UPS and LEED. We showed that in chapter 3, the 50 ML deposition of Te on Cu(111) at 673 K results in the formation of a Cu_3Te_2 like alloy terminated in the (111) direction. Hence the Te/Cu(111) substrate will now be referred to as Cu_3Te_2. CdTe was deposited onto Cu_3Te_2 at 423 K because an increase in substrate temperature has been shown to promote ordered, epitaxial growth [53,54] due to a reduction in kinetic roughening. However in this system, increasing the substrate temperature during deposition did not lead to improved epitaxy, but an increase in the rate of Cu^+ diffusion into the CdTe layer. The Cu_3Te_2 surface was chosen as a model substrate of CdTe back contacts, which are typically a Cu_xTe alloy. The lattice mismatch between the CdTe and Cu_3Te_2 is ~6 %, which is reasonably high, but it is still feasible for pseudomorphic growth of CdTe to occur. However, we found that this was not the case and our data showed that CdTe grew in a polycrystalline fashion with Cu^+ diffusion being detected above ~2 ML.

LEED patterns for 0, 1.5, 4.2 and 50 ML are shown in figure 4.11. The measured surface lattice parameter is shown in figure 4.12 as a function of coverage. Cu $2p^{3/2}$, Te $3d^{5/2}$ and Cd $3d^{5/2}$ XPS spectra were recorded for each coverage studied immediately after observation with LEED and are shown in figures 4.13, 4.14 (a) and 4.14 (b), respectively. UPS data for the Cd 4d states and the valance band are shown in figures 4.15 (a) and 4.15 (b) respectively. Figure 4.16 shows the intensity of the Cu components in the Cu $2p^{3/2}$ XPS spectra as a function of CdTe coverage. The measured work function data are shown in figure 4.17. For 0 ML, the symmetry and dimensions of the LEED pattern shown in figure 4.11, is consistent with a (111) termination of Cu_3Te_2. The Cu $2p^{3/2}$ XPS spectrum, shown in figure 4.13, displays a peak centred at 932.9 eV and is fitted to two components, Cu^+ and Cu^{2+}, in a ratio 1:2. This fitting procedure is the same as in the bulk Cu_3Te_2 like alloy, described in chapter 3. The UPS valence band spectrum displayed in figure 4.15 (b), are in good agreement with that of Cu_3Te_2 discussed in chapter 3.

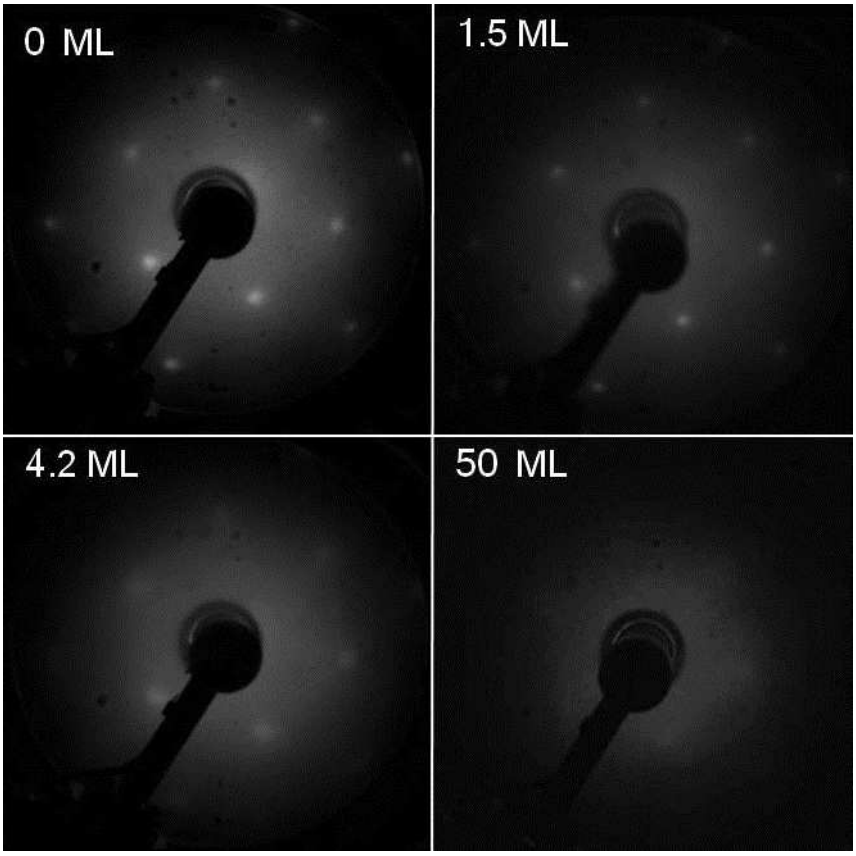

Figure 4.11. LEED patterns for the deposition of CdTe onto Cu_3Te substrate held at 423 K. The beam energy is 140 eV.

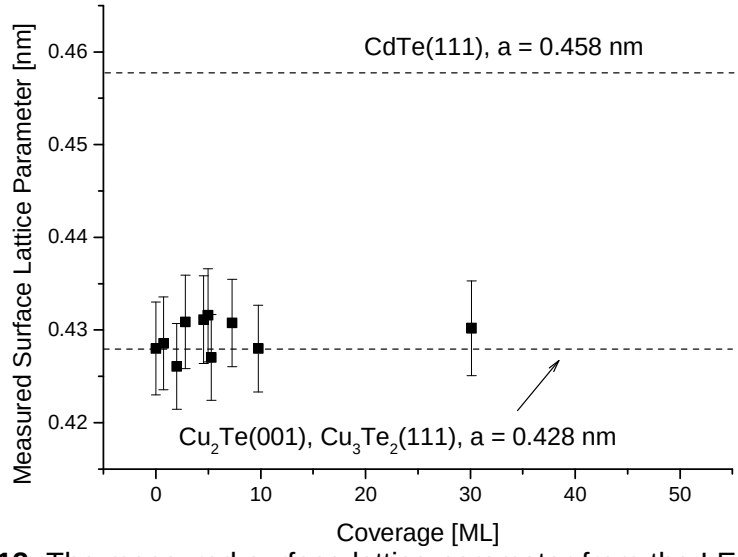

Figure 4.12. The measured surface lattice parameter from the LEED patterns of $CdTe/Cu_3Te_2$. The upper dashed line shows the bulk surface lattice parameter for the (111) termination of CdTe. The lower dashed line shows the surface lattice parameter for $Cu_2Te(001)$ and $Cu_3Te_2(111)$ surface terminations.

The 1.5 ML CdTe/Cu_3Te_2 LEED pattern, shown in figure 4.11, clearly illustrates that the hexagonal symmetry of the substrate is retained, although the pattern is more diffuse than 0 ML. The measured surface lattice parameter, shown in figure 4.12, is the same as the substrate lattice parameter. For a coverage of 1.5 ML, the Cu $2p^{3/2}$ XPS spectrum, displayed in figure 4.13, shows no shift in binding energy or change in width and hence are fitted to the same peak functions as 0 ML. The fitted Cu $2p^{3/2}$ XPS, for 1.5 ML, is consistent with an overlayer of CdTe on Cu_3Te_2 without any Cu diffusion. The LEED pattern is consistent with either a strained, psuedomorphic layer of CdTe, adopting the same lattice parameter as the substrate (figure 4.11); or island growth or polycrystalline growth. The fact that the 1.5 ML LEED pattern was far more diffuse than the 0 ML suggests that island or polycrystalline growth was the more likely growth mode. The Te $3d^{5/2}$ spectra, displayed in figure 4.14 (a), show a variation in binding energy of less than 0.05 eV, implying that the binding energy of the Cu-Te and Cd-Te bond in the Te $3d^{5/2}$ XPS spectrum is very similar and thus these core level peaks were not used for fitting. The Cd $3d^{5/2}$ spectra, displayed in figure 4.14 (b), show a peak centred at 405.1 eV, which grows with CdTe coverage and do not show a relaxation shift. A relaxation shift was observed in the Cd $3d^{5/2}$ XPS spectra from CdTe/Cu(111) but it is not observed in CdTe/Cu_3Te_2 because the Cu_3Te_2 substrate is a poorer conductor and hence has reduced electron mobility. Similar to Cd $3d^{5/2}$, the Cd 4d states, shown in figure 4.15 (a), display no relaxation shift. As in CdTe/Cu(111), the Cd 4d spectra are difficult to interpret because of their overlap with the Te 5s band and thus are not fitted in detail. It is interesting to note that the Te 5s state only becomes visible in photoemission when the CdTe layer reaches a thickness of 10 ML. The UPS valence spectrum for the 1.5 ML coverage is shown in figure 4.15 (b). It shows an initial suppression of the features at ~3.3, ~1.8 and ~1 eV associated with Cu_3Te_2(111). Two new features at ~2.2 eV and ~5.2 eV emerge which are from the valence band of CdTe [37,39], consistent with a disordered overlayer of CdTe on Cu_3Te_2.

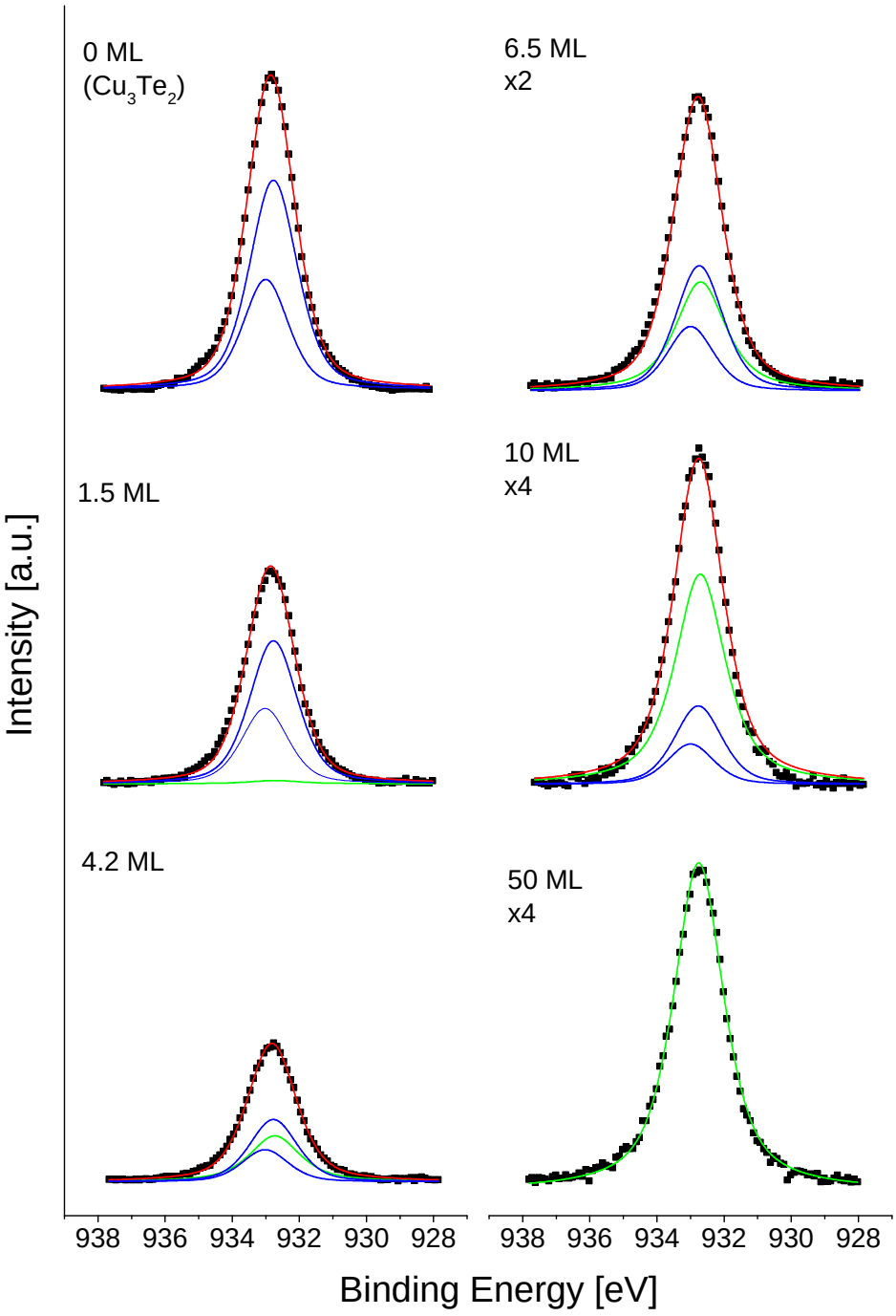

Figure 4.13. Cu $2p^{3/2}$ XPS spectra for increasingly larger doses of CdTe on $Cu_3Te_2(111)$ at 423 K. The blue lines are the substrate peaks of Cu_3Te_2. The green line is the peak from diffused Cu^+. The overall fit, where applicable is shown as a red line.

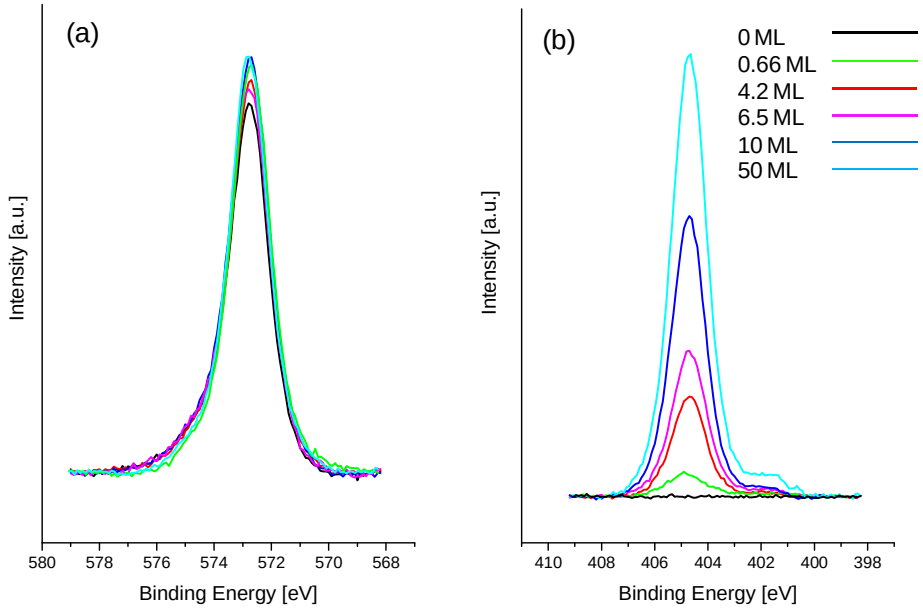

Figure 4.14. (a) Te $3d^{5/2}$ and (b) Cd $3d^{5/2}$ XPS spectra for increasingly larger doses of CdTe on Cu_3Te_2 at 423 K. The key applies to both (a) and (b)

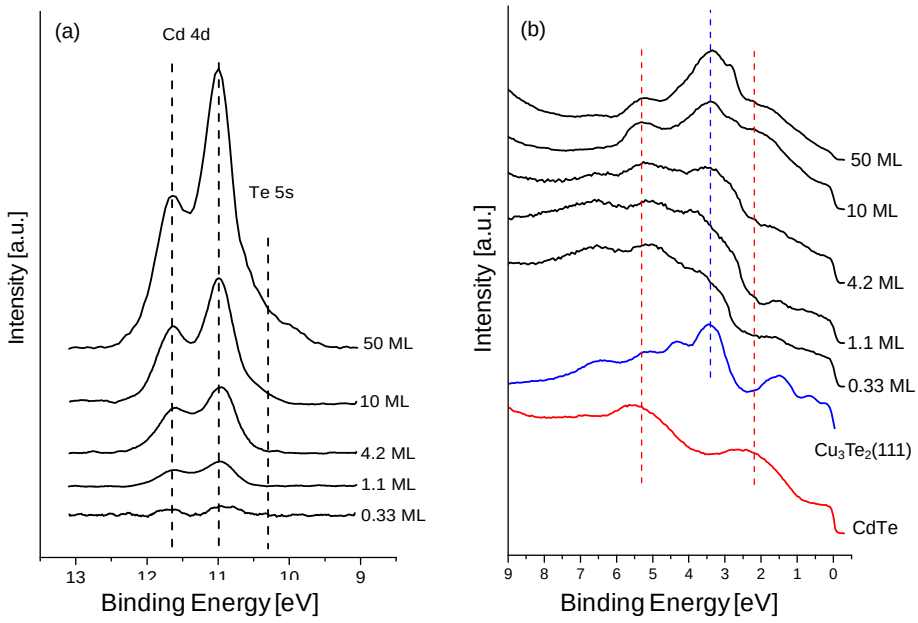

Figure 4.15. UPS spectra spanning (a) the Cd 4d states and (b) the valence band for increasingly larger doses of CdTe on Cu_3Te_2, deposited with the substrate temperature held at 423 K. The dashed lines in (b) are added to aid comparison of known compounds with the CdTe depositions.

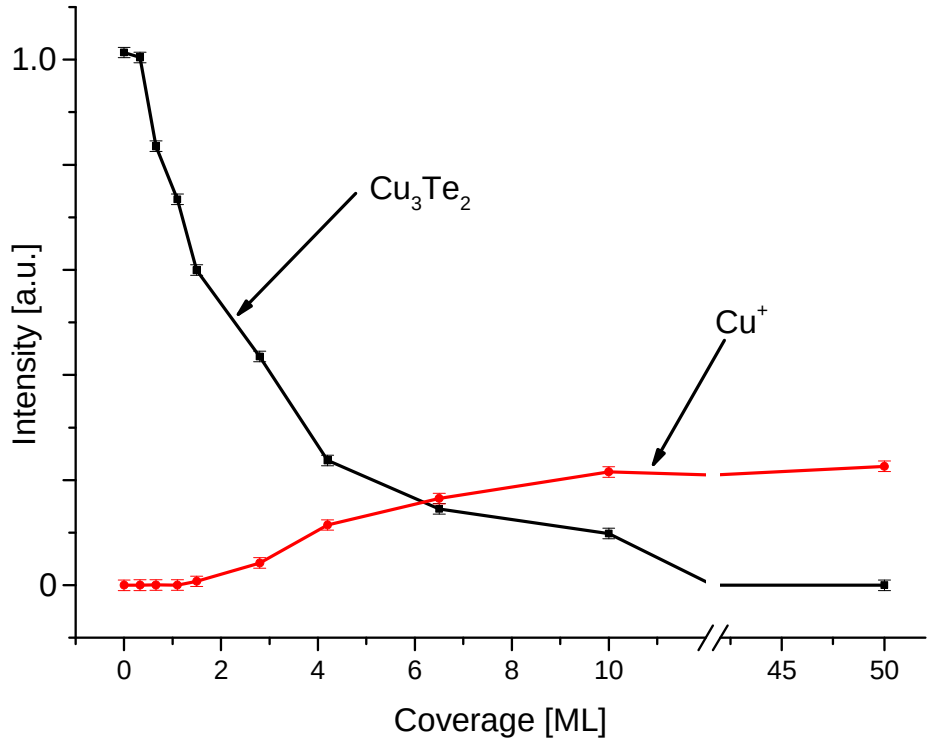

Figure 4.16. Summary of the intensities of Cu $2p^{3/2}$ XPS spectra as a function of CdTe coverage on Cu_3Te_2. The black line is Cu_3Te_2 and the red line is Cu^+. The Cu^+ component is undetectable below about 2 ML.

Above ~2 ML, the Cu $2p^{3/2}$ XPS data, shown in figure 4.13, begin to shift from 932.9 eV towards 932.7 eV. At 50 ML the Cu $2p^{3/2}$ XPS peak is well fitted to a single function centred at 932.7 eV, with the same parameters as the 50 ML Te/Cu_{poly} deposition (i.e. Cu_2Te, figure 3.10 (c)). Figure 4.16 summarises the change in Cu components in the Cu $2p^{3/2}$ XPS spectra for increasing CdTe coverage and shows that Cu^+ diffusion is detectable above ~2 ML. The fitted spectra strongly suggest that the near surface Cu in the CdTe layer is in the form of Cu_2Te. For the intermediate coverages, between 3 and 50 ML, the Cu $2p^{3/2}$ XPS spectra are fitted to a combination of the substrate peaks (i.e. Cu_3Te_2 Cu^+ and Cu^{2+} in a fixed ratio of 2:1) and a single function, representing the diffused Cu (Cu^+ from Cu_2Te). The width and asymmetry were fixed to that of the metallic Cu peak. The fitted Cu $2p^{3/2}$ XPS spectra show that the substrate components (Cu^+, Cu^{2+} in a ratio of 2:1) are progressively attenuated with increasing CdTe thickness, as expected for an overlayer of CdTe. The Cu^+ peak increases in intensity to a maximum at ~10 ML. Above 1.1 ML, the UPS spectra, displayed in figure 4.15 (b), show the re-emergence of the peak at 3.3 eV associated with Cu_3Te_2 or Cu_2Te.

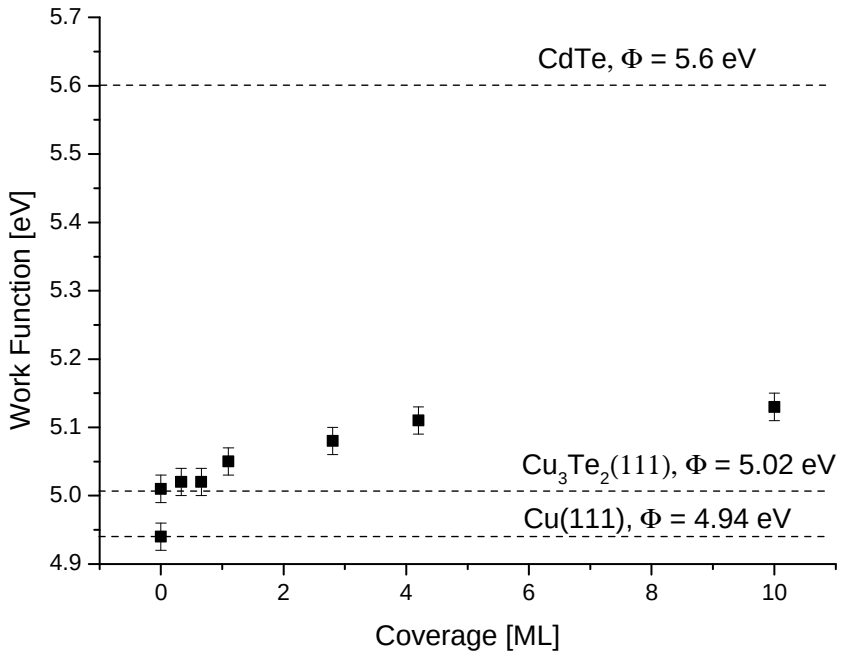

Figure 4.17. Measured work function of surface for increasing coverage of CdTe on Cu_3Te_2. The upper dashed line represents the work function of bulk polycrystalline CdTe. The middle dashed line represents the measured work function of Cu_3Te_2 and the lower dashed line represents the work function of Cu(111).

This shows that the presence of Cu^+ is not a result of CdTe island growth, as it would be expected that the UPS features associated with Cu_3Te_2 or Cu_2Te would be increasingly attenuated, not get larger for increasing CdTe thickness. The UPS is therefore consistent with Cu diffusion, detectable above ~2 ML. The presence of Cu in the near surface region of a (20-25 nm) 50 ML thick CdTe film was surprising but is ascribed to Cu diffusion into CdTe, in agreement with previous literature [10-27] and the TEM data which will be presented in section 4.2.4.2. Interestingly, the quantity of the near surface Cu in the $CdTe/Cu_3Te_2$ system is ~3 times that of the CdTe/Cu(111). This difference in Cu concentration is probably a result of the vacant Cu sites in the Cu_3Te_2 structure and will be discussed in greater detail when presenting the 50 ML CdTe films in section 4.2.4. The 50 ML LEED pattern was too diffuse to clearly identify spots. The assignment of Cu_2Te present in the near surface region of the 50 ML $CdTe/Cu_3Te_2$ film is backed by the UPS spectrum of the valence band, which is shown in figure 4.15 (b). The feature associated with Cu_2Te at 3.3 eV is distinct and clearly shows Cu_2Te present at the surface. The two

features corresponding to CdTe, at 2.2 eV and 5.2 eV are still present, which indicates that the surface comprises a mixture of Cu_2Te and CdTe. The work function data are displayed in figure 4.17 and lie between that of CdTe (5.6 eV) and Cu_2Te (5.0 eV), suggesting a mixture of both. The work function data are consistent with Cu_xTe forming a pseudo ohmic contact (i.e. Cu reduces the work function of CdTe at the back contact interface).

The proposed model for the growth of CdTe/Cu_3Te_2 at 423 K is summarised in figure 4.18. The growth of CdTe on Cu_3Te_2 is similar to CdTe/Cu(111). It was found that CdTe initially grows three dimensionally and is polycrystalline on Cu_3Te_2, identical to Cu(111). TEM data, which will be presented in section 4.2.4, indicates that the growth of CdTe on polycrystalline Cu_2Te is rough and polycrystalline and this is likely to be the case for initial stages of deposition of CdTe/Cu_3Te_2 and CdTe/Cu(111). At CdTe coverages greater than ~2 ML, Cu was detected as diffusing into the CdTe layer from both Cu(111) and Cu_3Te_2. Interestingly, the near surface concentration of Cu in the CdTe film is ~3 times greater from a Cu_3Te_2 substrate than a Cu(111) substrate. This observation motivated the study of these substrates with cross sectional TEM, section 4.2.4.2. The combination of FFT filtered BF images and EFTEM elemental mapping, obtained from the TEM indicated that there are segregated crystallites of CdTe and Cu_2Te, as described by equation 4.2, consistent with the XPS and UPS.

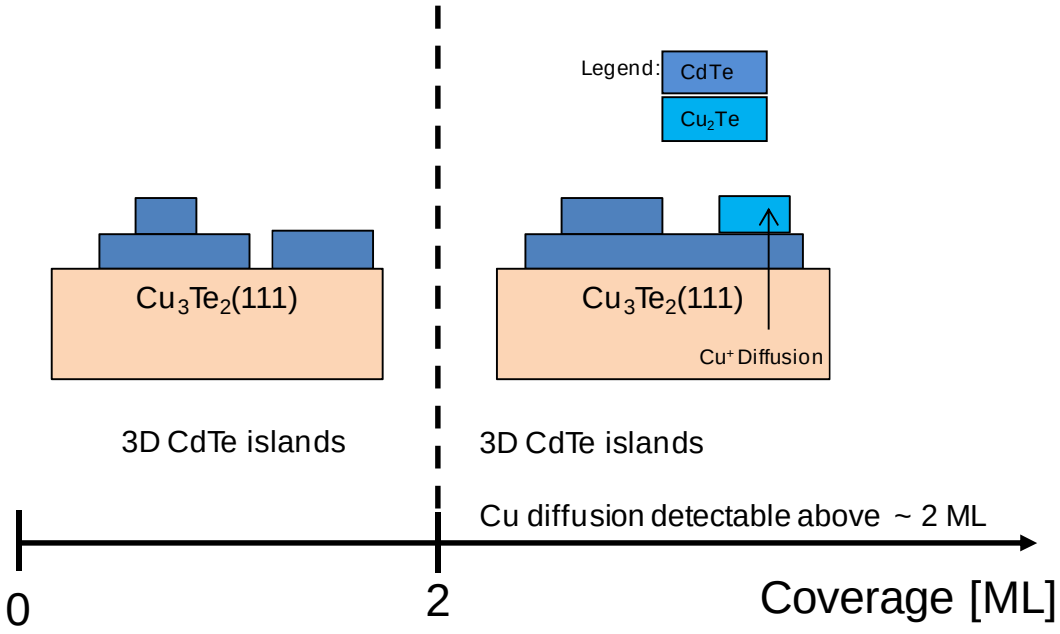

Figure 4.18. Schematic detailing the growth of CdTe/Cu_3Te_2(111) at 423 K.

4.2.4 Cu Diffusion into 50 ML CdTe films

In section 4.2.3, it was noticed that the amount of surface Cu^+ greatly increased (by a factor of ~3) when 50 ML CdTe was deposited on Cu_3Te_2 rather than on Cu(111). To understand Cu diffusion further, a combination of TEM and surface science techniques were employed, the results of which are presented in this section.

It has been shown that different Cu_xTe back contacts have markedly different properties on the CdTe photovoltaic cell [10-15]. These studies have focussed on the macroscopic properties of the cell, such as resistivity and cell efficiency. To simulate possible photovoltaic cell configurations, CdTe was deposited onto a variety of different Cu containing substrates. Experiments were performed by depositing 40-50 ML (20-25 nm) of CdTe onto Cu(111), polycrystalline Cu, Cu_2Te and Cu_3Te_2 at 300 K and the composition of the resulting CdTe films investigated. For brevity, the polycrystalline Cu specimen will be labelled Cu_{poly}. Specimens of Cu_{poly} were prepared *ex-situ* in a separate thermal evaporator system. An 80 nm thick Cu film, measured with atomic force microscopy (AFM), was deposited onto the native oxide of a Si(100) wafer, at 300 K. Si was chosen as the substrate because of the relative ease of preparing high quality specimens for the TEM. The Cu_2Te specimens were prepared by depositing 40-50 ML of Te onto the cleaned polycrystalline Cu at 300K. The roughness of Cu_{poly} and Cu_2Te was measured in TEM to be a maximum of ~5 nm, a result of the Ar^+ sputtering used to clean the surface. The data presented show the combination of TEM and surface science gives novel microscopic information that may help explain these device focussed studies.

4.2.4.1 Characterisation of Film Surface

This section begins by discussing the surface science measurements. XPS data spanning the Cu $2p^{3/2}$, Te $3d^{5/2}$ and Cd $3d^{5/2}$ states are shown in figures 4.19, 4.20 (a) and 4.20 (b), respectively . The UPS data covering the Cd 4d states and the valence band are shown in figures 4.21 (a) and 4.21 (b), respectively. Each Cu $2p^{3/2}$ spectrum, shown in figure 4.19 is fitted to the sum of a Gaussian and a DS function, as before. The shape and position of the fitted Cu $2p^{3/2}$ peak on each substrate, after CdTe deposition, matched that of the peak obtained from the polycrystalline Cu_2Te surface, indicating that Cu was in a 1+ oxidation state and strongly suggesting the formation of a Cu_2Te alloy in the near surface region for all four cases.

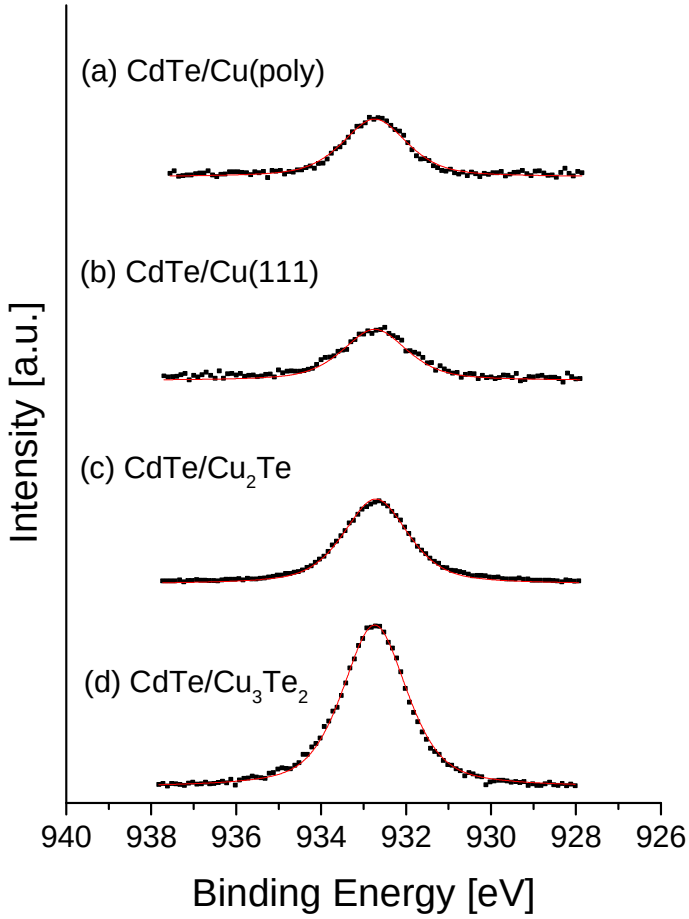

Figure 4.19. Cu $2p^{3/2}$ XPS spectra for 50 ML of CdTe deposited on (a) Cu_{poly}, (b) Cu(111), (c) Cu_2Te and (d) Cu_3Te_2(111) at 300 K. The red line represents the fit of the spectra to a Cu^+ component, with binding energy and width matching that of Cu_2Te.

Adding in another function, to represent Cu^{2+} at 933.0 eV did not improve the fit. The Te $3d^{5/2}$ and Cd $3d^{5/2}$ spectra, shown in figures 4.20 (a) and 4.21 (b), show less than 0.1 eV variation in binding energy and are therefore not appropriate for fitting. To measure relative compositions of Cu, Cd and Te we begin by noting that Cu and Te exist only as ionic Cu and Te and hence no elemental species are detected on the surface. The RSFs of S_{Cu} = 0.39 and S_{Cd} = 0.60, relative to S_{Te} = 1, derived in section 2.4.2, were used to evaluate the value of x in equation 4.5. Equations 4.4 and 4.6 have been disregarded because the TEM data, which will be presented subsequently, show that equation 4.5 (i.e. formation of Cu_2Te domains in the CdTe film) is the dominant process. The values obtained for x are listed in the second column of table 4.1 and show the extent of Cu

diffusion into CdTe layer is very similar from the Cu(111) and Cu_{poly} surfaces, which is reasonable since one would expect the polycrystalline surface to be dominated by (111) terminations. The additional grain boundaries in Cu_{poly} do not appear to have a large effect on the diffusivity of Cu into CdTe. Interestingly, the value for x is much larger from Cu_2Te and Cu_3Te_2 substrates, demonstrating that the diffusion of Cu is facilitated for these surfaces. This has been pointed out before by Mann et al. [55,56], who measured the coefficient for Cu diffusion into CdTe to be four orders of magnitude more in Cu_2Te than on polycrystalline Cu. Cu_3Te_2(111) further enhances Cu diffusion, which may be a result of the multiplicity of vacant octahedral and tetrahedral sites [57].

Substrate	x ± 0.1 (300 K)	x ± 0.1 (423 K)
Cu(111)	0.3	1.2
Polycrystalline Cu	0.3	-
Cu_2Te	0.6	-
Cu_3Te_2(111)	1.1	1.6

Table 4.1. The calculated stoichiometry parameter, x, as defined in equations 4.5-4.7, for 50 ML CdTe film deposited onto different Cu containing substrates.

The Cd 4d spectra obtained from each surface is presented in figure 4.21 (a). The spectra are not fitted in detail because of the dispersion of the Te 5s band. The binding energy of the Cd $4d^{5/2}$ and $4d^{3/2}$ states are in good agreement with previous studies of CdTe [38]. The peak shapes of the Cd 4d states and the Te 5s band (the shoulder at ~10.2 eV) differ slightly from surface to surface which could be due to changes in the Te 5s band that may arise from subtle changes in bonding or orientation in the CdTe layer, which have been described previously by Holsch et al. [38].

UPS data covering the valence band were collected from each of the surfaces and are presented in figure 4.21 (b) and provide strong evidence for the formation of Cu_2Te and metallic Cd in the surface region of CdTe. The bottom 3 traces are of known compounds collected in this system - CdTe, Cu_2Te and Cu_3Te_2 and are used as reference. To aid comparison, lines are drawn from the strong features of the reference spectra to the depositions on the different surfaces.

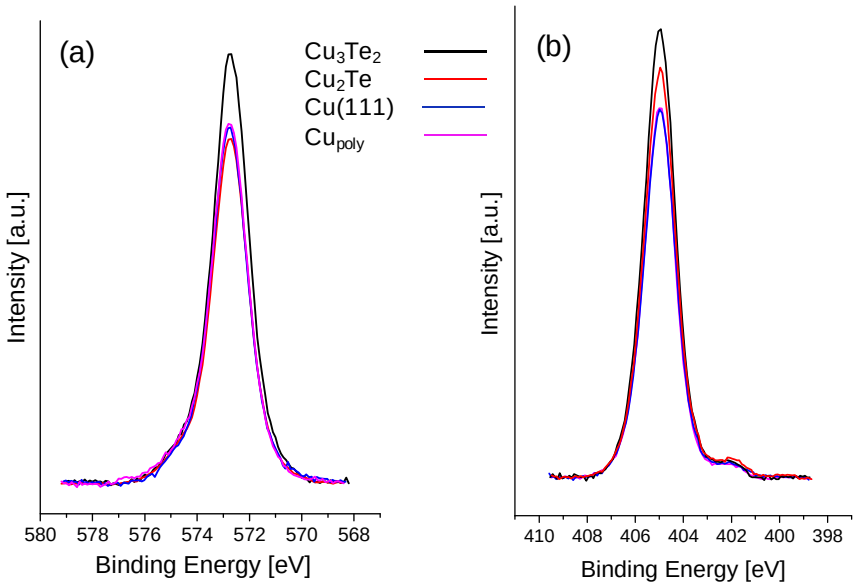

Figure 4.20. (a) Te $3d^{5/2}$ and (b) Cd $3d^{5/2}$ XPS spectra for 50 ML of CdTe deposited on the Cu_3Te_2 (black line), Cu_2Te (red line), Cu(111) (blue line) and is Cu_{poly} (magenta line). The change in binding energy between these spectra is less than 0.1 eV. The key applies to both (a) and (b)

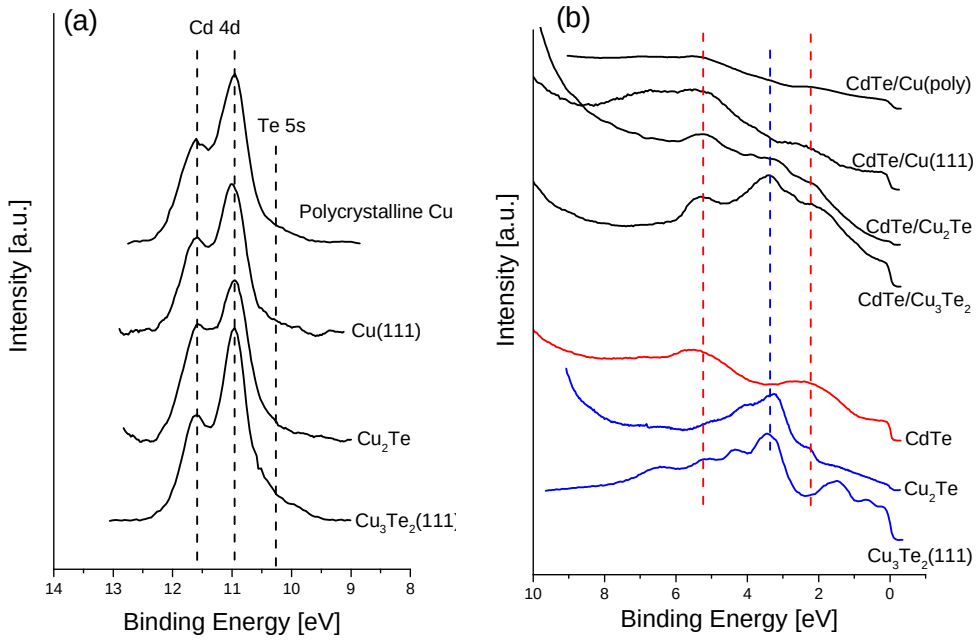

Figure 4.21. UPS spectra spanning (a) the Cd 4d states and (b) the valance band, obtained after depositing 50 ML of CdTe onto Cu and Cu_xTe. The dashed lines in (b) are used to aid comparison between known spectra and the spectra obtained after CdTe deposition.

The valence band for the CdTe/Cu_3Te_2(111) surface shows strong features at 5.4, 3.4 and 2.2 eV. The features at 5.4 and 2.2 eV appear in the CdTe spectra but the strong feature at 3.4 eV, only appears in the two Cu-Te spectra. Metallic Cd(0001) [41] has a feature at ~3 eV and is likely to contribute to the feature at 3.4 eV because in the formation of Cu_2Te, as described in equation 4.5, Cu displaces Cd from CdTe, resulting in Cd metal being formed. Indeed, the false coloured elemental map, which will be described in the following section, shows patches of Cd metal and Cu_xTe at the surface. In addition the CBED data, also described in the following section, confirm the presence of Cu_2Te in the CdTe film. The possibility of Cu_3Te_2 is ruled out on the basis of Cu $2p^{3/2}$ XPS, shown in figure 4.19, which shows no Cu^{2+} and the CBED data, which show no crystallographic evidence of Cu_3Te_2. The UPS spectra obtained from the deposition of CdTe onto the Cu_2Te substrate results in a similar spectrum to the Cu_3Te_2 substrate, albeit with a reduced component from Cu_2Te. This is consistent with the XPS data, which also shows a reduced Cu^+ content. The same is true for the Cu(111) and Cu_{poly} substrates, however, the Cu_2Te component is very small in these spectra, in agreement with XPS data. The prominence of the Cu_2Te feature at 3.4 eV is directly related to the quantity of Cu^+ measured in the Cu $2p^{3/2}$ XPS spectra.

4.2.4.2 Characterisation of Film Bulk

Further investigations into the nature of the Cu diffusion into the CdTe layer were performed with cross-sectional TEM. EFTEM elemental maps are displayed in figures 4.22, 4.23 and 4.24. Related HRTEM images are shown in figures 4.25 and 4.26. Finally, CBED patterns are displayed in figure 4.27, which provide nanometre-scale crystallographic information. These TEM experiments gave additional insight into the spatial distribution of elements on the surface and deeper within the CdTe layer, where XPS and UPS are unable to probe. BF imaging, HRTEM, CBED and EFTEM data sets were collected from cross sections of 40-50 ML (20-25 nm) of CdTe deposited onto Cu_2Te and Cu_{poly} at 300 K.

EFTEM images were recorded for the Cu-$L_{2,3}$, Te-$M_{4,5}$, Cd-$M_{4,5}$ and O-K core loss edges. To aid selection of appropriate energy filtering windows, a STEM EELS spectrum was obtained from the specimen. The STEM EELS spectrum was then divided into regions surrounding the Cu-$L_{2,3}$, Te-$M_{4,5}$, Cd-$M_{4,5}$ and O-K core ionisation edges. These spectra are shown in figure 4.22. Annotated on each core loss spectra are three grey boxes, which represent the two pre-edge windows (boxes 1 and 2) and the single post edge window (box 3).

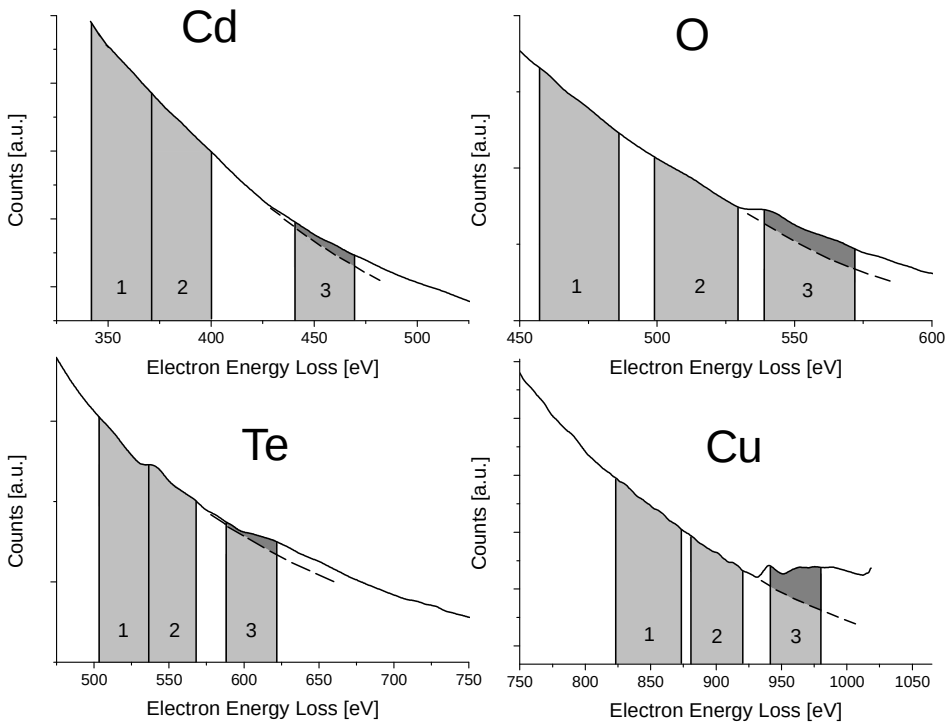

Figure 4.22. STEM EELS spectra obtained after summing a series of individual spectra taken as a line scan across the entire CdTe/Cu_{poly} cross section. The pre-edge windows are light grey shaded and are labelled 1 and 2 and the post-edge window is shaded light grey and labelled. 3. The dashed line shows the extrapolated power law background derived from the pre edge windows. The area shaded dark grey shows the net intensity.

Edge	Energy [eV]	Pre Edge 1 Centre [eV]	Pre Edge 2 Centre [eV]	Post Edge Centre [eV]	Width [eV]	Acquisition Time (s)
Cu $L_{2,3}$	931	851	901	961	40	10
Te $M_{4,5}$	573	522	552	606	30	10
Cd $M_{4,5}$	405	355	385	475	30	10
O K	532	472	512	553	30	5

Table 4.2. Acquisition parameters for EFTEM images shown in figures 4.23 and 4.24.

A detailed treatment of the background subtraction process is given in section 2.4.2. The O-K and Cu-$L_{2,3}$ edges are strong and have an abrupt onset and thus are easy to identify. The Te-$M_{4,5}$ and Cd-$M_{4,5}$ edges are weaker and thus appear as more as more gentle changes in the gradient of the curve. The presence of O will clearly have an effect on the Te elemental map because the Te pre-edge window lies on the O edge. Hence if O is present, the shape of the Te edge background will be influenced by the O edge. In practice this means that in the Te map, areas containing oxygen will exist as negative counts because the fitted background now lies above the edge. In the Te line traces, shown in figures 4.23 (f) and 4.24 (f), this effect manifests as a single negative peak at the SiO_x interface, which has been background subtracted from the displayed spectra for clarity as it is an artefact. The complete set of acquisition parameters that have been used to acquire EFTEM images is listed in table 4.2.

Figures 4.23 and 4.24 are EFTEM elemental maps showing the distribution of elements in the CdTe film deposited onto Cu_{poly} and Cu_2Te respectively. The Cu-$L_{2,3}$ signal was most intense in the Cu layer but was also clearly visible in the CdTe layers. The observation of Cu in the CdTe layer, coupled with the fact that the CdTe film is of near uniform thickness, shows that the surface Cu, measured with XPS, must come from the diffusion of Cu into the surface region of CdTe rather than the island growth of CdTe leaving an exposed Cu substrate. The bright band in the O elemental map in both figures 4.23 (e) and 4.24 (e) is from the oxidised surface of the Si wafer. The Te, Cd and Cu elemental maps show that the CdTe film is inhomogeneous when deposited on both Cu_{poly} and Cu_2Te. Annotated on the Cu and Cd elemental maps are arrows pointing towards areas of the CdTe film that are Cu rich and Cd deficient (i.e. showing Cu diffusion). The overlap between these two areas is good, indicating the displacement of Cd by Cu. The Te elemental map shows that Te is more uniformly distributed through the film. However, it is not perfect and the areas that are Te deficient tend to be Cd rich, which suggests the segregation of elemental Cd. The RGB images shown in figures 4.23 (f) and 4.24 (f) are instructive in assessing the distribution of the elements in the CdTe film. The CdTe/Cu_{poly} and CdTe/Cu_2Te images display the same features but are qualitatively different. Both RGB images show that CdTe is formed as there are regions that are cyan which are created only from the overlap of Cd (dark blue) and Te (dark green). Relative elemental quantification was performed using equation 2.28 and with partial ionisation cross sections, σ, that were extracted from the Gatan Digital Micrograph software [58]. The values of σ were determined to be σ_{Cu} = 0.16, σ_{Cu} = 0.83, relative to σ_{Cd} = 1. The elemental quantification revealed that the areas that appear dark on the Cu elemental map (and hence had Cu atomic concentrations less than 1 %) had a Cd : Te ratio of between 0.9-1.2. In the areas that appeared bright, the Cu

content varied substantially. The clearest way of indicating the stoichiometry is by using the right side of equation 4.5:

$$x\ \mathrm{Cu} + \mathrm{CdTe} \rightarrow (\mathrm{CdTe})_{1-x/2} + (\mathrm{Cu_2Te})_{x/2} + \mathrm{Cd}_{x/2} \qquad (4.5)$$

In that, the ratios of Cu:Cd:Te will be described as quantities of CdTe and Cu_2Te with compositional parameter, x, as indicated in equation 4.5. In the areas that had Cu present, as shown in the Cu elemental maps (figures 4.23 (c) and 4.24 (c)) the value of x was in the range 1.1 to 1.9. The fact that x does not reach 2 (i.e. full conversion to Cu_2Te) may be a result of TEM measurements being a projection of the entire thickness of the cross section (i.e. the signal is a combination of multiple grains of both CdTe and Cu_2Te). We also use HRTEM (figures 4.25 and 4.26) and CBED (figure 4.27) to identify the structure and composition of the Cu rich regions of the CdTe film.

The XPS data show, quantitatively, that the surface Cu concentration of CdTe/Cu_2Te is approximately twice that of CdTe/Cu_{poly}. We can also see, qualitatively, differences in surface Cu concentration with EFTEM. Both RGB images show that the Cu_xTe regions are distributed throughout the film and not just confined to the surface, however, Cu appears to favour accumulating at the surface, as shown in the Cu-$L_{2,3}$ image, figure 4.24 (c) and this effect is more pronounced in the CdTe/Cu_2Te system. The RGB images show qualitatively the same effect: there are far more Cu_2Te patches (light green) in the CdTe/Cu_2Te image than the CdTe/Cu_{poly} image, particularly at the surface. Also, both images show that there are dark blue regions that are solely comprised of Cd, formed from the displacement of Cd by Cu. The observation of elemental Cd in the EFTEM images is in agreement with the XPS data, which show that the Cd : Te ratio is greater than 1, i.e. there is an excess of Cd.

The UPS data are also in qualitative agreement with the EFTEM. The UPS data, figure 4.21 (b) show that there is a distinct feature in the CdTe/Cu_2Te system at 3.4 eV, while in the CdTe/Cu_{poly} system, this feature is not present. As previously stated, the RGB images show relatively few Cu_2Te patches on CdTe/Cu_{poly} than on CdTe/Cu_2Te. This shows that the feature at 3.4 eV must be associated with Cu_2Te (not Cu_3Te_2 as there is no Cu^{2+} fitted in the XPS or any evidence of Cu_3Te_2 in the CBED or HRTEM) as this is the major difference between both RGB images. The enhanced Cu diffusion from the Cu_2Te and Cu_3Te_2 substrates mean that it is possible for Cu to form discrete Cu_2Te units at the surface.

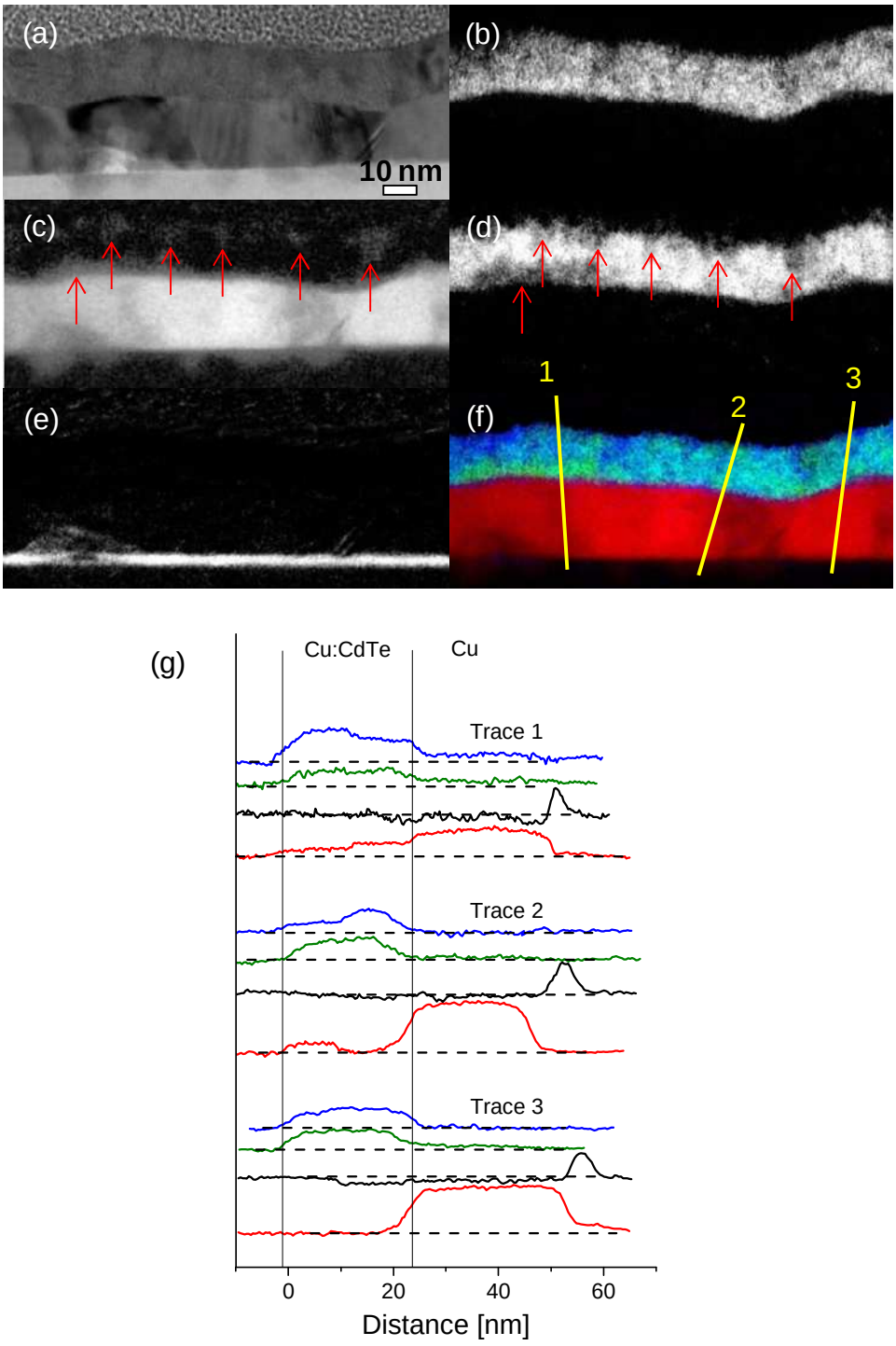

Figure 4.23. EFTEM images for 50 ML CdTe on Cu_{poly}. (a) is a BF image taken from the same area as elemental maps: (b) is the Te $M_{4,5}$ elemental map (c) is the Cu-$L_{2,3}$ elemental map, (d) is the Cd $M_{4,5}$ elemental map and (e) is the O-K elemental map. (f) is a false coloured RGB image created from the overlap of elemental maps of Cu (red), Te (green) and Cd (blue). The red arrows, in the Cu and Cd maps, indicate regions in the Cu:CdTe film that are either Cu rich or Cd deficient. (g) shows line traces taken from (f). The red line trace is Cu, the black line is O, the green line is Te and the blue line is Cd.

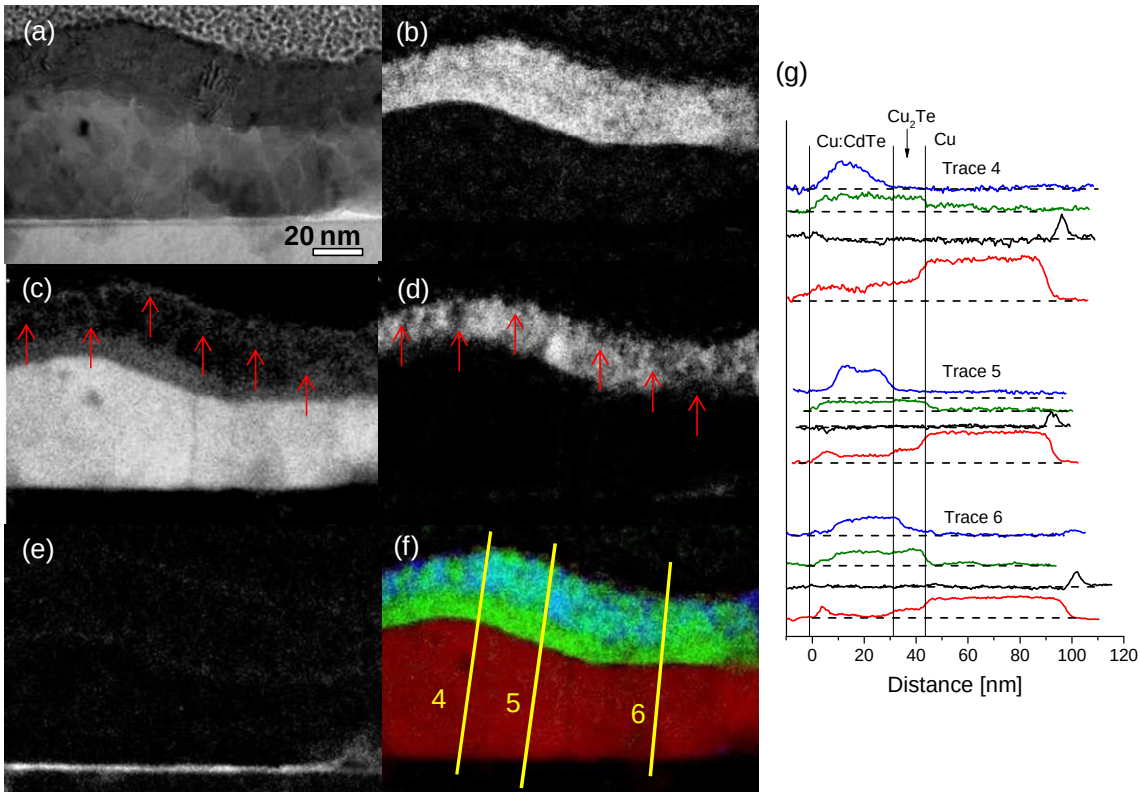

Figure 4.24. EFTEM images for 50 ML CdTe on Cu_2Te. (a) is a BF image taken from the same area as elemental maps: (b) is the Te $M_{4,5}$ elemental map (c) is the Cu-$L_{2,3}$ elemental map, (d) is the Cd $M_{4,5}$ elemental map, (e) is the O-K elemental map. (f) is a false coloured RGB image created from the overlap of elemental maps of Cu (red), Te (green) and Cd (blue). The red arrows, in the Cu map, indicate regions in the Cu:CdTe film that are Cu rich. While in the Cd map, the red arrows indicate regions in the Cu:CdTe film that are Cd deficient. The red line trace is Cu, the black line is O, the green line is Te and the blue line is Cd. The vertical lines are added to aid recognition of layer boundaries.

The EFTEM data are alternatively presented as a series of element specific line traces. These line profiles are shown in figures 4.23 (g) (CdTe/Cu_{poly}) and 4.24 (g) (CdTe/Cu_2Te). The line traces are numbered in correspondence to the lines indicated on figures 4.23 (f) and 4.24 (f). The integration window has been kept small, ~2 nm, as the film is clearly spatially inhomogeneous and one of the purposes of the line profile is to probe the spatial inhomogeneity. Although the RGB images suggests that there is a dark region at the Cu interface, the line profiles show a substantial intensity in this region, which means that this lack of signal is simply an effect of overlaying the spectra. The integrated line profiles were chosen to demonstrate different aspects of the Cu:CdTe film. Traces 1 and 2 clearly show that an increase in Cu signal in the CdTe layer is accompanied by a decrease in Cd signal, confirming the observations in the elemental maps in figures 4.23 and 4.24 and implying that Cu_2Te and CdTe are separate. The line profiles also illustrate the fact that TEM images are projections of the entire cross section and hence the Cu and Cd signals do not drop to zero. This behaviour is typical of both CdTe on Cu_{poly} and Cu_2Te. Trace 3 is displayed to show that there are still regions where Cu has not penetrated and the surface of the film remains CdTe. Traces 4, 5 and 6 show that Cu readily penetrates to the surface of the CdTe film when it is deposited on Cu_2Te: a peak which can be observed in the Cu signal and is also visible in the EFTEM image. The corresponding surface Cd signal drops close to zero when the Cu peak is observed at the surface. The Te signal also shows that it is present at the surface, which agrees with the XPS, as no elemental Cu was detected. In particular, traces 5 and 6 show that there is a distinct increase in surface Cu concentration, implying that there is tendency for Cu_2Te to segregate at the surface.

Cu_2Te and CdTe have very similar crystallography, which meant that the structural information obtained from BF and HRTEM imaging had to be correlated with the elemental mapping of EFTEM. Cu_2Te crystallises as a hexagonal unit cell, with space group $P6/mmm$ and lattice parameters of a = 0.426 nm, c = 0.729 nm and γ = 120° [60]. CdTe normally adopts a cubic $F\bar{4}3m$ structure [61] in the bulk but in thin film systems, a hexagonal $P6_3mc$ unit cell [62] is known to be stable and has lattice parameters of a = 0.457 nm, c = 0.750 nm and γ = 120°, which are very similar to Cu_2Te. The correlated HRTEM and EFTEM images are shown for the CdTe/Cu_3Te_2 and CdTe/Cu_{poly} systems in figures 4.25 and 4.26, respectively, with each layer labelled appropriately. By analysing the HRTEM images in this way, individual grains of Cu_2Te and CdTe could be identified in the Cu:CdTe film. Figure 4.25 (a) shows a Cu elemental map with the three different layers: Cu, Cu_2Te and Cu:CdTe. Presented in figure 4.25 (b) is a BF image of the elemental map shown in figure 4.25 (a). There is good Z contrast between the Cu and Cu_2Te layers in this image and hence it is easy to identify the interface. Unexpectedly, the

Cu film does not show clear fringes. However, several small (~10 nm) crystalline Cu grains were identified with BF imaging (not shown). The Cu_2Te interface is indistinct but the Cu_2Te layer is clearly observable as a well defined edge in the line profiles of the Cu elemental map, shown in figure 4.24 (g). Lattice fringes are visible in the Cu_2Te layer at this magnification and figure 4.25 (d) shows a FFT filtered image with the periodicity picked out to match that of the fringes in the Cu_2Te layer. It shows that the planes defining the Cu_2Te lattice are in present in the CdTe layer and are in reasonable agreement with the distribution of Cu in CdTe. The Cu elemental map shows an almost continuous surface Cu layer, although from other images (e.g. figure 4.24 (f)), CdTe terminated surfaces were also observed in the Cu:CdTe layer. The FFT filtered image shows that there are several different grains, indicating a polycrystalline surface. Several Cu_2Te grains do not show up in the image because of their orientations with the electron beam. The BF/EFTEM data are consistent with the UPS data, as they both indicate that Cu_2Te is formed close to the surface. The red dashed box in the Cu elemental map defines the area where the HRTEM image in figure 4.25 (d) was taken from. From the HRTEM image, we measure a lattice spacing of 0.73 ± 0.01 nm. This corresponds to the [0001] spacing in either CdTe (0.75 nm) or Cu_2Te (0.72 nm). But from the correlation of the FFT filtered HRTEM image (figure 4.24 (e)) with the Cu elemental map, we know that this must be Cu_2Te as it is Cu rich. The HRTEM also shows that the growth direction is with the *c* axis normal to the surface. The HRTEM and EFTEM images show that the Cu_2Te crystallites in the CdTe film tend to be orientated well with the Cu_2Te layer, which may facilitate the diffusion of Cu into CdTe.

The correlation of HRTEM and EFTEM for the $CdTe/Cu_{poly}$ system is displayed in figure 4.26. The orientation of the grains show narrower spaced lattice fringes which means that HRTEM images are required to resolve the lattice fringes. The Cu elemental map, displayed in figure 4.26 (a), shows that there are two grains that are clearly Cu rich. Figure 4.26 (c) shows the FFT filtered image of the leftmost Cu grain and is clearly identifiable as a separate grain. The lattice spacing is measured to be 0.38 ± 0.01 nm which corresponds to the [1010] spacing in Cu_2Te. In figure 4.26 (d), the FFT filtered image shows lattice fringes that correspond to the Cd rich grain situated between the top Cu rich regions. Interestingly, these fringes protrude into the Cu rich region, which suggests epitaxial growth. The rightmost Cu rich region of figure 4.26 (a) shows a Moiré pattern in the HRTEM image, whose fringes are picked out in figure 4.26 (d). A Moiré pattern is a result of two or more different grains lying on top of each other and shows why the fringe separation does not match exactly to the extent of Cu rich region, shown in the elemental map of figure 4.26 (a).

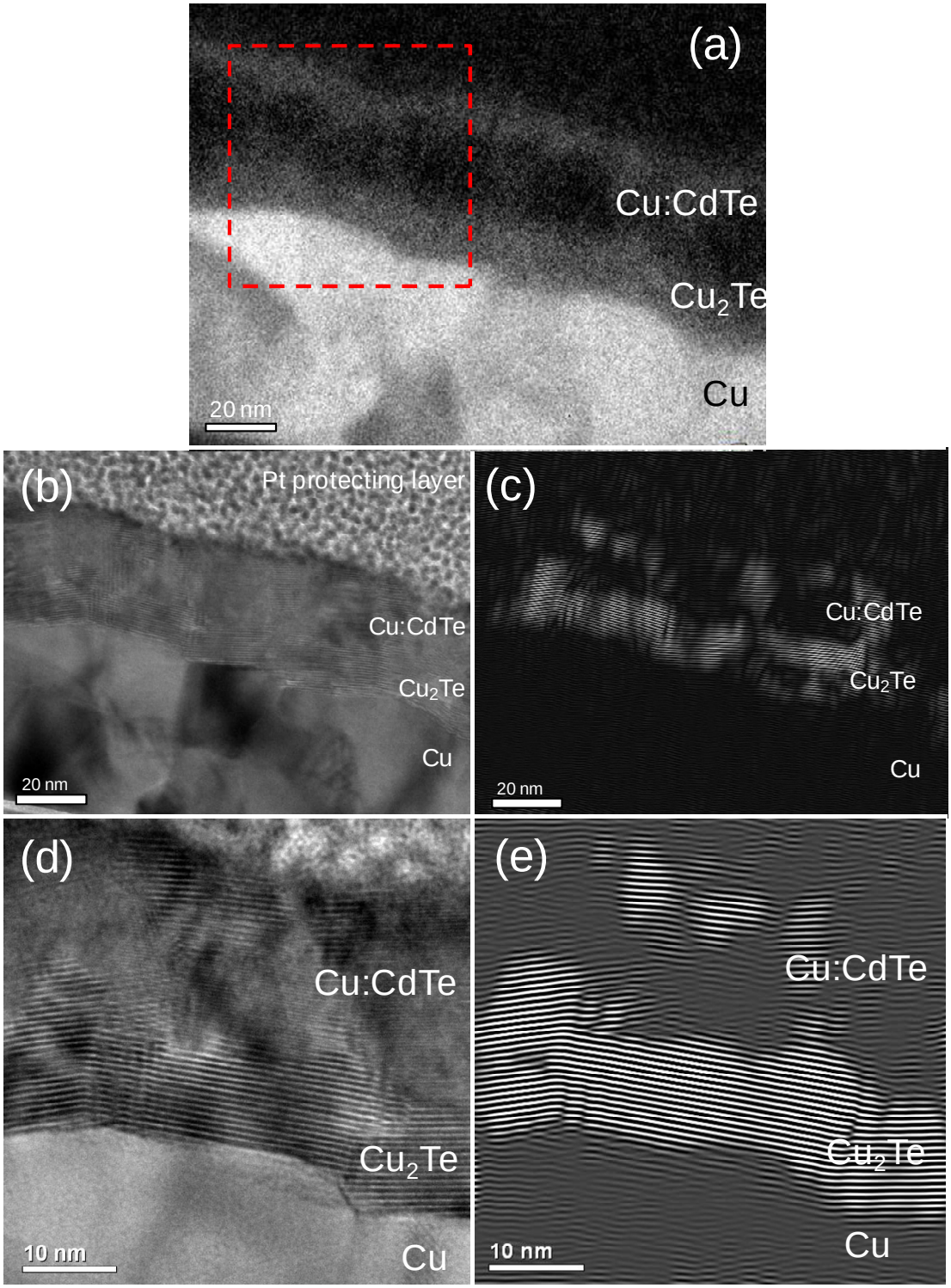

Figure 4.25. (a) EFTEM elemental Cu map from the CdTe/Cu_2Te specimen. (b) Medium magnification BF image of the EFTEM map in (a). (c) FFT filtered of image (b) with the periodicity picked to match the Cu_2Te layer. (d) HRTEM image of area denoted as the red dashed box in (a). (e) FFT filtered of image (d) with the periodicity picked to match the Cu_2Te layer. Each layer is labelled to according to its constituents.

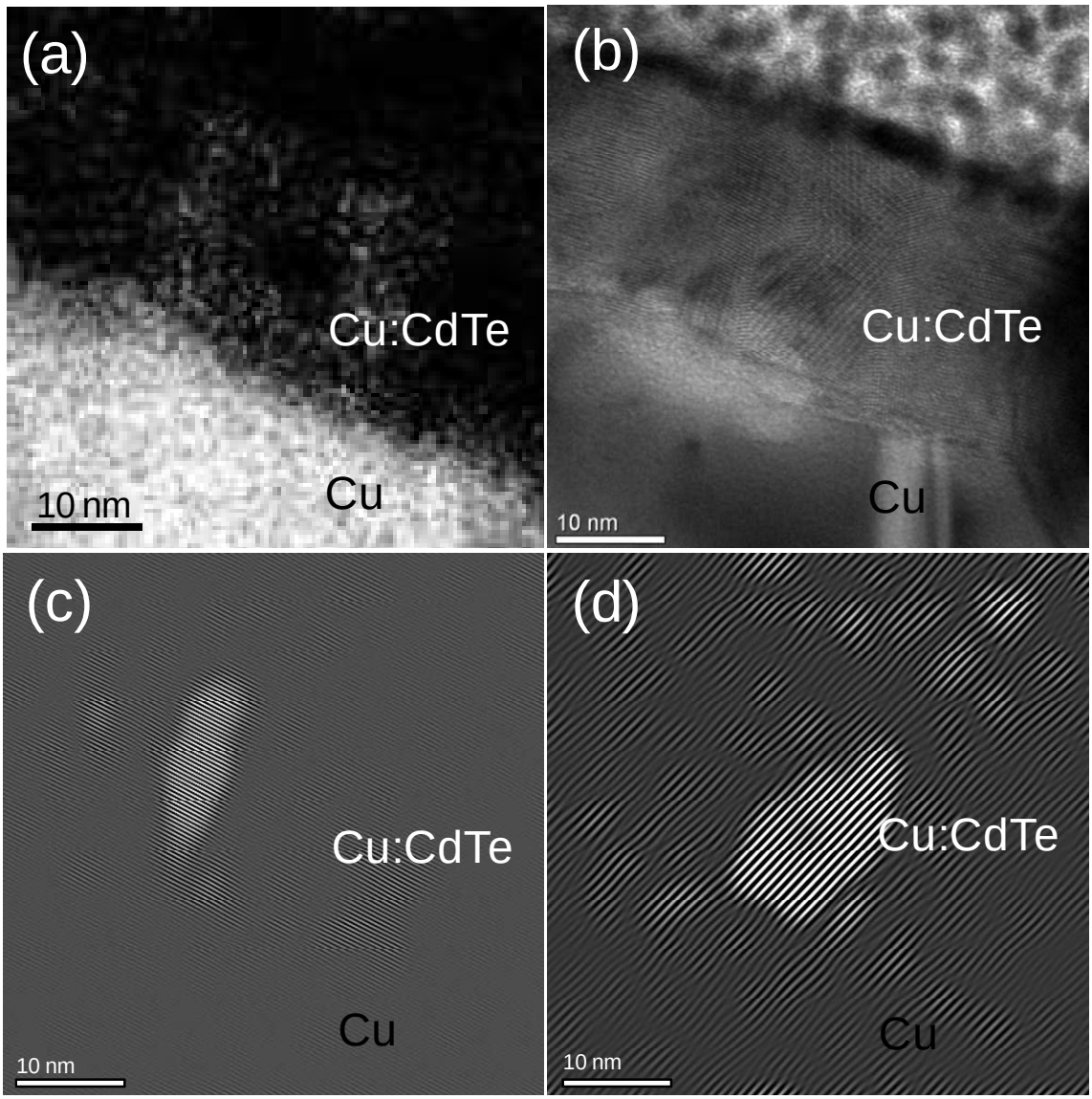

Figure 4.26. (a) EFTEM elemental map from the CdTe/Cu_{poly} specimen. (b) HRTEM image of the same as the Cu elemental map. (c) FFT filtered image of (b) illustrating a Cu rich grain. (d) FFT filtered image of (b) illustrating a Cd rich grain that has a degree of overlap with a Cu rich grain.

CBED was also used to probe the crystal structure of the Cu:CdTe film. As described in chapter 2, CBED is the appropriate diffraction technique to use when the grain size of the crystallites are small (< 100 nm). Figure 4.27 (a) is from the Cu_{poly} substrate and is typical of the sample. No data set could be obtained that was of a single crystal of Cu. The FWHM of the condensed electron beam was estimated to be 23 nm, which would imply that the grain size of Cu was less or approximately equal to the FWHM of 23 nm. The lattice parameter obtained from the Cu_{poly} layer was measured to be 0.36 ± 0.01 nm, which is in good agreement with the reported unit cell of Cu [49], a = 0.3608 nm. Figure 4.27 (b) shows a CBED pattern from the Cu_2Te interlayer. This pattern was indexed to $P6/mmm$-Cu_2Te with a = 0.43 ± 0.02 nm, in good agreement with the ideal Cu_2Te unit cell which has a lattice parameter of a = 0.424 nm [60]. Figures 4.27 (c) and 4.27 (d) show CBED patterns obtained from the CdTe film. As the lattice parameter of hexagonal CdTe differs only by ~6 % from that of Cu_2Te, a longer TEM camera length of 2902 ± 9 mm, is required to differentiate between these two structures. The CBED pattern shown in figure 4.27 (c) was obtained from the Cu:CdTe layer deposited on Cu_2Te and can only be reasonably indexed to the hexagonal CdTe lattice. The CBED pattern has measured lattice parameters of a = 0.458 ± 0.008 nm and c = 0.771 ± 0.008 nm. The lattice parameters compare favourably to the reported structure, which has values of a = 0.457 nm and c = 0.752 nm [62]. The CBED data presented here shows that there is a ~2 % expansion of the c axis with respect to the native *hexagonal* CdTe structure, consistent with Cu occupying interstitial sites of CdTe, equation 4.1. In a previous study, Dzhafarov et al. [20] saw no change in the lattice parameter of *cubic* CdTe when Cu occupied interstitial sites. The different polymorphs of CdTe may explain why an expansion is found here. It is noted that, of the CBED patterns obtained, an increase in the c lattice parameter of CdTe was only observed in less than 10 % of CBED patterns, indicating that it was a relatively minor process. Figure 4.27 (d) is also obtained from the Cu:CdTe layer deposited onto Cu_2Te and can only be sensibly indexed to Cu_2Te. From the diffraction pattern, we measure the lattice parameters to be a = 0.436 ± 0.008 nm and c = 0.722 ± 0.008 nm. These dimensions compare well with the ideal unit cell of Cu_2Te which has lattice parameters of a = 0.424 nm and c = 0.727 nm [60]. No measurement from the CBED patterns or the HRTEM from the Cu:CdTe layer could be found to match the dimensions or symmetry of the cubic CdTe unit cell nor any other phase of Cu_xTe, other than Cu_2Te.

In summary, the CBED patterns and HRTEM, in conjunction with EFTEM, confirm that crystallites of Cu_2Te form in the Cu:CdTe layer. The CBED and HRTEM also show that CdTe exists in its hexagonal unit cell, which is known to exist in thin films [62]. The symmetry and lattice parameters of the CdTe and Cu_2Te crystallites compare well with the

ideal unit cells. The TEM data presented here are consistent with the XPS and UPS data shown earlier in this chapter. The XPS data shows that the surface Cu concentration of a 50 ML Cu:CdTe film is twice as large on Cu_2Te than on Cu and UPS data shows qualitatively that Cu_2Te forms. XPS and UPS can only probe the outermost ~2 nm of the surface while TEM has the advantage that it can probe the entire specimen. Consequently, the TEM data shows that Cu_2Te occurs throughout the CdTe layer and not just at the surface.

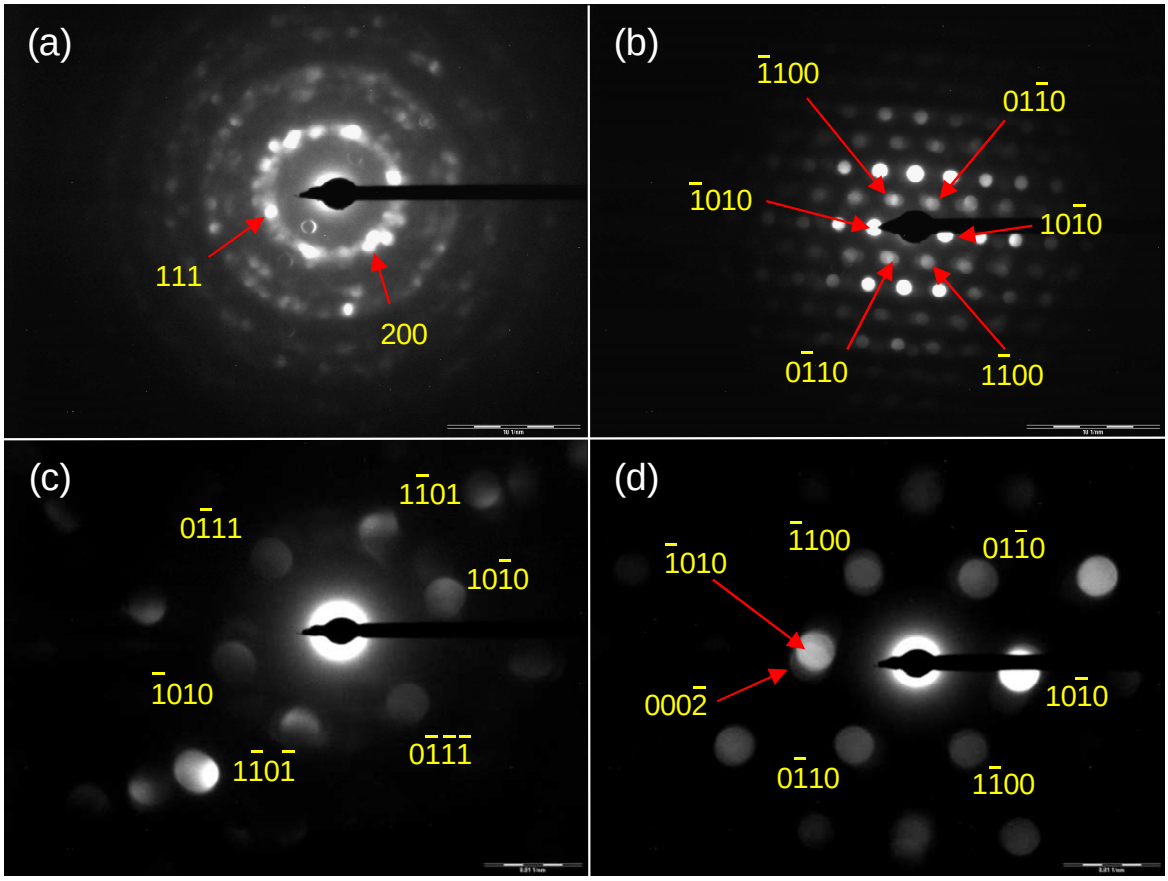

Figure 4.27. CBED patterns of (a) Cu_{poly} (b) Cu_2Te, from the deposited Cu_2Te layer (c) CdTe and (d) Cu_2Te obtained from the CdTe layer. (a) and (b) are obtained at a camera length of 984 ± 8 mm. (c) and (d) are obtained from a camera length of 2902 ± 9 mm.

From previous work, it was thought that Cu diffusing into CdTe could result in three different structures being formed. Based on the results of surface sensitive spectroscopies (XPS, UPS) and the electron microscopy (BF, CBED and EFTEM), we conclude that the dominant process is the displacement of Cd by Cu in the CdTe structure or Cu occupying

a vacant Cd site, as described in equation 4.2. A small amount of Cu may occupy interstitial sites as shown by a slight increase in the measured lattice parameter that was occasionally observed. Diffusion is greatly enhanced by interfacing CdTe with Cu_2Te or Cu_3Te_2(111). The quantity of diffused Cu is high enough from Cu_{poly}, Cu(111), Cu_2Te or Cu_3Te_2(111) to permit growth of discrete grains of Cu_2Te that have a tendency to segregate to the surface. The displaced Cd exists as patches of Cd metal that also has a propensity to segregate at the surface. There is a small amount of overlap between Cd and Cu, especially in the CdTe/Cu_{poly} system, where the crystallography suggests multiple grains layer on top of each other. The most dominant process occurring is ascribed to the formation of a segregated mixture of CdTe, Cu_2Te and metallic Cd:

$$x\ \mathrm{Cu} + \mathrm{CdTe} \rightarrow (\mathrm{CdTe})_{1-(x/2)} + (\mathrm{Cu_2Te})_{x/2} + \mathrm{Cd}_{x/2} \qquad (4.5)$$

4.2.5 Thermal Processing

Several of the deposition protocols require high substrate temperatures during deposition and subsequent chemical treatments [8]. To assess the effects of temperature on the diffusion of Cu into CdTe, 50 ML of CdTe was deposited at 300 K on Cu(111) and Cu_3Te_2 and then annealed in 25 K increments. Each anneal was held at temperature for 10 minutes. Data was collected as the sample was slowly cooling.

The evolution of the Cu $2p^{3/2}$, Te $3d^{5/2}$ and the Cd $3d^{5/5}$ XPS peaks were monitored at each stage. The intensities of the Cu $2p^{3/2}$, Te $3d^{5/2}$ and the Cd $3d^{5/5}$ XPS peaks used to calculate x, the stoichiometry parameter, in exactly the same manner as in section 4.2.4.1. The value of x, as defined in equation 4.5, is plotted in figure 4.28 as a function of temperature. There was no observed change in peak shape or position of any of the Cu $2p^{3/2}$, Te $3d^{5/2}$ and the Cd $3d^{5/2}$ XPS spectra in the region of 300 to 500 K, indicating no chemical changes. The spectral intensity of these peaks remained constant from 300 K to 400 K but from 400 K to 500 K there was a slow reduction of Cd signal and a gradual increase in the Cu signal, while the Te signal remained approximately constant, suggesting an increase in diffusion of Cu to the surface and/or increased Cd desorption. Between 500 K and 550 K the Cd signal decreased dramatically and reached zero at 550 K. At 550 K, the structure that remained on the surface was consistent with that of the Cu_2Te (30 ML Te/Cu_{poly}). We ascribe the reduction of the Cd signal to sublimation as Cd has a high vapour pressure. There are two processes contributing to Cd desorption from the CdTe film. Firstly, the increase in temperature will increase the rate of Cu diffusion into the CdTe film, displacing metallic Cd. Metallic Cd can then desorb at a lower temperature

than the Cd^{2+} present in CdTe. Secondly, the rate of metallic Cd desorption will also be increased with temperature. The experiment was repeated on the Cu_3Te_2 substrate with the same effect as Cu(111), albeit with a higher initial Cu concentration.

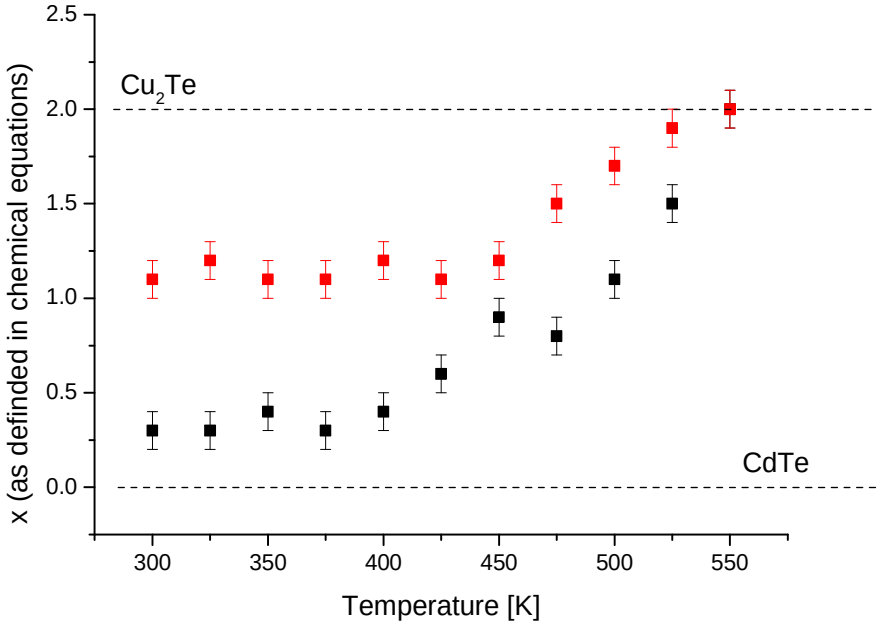

Figure 4.28. Variation in stoichiometry parameter, x, as a function of temperature. Calculated from the Cu $2p^{3/2}$, Te $3d^{5/2}$ and Cd $3d^{5/2}$ XPS spectra. The red squares are from 50 ML CdTe deposited on the $Cu_3Te_2(111)$ substrate at 300 K and then annealed. The black squares are from 50 ML CdTe deposited on the Cu(111) substrate at 300 K and then annealed.

To further probe the impact of temperature on the structure and composition of the CdTe film, we deposited 50 ML of CdTe onto Cu(111) and Cu_3Te_2, with the substrate temperature fixed at 423 K during deposition and allowed to cool to 300 K for analysis. 423 K was chosen as the upper maximum temperature studied so to limit Cd desorption. The Cu $2p^{3/2}$ XPS signal is shown in figure 4.29. Data collected at 300 K, is also shown as a blue line, to aid comparison. The same process used to estimate x for the 300 K data was used here and the values are listed in the third column of table 4.1. The calculated value of x clearly shows an increase in the surface Cu concentration with deposition temperature. It is interesting that the CdTe film deposited at 423 K is not the same, in terms of Cu content, as the film that is deposited at 300 K and annealed to 423 K. This implies that the deposition process is linked to the migration of Cu into the CdTe film and

that Cu from the substrate actively diffuses through the CdTe layer as it is being deposited.

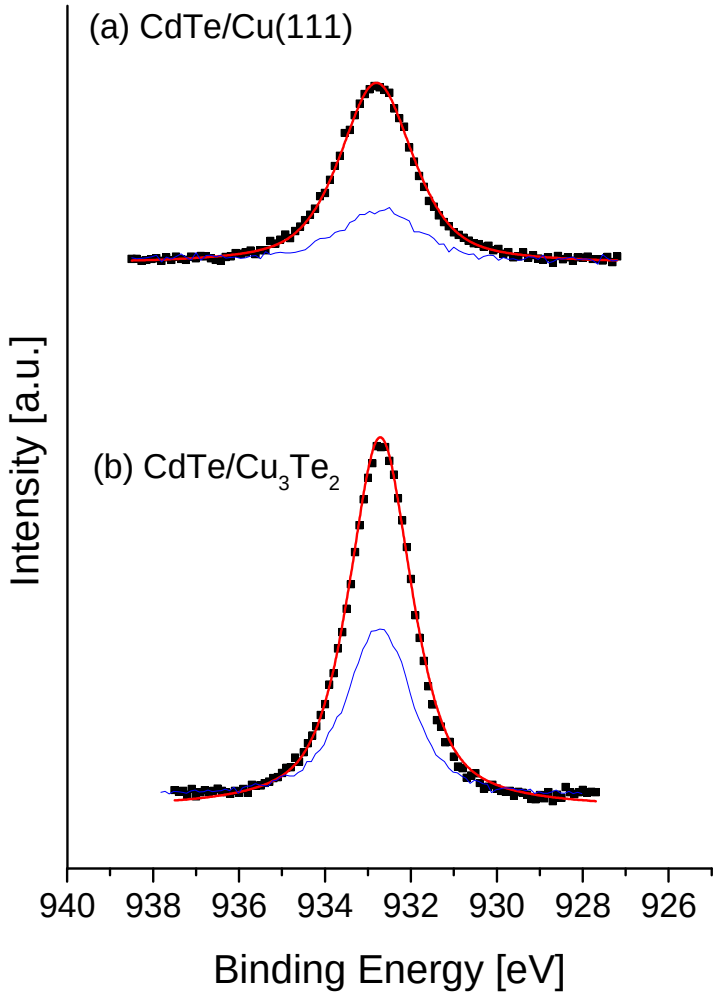

Figure 4.29. Cu $2p^{3/2}$ spectra recorded after depositing 50 ML CdTe on (a) Cu(111) or (b) Cu_3Te_2(111) at 423 K and 300 K. The black squares represent the Cu $2p^{3/2}$ XPS spectra from a deposition with the substrate temperature held at 423 K. The red line is the fitted spectra that corresponds well to the Cu^+ fit in Cu_2Te. The blue line is the spectra obtained at 300 K, which is added for comparison.

4.3 Summary

The results reported here improve our fundamental understanding of how Cu interacts with a CdTe film during the initial stages of deposition and subsequent thermal processing. Of the three processes described in the literature (equations 4.1 to 4.3), we have shown that phase segregation of Cu_2Te and CdTe is the dominant process occurring in the Cu:CdTe film. There is some evidence to suggest interstitial Cu but this appears only to be a minor contribution to the overall film structure.

It is interesting that Cu_xTe substrates, substantially increase the quantity of Cu that diffuses into the CdTe film. In terms of device performance, Cu_xTe back contacts need to provide the CdTe layer with the correct amount of Cu: enough Cu to form a pseudo ohmic contact but not too much as this can lead to device instability. Cu_xTe with $x > 1.4$ has been reported to be unstable and can release excess Cu into the CdTe layer which can segregate at the CdTe/CdS interface [9,10,63], reducing device lifetime. This chapter has provided a quantitative study of the extent of Cu diffusion into a CdTe film and the resulting composition, from various Cu_xTe and Cu surfaces, in the context of back contacts. It is suggested by Wu et al. [9] that a mixture of Cu_xTe with $x = 1.4$ and $x = 1$ gave the best device performance as only a small amount of Cu doping is required to form ohmic contacts between the back contact and the CdTe layer. Although we have studied different Cu_xTe substrates ($x = 1.5$ and 2), the data presented in this chapter highlight that precise control of the structure of the Cu_xTe back contact layer is paramount in achieving the desired level of Cu doping in the CdTe film, for optimal device performance.

Teeter [16,25] and Spath et al. [26] determined that Cu, when added in small amounts to the CdTe surface formed Cu_2Te, through the partial displacement of Cd by Cu as described in equation 4.2. In this chapter we probed not only the reaction between Cu and CdTe, but also the extent of Cu diffusion from different surfaces, in addition to the structure within the film and not just at the surface. It was noted that studies [16,25,26] were limited to surface composition only. The data presented in this chapter is in agreement with the reaction proposed by Teeter [16,25] and Spath et al. [26]: Cu_2Te is formed through the reaction of Cu with CdTe. We extended this work to the bulk of Cu:CdTe film using TEM. The BF and elemental specific EFTEM images provided a novel visualisation of the Cu:CdTe film. In particular, it showed that Cu_2Te was phase segregated throughout the film and not just at the surface. It also confirmed the presence of Cd metal on the surface. The HRTEM image, in figure 4.25, also showed that epitaxial Cu_2Te crystallites extended through the entire thickness of the 20 nm thick CdTe film. This

is important because it shows that pseudo ohmic contacts to the CdTe, formed through the doping or diffusion of Cu into the interfacial region of CdTe, exist because of the crystallites of Cu_2Te present. These have been previously described in the literature [10-15] but not visualised. In this study, we see that Cu induced desorption of Cd occurs in the region of 500 to 550 K (caused by the reduction of Cd^{2+} to Cd^0 by Cu) which is in good agreement to the TDMS data reported by Teeter which was in the range of 500 to 600 K [25]. There has also been an XRD study [10], looking at the deposition of Cu onto a Te enriched CdTe surface, which also observed Cu_2Te at 300 K. However, after annealing to higher temperatures other Cu-Te compounds were identifiable which we do not see here.

Singh et al. [64] studied the performance of a CdTe solar cell that has been fabricated from the vacuum deposition of CdTe on $Cu_{2-x}Te$, with the substrate held at 493 K during deposition. From our work, it is clear that 493 K is around the upper limit of substrate temperature during deposition to ensure Cd remains on the surface. The fact that Singh used a 5 µm (typical in devices) thick CdTe layer may explain why high temperature anneals and $CdCl_2$ treatment, did not have a detrimental effect on the CdTe layer, in terms of excess Cu diffusion. A depth profiling study carried out using secondary ion mass spectrometry (SIMS) [13] showed that concentration of Cu was 3 orders of magnitude greater in the first µm of CdTe immediately adjacent to the back contact.

In the discussion of the theory of XPS quantification, section 2.4.2.1, it was stated that for the model to quantify XPS spectra to be applicable (i.e. equation 2.15), there are several key assumptions that need to be valid. Firstly, the specimen is assumed to be homogeneous, in terms of depth. Clearly, in the case of CdTe on Cu it has been shown, for example in figure 4.24, that the film is spatially inhomogeneous. However, within the information depth of XPS, ~0.5-2 nm, the films are virtually homogenous in terms of depth. There are different grains distributed laterally across the specimen surface which contribute to the total XPS signal. Another assumption is that the surface is flat. However, it is clear that the Cu_{poly} surface is not atomically flat: it has a roughness amplitude of ~5 nm and period of ~100 nm, estimated from the TEM images. This will have an effect on the XPS signal as the roughness will affect the emission angles. Sophisticated Monte Carlo modelling of how roughness affects XPS has been published [65]. Using these values for roughness amplitude and period, it was estimated from equations in [65] that the photoelectron yield drops by only 1-3 %. Hence, the comparisons of the composition of the CdTe film on the Cu(111) and the Cu_{poly} substrate remain valid.

4.4 Conclusions

This chapter has focused on: (a) the growth modes of CdTe on Cu(111) and Te/Cu(111) (Cu_3Te_2) and (b) the diffusion of Cu into CdTe. We showed that the initial deposition of CdTe onto Cu(111) results in a Cu-Te SSA with Cd also present on the surface. However, we were unable to determine the atomic position of the Cd atoms. Further deposition of CdTe on Cu_3Te_2 and Cu(111) results in polycrystalline or three dimensional growth of CdTe. Cu diffusion is detectable above ~2 ML and forms phase segregated Cu_2Te crystallites in CdTe film.

The surface science experiments, described in sections 4.2.1 and 4.2.2, describe model systems on well defined Cu single crystals. There has been debate on how appropriate these model systems are in simulating real conditions (e.g. in catalysis [66]). In this chapter we demonstrated that from the single crystal Cu(111) and Cu_3Te_2 substrates are in good agreement with the studies on more realistic polycrystalline surfaces and therefore the learning from these experiments remain valid. For example, the measured stoichiometry in the Cu:CdTe film, with XPS, from the Cu(111) surface is in good agreement with the Cu_{poly} surface. Furthermore, both XPS and UPS measurements from the Cu:CdTe film on Cu single crystals were consistent with the formation of Cu_2Te grains in the Cu:CdTe film. The TEM data also demonstrated that the Cu:CdTe film grown on polycrystalline Cu substrates contained grains of both Cu_2Te and CdTe.

The combination of surface science techniques (XPS, UPS, LEED) and electron microscopy (TEM, EFTEM) gives a much more comprehensive picture of the system than using the two families of techniques in isolation. This chapter also demonstrates the limitations of each set of techniques. The most obvious advantage TEM has over surface science techniques is that surface science techniques, by definition, can only penetrate a few layers into surface and are therefore less appropriate for determining the structure of fairly thick films (10s of MLs). Surface science techniques are more appropriate in examining the layer by layer growth of ML scale films as described for Te/Cu(111) and Te/Cu(643) in chapters 3 and 5, respectively. Cross sectional TEM is clearly not limited to the surface. Surface science techniques used here (XPS, UPS and LEED) have the advantage over TEM in that TEM only provides *local* information - the surface science techniques give a overview of the entire surface. TEM data sets provide high resolution structural and chemical information, which was invaluable in determining the composition of the Cu:CdTe film. For instance, the EFTEM data give the spatial distribution of the elements within the CdTe film which was invaluable when deciding if Cu was segregated

from Cd. It would be impossible to do this unambiguously with XPS and UPS. Furthermore, the distinction between Cd^{2+} and Cd^0 is ambiguous in Cd 3d and 4d XPS, while the RGB EFTEM image clearly shows that Cd^{2+} (cyan) and Cd^0 (dark blue) coexist in the CdTe film. LEED was not an effective technique on determining the structure of this system. LEED patterns obtained for CdTe on the single crystal substrates could not distinguish between rough, polycrystalline or amorphous films. However, BF imaging clearly shows that the growth is both rough and polycrystalline and it is straightforward to measure the degree of roughness and grain size. The strength of LEED is in its precise determination of surface atomic structure from well defined single crystal surfaces and is more appropriate in the Te/Cu(111) and Te/Cu(643) systems, as described in chapter 3 and 5.

The data presented in this chapter illustrates that the choice of Cu_xTe is of crucial importance in obtaining the desired amount of Cu diffusion. We also showed that pseudo ohmic back contacts may be a result of the Cu_2Te units present in the CdTe film. Future work would entail assessing how the quantity of diffused Cu directly affects the device performance. For example, a series of CdTe films could be deposited onto a range of different Cu and Cu_xTe back contacts and studied as in this chapter. The next step would be to deposit layers of CdS and ITO to complete the photovoltaic module. The aim of this experiment would be to measure important device characteristics, such as conversion efficiency, stability and lifetime, and directly correlate this to the different properties of the back contacts, particular the quantity of diffused Cu in the CdTe film. Although the diffusion of Cu into the CdTe layer enhances the ohmic back contact, an excess of Cu has been known to cause detrimental effects on the performance of the CdTe photovoltaic by agglomerating at the CdTe-CdS interface [67]. Therefore, it is of high importance to optimally tune Cu diffusion for device performance, which this work would aim to do.

4.5 References

[1] R.W. Birkmire, B.E. McCandless, *Curr. Opin. Solid St. M*. **14** (2010) 139.

[2] A. Bosio, D. Menossi, S. Mazzamuto, N. Romeo, *Thin Solid Films* **519** (2011) 7522.

[3] X. Wu, *Sol. Energy* **77** (2004) 803.

[4] B.E. McCandless, K. D. Dobson, *Sol. Energy* **77** (2005) 839.

[5] J. Britt, C. Ferekides, *Appl. Phys. Lett.* **62** (1993) 2851.

[6] J.J. Loferski*, J. Appl. Phys*. **27** (1956) 777.

[7] N. Romeo, A. Bosio, V. Canevari, A. Podesta, *Sol. Energy* **77** (2004) 795.

[8] http://wwwold.ece.utep.edu/research/webedl/cdte/

[9] M.M. Aliyu, M.A. Islam, N.R. Hamzah, M.R. Karim, M.A. Matin, K. Sopian, N. Amin, *Int. J. Photoenergy* (2012) 351381.

[10] X. Wu, J. Zhou, A. Duda, Y. Yan, G. Teeter, S. Asher, W.K. Metzger, S. Demtsu, S-H. Wei, R. Noufi*, Thin Solid Films* **515** (2007) 5798.

[11] S. Erra, C. Shivakumar, H. Zhao, K. Barri, D.L. Morel, C.S. Ferekides, *Thin Solid Films* **515** (2007) 5833.

[12] F. Debbagh, E.L. Ameziane, M. Azizan, M. Brunel, T.T.A. Nguyen, *Mater. Sci. Eng,* **B38** (1996) 223.

[13] H.R. Moutinho, R.G. Dhere, C.S. Jiang, T. Gessert, A. Duda, M. Young, W.K. Metzger, M.M. Al-Jassim, *J. Vac. Sci. Technol. B*. **25** (2007) 361.

[14] F. de Moure-Flores, J.G. Quinones-Galvan, A. Guillen-Cervantes, J. Santoyo-Salazar, A. Hernandez-Hernandez, M. de la L. Olvera, M. Zapata-Torres, M. Melendez-Lira, *AIP Advances* **2** (2012) 022131.

[15] S. Vatavu, H. Zhao, I. Caraman, P. Gasin, C. Ferekides, *Thin Solid Films* **517** (2009) 2195.

[16] G. Teeter, *J. Appl. Phys.* **102** (2007) 034504.

[17] H. B. Michaelson, *CRC Handbook of Chemistry and Physics*, 64th ed., CRC Press, Inc., Boca Raton, 1983.

[18] S.S. Hegedus, B.E. McCandless, *Sol Energ. Mat Sol. C.***88** (2005) 75.

[19] D. Grecu, A.D. Compann*, Appl. Phys. Lett.* **75** (1999) 361.

[20] T. Dzhafarova, S. Yesilkayaa, N. Y. Canlia, and M. Caliskan, *Sol. Energy Mater. Sol. Cells* **85** (2005) 371.

[21] T. D. Dzhafarov, S. S. Yesilkaya, *Cryst. Res. Technol.* **42** (2007) 834.

[22] H. Wolfa, F. Wagnera, T. Wicherta, ISOLDE collaboration, *Physica B* **340** (2003) 275.

[23] J.P. Laurenti, G. Bastide, M. Rouzeyre, R. Triboulet, *Sol. Stat. Comms*. **67** (1988)

1127.

[24] G. Zoth, F.G. Riedel, W. Schroter, *Phys. Status Solidi (b)* **172** (1992) 187.

[25] G. Teeter, *J. Chem. Phys.* **123** (2005) 184713.

[26] B. Späth, K. Lakus-Wollny, J. Fritsche, C.S. Ferekides, A. Klein, W. Jaegermann, *Thin Solid Films* **515** (2007) 6172.

[27] S.D. Feldman, R.T. Collins, V. Kaydanov, T.R. Ohno, *Appl. Phys. Lett*. **85** (2004) 1529.

[28] S. Jiménez-Sandovala, S. López-López, B.S. Chaoc, M. Meléndez-Lira, *Thin Solid Films* **342** (1999) 1.

[29] A.B. Christie, I. Sutherland, J.M. Wallis, *Surf. Sci*. **135** (1983) 225.

[29] M. Bennett, A.A. Cafolla, J.W. Cairns, C.J. Dunscombe, R.H. Williams, *Surf. Sci*. **360** (1996) 187.

[30] Y. Xin, N.D. Browning, S. Rujirawat, S. Sivananthan, Y.P. Chen, P.D. Nellist, S.J. Pennycook, *J. Appl. Phys*. **84** (1998) 4292.

[31] H. Nishino, Y. Nishijima, *J. Cryst. Growth* **167** (1996) 488.

[32] S. Neretina, R.A. Hughes, N.V. Sochinskii, M. Weber, K.G. Lynn, J. Wojcik, G.N. Pearson, J.S. Preston, P. Mascher, *J. Vac. Sci. Technol. A* **24** (2006) 606.

[33] T. van Gemmeren, R.L. Johnson, R. Sporken, P.A. Thiry, *Surf. Sci.* **377** (1997) 882.

[34] J.J. Dubowski, D. F. Williams, P. B. Sewell, P. Norman, *Appl. Phys. Lett*. **46** (1985) 1081.

[35] S. Sone, M. Ekawa, K. Yasuda, Y. Sugiura, M. Sail, A. Tanaka, *Appl. Phys. Lett*. **56** (1990) 539.

[36] J.L. Reno, M.J. Carr, P.L. Gourley, *J. Appl. Phys*. **67** (1990) 4114.

[37] H. Hochst, D.W. Niles, I. Hernandez-Calderon, *Phys. Rev. B* **40** (1989) 8370.

[38] L. Zhang, D. Wett, M. Nagel, H. Peisert, R. Szargan, T. Chasse, *J. Electron Spectrosc. Relat. Phenom.* **154** (2007) 48.

[39] C. Janowitz, R. Manzke, M. Skibowski, B.A. Orlowski, *Surf. Sci.* **247** (1991) 100.

[40] H.S. Chauhan, L. Ilver, P.O. Nilsson, J. Kanski, K. Karlsson, *Phys. Rev. B* **48** (1993) 4729.

[42] J.J. Yeh, I. Lindau, *At. Data Nucl. Data Tables* **32** (1985) 1.

[43] J.J. Yeh*, Atomic Calculation of Photoionisation Cross-Sections and Asymmetry Parameters*, Gordon and Breach Science Publishers, Langhorne, Pe (USA), 1993.

[44] S. W. Gaarenstroom, N. Winograd*, J. Chem. Phys*. **67** (1977) 3500.

[45] A.B. Christie, I. Sutherland, J.M. Wallis, *Surf. Sci.* **135** (1983) 225.

[46] A. Ricco, H. S. White, M. S. Wrighton, *J. Vac. Sci. Technol. A* **2** (1984) 910.

[47] V. Di Castro, G. Polzonetti, G. Contini, *Surf. Sci.* **251** (1991) 814.

[48] S. Ciampi, V. Di Castro, C. Furlani and G. Polzonetti, *Appl. Surf. Sci*. **60** (1992)

375.

[49] *CRC Handbook of Chemistry and Physics,* 89th ed. CRC Press: Boca Raton, FL, 2008-2009.

[50] M. Polak, *J. Electron Spectrosc. Relat. Phenom*. **28** (1982) 171.

[51] W. Danaher, L. Lyons, M. Marychurch, G. Morris, *Appl. Surf. Sci.* **27** (1986) 338.

[52] D. Westphal, A. Goldmann, *Surf. Sci.* **131** (1983) 113.

[53] R. Pfandzelter, T. Igel, H. Winter, *Surf. Sci.* **389** (1997) 317.

[54] A.J. Francis, A.J. Koritnik, A. Gellman, P.A. Salvador, *Surf. Sci*. **601** (2007) 1930.

[55] H.H. Woodbury, M. Aven*, J. App. Phys*. **39** (1968) 5485.

[56] H. Mann, G. Linker, O. Meyer, *Sol. Stat. Comms*. **11** (1972) 475.

[57] A.L.N. Stevels, G.A. Wiegers, *Recueil des Travaux Chimiques des Pays-Bas* **90** (1971) 352.

[58] P.J. Thomas, P.A. Midgley, *Top. Catal.* **21** (2002) 109.

[59] http://www.gatan.com/

[60] H.N. Nowotny, *Z. Metallk*. **37** (1946) 409.

[61] M. Rabadanov, I. Verin, Y. M. Ivanov, I. Simonov, *Kristallografiya* **46** (2001) 703.

[62] I. Dima, D. Borsan, *Phys. Stat. Sol*. **23** (1967) K133.

[63] A. Bosio, A. Romeo, D. Menossi, S. Mazzamuto, N. Romeo, *Cryst. Res. Technol*. **46** (2011) 857.

[64] V.P. Singh, J.C. McClure, *Sol. Energy Mater. Sol. Cells* **76** (2003) 369.

[65] L.S. De Bernardez, J. Ferrón, E.C. Goldberg, R.H. Buitrago, *Surf. Sci.* **139** (1984) 541.

[66] D.A. King, D.P. Woodruff ,*The Chemical Physics of Solid Surfaces and Heterogeneous Catalysis*, vol 4, Elsevier, Amsterdam, 1982.

[67] Y. Yan, K. Jones, J. Zhou, X. Wu, M. Al-Jassim, *Mater. Res. Soc. Symp. Proc.* **1012** (2007) 241.

5. Chiral Alloying on an Intrinsically Chiral Copper Surface

5.1 Introduction

In chapter 3, it was shown that Te and Cu(111) form an unusual, Cu_3Te_2-like alloy phase, driven by the favourable lattice match between the Cu(111) substrate and the growing Cu_3Te_2 alloy. In this chapter, the study of the interaction of Te with a Cu surface is extended to a chiral Cu surface, Cu(643). The data presented here shows that faceting of the surface occurs and two unique Cu-Te alloy phases develop, a direct consequence of the structure of the Cu(643) substrate.

In general, chirality is the geometric property that an object cannot be superimposed on its mirror image. The two different forms of the object are called enantiomers, usually labelled (R), *rectus* and (S), *sinister*. Chirality is ubiquitous in nature at microscopic and macroscopic length scales. For example, human hands are chiral, as are amino acids which exist naturally as only a single enantiomer [1]. In terms of chemistry, knowledge of enantiospecific synthesis has been developing for decades from the desire to produce molecules of a single enantiomer [1,2]. In this chapter, we wish to talk not about the chirality of molecules but the chirality of surfaces. FCC, HCP or BCC lattices are achiral in the bulk; however, certain surface terminations can result in a chiral surface layer being exposed. For a FCC lattice, a surface termination given by the miller indices [hkl] will be chiral if $h \neq k \neq l \neq 0$ [3]. A consequence of this rule is that chiral surfaces will have a high miller index plane and thus the surface will be stepped [4,5]. The opposite enantiomer of the surface will be the surface defined by the negative miller indices.

5.1.1 The (643) Surface

The (643) termination of a generic FCC lattice is shown in figure 5.1. The surface has three main features: (111) terraces, (110) kinks and (100) steps. The chirality of this surface stems from the orientation of kink sites. Figure 5.2 shows the ideal (643) surface at high magnification. McFadden et al. [6] generalised the standard Cahn-Ingold-Prelog priority rules for naming stereoisomers to surface structures. They proposed that the handedness of a surface should go in order of priority, analogous to the Cahn-Ingold-Prelog rules for molecules, described pictorially in figure 5.2. The order of priority is (100) steps → (110) kinks → (111) terraces. If this sequence is clockwise, then the surface is assigned as the R enantiomer and if it is counter clockwise then the surface is assigned as the S enantiomer

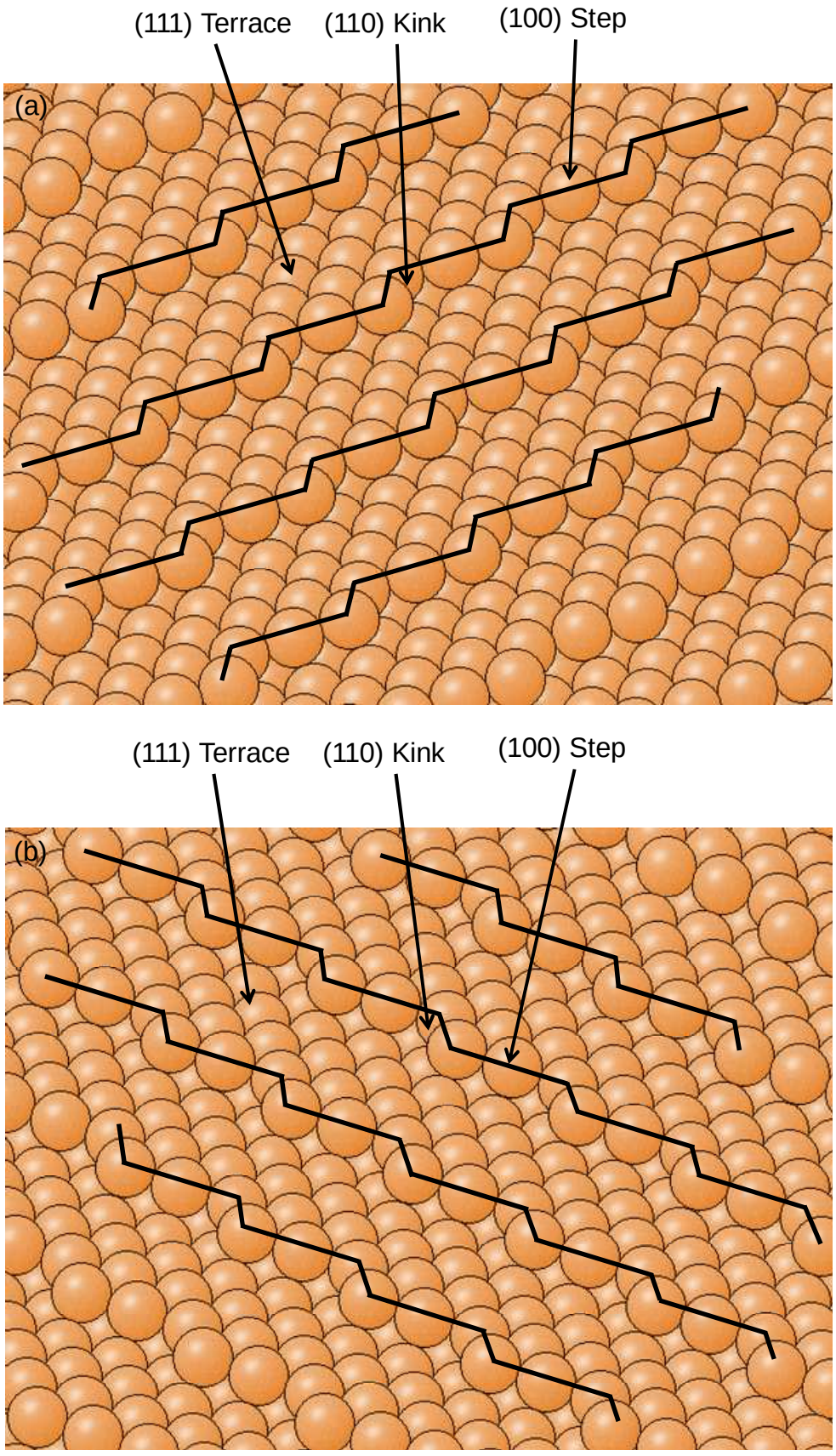

Figure 5.1. The ideal structure of (a) (643) and (b) ($6\bar{4}\bar{3}$). The black lines are added to highlight the step edges.

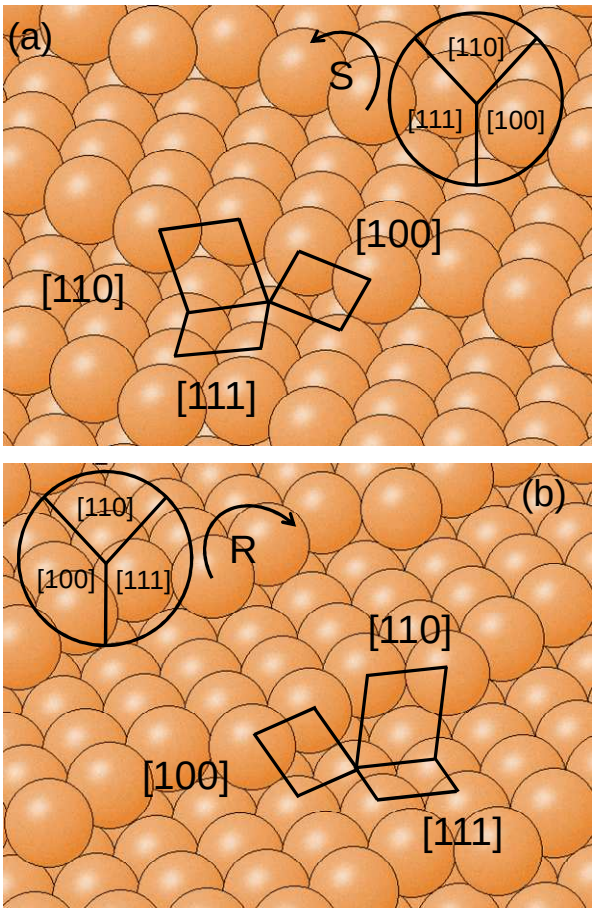

Figure 5.2. The ideal (a) $(643)^S$ and (b) $(643)^R$ surfaces. The solid black lines show the unit cells of the micro facets. The step site is [100], the kink site is [110] and the terrace is [111]. The handedness of the surface is defined using the Cahn-Ingold-Prelog rules, as outlined by McFadden et al. [6]. Diagram adapted from reference [7]. Priority is in order of [100] steps [110] kinks and [111] terraces.

Figure 5.2 (a) shows the (643) surface as the steps → kinks → terraces run clockwise and hence the (643) surface is relabelled $(643)^S$. Figure 5.2 (b) shows $(\overline{643})$: steps → kinks → terraces run clockwise and hence the $(\overline{643})$ surface is relabelled $(643)^R$.

More precisely, the geometry of the (643) surface is a miscut of the (111) plane at an angle of φ ~16.1° along the $[\bar{1}3\bar{2}]$ direction [8]. Figure 5.3 shows the (643) surface viewed along the $[\bar{1}3\bar{2}]$ direction with the vectors normal to the (111) and (643) planes shown to be misaligned by φ, the miscut angle (~16.1°). Chiral surfaces are always vicinal and hence have a stepped structure. The average step separation (i.e. the terrace width), d, can be calculated from the ideal surface model [9]:

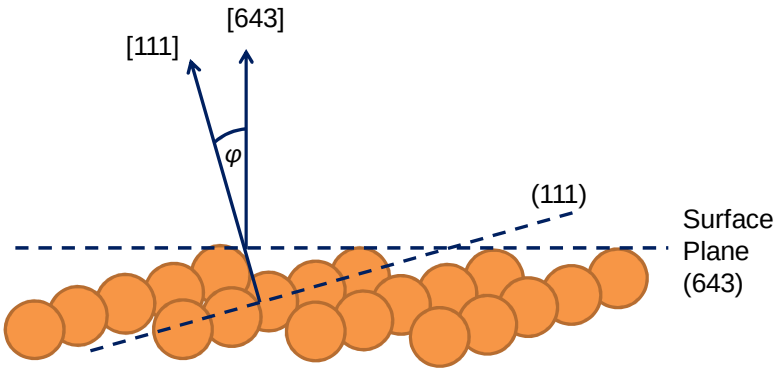

Figure 5.3. The (643) surface viewed side on. The angle between the miscut plane (643) and the (111) is shown as φ which is in the case of the (643) surface ~16.1°.

$$d = \frac{h}{\sin \varphi}, \tag{5.1}$$

where,

$$h = \frac{a_0}{\sqrt{3}}. \tag{5.2}$$

h is the step height, which is derived from the lattice parameter, a_0. For Cu, a_0 = 0.360 nm and hence h = 0.208 nm. φ is the miscut angle, which for Cu(643), is 16.1°. This gives an average value for d of 0.750 nm, which is ~3 Cu atoms, in agreement with the pictorial representation of the surface in figure 5.1. The experimentally observed LEED pattern can also be used to measure the Cu-Cu separation in the terrace and the step separation, d, which was measured to be 0.73 ± 0.01 nm. Figure 5.4 shows the LEED pattern obtained from a clean Cu(643) surface. The LEED pattern comprises of the pattern of the (111) terrace, shown as a dashed white line in figure 5.4. Each terrace spot is split into two distinct spots (dashed red line on figure 5.4), the separation of which is defined by the periodicity of the stepped superstructure. The angle at which the spot is split, with respect to the (111) lattice indicates the orientation of the miscut. The angle of the split spot, was measured on figure 5.4 to be 15 ± 2°, in good agreement with the ideal model of the $(643)^R$ surface, ~16.1°. Indeed, the first study of a chiral surface from an achiral bulk metal, by McFadden et al. [6], used the orientation of split spots in the LEED to identify that the Ag(643) and Ag($\overline{643}$) surfaces were non-superimposable mirror images and were therefore chiral.

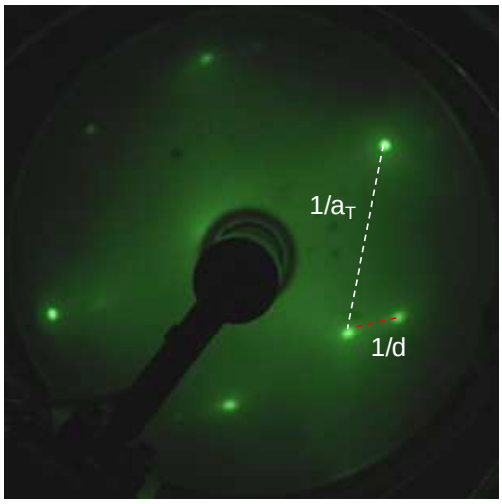

Figure 5.4. LEED pattern obtained from clean Cu(643)^R at a beam energy of 138 eV. The white dashed line indicates part of the surface unit cell. The red line shows that the (0,1) spot has been split by a length inversely proportional to the step separation.

The discussion of the (643) surface will now turn to experimental observations of the Cu(643) surface and related surfaces, e.g. Cu(531). It has been shown that the real Cu(643) surface has significant deviations from its ideal structure. This is because the surface Cu atoms are under co-ordinated and thus are quite mobile. Through DFT calculations [10], Monte Carlo simulations [11] and STM [12], it has been shown that the surface undergoes thermal roughening. Figure 5.5 (b) shows the results of a typical roughening simulation [11], which has been corroborated with STM [12]. The result of thermal roughening is a non uniform distribution of steps and kinks and a larger proportion of (111) terraces. However, simulations [10,11] show that the surface retains its overall chirality, as the kinks are still of a single handedness. In contrast to Cu(643), the LEED IV curves extracted from the clean Cu(531) surface could be matched to DFT calculations that assumed that the surface was non-roughened [13]. The reason for this difference may be the fact that Cu(643) is a more open surface than Cu(531) and hence the surface Cu atoms will lower coordination. This will result in a higher surface atom mobility and a larger degree of surface roughening. However, a more recent study of the Cu(531) surface with STM [14] showed that there was a degree of thermal roughening, suggesting this phenomena was common in high miller index Cu surfaces. Although this chapter does not explicitly explore the roughening of Cu(643), it is still important to be aware of this fact when describing the structure of Te/Cu(643)^R.

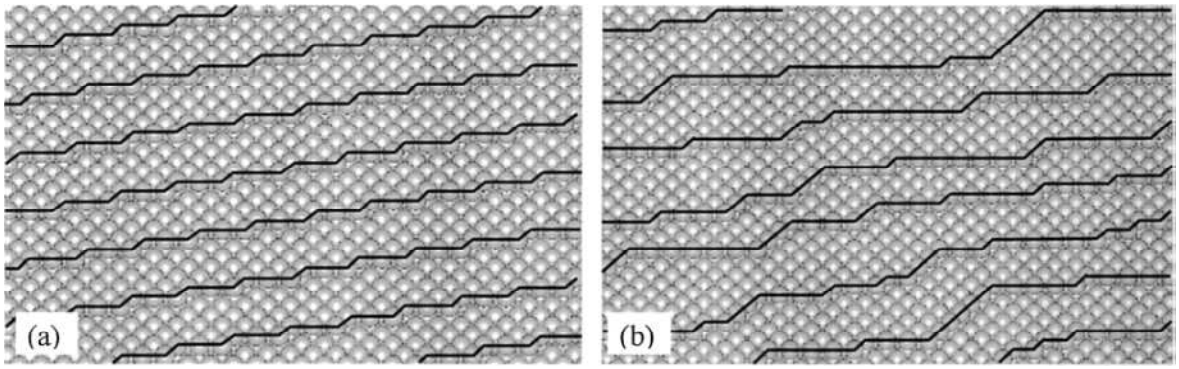

Figure 5.5. Schematic of (a) the ideal (643) surface and (b) the (643) surface that has undergone thermal roughening. Black lines highlight the step edges. The figure has been extracted from reference [11].

5.1.2 Atomic Growth on Vicinal Surfaces

As this chapter describes a study of the growth of adsorbate atoms on a vicinal metal surface, it is relevant to summarise the previous work on this aspect of thin film growth. There are several vicinal systems that have been extensively characterised including Ag on vicinal Cu [8,15-18], NaCl on Cu [19,20] and Ni on Cu [20]. Bachmann et al. [8,15-17] deposited sub-monolayer coverages of Ag on Cu(223) and observed that Ag induced a periodic faceting of the Cu surface into a "hill and valley" type structure, similar to what will be described in this section for Te/Cu(643). The surface consisted of Ag covered facets, which grew with increasing Ag exposure at the expense of clean Cu areas, with a preference of the Ag adatoms to grow on (112) orientated facets. The authors proposed that the driving force behind this observation was the good lattice match (of 0.12 %) between fitting 5 closed packed Ag rows and 2 terraces of Cu(112). A further study [18] of Ag deposition on vicinal Cu surfaces was performed on Cu(211) and Cu(433) with grazing incidence X-ray diffraction. The data showed that Ag forms a c(2x10) surface reconstruction on Cu(211) for 0.3 ML of Ag, with no faceting of the Cu(211) surface observed. On the Cu(433) surface, 0.6 ML of Ag was observed to cause reconstruction of the surface to the (533) facet. The deposition of Ni on Cu(211) has been studied with LEED [20]. The data showed that Ni grew commensurately with the underlying Cu(211) surface analogous to Ag on Cu(211) up to ~3 ML. NaCl was deposited on Cu(532) and also studied with LEED [20]. This induced the reconstruction of the facets on the surface to (111), (311) and (531) orientations. The microscopic orientation of NaCl was in the close packed (100) direction. These studies clearly show that the deposition of metallic adatoms onto high miller index surfaces have the tendency to cause the surface to facet towards

more close packed orientations (i.e. in FCC lattices towards the (111) and (100) planes), while maintaining the macroscopic surface normal.

The study of metallic deposition onto vicinal surfaces that are also chiral is a much less studied topic. Indeed, to our knowledge there are only two chiral substrates, $SrTiO_3$(621) and Pt(321) that have been used to template metal overlayer growth. On the $SrTiO_3$(621) surface, a series of studies were performed [21-23] concerning the growth of overlayers of Pt and Cu, via pulsed laser deposition. It was deduced from LEED patterns that Pt and Cu grew pseudomorphically with thicknesses up to several atomic layers. Hazzazi et al. [24] studied the deposition of Au, Ag and Bi on Pt(321) by monitoring voltammetric profiles. They found that Bi and Au selectively populate the chiral kink sites of the surface with no occupancy of the (111) terraces before the saturation of the kink sites is complete. In contrast, Ag shows a preference to occupy the kink sites, however, some (111) sites are occupied before all the kink sites are filled. This implies that the kink sites may act as nucleation sites for metal growth.

There have been other theoretical and experimental studies into the role of the kink site in overlayer growth on Cu(643). Nucleation has been demonstrated to favour kink sites in several different studies both with calculations and experiment. Using DFT calculations, Kamakoti et al. [25] showed that the adsorption energy of iodine on thermally roughened Cu(643) was maximised at kinks sites because it maximised its co-ordination to Cu. The role of the kink sites were confirmed in a further experimental study by Kamakoti et al. [25] using TPD. This study showed that pre-adsorbed iodine inhibited the population of the kink site by adsorbed R-3-methylcyclohexanone, indicating that iodine preferentially occupied the kink site. The rate of Br diffusion across different Cu surfaces was analysed by Rampulla et al. [26] with DFT calculations. They showed that the rate of diffusion of Br was many orders of magnitude less on a kinked or stepped surface than on a flat Cu surface. Indeed, of all the surfaces studied, the Cu(643) surface was found to inhibit the diffusion of Br most effectively. This implies that the kink site may be an effective nucleation site. These studies indicate that adatoms have a tendency to preferentially occupy kink sites on the Cu(643) surface.

5.2 Results

The experimental data for the deposition of Te on Cu(643)^R will now be presented. The LEED and XPS data show that there are two ordered Cu-Te phases and a disordered phase for thicker Te films. The STM data are tentatively interpreted in terms of an atomic

model, faceting of the surface and step bunching.

5.2.1 Low Coverage Alloy (0.18 < θ_{Te}< 0.45 ML)

The Cu single crystal obtained for this study was cut to reveal the ($\overline{643}$) facet. The handedness of the surface was determined by LEED, figure 5.4, by assessing the direction of the split spots as in Ag(643) [6], which determined it to be Cu($\overline{643}$). Hence the substrate was relabelled Cu(643)^{R} in the same convention outlined by McFadden et al. [6]. Te was deposited from the homemade thermal evaporator that was described in section 2.2. The evaporator as held at 610 K during deposition which led to an approximate growth rate for Te of 0.5 MLmin^{-1}. The structure of Te/Cu(643)^{R} alloy was initially studied with LEED, XPS and UPS at the University of Glasgow. The STM data presented in this chapter were collected at the University of Liverpool. The coverage of each deposition was calculated from the intensity of the Cu 2p$^{3/2}$ and Te 3d$^{5/2}$ peaks in the appropriate XPS spectra, using equations 2.11, 2.13 and 2.14. In all cases, Te coverage is quoted with an error of ± 0.05 ML. As in chapter 3, 1 ML refers to the number of atoms in the ideal Cu(111) plane. The stoichiometry of the film was measured using integrated intensities of Cu 2p$^{3/2}$ and Te 3d$^{5/2}$ XPS peaks, equation 2.15 and sensitivity factors derived in section 2.4.2.1.

Figure 5.6 shows the LEED patterns obtained for 0, 0.28, 0.53, 0.85, 1.5 and 5 ML of Te/Cu(643)^{R}. These surfaces have been prepared by depositing the appropriate coverage of Te on Cu(643)^{R} at 300 K. Each surface was then annealed to 773 K for 10 minutes and allowed to cool slowly back to 300 K where the LEED patterns were recorded. It was necessary to anneal to 773 K because the LEED patterns after depositing at 300 K were diffuse, implying a significant amount of disorder. Significantly sharper LEED patterns, shown in figure 5.7, were observed after annealing then cooling with liquid nitrogen to 110 K. Figures 5.8 and 5.9 show LEED patterns of 0.28 ML and 0.85 ML Te coverages, respectively, at several different beam energies to illustrate how the LEED patterns were interpreted. This aspect will be discussed in detail when the description of each LEED pattern is presented. Cu 2p$^{3/2}$ and Te 3d$^{5/2}$ XPS spectra were collected immediately after deposition at 300 K, after annealing each surface to 773 K and cooling to 300 K and 110 K. There was no change in peak shape or intensity of each XPS spectrum after annealing, implying that annealing was inducing surface ordering, rather than chemical changes. Therefore, only one set of Te 3d$^{5/2}$ and Cu 2p$^{3/2}$ XPS spectra are presented in figures 5.10 and 5.11, respectively. UPS spectra were also acquired and are shown in figure 5.12. STM data were collected, from θ_{Te} = 0.28 ML and θ_{Te} = 0.85 ML coverages that had been

annealed to 773 K. STM data were acquired at room temperature and is displayed in figures 5.13-5.16.

The first ordered LEED pattern, shown in the upper right panel of figure 5.6, at 300 K and in figure 5.7 (a) at 110 K, was observed for Te coverage in the range of 0.18 to 0.45 ML and will be referred to as structure 1. The sharpest pattern was observed for 0.28 ML. A progressive degradation in quality was observed above 0.28 ML until 0.45 ML, where extra spots started to emerge in the LEED pattern. The unit cell of the 0.28 ML surface was determined using dynamical LEED (i.e. monitoring the LEED pattern as the incident beam energy was varied). Figure 5.8 shows the 0.28 ML pattern at a series of different beam energies. The red circle highlights two spots that pass through each other, implying that these spots are from separate domains on the surface. To identify the surface unit cell(s), a series of lines passing through LEED spots were applied to the LEED pattern. Figure 5.7 (a) shows the LEED pattern collected at a beam energy of 140 eV. In figure 5.7 (b) a red grid is added to the native LEED pattern and shows that there is a repeating unit on the surface. However, the red grid does not account for all of the observed spots and thus another grid, shown as blue lines in figure 5.7 (c) is required. Figure 5.7 (d) shows the unit mesh for both the red and blue meshes and when rotated, these unit cells form mirror images of each other and hence the surface can be described as comprising of both enantiomers of a chiral surface unit cell. Indeed, the surface unit is an oblique lattice with parameters of a_1 = 0.51 ± 0.01 nm, b_1= 0 71 ± 0.01 nm and an acute internal angle, α_1= 57 ± 3°, as shown on figure 5.7 (d). It is intere sting to note that the red and blue grids are rotated by 60 ± 2° which is likely to be a resu lt of the hexagonal symmetry of the (111) terrace.

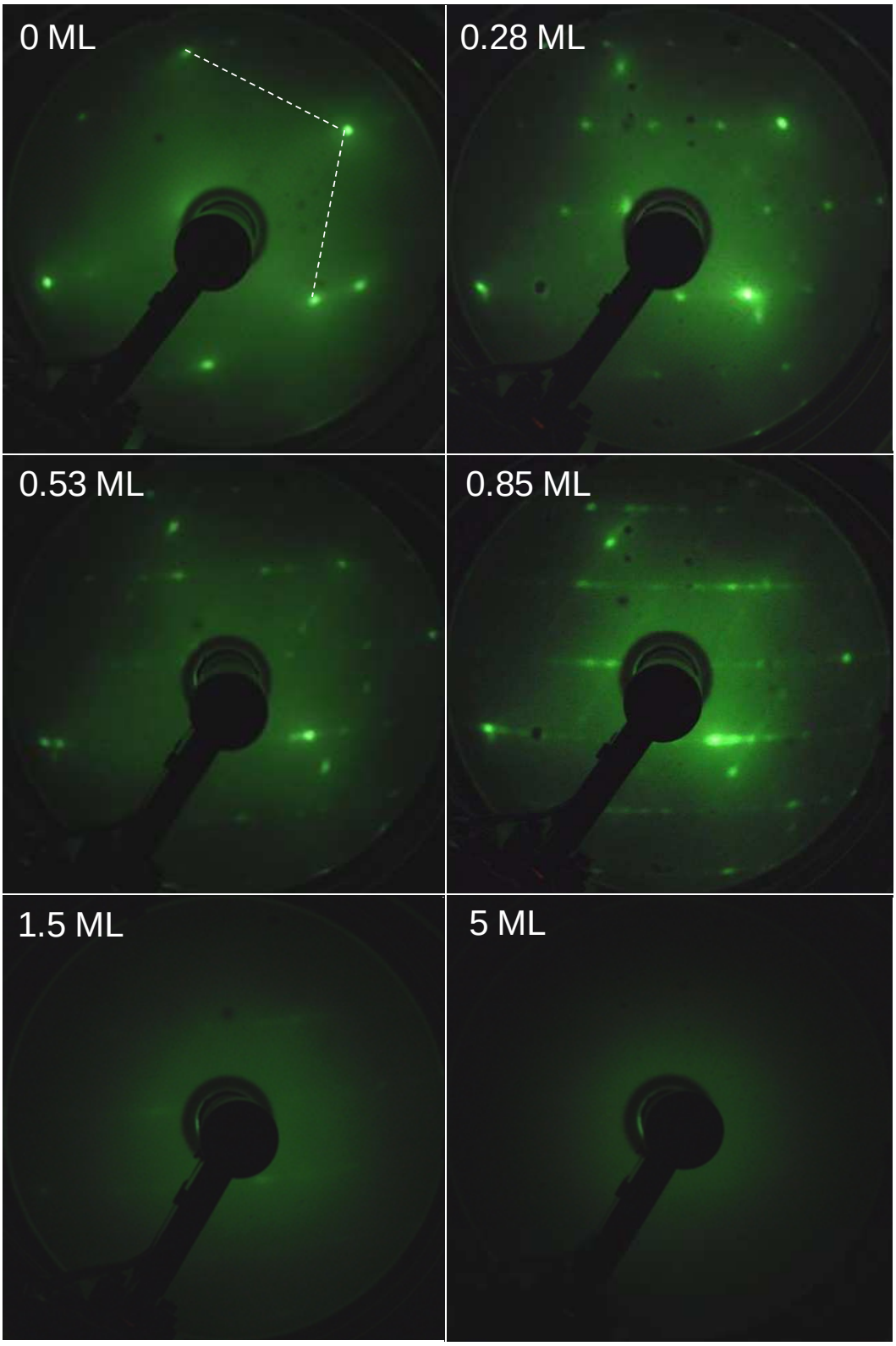

Figure 5.6. LEED patterns obtained after depositing Te on Cu(643)^{R} at 300 K then annealing to 773 K for 10 minutes and then allowing to cool back to 300 K for LEED acquisition. The dashed white line shows the partial Cu(643)^{R} unit cell. The beam energy is 138 eV.

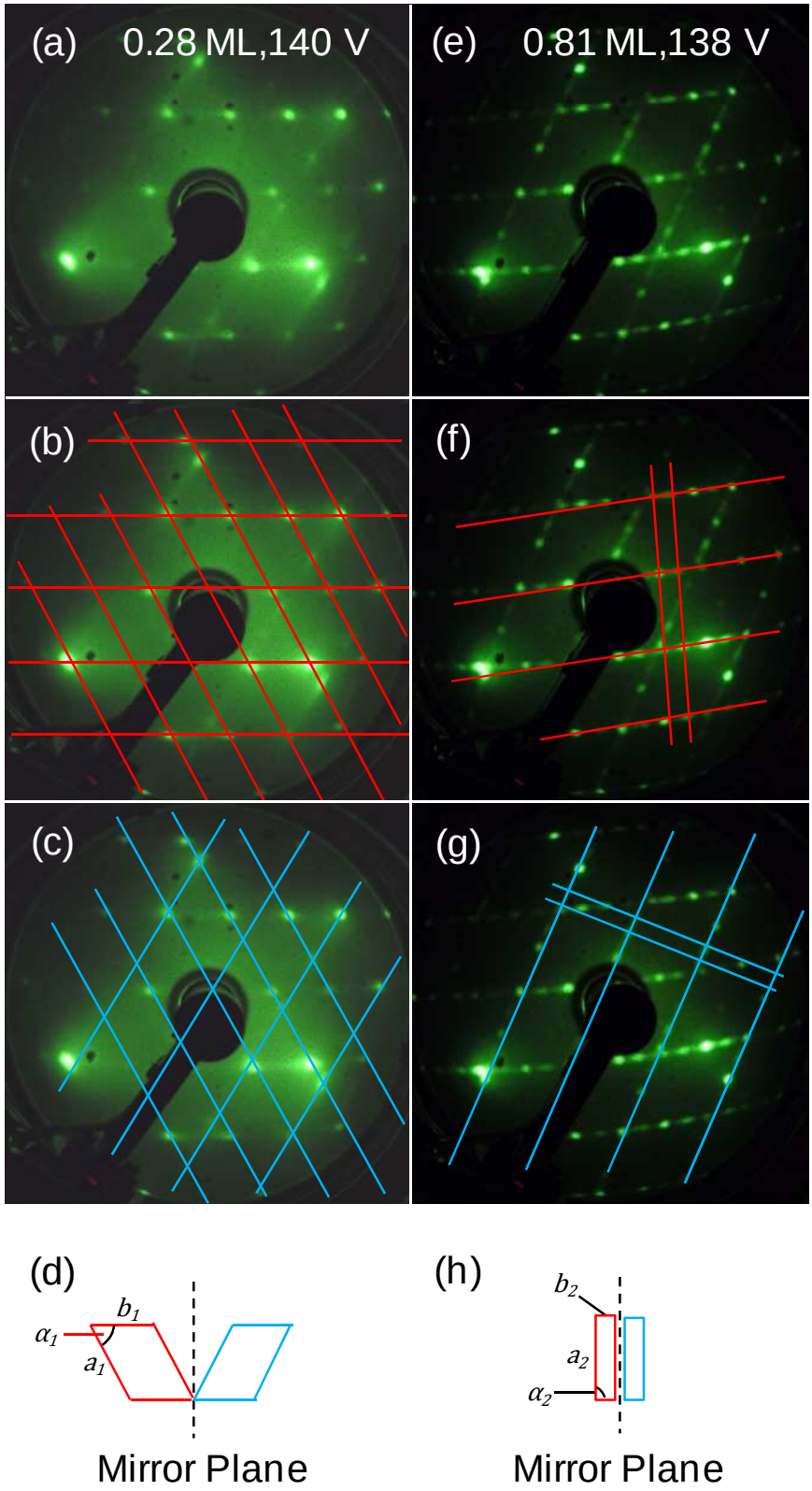

Figure 5.7. (a-c) LEED pattern from 0.28 ML of Te/Cu(643)^R. (b) and (c) have overlaid red and blue lines to indicate the surface unit cell. (d) is a comparison of the unit cell of the red and blue lines. (e-g) LEED pattern from 0.85 ML of Te/Cu(643)^R. (f) and (g) have overlaid red and blue lines to indicate the surface unit cell. (h) is a comparison of the unit cell of the red and blue lines.

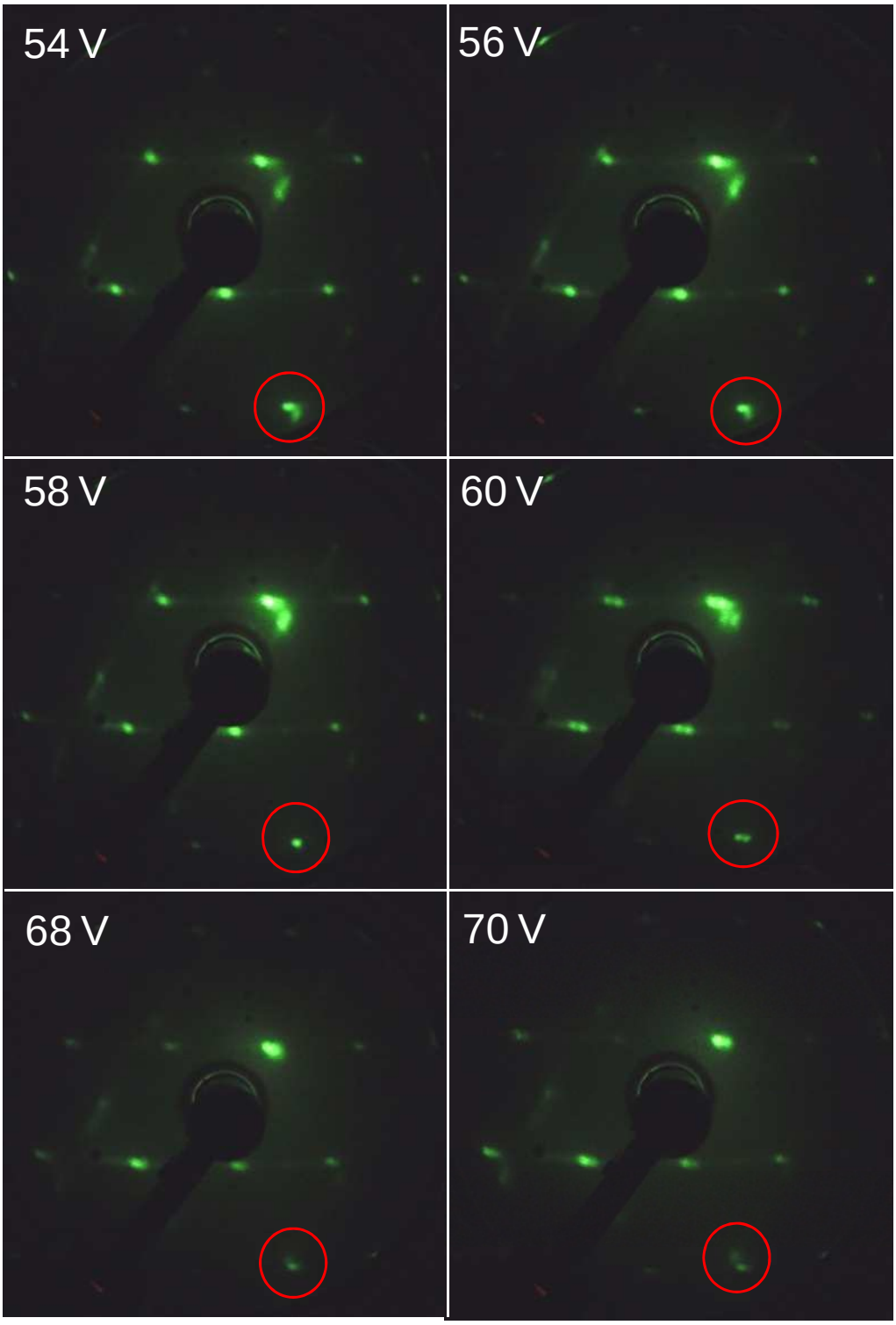

Figure 5.8. LEED patterns from 0.28 ML Te/Cu(643)^{R} at 110 K for different beam energies. The red circle highlights how some LEED spots pass through each other as the incident beam energy is varied. At 58 V, the highlighted LEED spots are on top of each other.

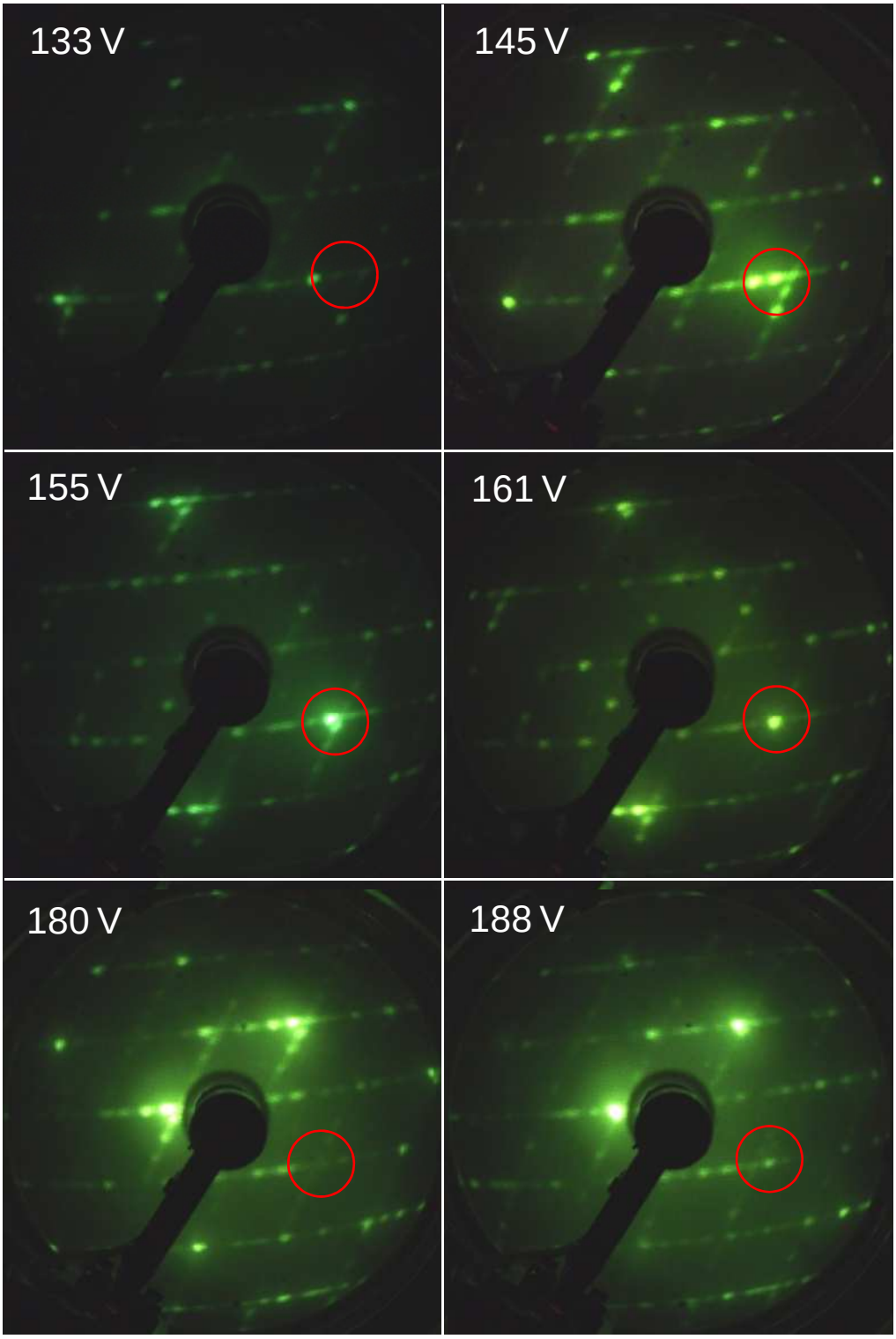

Figure 5.9. LEED patterns from 0.85 ML Te/Cu(643)^{R} at 110 K for different beam energies. The red circle highlights how some LEED spots pass through each other as the incident beam energy is varied. At 161 V, the highlighted LEED spots are on top of each other.

In contrast to Te/Cu(111) described in chapter 3, the Te $3d^{5/2}$ XPS spectra, collected immediately after LEED, and shown in figure 5.10, did not indicate surface substitutional alloying. Each Te $3d^{5/2}$ and Cu $2p^{3/2}$ spectrum was fitted to the sum of a Gaussian and DS function and the fitted binding energies were in agreement with previous studies of copper and tellurium systems [27-30]. The width and asymmetry of each peak was fixed to that obtained from an elemental Cu or Te film. The 0.28 ML Te/Cu(643)^{R} film was well fitted with a single Gaussian-DS function, with binding energy matching that of *bulk* Te^{2-} (572.7 eV). The fitting parameters are displayed in table 5.1. For comparison, the SSA described in chapter 3 for Te/Cu(111) has a binding energy of 572.3 eV. The data suggest that the Te atoms are being incorporated into a bulk-like alloy immediately upon deposition rather than occupying surface sites, as was observed for Te/Cu(111). Vicinal surfaces have been previously shown to facilitate adatom diffusion into the bulk as the under coordinated step atoms provide a low energy pathway for adatoms to enter the bulk. For example, Fe has been shown to diffuse into the vicinal Pt(997) surface (and form a bulk like FePt alloy) at a temperature 100-150 K lower than for the close packed Pt(111) surface [31]. Therefore, it is reasonable that Te/Cu(643)^{R} shows step mediated alloying immediately upon deposition.

The Cu $2p^{3/2}$ XPS spectra, shown in figure 5.11, were fitted to a series of functions representing elemental $Cu^{(0)}$, Cu^{+} and Cu^{2+} with fitting parameters given in table 5.1. The 0.28 ML Cu $2p^{3/2}$ XPS spectrum was best fitted to three functions: $Cu^{(0)}$, Cu^{+} and Cu^{2+}. The $Cu^{\delta+}$ component was not fitted as the Te $3d^{5/2}$ XPS spectra indicated that the SSA was not present. The widths and asymmetries of Cu^{+} and Cu^{2+} were fixed to that of $Cu^{(0)}$. As was the case for Cu $2p^{3/2}$ XPS fitting in chapter 3, the binding energies of Cu^{+} and Cu^{2+} were fixed to that of similar Te and Cu compounds [27-30]. The values for the width, asymmetry and binding energy of $Cu^{(0)}$, Cu^{+} and Cu^{2+} components in Cu $2p^{3/2}$ XPS spectra are listed in table 5.1.

The fit of the 0.28 ML Cu $2p^{3/2}$ XPS showed that the ratio of Cu^{+} : Cu^{2+} = 1 : 2.2 ± 0.1. Table 5.2 shows the range of known Cu-Te alloys and their expected Cu^{+} : Cu^{2+} ratio. The ratio of Cu^{+} : Cu^{2+} = 1 : 2.2 does not match a known alloy, and so indicates a mixture of different phases. As shown in table 5.2, fixing the area of the Cu^{+} component to zero, to represent the CuTe alloy (which consists only of Cu^{2+}), is only a marginally worse fit to that when all area parameters are free. The ratio of Cu^{+} : Cu^{2+} suggests that there is a mixture of CuTe and another compound, which is most likely to be Cu_2Te as this is observed at high coverages (θ_{Te} > 1 ML). The measured stoichiometry gives a Cu : Te ratio of 1.3 ± 0.1 : 1, which is also consistent with there being a mixture of CuTe and Cu_2Te.

UPS data collected from this surface are displayed in figure 5.12. The UPS spectrum from the clean Cu(643)^{R} surface shows the Cu 3d states between 2-4 eV. The energy distribution in the DOS of Cu 3d from the Cu(643)^{R} surface differs from the Cu(111) surface due to the geometric effects of the miscut surface. There are no surface states visible from the UPS of the Cu(643)^{R} surface. The addition of 0.28 ML Te only perturbs the UPS spectra slightly, with a small decrease in Cu 3d intensity.

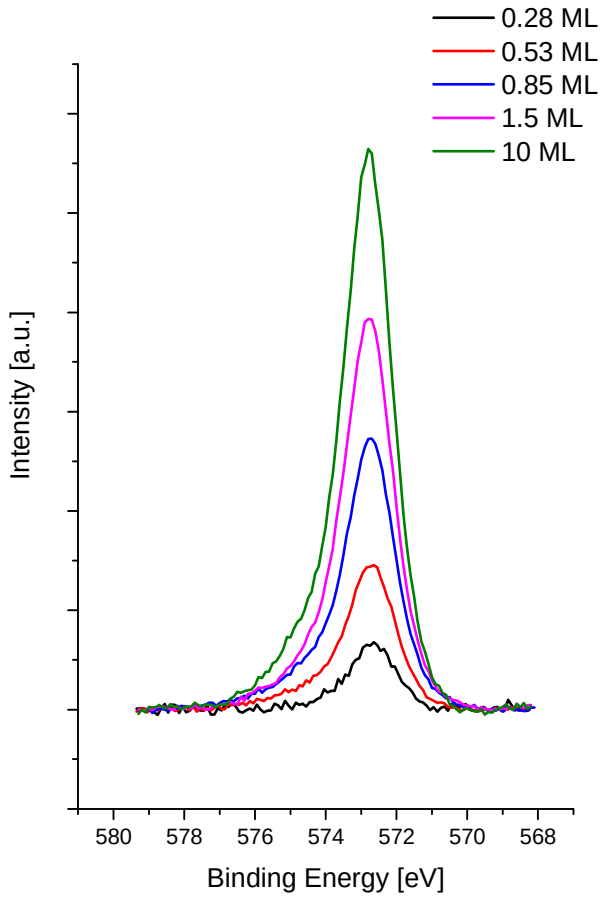

Figure 5.10. XPS spectra for the Te 3d$^{5/2}$ core level. These spectra have been collected at room temperature after annealing to 773 K. The binding energy of this peak is 572.7 eV, corresponding to Te^{2-}.

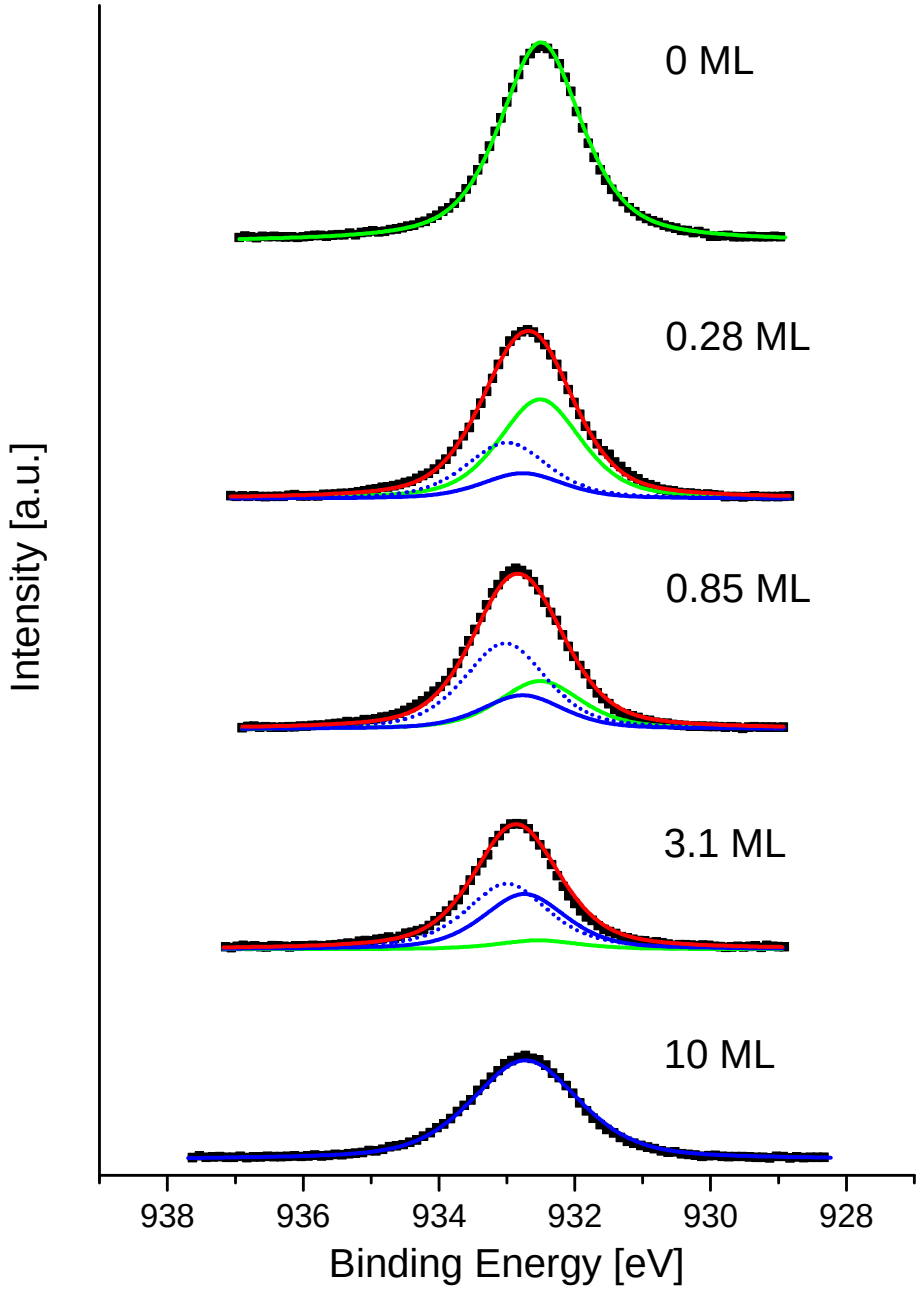

Figure 5.11. XPS spectra for the Cu $2p^{3/2}$ core level. Each panel is a spectrum obtained after deposition at room temperature which then was annealed to 773 K. Spectra are collected after slowly cooling back to 300 K. The green line is elemental Cu, the solid blue line is ionic Cu^{+} and dashed blue line is Cu^{2+}.

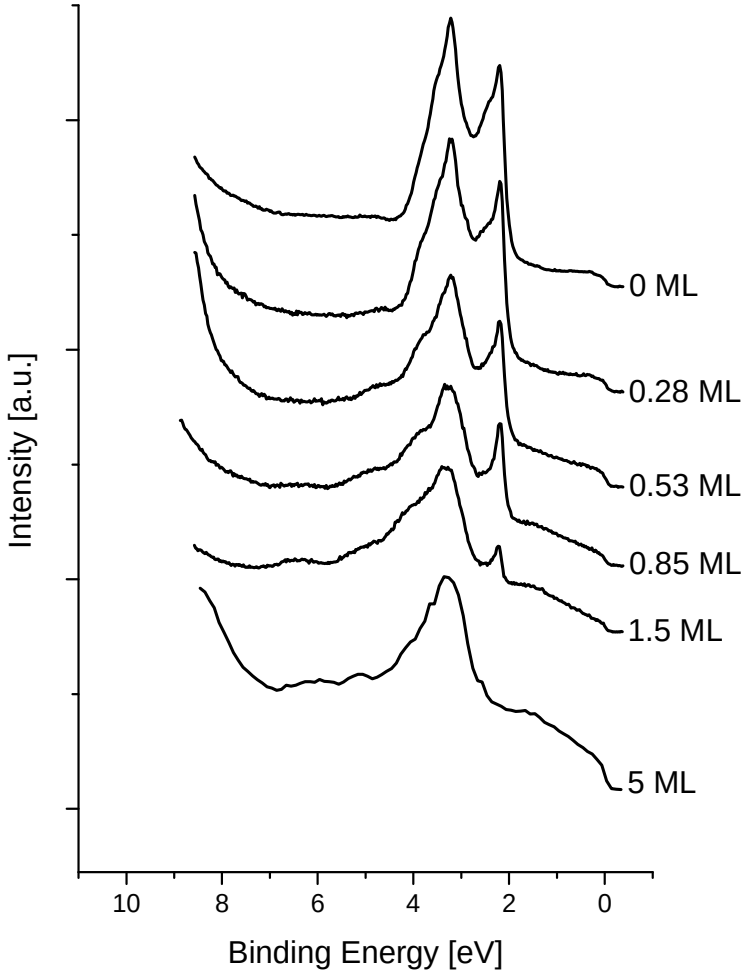

Figure 5.12. Series of UPS spectra for increasingly thick Te films on Cu(643)^{R}.

	Cu $2p^{3/2}$			Te $3d^{5/2}$	
	Cu	Cu^{+}	Cu^{2+}	Te	Te^{2-}
Binding Energy [eV]	932.4	932.7	933.0	573.1	572.7
FWHM [eV]	1.8	1.8	1.8	1.6	1.6
Asymmetry	0.02	0.02	0.02	0.12	0.12

Table 5.1. Parameters used to fit Cu $2p^{3/2}$ and Te $3d^{5/2}$ XPS spectra.

Alloy	Cu^{+} : Cu^{2+}	Goodness of Fit (χ^2/DoF) (x 10^6)
Cu_2Te	1 : 0	0.83
CuTe	0 : 1	0.28
$CuTe_2$	0	n/a
$Cu_{2.8}Te_2$	4 : 3	0.48
Cu_3Te_2	2 : 1	1.93
$Cu_{3.18}Te_2$	3 : 1	2.01
Cu_7Te_4	6 : 1	4.31
(Best Fit)	**1 : 2.2 ± 0.1**	**0.24**

Table 5.2. The goodness of fit for fixed various Cu_xTe alloys for the deposition of 0.28 ML Te/Cu(643)^R. In each case, the ratio of Cu^{+} : Cu^{2+} has been fixed to the value shown. With the ratio of Cu^{+} to Cu^{2+} a free parameter, the best fit is for Cu^{+} :Cu^{2+} = 1:2.2.

LEED provides good information on the symmetry and lattice parameters of the unit cell. Without analysing LEED IV curves derived from the LEED patterns, atomic positions are impossible to deduce and hence a basis (i.e. the atomic positions) cannot be determined explicitly. In addition, LEED IV analysis of this surface would prove very difficult because the analysis of LEED IV curves require a reasonably accurate starting model. An intuitive model from the symmetry of the LEED pattern is not forthcoming for this system. This is where microscopy techniques are invaluable tools in determining the atomic structure of the surface. In the case of atomically ordered substrates, STM is the most appropriate technique. The STM available had only the capability of operating at room temperature, hence no STM data could be acquired at 110 K, where the LEED pattern was noticeably sharper. Despite this, atomic resolution was readily obtainable for the 0.28 ML and 0.85 ML Te/Cu(643)^R films at 300K, unlike the native Cu(643)^R surface which was only imaged at 77 K and after a considerable period of time [9]. This implies that the addition of Te significantly reduces surface atom mobility.

Low magnification STM images, shown in figure 5.13 (a) and (c) reveal that 0.28 ML of Te

deposited onto the Cu(643)^R surface has induced the faceting of the Cu(643)^R surface. There is a distinct "hill-valley" type structure which has been observed in a wide range of different vicinal systems including, Ag/Cu [8,15-18] and Ni/Cu [20] and is symptomatic of faceting. The surface is clearly heterogeneous, with facets being of a variety of widths and lengths. The facets shown in figures 5.13 (a) and (c) are typical of the surface. A series of line traces revealed that the facets were up to 150 nm wide. Measurement of the orientation of the facets suggested that the large facets in figure 5.13 were (111) orientated. Although we do not observe (111) patterns with LEED, the observed pattern may be a chiral CuTe alloy sitting on top of the (111) facet.

High magnification STM images of the surface were obtained to identify the atomic structure of the surface. During the time spent imaging, only a single patch (~100 x 100 nm^2) of the surface was able to be imaged successfully. Therefore, it is stressed that the following description may not be representative of the surface as a whole. Indeed, it is unlikely that the STM image in figure 5.14 is representative of surface as a whole as structure 2 (θ_{Te} = 0.85 ML) does not follow naturally on from the structure implied here for structure 1 (θ_{Te} = 0.25 ML), as structure 1 is atomically flat while structure 2 is stepped. It is still worthwhile analysing the STM in figure 5.14 as it shows that the surface is inhomogeneous and can give an indication of the local coverage. Figure 5.14 (a) shows an STM image recorded after depositing 0.28 ML Te/Cu(643)^R at 300 K and then annealing to 773 K. Images were recorded after slowly cooling to 300 K. Figure 5.14 (a) is a higher magnification image of figure 5.13 (c). The STM data collected from this part of the surface shows that the surface is atomically flat, in contrast to the stepped Cu(643)^R surface.

As stated in section 2.4.1, care has to be taken when assigning chemical identity of protrusions in bimetallic thin films. In previous STM studies of Te, (e.g. Te/Pt(111) [32,33]), Te adatoms were imaged as bright protrusions and hence this gives confidence to the assignment of the bright protrusions as Te atoms here. Sample drift is clearly evident in this image as the separation of Te atoms is not constant. The bright protrusions on figure 5.9 give a measured unit cell of a_1 = 0.6 ± 0.1 nm and b_1 = 0.7 ± 0.1 nm, with the acute internal angle measured as, α_1 = 57 ± 4°. Note that the drift in the image has be en accounted for by the rather large errors on these values. The values of a_1, b_1 and α_1 are in reasonable agreement with the unit cell parameters measured with LEED which were a_1 = 0.51 ± 0.01 nm, b_1= 0.71 ± 0.01 nm and, α_1= 57 ± 2°. At 300 K, the opposite enantiomer is also present on the surface, inferred from its LEED pattern, shown in figure 5.5. However, we were not able to image any areas of the surface with STM for the

weakly diffracting domain. The apparent Te coverage of the 0.28 ML Te/Cu(643)^R surface can be estimated from the density of Te on the high magnification STM image shown in figure 5.14 (a). 1 ML is defined as a complete layer of Cu(111) surface. Hence, by dividing the area of the surface unit cell of the 0.28 ML Te/Cu(643)^R, figure 5.14 (a), with that of the area of the surface unit cell of Cu(111), a local Te coverage can be obtained. The area of the 0.28 ML Te/Cu(643)^R and Cu(111) surface unit cells are 0.31 ± 0.08 nm^2 and 0.0563 ± 0.0005 nm^2, respectively. Hence, the local coverage is 0.18 ± 0.05 ML, which is ~35 % lower than what was measured with XPS for the surface as a whole. A lower surface density of Te suggests that some Te may be sub-surface which is consistent with the Te 3d$^{5/2}$ XPS, which shows that it does not exist as an alloy confined exclusively to the surface. It is likely that there is an even greater concentration of Te sub-surface because many parts of the surface could not be imaged at atomic resolution, suggesting that these areas were bare Cu. Atomic resolution STM is difficult to achieve with elemental Cu because the d-electrons are delocalised and especially on stepped Cu as the surface atoms also have substantial mobility. This implies that there is an even greater density of Te sub-surface. Also present on the STM images are a row of protrusions sticking out from the flat surface, figure 5.14 (a). The protrusions may be a contaminant, however, no carbon or oxygen species were detected as measured by the XPS signals from the C 1s and O 1s, respectively. Therefore, it is more likely that the row of protrusions are the next layer of Te (or Cu-Te) which has been partially formed.

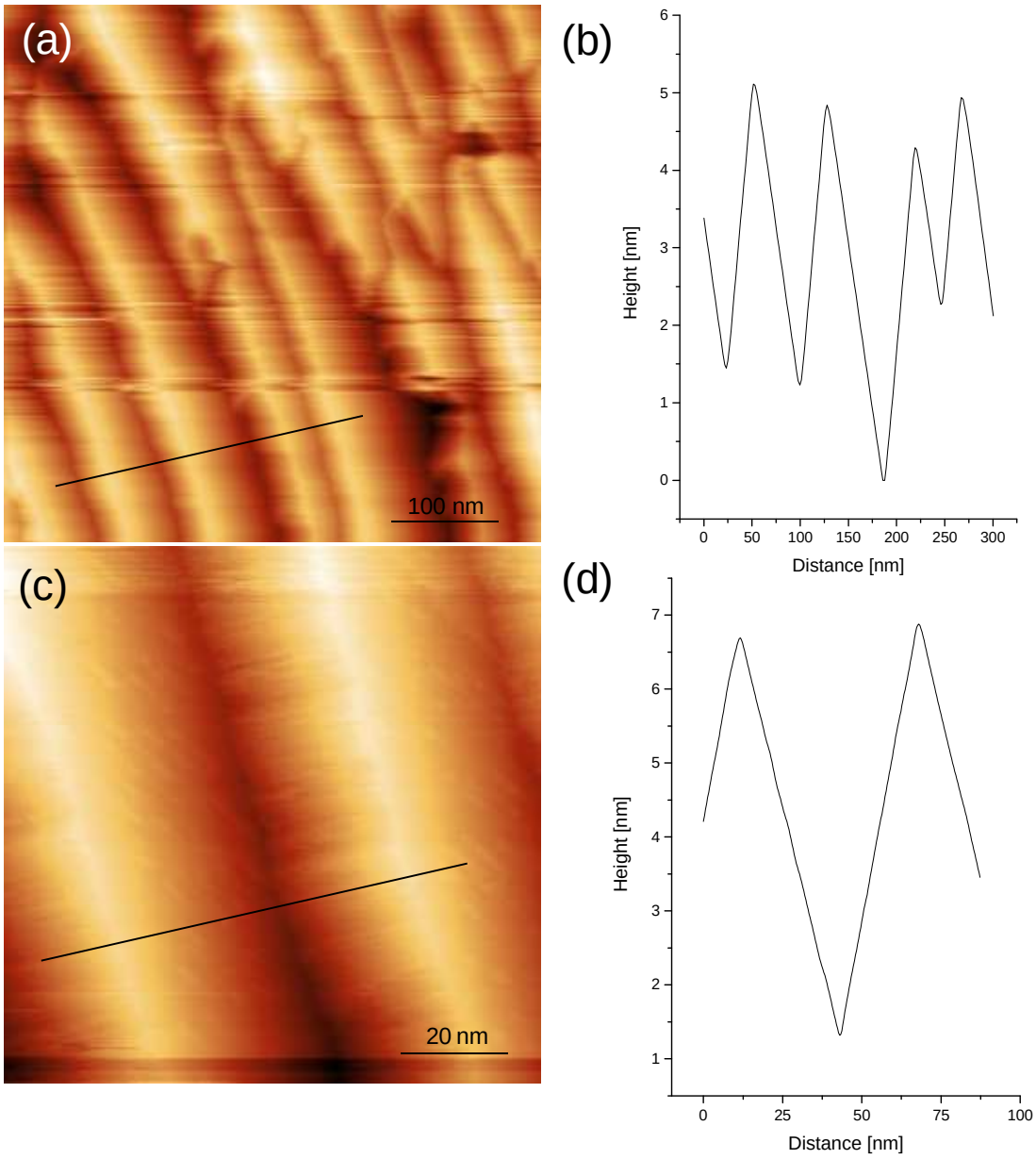

Figure 5.13. STM of 0.28 ML Te/Cu(643)^{R}, deposited at 300 K, annealed to 773 K for 10 minutes and then allowed to cool to 300 K for STM acquisition. In images (a) and (c) the tip parameters are I_t = 900 pA, V_{gap} = 1.1 V. (a) shows a low magnification image of the facetted surface. (b) shows the line trace indicated on (a). (c) is a higher magnification image of the facetted surface taken from a different region from (a). (d) is a line profile from the black line on figure (c).

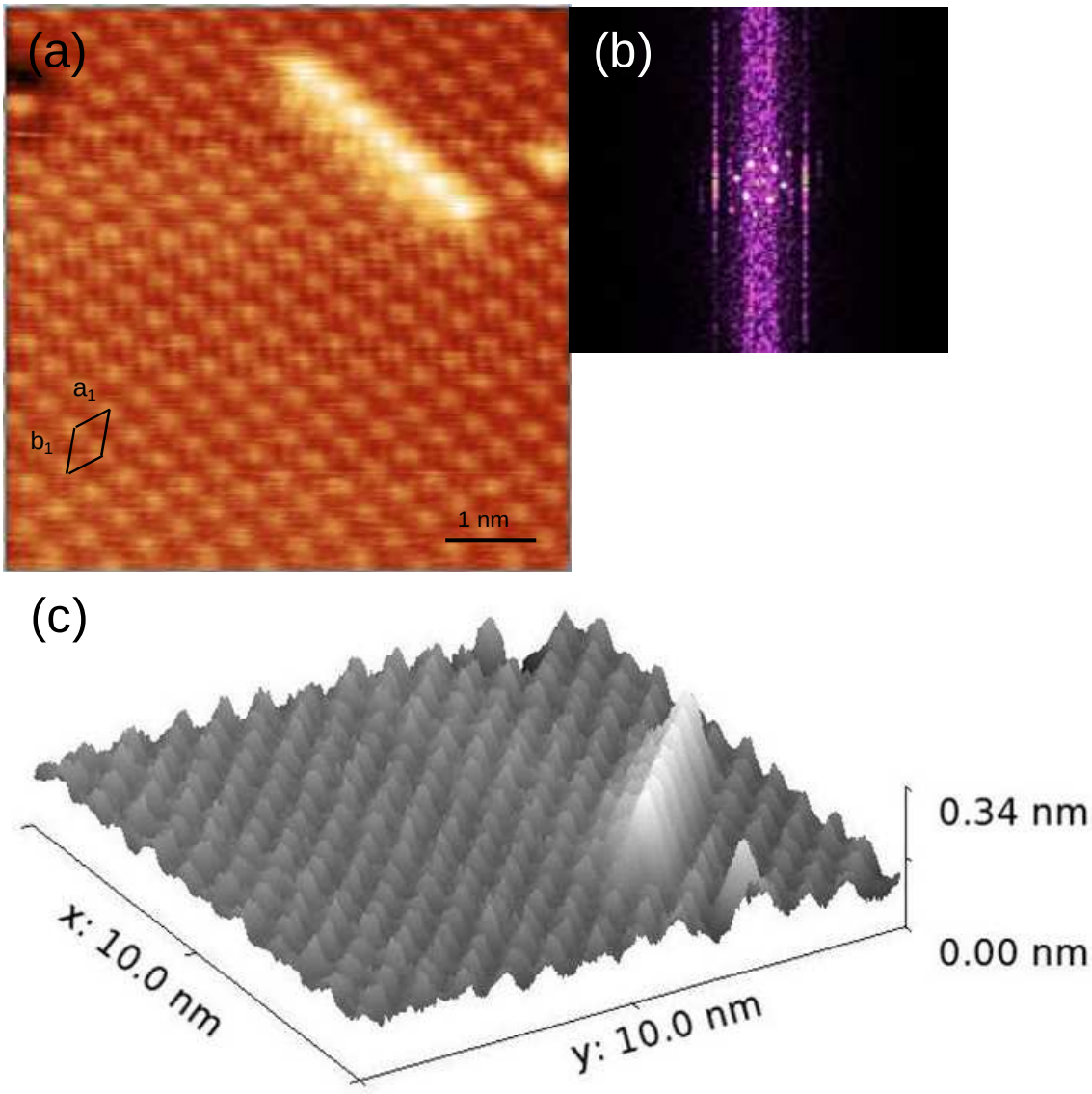

Figure 5.14. (a) STM of 0.28 ML Te/Cu(643)^R, deposited at 300 K, annealed to 773 K for 10 minutes and then allowed to cool slowly to 300 K for STM acquisition. The image size is 10 x 10 nm^2 and the acquisition parameters are I_t = 900 pA and V_{gap} = 1.8 V. The black parallelogram shows the surface unit cell, with dimensions a_1 = 0.6 ± 0.1 nm, b_1 = 0.7 ± 0.1 nm and an acute internal angle of α_1 = 57 ± 4°, measured from (b), the FFT. (c) shows a three dimensional visualisation of the surface displayed in (a).

5.2.2 High Coverage Alloy (0.45 < θ_{Te} < 1.5 ML)

A second ordered structure, labelled structure 2, becomes visible with LEED above 0.45 ML and reaches its maximum in sharpness at 0.85 ML. Figure 5.7 (e) shows the LEED pattern for 0.85 ML of Te/Cu(643)^{R}, that has been annealed to 773 K, then cooled to 110 K. Distinct streaking of spots can be observed in the direction of closely spaced spots, indicating anisotropic disorder in this direction. On first assessment, the 110 K LEED pattern, shown in figure 5.7 (e) is apparently formed of rhombohedra. However, varying the incident beam energy causes spots to pass through each other, indicating that the LEED pattern consists of more than one domain. Figure 5.9 shows the LEED patterns of 0.85 ML Te/Cu(643)^{R} taken between 133 V and 188 V. The spots highlighted by the red circle clearly show that spots pass through each other, indicating that the LEED pattern consists of multiple domains.

Two domains were identified on the LEED pattern. Figure 5.7 (f) shows blue lines that indicate several unit cells. There is a curvature in the rows of spots that run close to the horizontal which is attributed to the curvature in the LEED screen and therefore the blue line does not pass through all spots. Also, the spots are not always equally spaced which means that the unit cell is not unique. However, a unit cell is still able to be obtained albeit with a large error in the value for b_2 and the internal angle, α_2. Figure 5.7 (g) shows the surface unit cell defined by the red grids. Together the red and blue grids account for all of the spots on the LEED image. These boxes define either a rectangular unit cell (if α_2 = 90°) or a oblique surface unit cell (if $\alpha_2 \neq 90°$), with dimensions of a_2 = 0.46 ± 0.01 nm, b_2 = 2.2 ± 0.2 nm and α_2 = 85 ± 7°. However, the STM images from this surface shown in figure 5.16, indicate that the surface unit cell is rectangular. It is clear from the LEED patterns that the spots are streaked and unevenly distributed in the b_2 direction. The STM images, discussed below, show that this is a result of terraces having a range of lengths. If we assume that α_2 = 90° then, when rotated, the two unit cells from figure 5.7 (h) are super-imposable mirror images of each other and are hence achiral. The unit cells are rotated by an angle of 60 ± 2°, which probably reflects the hexagonal symmetry of the (111) terraces on the surface.

The Te 3d$^{5/2}$ XPS spectrum from the 0.85 ML Te/Cu(643)^{R} surface is shown in figure 5.11. This spectrum could also be fitted to a single function with a binding energy of 572.7 eV, corresponding to bulk Te^{2-}, indicating the bonding of Cu-Te was similar to that of the 0.25 ML coverage. The Cu 2p$^{3/2}$ spectrum was fitted to three separate peaks, representing elemental Cu, Cu^{+} and Cu^{2+}. The fit has been done with the parameters given in table 5.1.

The best fit yields a ratio of Cu^{+} : Cu^{2+} of 1 : 3.1 ± 0.1, which indicates that the surface is rich in Cu^{+} but does not correspond to a known Cu-Te alloy, implying an inhomogeneous surface. As with the 0.28 ML Te coverage, fixing the Cu^{+} component to zero, to represent CuTe ($Cu^{2+}Te^{2-}$), is only a slightly worse fit to when all three integrated intensities are allowed to vary, suggesting that CuTe was present on the surface. As with the Te coverage of 0.28 ML, the best estimate of the composition of the 0.85 ML surface is that of a mixture of CuTe and Cu_2Te. The assignment of CuTe is consistent with the STM data, which will be presented subsequently. The relative amount of Cu^{2+} to Cu^{+} is larger on the 0.85 ML Te/Cu(643)^{R} surface (3.1 : 1 for 0.85 ML compared to 2.2 : 1 for 0.28 ML). The increase in Cu^{2+} may indicate that the growth of the CuTe alloy is the favoured growth mechanism for Te coverages between 0.28 ML and 0.85 ML. The ratio of Cu : Te = 1.1 ± 0.1, calculated using equation 2.10 and appropriate sensitivity factors given in section 2.4.2, is in agreement with a mixture of CuTe and a small amount of Cu_2Te.

Alloy	Cu^{+} : Cu^{2+}	Goodness of Fit (χ^2/DoF) (x 10^6)
Cu_2Te	1 : 0	0.57
CuTe	0 : 1	0.34
$CuTe_2$	0	n/a
$Cu_{2.8}Te_2$	4 : 3	0.84
Cu_3Te_2	2 : 1	3.10
$Cu_{3.18}Te_2$	3 : 1	3.12
Cu_7Te_4	6 : 1	4.12
Best Fit	**1 : 3.1 ± 0.1**	**0.27**

Table 5.3. The goodness of fit for fixed various Cu_xTe alloys for the deposition of 0.85 ML Te/Cu(643)^{R}. In each case, the ratio of Cu^{+} : Cu^{2+} has been fixed to the value shown. With the ratio of Cu^{+} to Cu^{2+} a free parameter, the best fit is for Cu^{+} :Cu^{2+} = 1 : 2.2.

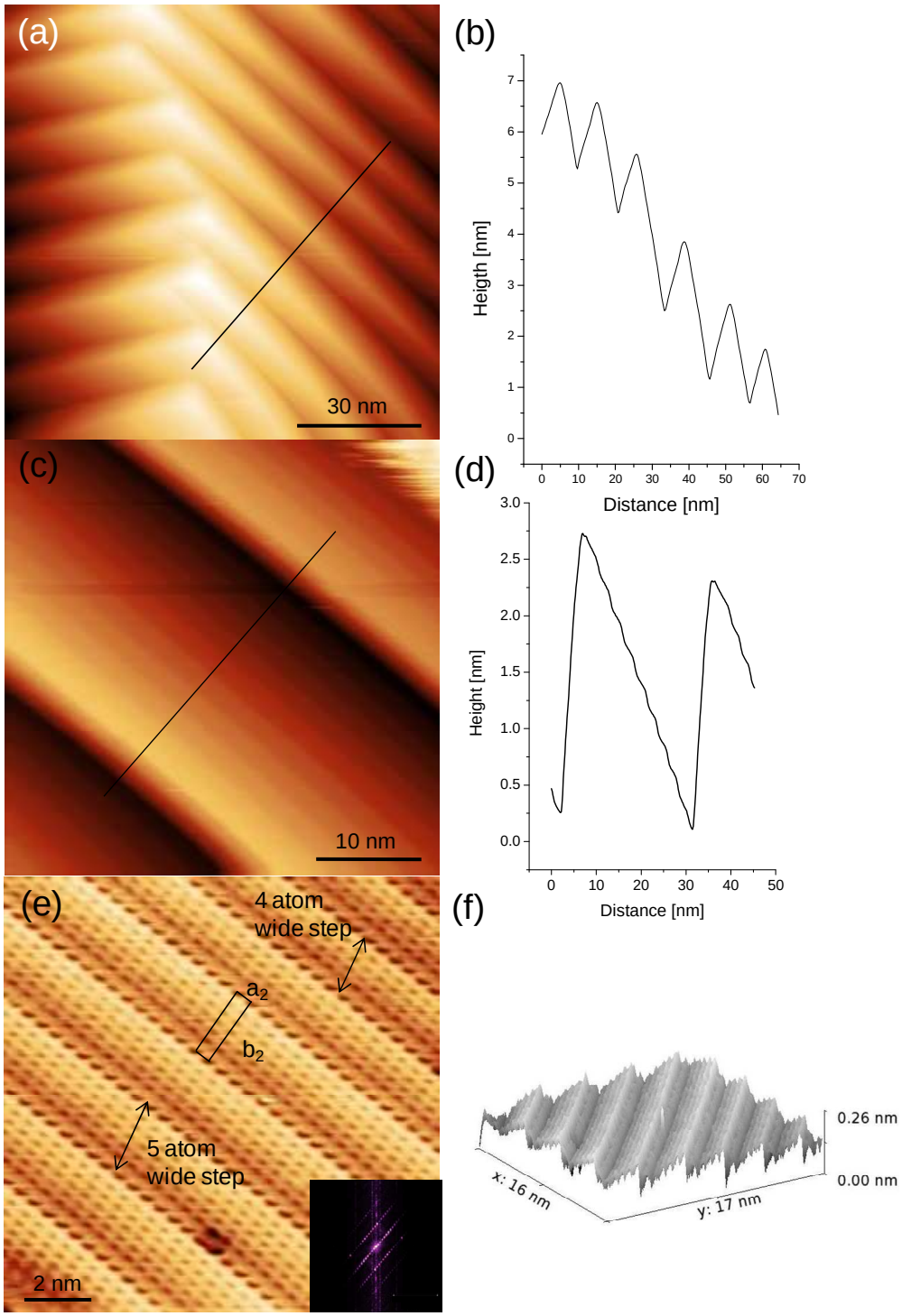

Figure 5.15. STM of 0.85 ML Te/Cu(643)^{R}, deposited at 300 K, annealed to 773 K for 10 minutes and then allowed to cool to 300 K for STM acquisition. In all images, the tip parameters are I_t = 800 pA, V_{gap} = 1.1 V. (a) shows a low magnification image. (c) shows a higher magnification of step bunches. (b) and (d) are line profiles of the black lines on (a) and (c) respectively. (e) is a high magnification image of a step bunch. (f) is a three dimensional representation of image (e), showing how the levelling has been performed.

As in elucidating the nature of structure 1, STM becomes an invaluable tool in examining both the mesoscopic faceting and the atomic structure of structure 2. Figures 5.15 (a), (c) and (e) show STM images taken from a surface prepared from 0.85 ML of Te/Cu(643)^R that has been annealed to 773 K for 10 minutes. Imaging was performed after the sample had slowly cooled to 300 K. Figure 5.15 (a) shows a 100 x 100 nm^2 STM image that reveals that the surface has also facetted at this coverage. The line profile, taken from the black line on figure 5.15 (a), is displayed in figure 5.15 (b) and shows a distinct "hill-valley" structure, common in facetted systems. Figure 5.15 (d) shows the line profile taken from figure 5.15 (c) and shows that on each large facet (~30 nm wide on the line profile) there are multiple small steps that are 2-3 nm wide. This indicates step bunching and is again common on vicinal surfaces [9,34-36]. The orientation of these facets suggests that is misaligned with respect to the (111) plane by ~5° which may explain why steps are observed.

Figure 5.15 (e) shows a higher magnification image of the closely spaced steps, with atomic information clearly visible. As is noted in the discussion of structure 1 and in section 2.4.1, STM probes the local variation in electronic structure and therefore the interpretation of the protrusions and dips on bimetallic surfaces and alloys is non-trivial. As for the interpretation of the STM images in structure 1, the assignment of the bright areas in figure 5.15 (e) are as Te atoms. Figure 5.15 (e) has been plane levelled, which visualises the surface as a sawtooth shape, as shown in the three dimensional image of figure 5.15 (e). It is necessary to level the data in this way because there are large differences in height, generated from the steps which mask the variations in height from the atomic corrugations, as evident in the line trace shown in figure 5.10 (d). In contrast to the flat nature of the surface observed with STM for structure 1, structure 2 is stepped. The height of the step was measured to be 0.10 ± 0.02 nm which is less than the anticipated step for ideal Cu(643)^R surface, 0.22 nm. As will be described below, structure 2 is tentatively assigned to be a distorted version of CuTe. CuTe has an ideal atomic step height of 0.15 nm, which is also slightly too large to account for the measured height. As this a surface phase the step height may be slightly relaxed with respect to the bulk phase.

Figure 5.15 (c) shows that there is variability in how many atoms make up a terrace - in STM images observed here, the terraces are either comprised of 4 or 5 atoms. This means that two different surface unit cells are possible. The dimensions of this unit cell are a_1 = 0.54 ± 0.05 nm, b_2 = 2.20 ± 0.05 nm (4 atom wide terrace) or b_2 = 2.71 ± 0.05 nm (5 atom wide terrace) and α_2 = 88 ± 3°. The 4 atom wide terrace is in excellent agreement

with the dimensions extracted from the LEED pattern in figure 5.7 (e), which are a_2 = 0.46 ± 0.01 nm, b_2 = 2.21 ± 0.10 nm, and α_2 = 87 ± 3°. The angle, α_2, is within error of 90° and thus the surface unit cell is interpreted as being rectangular and therefore achiral. The variability in the step separation, b_2, figure 5.15 (b), shows why there is anisotropic disorder (streaking) in the b_2 direction observed with LEED. The steps are either 4 or 5 atoms wide and hence the LEED pattern originating from these structures will be a summation of the diffraction from both lengths of step.

High magnification images were obtained from the 0.85 ML Te/Cu(643)^R surface, presented in figure 5.16, are now tentatively interpreted. Figure 5.16 (a) shows the high magnification image that has had the same planar subtraction performed on it as in figure 5.15 (c). In an effort to make the atomic detail clearer, a FFT filtered image was produced and is shown in figure 5.16 (b). The FFT was used to filter out the high frequency noise from the image and allows for extra features of the STM image to be identified. Figure 5.16 (b) shows the surface unit cell defined from figure 5.15 (c) as a white box in figure 5.16 (b). The dimensions of the unit cell are in good agreement with each other. Within the unit cell defined by the white box, there are regular protrusions visible. A unit cell for these protrusions can be drawn, which is named the terrace unit cell, as the structure is repeating only on the terraces. The terrace unit cell has dimensions of a_T = 0.41 ± 0.05 nm, b_T = 0.63 ± 0.05 nm and α_T = 99 ± 2°. This is an oblique unit cell and thus t he structure of the terraces can be thought of as being chiral. This unit cell implies a local Te coverage of just 0.26 ML, in comparison to the 0.85 ML measured with XPS. As in structure 1, this suggests that large proportion of Te has migrated sub-surface, which is in agreement to the Te 3d$^{5/2}$ XPS which indicates that bulk Cu-Te alloying is occurring.

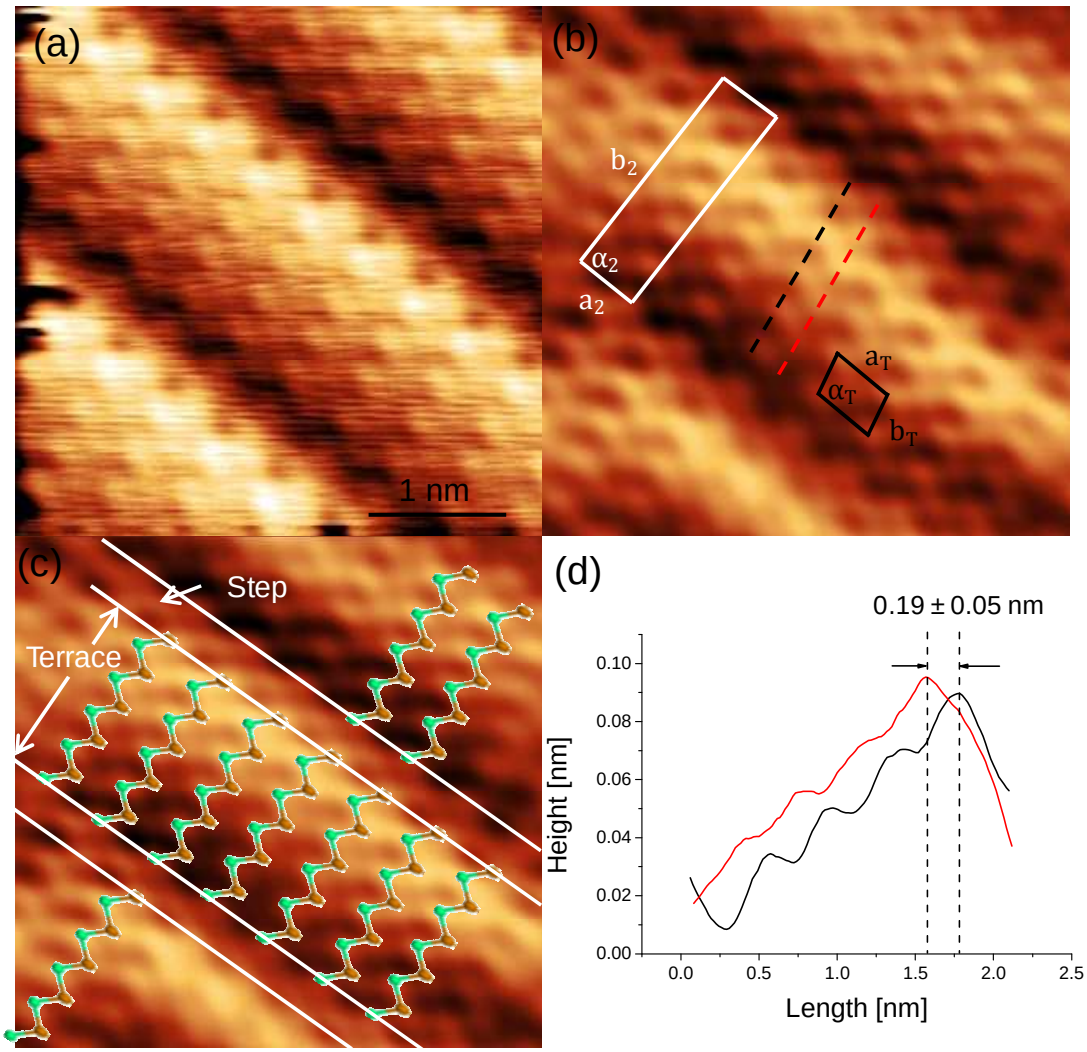

Figure 5.16. (a) High magnification images of the 0.85 ML Te/Cu(643)^{R} surface. (b) FFT filtered image of (a). The white unit cell on (b) defines the unit cell of structure 2, as defined in figure 5.15 (c). The black unit cell in (b) denotes the unit cell found exclusively on the terraces of stucture 2. The terrace unit cell has dimensions: a_T = 0.63 ± 0.05 nm, b_T = 0.41 ± 0.05 nm and α_T = 99 ± 3°. The dashed red line and black lines cor respond to the lines where the line profiles in (d) was taken from. (c) shows the FFT filterd image from (b) with CuTe (Vulcanite) chains superimposed on top of the image (see figure 5.17 for Vulcanite structure). The scale bar in (a) also applies to images (b) and (c).

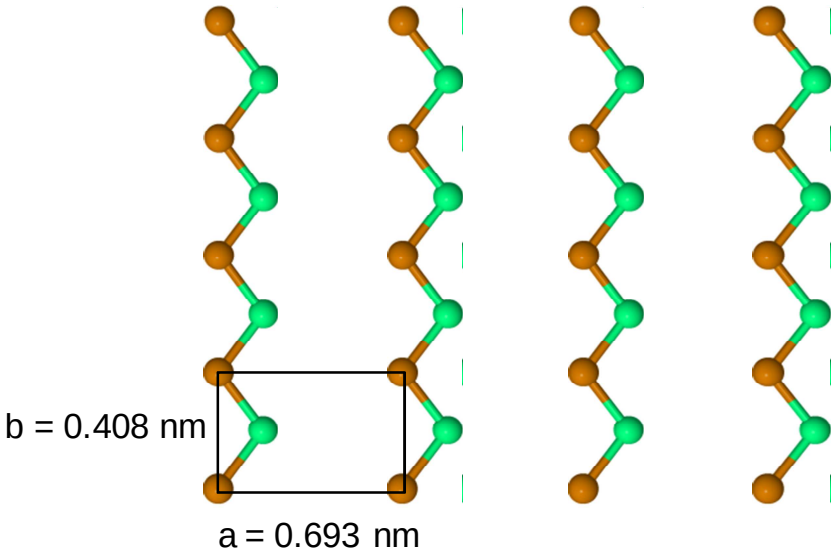

(010) Termination of CuTe “Vulcanite”

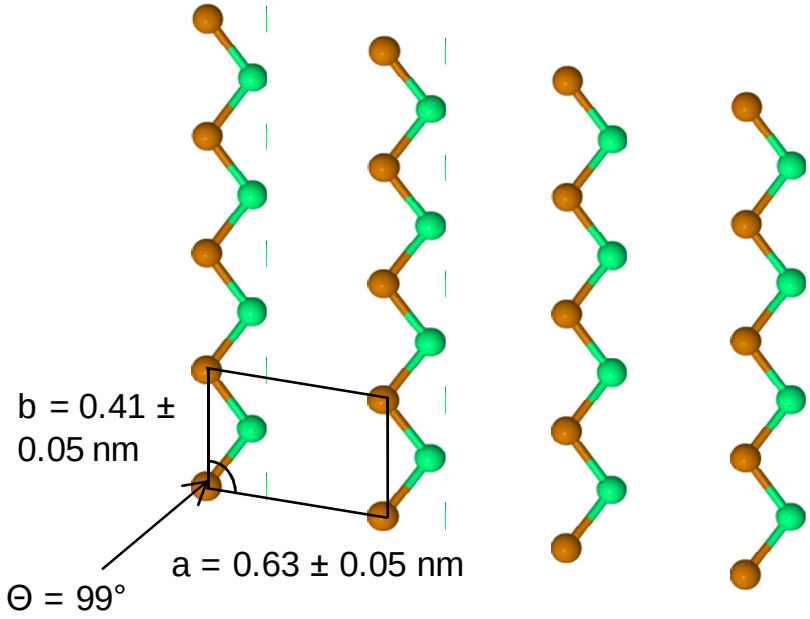

Distorted CuTe, “Chiral Vulcanite”

Figure 5.17. The upper panel shows the (010) termination of the CuTe structure known as Vulcanite on which the surface unit cell is annotated. The lower panel shows the hypothesised terrace structure.

We now compare the data obtained from the 0.85 ML Te/Cu(643)^{R} film to known bulk alloys. The XPS data obtained from this surface indicates that the ratio of Cu : Te is 1 : 1.1 and the ratio of Cu^{+} : Cu^{2+} is 1 : 3.1 (i.e. rich in Cu^{2+}). These two ratios are in agreement with a surface alloy phase predominantly formed of a $Cu^{2+}Te^{2-}$ alloy (i.e. CuTe). The STM images in figure 5.16 are tentatively interpreted as being in agreement with the assignment of CuTe as identified with XPS. The (010) termination of the mineral "Vulcanite", CuTe [37,38], is shown in the upper panel of figure 5.17. CuTe has zigzag chains of chemically bonded Te and Cu atoms, with each chain interacting via Van der Waals' forces and laterally displaced from each other by 0.693 nm. The intra chain Cu-Cu and Te-Te separations are 0.408 nm. The chain structure is further suggested by the line profiles displayed in figure 5.16 (d) which where integrated over a 0.5 nm window. Both the line profiles obtained show that the separation of the protrusions are 0.41 ± 0.05 nm, in agreement with the terrace unit cell. The line profiles also show that the sets of protrusions are at 0.19 ± 0.05 nm out of phase with each other. This is also in agreement with the terrace unit cell as the projection of the Cu-Te distance along the b axis is half that of the terrace unit cell (0.41 ± 0.05 nm).

The measured intra-chain atomic separations are in excellent agreement with Vulcanite probably because of the strength of the covalent character of these bonds. However, the conjectured CuTe surface alloy phase is slightly distorted along a_T, (i.e. the chains are misaligned) which results in the chiral, oblique, terrace lattice observed in the STM images. Unlike in the reported CuTe structure, the proposed CuTe structure here has chains that are misaligned by ~9°, so although the unit cell is achiral, the atomic positions within the terrace are chiral. The origin of this chirality we suggest is a result of the Cu(643)^{R} substrate acting as a template for growth, which will be further explored in section 5.3. The distortion of the chains seems reasonable as these chains are far enough apart only to interact through weak Van der Waals' interactions.

To show the good alignment of the CuTe structure with the observed STM image, CuTe chains are overlaid on the FFT image, shown in figure 5.16 (c). The proposed structure of the chiral Vulcanite-like CuTe alloy has a flat surface but clearly the brighter protrusions are higher than the fainter ones. It is well known that STM can give false measurements of height in heterogeneous systems because STM is an intrinsic measure of the local electronic structure [39]. Therefore, it is argued that the apparent change in height could be a change in element, which then would be consistent with the alternating Cu-Te chain structure of CuTe. Identifying the chemical identity of the protrusions is difficult and an unambiguous answer is impossible without using a technique such as scanning tunnelling

spectroscopy (STS). The STM data suggest that even though the overall surface unit cell of structure 2 is achiral, the atomic structure contained within the unit cell is in fact chiral. We conclude by noting that the hypothesised distorted Vulcanite structure only accounts for the structure of the terrace, it does not relate to the nature of the steps and hence, on figure 5.16 (c), the steps are intentionally left blank.

5.2.3 Disordered Alloy Phase (θ_{Te}> 1.5 ML)

The LEED pattern described as structure 2 reaches its maximum in intensity and sharpness at 0.85 ML of Te/Cu(643)^{R}, figure 5.10 (e) and gradually becomes more diffuse with increasing Te coverage. LEED patterns obtained above 1.5 ML showed no sharp spots. Te 3d$^{5/2}$ XPS data collected for Te coverages greater than 0.85 ML were again fitted to a single function at 572.7 eV representing a bulk alloy of Te^{2-}. The Cu 2p$^{3/2}$ spectra collected above a Te coverage of 0.85 ML were again fitted to three components: representing elemental $Cu^{(0)}$, Cu^{+} and Cu^{2+}. Identical to lower coverages, the fit was performed by fixing the binding energies, widths and asymmetry parameters to those displayed in table 5.1, with the area of each function allowed to vary. The Cu 2p$^{3/2}$ XPS spectra revealed that, as the Te coverage increased, the Cu^{+} component grew, at the expense of the $Cu^{(0)}$ and Cu^{2+} components. At 10 ML, the stoichiometric ratio of ionic Cu : Te was measured to be 2.1 ± 0.1, within error of Cu_2Te. The Cu 2p$^{3/2}$ XPS spectrum is well fitted to a single function, corresponding to Cu^{+} and hence also implies Cu_2Te. Fixing the ratios to other Cu-Te alloys significantly worsens the fit. The results of the fitting process (goodness of fit) are listed in table 5.4.

Together with the diffuse LEED patterns, the XPS data indicate that a rough or polycrystalline Cu_2Te alloy dominates the surface above a Te coverage of ~1 ML. The data also indicate that Cu diffuses through the Te film, as in Te/Cu(111) and Te/Cu_{poly} for even the thickest Te coverages studied in this chapter, 50 ML. The Cu^{2+} component of the Cu 2p$^{3/2}$ XPS only slowly decreases which suggests that the CuTe chains are retained, most likely at the Te/Cu(643)^{R} interface, with the rough Cu_2Te film growing on top. Indeed, the measured Cu : Te ratio gradually shifts from ~1.3 at sub-monolayer coverages to ~2.0 at θ_{Te} > 5 ML. A plot of the Cu : Te ratio is shown in figure 5.18. It shows a gradual shift between a surface comprising CuTe and a minor amount of Cu_2Te at low coverage, to a surface that comprises only of Cu_2Te at high coverage. The UPS spectra obtained for increasingly thicker films of Te show a gradual attenuation of the Cu 3d states and the gradual development of features associated with Cu_xTe alloys, as shown in chapter 3. The UPS spectrum from the 5 ML Te coverage is in good agreement with the UPS spectrum

from the Cu_2Te film, as shown in chapters 3 and 4.

Alloy	$Cu^+ : Cu^{2+}$	Goodness of Fit (χ^2/DoF) (x 10^6)
Cu_2Te	**1 : 0**	**0.25**
CuTe	0 : 1	4.10
$CuTe_2$	0	n/a
$Cu_{2.8}Te_2$	4 : 3	2.10
Cu_3Te_2	2 : 1	1.85
$Cu_{3.18}Te_2$	3 : 1	1.21
Cu_7Te_4	6 : 1	0.82
(Best Fit)	**1 : 0**	**0.25**

Table 5.4. The goodness of fit for fixed various Cu_xTe alloys for the deposition of 10 ML Te/Cu(643)^R. In each case, the ratio of $Cu^+ : Cu^{2+}$ has been fixed to the value shown. With the ratio of Cu^+ to Cu^{2+} a free parameter, the best fit is for $Cu^+ : Cu^{2+}$ = 1 : 0.

5.2.4 Summary and Surface Phase Diagram

This section recaps the main observations for the Te/Cu(643)^R system. Te deposition causes the Cu(643)^R surface to facet and form novel Cu-Te alloy structures. There are two different ordered structures observed with LEED, labelled structure 1 and structure 2. Structure 1 exists for 0.18 ML < θ_{Te} < 0.45 ML and structure 2 exists for 0.45 ML < θ_{Te} < 1.5 ML. The maximum ordering of the LEED pattern of structure 1 is at 0.28 ML while the maximum ordering of the LEED pattern of structure 2 is 0.85 ML. At low coverage the Cu-Te surface comprises CuTe and Cu_2Te, with CuTe being far more abundant than Cu_2Te. However as Te coverage increases, the rough or polycrystalline Cu_2Te islands continually grow, up to the maximum Te coverage studied here, 50 ML. The growth of Te/Cu(643)^R is summarised in figure 5.18.

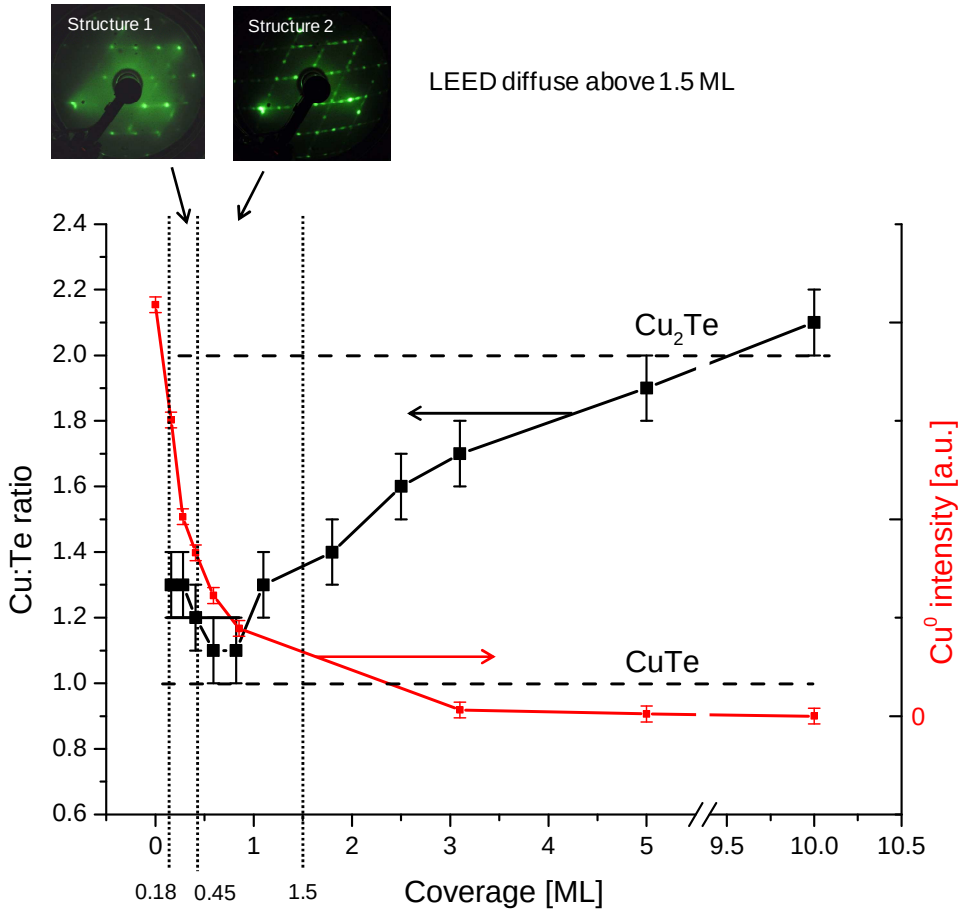

Figure 5.18. Schematic surface phase diagram for Te/Cu(643)^{R} after depositing at 300 K and annealing to 773 K. The black line shows the change in the stoichiometry of the Cu-Te film as a function of Te coverage. The red line shows the change in intensity of the elemental Cu peak as a function of Te coverage. The dashed black lines indicate the Cu:Te ratio for CuTe and Cu_2Te and do not apply to the Cu^0 intensity plot. The LEED patterns are added to show the Te coverages at which these patterns exist. There are no visible spots in the LEED patterns above 1.5 ML.

The elemental Cu signal (Cu^0) is also added to assess if the phase change from structure 1 to structure 2 is linked to a greater inclusion of Cu into the CuTe alloy. The intensity change of Cu^0 as a function of Te coverages reveals a smooth decrease in intensity consistent with a growing overlayer. There is no evidence of any anomalous changes in Cu^0 signal around the phase change (~ 0.45 ML) which would indicate a rapid uptake of Cu by the alloy phase transition. We conclude that the phase change from structure 1 to structure 2 is a rearrangement to accommodate the growing Te film. We conclude that the lower the coverage, the more influence the chiral Cu substrate has on templating the

growth modes of Te/Cu(643)^R. With increasing coverage, registry between the substrate and the growing film is progressively lost, leading to the diffuse LEED patterns observed for coverages above 1.5 ML. The role of Cu(643)^R in directing growth will be further discussed in section 5.3.

5.2.5 Thermal Processing

As with Te/Cu(111), the alloying phase transition temperature in the Te/Cu(643)^R system can be measured. To do this, a thick 30 ML film of Te was deposited onto Cu(643)^R at 110 K. This temperature was too low to permit alloying of Te with the Cu(643)^R surface and the Te film was thick enough so that the Cu $2p^{3/2}$ XPS signal was completely attenuated. The substrate was then annealed for 10 minutes at a particular temperature and Cu $2p^{3/2}$ and Te $3d^{5/2}$ XPS data collected. Figure 5.19 shows the change in Te $3d^{5/2}$ binding energy and Cu $2p^{3/2}$ signal with increasing annealing temperature.

The Te $3d^{5/2}$ and Cu $2p^{3/2}$ XPS data show a single sharp transition at 225 K. At this point the binding energy of Te $3d^{5/2}$ shifts from 573.1 eV, which is characteristic of elemental Te to 572.7 eV, which is characteristic of the bulk alloy of Cu-Te, clearly indicating alloying. Thermodynamically, alloying of Cu and Te is favourable even at 110 K but, as in Te/Cu(111), it was found that alloying was kinetically inhibited below the transition temperature. In Te/Cu(111) it was found that the alloying transition temperature is ~275 K. However, in Te/Cu(643)^R it was discovered that the alloying phase transition temperature is significantly lower, ~225 K. The reduction of the alloying phase transition temperature is consistent with step mediated growth mechanism whereby the step facilities Te intermixing with the Cu substrate. Step mediated growth has been observed in a wide range of systems, including Pt/Cu(111) [31], Ag/Pt(111) [40] and Fe/Pt(111) [41]. Cu(643)^R is a stepped structure and therefore surface atom mobility is increased, with respect to Cu(111), due to the reduced atomic co-ordination at steps and kinks, which would permit the interdiffusion of Te and Cu at a lower temperature. The increased substrate surface atom mobility is likely to be the driving force behind the reduced alloying phase transition temperature for 30 ML Te/Cu(643)^R, permitting facile mixing of Te and Cu. The concept of step mediated alloying is further explored in the discussion, section 5.3.

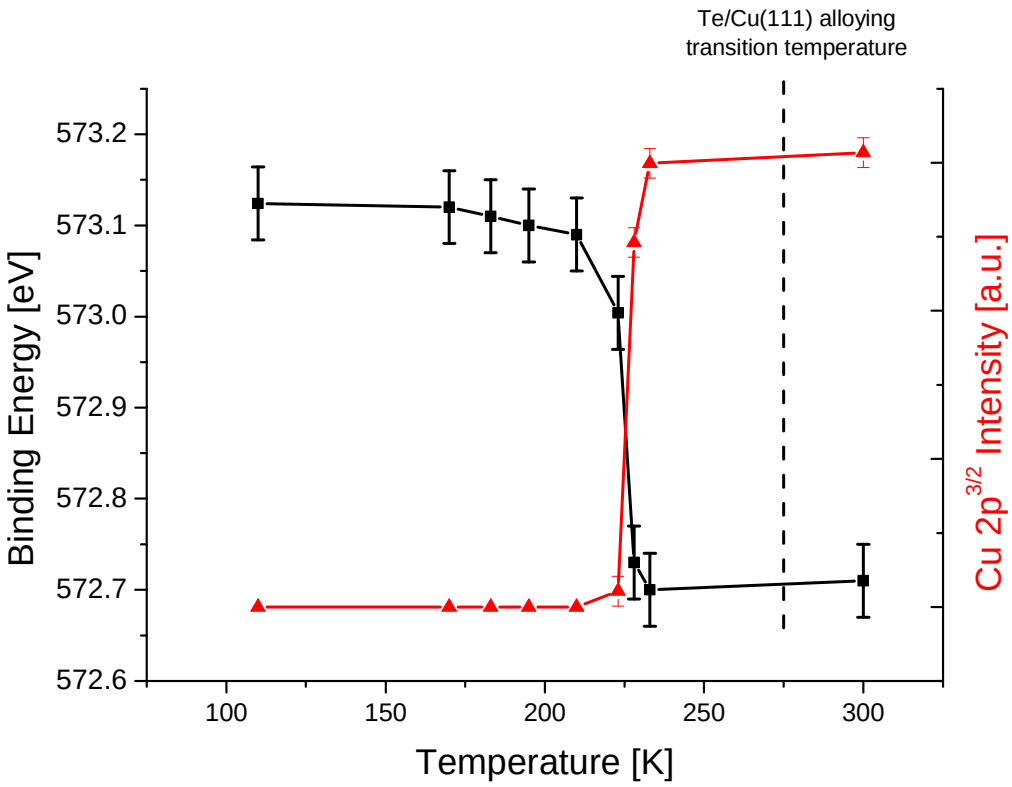

Figure 5.19. The variation of Te $3d^{5/2}$ binding energy (black line) and Cu $2p^{3/2}$ XPS intensity (red line) with temperature for a Te coverage of 30 ML initially deposited at 120 K. A single sharp transition was observed at 225 K. The dashed black line is the alloying transition temperature observed for 30 ML Te/Cu(111), which is 275 K.

5.3 Discussion

There are several interesting questions that arise from the observations described in this chapter. The STM images from structure 1 (figure 5.14) implies that there is no step bunching (i.e. it is flat) while the STM of structure 2 (figure 5.15) implies that there is step bunching on the facetted surface. It is implausible that the steps on the native $Cu(643)^R$ surface have been lost (structure 1) and regained (structure 2). As with all microscopies, it is necessary to ask whether the image is representative of the specimen as a whole. We therefore conclude that as the surface is inhomogeneous, what we have imaged in structure 1 is not representative of the surface as a whole (i.e. there is step bunches in structure 1 that have not been imaged so that the macroscopic surface normal remains unchanged). Indeed, (spatially integrating) XPS shows that the stoichiometry does not match any known Cu_xTe alloy and thus implies that the surface is indeed inhomogeneous.

A further question arises: why from a homochiral substrate, $Cu(643)^R$, do we observe domains of CuTe that have opposite handedness (i.e. are different enantiomers), after deposition of Te? To have a chiral overlayer from an achiral adsorbate (i.e. the Te adatoms) there needs to be a chiral influence in the growth process. Adatoms arriving on the (111) terrace would not receive a chiral influence as the (111) terrace is achiral because each of the 6-fold positions are equally as likely. On the (643) surface there are additional considerations: chiral kink sites and hence, there must be some chiral perturbation to the arriving adatoms. Secondly, it is likely that the mesoscopic facets are bound by chiral kinks and steps because the macroscopic miscut of the surface must be maintained. These kinks would be expected to provide a weak chiral influence on the overlayer and thus the handedness of the surface would be dependent on the diffusion length of the Te atoms. If the Te diffusion length was greater than the facet size, then may be possible for Te adatoms to migrate across the surface and interact with the chiral kink site and form aggregates and islands. If the diffusion length of Te was less than the size of the facet then it would be more likely to favour racemic or achiral growth.

Following from the question of both enantiomers existing on a previously homochiral surface, is the question: can we quantify the relative amounts of each enantiomer on the surface? From inspection, the intensities of the spots that comprise the opposite enantiomers (blue and red boxes in figure 5.7 (d)) of structure 1 are different, as shown in figure 5.7. Chen et al. [42] commented in their study on the adsorption of R- and S-phenylglycine on Cu(110) that the ratio of R/S mixture is directly related to the relative intensity of the LEED spots, for the R- and S- patterns. For example, a coverage of R- and S-phenylglycine with the ratio of R/S = 1 gave LEED spot intensities that were similar and for a ratio of R/S = 3, the LEED spots from the R enantiomer were much more intense. Therefore, as a first approximation, the LEED spot intensities were assessed to estimate the enantiomeric excess of one enantiomer over the other. The quantitative analysis of LEED patterns in this manner is fraught with difficulties. Other factors, than simply the fraction of a surface covered by the LEED structure, contribute to the intensity of the observed LEED pattern. For example, LEED is sensitive to subtle variations in height and orientation, so the facets of the $Te/Cu(643)^R$ surface not aligned well with the LEED optic will be weaker than facets that are well orientated, although both may contain similar quantities of alloy. Also, small changes the nature of the unit cell may cause constructive or destructive interference of the scattered electron waves and drastically change the intensity of an observed LEED spot. Therefore, it is stressed that the following analysis of the spot intensity of the LEED pattern is a rough estimate.

The enantioselectivity and enantiomeric excess can be estimated by using line profiles, integrated over the width of the spot. To improve the reliability of the measurement equivalent spots for each enantiomer were used, as shown in figure 5.20. Previous studies of enantiomeric excess have studied the yield of a particular handedness of molecule from a chiral surface. The enantioselectivity (ES_x) of reaction x is defined as [41]:

$$ES_x = \frac{Y_x^{R/R}}{Y_x^{R/S}}, \tag{5.3}$$

where $Y_x^{R/R}$ is the yield of the (R) enantiomer on the R surface for reaction x and $Y_x^{R/S}$ is the yield of the S enantiomer on the (R) surface for reaction x. This definition implies that a racemic mixture has ES_x = 1. One can also calculate the enantiomeric excess (EE_x) of reaction x, using the following definition [43, 44]:

$$EE_x = \left|\frac{ES_x - 1}{ES_x + 1}\right|, \tag{5.4}$$

where ES_x is defined as in equation 5.3. Typically, ES_x has been calculated from TPD data. Here, the idea of measuring enantioselectivity is extended to the intensity profiles of LEED patterns. For the Te/Cu(643)^R system the enantioselectivity can be written, as a first approximation as:

$$ES_1 = \frac{I_1^{R/R}}{I_1^{S/R}}, \tag{5.5}$$

where ES_1 is the enantioselectivity of the Cu(643)^R surface for structure 1. $I_1^{R/R}$, is the intensity of the LEED spots for the (R) overlayer enantiomer and $I_1^{S/R}$ is the intensity of the LEED spots for the (S) overlayer enantiomer on the Cu(643)^R surface. As the substrate is the (R) enantiomer the most intense spots of structure 1 (as defined by the red box in figure 5.7 (d)) are also labelled as (R). It is noted that care must be taken in measuring the intensity of LEED spots, that *equivalent* LEED spots are compared. Figure 5.20 (a) shows the LEED pattern obtained for structure 1 at 110 K, annotated with a red line and blue line, indicating where line profiles were taken. The line profiles obtained from figure 5.20 (a) are displayed in figure 5.20 (c) and are typical of the LEED patterns from a 0.28 ML Te coverage. The surface unit cell is highlighted by the blue box, in figure 5.7 (d), as the (R)

enantiomer because the surface is Cu(643)^R and it is hypothesised that the handedness of the surface favours the growth of one enantiomer over the other. It is first noted that the width of the LEED spots are the same for both the (R) and (S) enantiomers, implying that the ordering in (R) and (S) enantiomers are similar. After averaging over 50 different line profiles from 10 different beam energy LEED patterns, it was found that, the (R) enantiomer is favoured for structure 1, with ES_1 = 4.4 ± 0.5:1 and EE_1 = 63 ± 15 %.

In the same way as for structure 1, the intensity of equivalent spots can be measured on the LEED patterns of structure 2 to estimate the enantiomeric excess of one enantiomer over the other. Even though the unit cell of structure 2 has been found to be within error rectangular and therefore achiral, it is still valid to assess the difference in intensity of each domain to gain a rough insight into relative concentration of each structure on the surface. This is done in exactly the same way as was done with structure 1 - by comparing the relative intensities of equivalent pairs of spots, over a large series of patterns from different beam energies. A typical line profile is displayed in figure 5.20 (d). This line profile highlights the variation in spot width and position from the LEED patterns of structure 2: not all spots overlap, due to the variation in terrace size. Averaged over a total of 50 line profiles, of the same length as in figure 5.20 (d), it was found that the (R) enantiomer has, ES_2 = 1.3 ± 0.5 and EE_2 = 13 ± 15 %. The enantiomeric excess lies within error of 0 %, implying that the alloyed surface contains equal concentrations, which is not surprising since the unit cell is achiral. It is hypothesised that the thicker the Te film, the less influence the Cu(643)^R substrate has on dictating the handedness of the overlayer. Structure 1, which has a maximum ordering at 0.28 ML, shows a large enantioselectivity (EE_1 = 62 ± 15 %) in the (R) handed overlayer. Whereas structure 2, which shows a maximum ordering at 0.85 ML, shows little preference to which domains grows (EE_2 = 13 ± 15 %). As the coverage increases, the energy barrier in forming the unfavoured structure may be reduced. The Cu(643)^R substrate also dictates that the alloy is the rather unusual CuTe structure. Beyond a single monolayer, the Cu(643)^R substrate is no longer directing the growth mode of the alloy and is free to form a rough or polycrystalline Cu_2Te alloy.

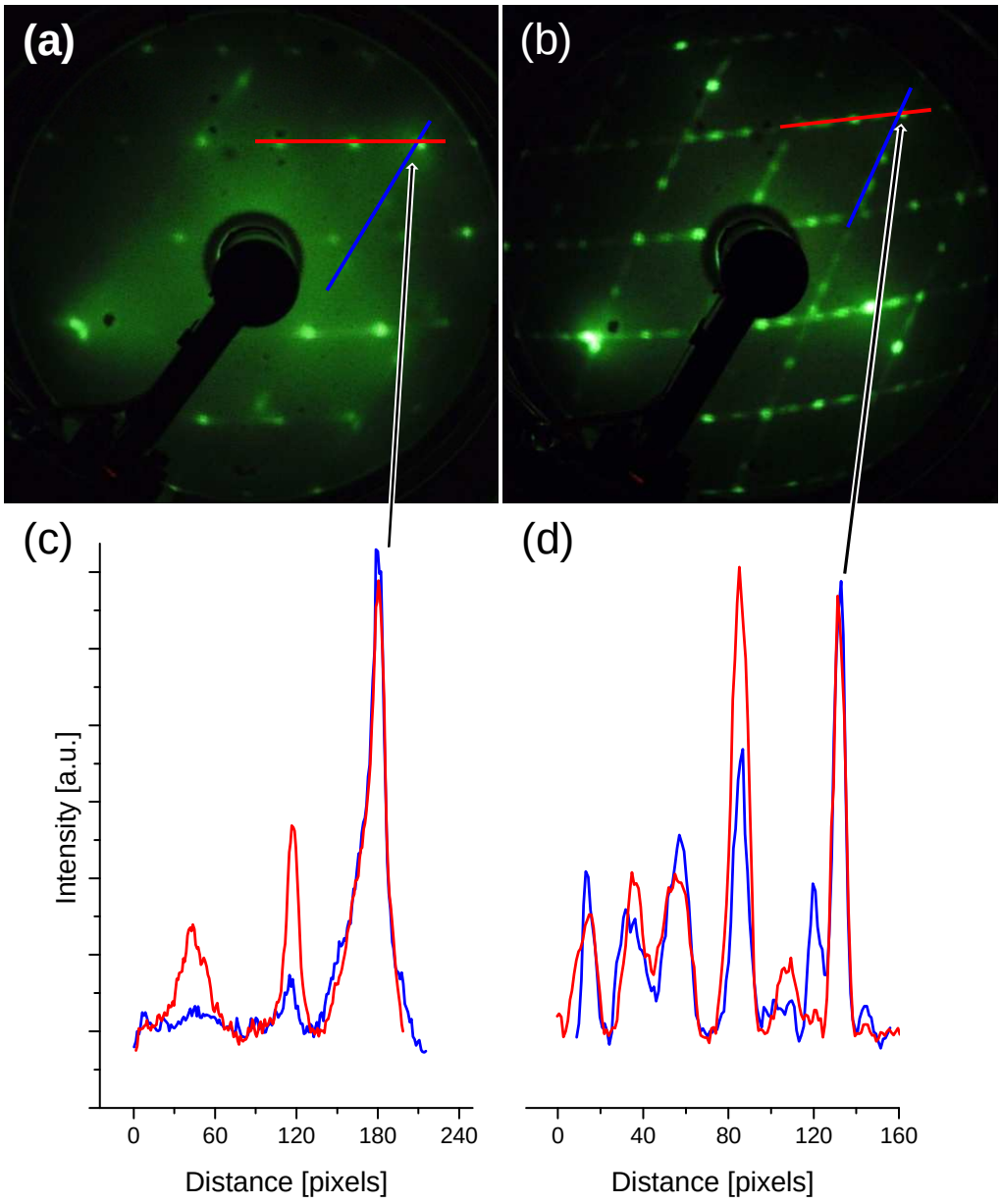

Figure 5.20. (a) 0.28 ML Te/Cu(643)^{R} and (b) 0.85 ML Te/Cu(643)^{R} LEED patterns obtained at 110 K. The beam energy is 138 eV. Graphs (c) and (d) show the background subtracted, integrated line profiles obtained from the red and blue lines, annotated on LEED patterns (a) and (c), respectively. The integrated intensity ratio of red to blue line profiles from (a) is 4.4 ± 0.5:1 and (b) is 1.3 ± 0.5 :1.

Another question, one might ask is: what features of the Cu(643)^R surface drives the observed CuTe surface structure? Since the growth modes of the Te/Cu(643)^R system are completely different to that of Te/Cu(111) (section 3.2.1) and Te/Cu_{poly} (section 3.2.2), it is clear that the surface termination has a strong impact on the composition and structure of the Cu-Te alloys formed (i.e. Cu(643) acts as a template for Cu-Te growth). If one considers the Cu(643)^R surface, the kink sites are the intuitive points for Te nucleation. Indeed, DFT calculations show that I [18] and Br [19] preferentially adsorbs at kink sites of Cu(643)^R. In addition, Hazzazi et al. [20] demonstrated that at low surface coverage, Bi, Au and Ag selectively adsorbed on the chiral Pt(321) surface in kink and step sites. Only when the kink and step sites were full, that Bi, Au and Ag began to fill the terrace sites. Furthermore, the observed reduction in temperature of the alloying phase transition temperature, shown in figure 5.19, is consistent with a step mediated alloying mechanism between Te and Cu. Figure 5.21 shows the mechanism for step mediated alloying, in agreement with the proposed mechanism for the alloying of Pt on the vicinal Cu(12 12 11) surface [40]. The model proposed involves, firstly, the nucleation of a Te adatom at a kink site or step edge and then the rapid diffusion of Te into subsurface layer, forming a bulk like CuTe alloy. The diffusion of an adatom at a step or kink is much more facile than on a flat surface (e.g. Cu(111)). Figure 5.21 shows that relatively few, under co-ordinated, substrate atoms require to move for the inclusion of a foreign adatom below the surface. This is in agreement with the XPS data which implies that the Te adatoms are rapidly incorporated within a bulk alloy (i.e. some Te atoms are below the surface). The fact that Te readily diffuses into Cu(111) at room temperature, a close packed surface (chapter 3) implies that the diffusion Te/Cu(643)^R will be even more facile.

In agreement with the literature on atomic and molecular adsorption on kinked metal surfaces and the observation of step mediated alloying, it is proposed that the kink sites influences the resulting Cu-Te alloy structures for the Te/Cu(643)^R system. The use of the kink sites as effective nucleation sites for Te adatoms will now be discussed. Figure 5.22 shows the ideal Cu(643)^R surface looking directly down upon it with Te atoms adsorbed at some of the kink sites. The proposed nucleation site of structure 1 has Te atoms occupying all the kink sites on the Cu(643)^R surface. This gives unit cell parameters of a_1 = 0.675 nm, b_1 = 0.742 nm and α_1 = 69°.

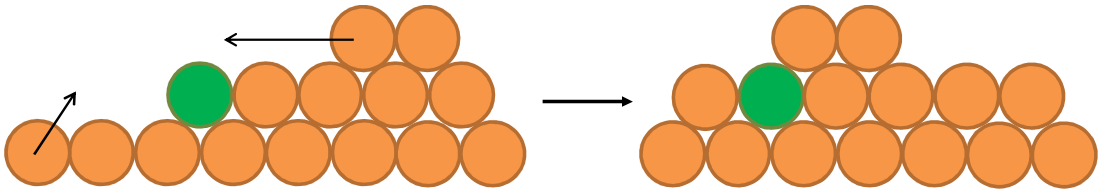

Figure 5.21. Proposed model for the step mediated alloying of Te on Cu(643)^R. This figure shows the nucleation and subsequent diffusion of a Te adatom into sub-surface region of the vicinal Cu surface. Only a few under co-ordinated substrate atoms require to move.

Table 5.4 shows that these parameters are reasonably close to the dimensions observed with LEED and STM. Structure 1 was determined with LEED and STM to be flat, as illustrated by the STM pattern in figure 5.9, with lattice parameters of a_1 = 0.51 ± 0.01 nm, b_1 = 0.71 ± 0.01 nm and α_1 = 57 ± 2°. The difference between the value of a_1 predicted by our nucleation model and observed lattice parameter is reasonably large ~0.1 nm. This discrepancy may be accounted for by the fact that a proportion of exists Te subsurface and may cause changes in the lattice parameter. In addition, the substrate is subject to a high temperature anneal to 773 K after deposition and may give the surface atoms sufficient energy to restructure into the structure observed with LEED. The b_1 direction of the proposed model of nucleation is in good agreement with the observed unit cell. In addition, the surface atoms on steps have high mobility and a high temperature anneal allow the atoms to reorder into the structure observed with LEED and STM.

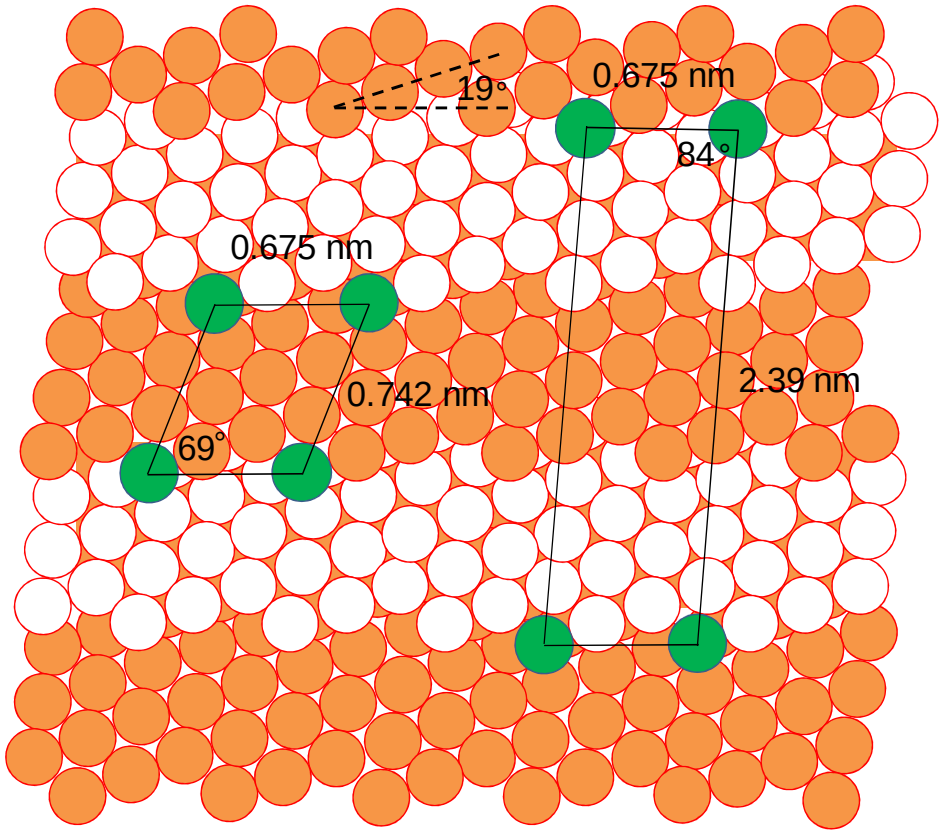

Figure 5.22. Ideal Cu(643)^R substrate with Te atoms adsorbed at some of the kink sites. The orange and white spheres represent C atoms. The alternating colour scheme, of white and orange spheres, is used to aid visualisation of the steps and kinks. Green spheres indicate Te atoms. The two black boxes indicate the proposed nucleation sites for structures 1 and 2 of the CuTe alloy. Some Te atoms have been omitted for clarity (see text for details).

Dimension	Lattice parameter of kink site nucleation on Cu(643)^R	Measured dimension with LEED/STM (after annealing to 773 K)
a_1	0.675 nm	0.51 ± 0.01 nm
b_1	0.742 nm	0.71 ± 0.01 nm
α_1	69°	57 ± 4°
a_2	0.675 nm	0.63 ± 0.01 nm
b_2	2.39 nm	2.21 ± 0.05 nm (4 atom terrace) 2.74 ± 0.05 nm (5 atom terrace)
α_2	84°	87 ± 4°

Table 5.4. Comparison of unit cell dimensions of idealised kink site nucleation with the lattice parameters obtained with LEED and STM.

The CuTe alloy labelled structure 2 can only be partially explained using the Cu(643)^R substrate as a template for growth. The larger box in figure 5.22 shows the proposed nucleation sites for the formation of structure 2. As structure 2 is formed from a higher coverage than structure 1, there will be naturally more Te atoms on the surface. Hence, the model shown in figure 5.22 will have Te atoms adsorbed at other kink sites, along step edges and on the (111) terraces, which are omitted on the diagram for clarity. Structure 1 has all kink sites filled, which implies that Te atoms in structure 2 have also nucleated along steps and on terraces. The dimensions shown on figure 5.22, for the nucleation sites are in reasonable agreement with the observed LEED and STM data, if Te atoms form unit cells that are 3 steps in length. Dimensions of the proposed nucleation sites for the formation of the unit cell were determined as being a_2 = 0.675 nm, b_2 = 2.39 nm α_2 = 83°. The length of the step is variable, as shown i n the STM (figure 5.15) and the streaked nature of the LEED pattern in the direction of the steps, b_2 (figure 5.7). The variation arises from the number of atoms that make up a step: a 4 atom wide step has b_2 = 2.21 nm and a 5 atom wide step has b_2 = 2.74 nm. The kink site separation in structure 2 (figure 5.22) is 2.39 nm, which is a non integer chain length of CuTe. It is proposed that the high mobility of the atoms (also assisted by the high temperature anneal) on the surface mean that the surface reconstructs to form energetically more stable 4 or 5 atom wide terraces on the surface. It is interesting yet unclear why the kink sites 3 steps apart appear to be acting as a unit cell for structure 2. There is nothing unique about a CuTe step length being 3 times that of the step of Cu(643)^R other that the fact that it is a reasonably good match to a 4 or 5 atom wide step. It is suggested that the driving force must be the most energetically favourable state for incorporating all Te atoms into a Cu-Te alloy.

5.4 Conclusions

Chapter 5 has examined the alloying of Te with the Cu(643)^R substrate. To our knowledge, this is the first example of using a chiral substrate to fabricate an overlayer alloy that retains the chirality of the substrate. In summary, the addition of Te onto the Cu(643)^R surface and subsequent annealing to 773 K induces extensive surface reconstruction and faceting. The alloying of Te on Cu(643)^R is step mediated which results in the alloying phase transition temperature being ~50 K less than on the nominally flat Cu(111) substrate. Below 225 K, alloying of Cu-Te is kinetically limited, with a rough, disordered Te film growing on the Cu(643)^R surface, analogous to Cu(111). Above 225 K, the deposition of Te leads to two distinct alloy phases. The first of which, structure 1, exists in range of θ_{Te} = 0.18-0.45 ML with lattice parameters of a_1 = 0.51 ± 0.01 nm, b_1 = 0.71 ± 0.01 nm

and α_1 = 57 ± 3°. The second structure, structure 2, exis ts in the range of θ_{Te} = 0.45-1.5 ML and forms a stepped structure also with a rectangular cell. The unit cell has parameters of a_2 = 0.48 ± 0.01 nm, b_2 = 2.25 ± 0.05 nm and α_2 = 87 ± 4°. Patches of disordered Cu_2Te begin also to form immediately upon deposition and dominate the film composition above 1 ML.

It is tentatively proposed that the kink sites of $Cu(643)^R$ act as nucleation centres for the growth of these unusual Cu-Te alloys. Both chiral surface alloys have a stoichiometry close to that of CuTe: structure 1 is a unique surface phase, while structure 2 is cautiously described as a distorted form of the mineral Vulcanite, with both structures using the $Cu(643)^R$ kink sites as a template for growth. To a first approximation, it is estimated that structure 1 demonstrates enantiomeric excess of greater than 50 % of the (R) CuTe enantiomer, due to good registry with the $Cu(643)^R$ surface. The thicker Cu-Te film has equal concentrations of domains, to a first approximation, due to the decreasing influence of the substrate in dictating growth. High miller index surfaces are intrinsically unstable because of the under coordinated surface atoms, as shown by thermally roughened STM images that can only be collected at 77 K [9]. The ease of collection STM data from the $Te/Cu(643)^R$ surface at 300 K, shows that Te must have a stabilising effect on the atomic mobility of the $Cu(643)^R$ surface. It is suggested that the Te structures, formed by deposition at 300 K are rough or disordered, but crucially Te nucleates in kink sites that promote the growth of ordered CuTe structures after annealing. Rapid, step mediated alloying of Te into a bulk like alloy occurs, with annealing to 773 K allowing the Te covered $Cu(643)^R$ surface to reconstruct to a more energetically favourable structure. The reconstructions observed imply significant Te diffusion and Cu faceting, which is reasonable, as stepped surfaces have high atomic mobility due to lower co-ordination.

The data presented here is interesting and provides good insight into the alloying of Te and $Cu(643)^R$ but it does not provide an complete description of the growth modes. Further work with, for example, STM, STS and LEED IV, is required to fully elucidate the atomic structure of the surface. For example, current STM data suggest a counter intuitive growth mode, with the surface going from stepped (0 ML) → flat (0.28 ML) → stepped (0.85 ML). Additional STM images are also required to fully understand the mesoscopic faceting observed in this system.

The $Te/Cu(643)^R$ system is a useful prototype to assess the feasibility and structure of novel chiral surface alloys, chosen because of the strong interaction between Cu and Te, as demonstrated in chapter 3. Our study gives precedent into studying other systems,

such as the topological insulator, Bi_2Te_3 [45], where it has been shown that electron spin chirality is of crucial importance in the electronic structure of the topological insulator. It has been recently shown in the $Pb_{1-x}Sn_xSe$ system [46] that crystalline (physical) symmetry can also topologically protect surface electronic states. It would be therefore interesting to produce a chiral Bi single crystal and look at the deposition of Te onto it, to firstly assess if any chiral alloy structures formed. If they did form, then it would be of significant interest to the wider scientific community to test their topological insulating properties (this is generally done with ARPES, whereby the full band structure can be determined). In addition, modifying the surface composition of a naturally chiral surface offers the prospect of tuning the enantioselectivity of a particular catalytic surface reaction [4,47,48]. However, relatively little work has been devoted to this due to fact that naturally chiral substrates, at the moment, cannot be produced in large enough quantities to be of practical use [48].

5.5 References

[1] J. Clayden, N. Greeves, S. Warren, P. Wothers, *Organic Chemistry*, 1st ed., Oxford University Press, 2001.

[2] H.C. Kolb, M.S. Van Nieuwenhze, K. B. Sharpless, *Chem. Rev*. **94** (1994) 2483

[3] G. Held, M.J. Gladys, *Top. Catal*. **48** (2008) 128.

[4] D.P. Woodruff, T.A. Delchar, *Modern Techniques of Surface Science*, 2nd ed, Cambridge University Press, 1994.

[5] M. Giesen, S, Dieluweit, *J. Mol. Catal. A: Chem.* **216** (2004) 263.

[6] C.F. McFadden, P.S. Cremer, A.J. Gellman, *Langmuir* **12** (1996) 2483.

[7] A. Ahmadi, G. Attard, J. Feliu, A. Rodes, *Langmuir* **15** (1999) 2420.

[8] X. Zhou, S. Perry, *J. Mole. Catal. A: Chem.* **216** (2004) 257.

[9] A.R. Bachmann, F. Ostendorf, S. Speller, *J. Phys.: Condens. Matter* **15** (2003) S3337.

[10] D.S. Sholl, A. Asthagiri, T.D. Power, *J. Phys. Chem. B* **105** (2001) 4771.

[11] T.D. Power, A. Asthagiri, D.S. Sholl, *Langmuir* **18** (2002) 3737.

[12] A.E. Baber, A.J. Gellman, D.S. Sholl, E.C.H. Sykes, *J. Phys. Chem. C* **112** (2008) 11085.

[13] G. Jones, M.J. Gladys, J. Ottal, S.J. Jenkins, G. Held, *Phys. Rev. B* **79** (2009) 165420.

[14] M.L. Clegg, S.M. Driver, M. Blanco-Rey, D.A. King, *J. Phys. Chem. C* **114** (2010) 4114.

[15] A.R. Bachmann, A. Mugarza, J.E. Ortega, S. Speller, *Phys. Rev. B* **64** (2001)

153409.

[16] A.R. Bachmann, S. Speller, A. Mugarza, J.E. Ortega, *Surf. Sci.* **526** (2003) L143.

[17] J. Lobo, E.G. Michel, A.R. Bachmann, S. Speller, J. Kuntze, J.E. Ortega, *Phys. Rev. Lett.* **93** (2004) 137602.

[18] A. Conti, J. Creuze, Y. Garreau, *Phys. Rev. B* **72** (2005) 115424.

[19] S. Fölsch, A. Helms, S. Zöphel, J. Repp, G. Meyer, K.H. Rieder, *Phys. Rev. Lett.* **84** (2000) 123.

[20] A. Riemann, B.N. Satterwhite, B.E. Owens, *Surf. Sci.* **604** (2010) 2157.

[21] A.J. Francis, P.A. Salvador, *J. Appl. Phys.* **96** (2004) 2482.

[22] A.J. Francis, P.A. Salvador, *Ceram. Trans,* **158** (2005) 37.

[23] A.J. Francis, A.J. Koritnik, A. Gellman, P.A. Salvador, *Surf. Sci*. **601** (2007) 1930.

[24] O.A. Hazzazi, C.A. Harris, P.B. Wells, G.A. Attard, *Top. Catal*. **54** (2011) 1392.

[25] P. Kamakoti, J. Horvath, A.J. Gellman, D.S. Sholl, *Surf. Sci.* **563** (2004) 205.

[26] D.M. Rampulla, A.J. Gellman, D.S. Sholl, *Surf. Sci.* **600** (2006) 2177.

[27] H. Neumann, M. Mast, J. Enderlein, R.D. Tomlinson, M.V. Yakushev, *Cryst. Res. Technol*. **31** (1996) 75.

[28] A.J. Ricco, H.S. White, M.S. Wrighton, *J. Vac. Sci. Technol*. **2** (1984) 910.

[29] F. Debbagh, E.L. Ameziane, M. Azizan, M. Brunel, T.T.A. Nguyen, *Mater. Sci. Eng*. **38** (1996) 223.

[30] S. Hufner, G.K. Wertheim, J.H. Wernick, *Solid State Commun*. **17** (1975) 417.

[31] T.Y Lee, S. Sarbach, K. Kuhnke, K. Kern, *Surf. Sci.* **600** (2006) 3266.

[32] C.K. Rhee, C. Jung, B. Ku, *J. Sol. Stat. Electrochem.* **9** (2005) 247.

[33] P. Rodriguez, E. Herrero, A. Aldaz, J.M. Feliu, *Langmuir* **22** (2006) 10329.

[34] J. Tersoff, Y.H. Phang, Z.Y. Zhang, M.G. Lagally, *Phys. Rev. Lett.* **75** (1995) 2730.

[35] P. Müller, A. Saúl, *Surf. Sci. Rep.* **54** (2004) 157.

[36] Y.N. Yang, E.S. Fu, E.D. Williams, *Surf. Sci.* **356** (1996) 101.

[37] F. Pertlik, *Miner. Petrol.* **71** (2001) 149.

[38] R.V. Baranova, Z.G. Pinsker, *Kristallografiya* **9** (1964) 104.

[39] D.P. Woodruff, *Curr. Opin. Sol. Stat. Mater. Sci.* **7** (2003) 75.

[40] P.C. Dastoor, D.J. O'Connor, D.A. MacLaren, W. Allison, T.C.Q. Noakes, P. Bailey, *Surf. Sci.* **588** (2005) 101-107.

[41] H. Röder, E, Hahn, H. Brune, J.P. Bucher, K. Kern, *Nature* **366** (1993) 141.

[42] O. Chen, C.W. Lee, D.J. Frankel, N.V. Richardson, *PhysChemComm* **2** (1999) 41.

[43] D.M. Rampulla, A.J. Gellman, *Surf. Sci*. **600** (2006) 2833.

[44] D.M. Rampulla, A.J. Francis, K.S. Knight, A.J. Gellman, *J. Phys. Chem. B* **110** (2006) 10411.

[45] H. Zhang, C. Liu, X. Qi, X. Dai, Z. Fang, S. Zhang, *Nature Phys.* **5** (2009) 438.

[46] P. Dziawa, B.J. Kowalski, K. Dybko, R. Buczko, A. Szczerbakow, M. Szot, E. Łusakowska, T. Balasubramanian, B. M.Wojek, M. H. Berntsen, O. Tjernberg, T. Story, *Nature Mater.* **11** (2012) 1023.

[47] F. Zaera, *J. Phys. Chem. C* **112** (2008) 16195.

[48] A.J. Gellman, *ACS Nano* **4** (2010) 5.

6. A Study of the Core-Shell Architecture in Nanoribbons of TaS_3

6.1 Introduction

Chapters 3, 4 and 5 have dealt with thin film growth on single crystal surfaces, which naturally favours the use of surface science techniques (XPS, UPS, LEED and STM) over electron microscopy. We now turn to a system that would normally lend its self well to materials characterisation techniques based on electron microscopy - nanoribbons of TaS_3. Like in the previous experimental chapters (chapters 3, 4 and 5), one of the aims of this chapter was to compare and contrast the information gathered from both sets of techniques, with particular emphasis on the difference between the core and shell of the nanoribbon. The study presented in this chapter has been published in *Nanoscale* (M.O. King et al., *Nanoscale* **4** (2012) 607).

TaS_3 belongs to a large set of inorganic solids known as transition metal chalcogenides (TMCs) [1,2]. As stated in chapter 1, TMCs display a variety of interesting phenomena: in the case of TaS_3, it is known to undergo a Peierls transition with the formation of a charge density wave (CDW) state [3]. In recent years, a number of methodologies have been developed to synthesise TMCs nanomaterials [4-8] and in the case of TaS_3 have yielded wires, ribbons and belts that are typically up to millimetres long, microns wide but only a few tens to hundreds of nanometres thick [7,8]. The resultant surface to volume ratios, which are orders of magnitude larger than those of bulk materials, are often the reason for the unusual properties of TMCs at the nanoscale, since these ratios imply that surface electronic states can dominate the material's characteristics. However, as it is shown here, it is essential to establish the existence and role of phases at the interfaces of such materials and the contribution that such species could make towards observed chemical and physical phenomena. For example, a core-shell architecture may not be detectable through bulk analytical techniques but the shell would nevertheless present an additional interface that mediates direct contact to the TMC and thereby affects the TMC's apparent properties.

It has been reported that bulk TaS_3 can crystallise in two different unit cells: monoclinic [9,10] or orthorhombic [11,12]. The monoclinic structure is shown in figure 6.1 and is denoted *m*-TaS_3. It belongs to the $P2_1/m$ space group and has unit cell parameters of a = 0.9515 nm, b = 0.33412 nm, c = 1.4912 nm, α = 90°, β = 109.99° and γ = 90°. The orthorhombic cell is labelled *o*-TaS_3 and has unit cell dimensions of a = 3.6804 nm, b = 1.5173 nm, c = 0.3340 nm and $\alpha = \beta = \gamma$ = 90°. *o*-TaS_3 belongs to the $C222_1$ space group.

To our knowledge, the positions of the atoms within the *o*-TaS_3 cell have never been published, which is surprising given the volume of work undertaken on this material, and hence a diagram cannot be given. However, Roucau et al. [11] states that *o*-TaS_3 contains 24 TaS_3 chains per unit cell and hence we still regard *o*-TaS_3 as a one dimensional material. Recently, nanobelts of TaS_3 [8] have been reported and form with *o*-TaS_3 structure. Both *m*- and *o*- unit cells of TaS_3 have chains of Ta^{4+} running through the crystal, with individual chains interacting with each other through weaker Van der Waals' forces. Electrons can only easily propagate along the long chains of Ta^{4+} ions which gives rise to TaS_3 being regarded as a quasi one dimensional conductor. The structure of TaS_2, on the other hand, is shown in figure 6.1 (b). It is a layered structure with two dimensional sheets of S^{2-} and Ta^{4+} and hence is described as a two dimensional conductor. It is important to describe TaS_2 because TaS_3 decomposes into TaS_2 and S above 1073 K, as we will show with TEM in figure 6.13.

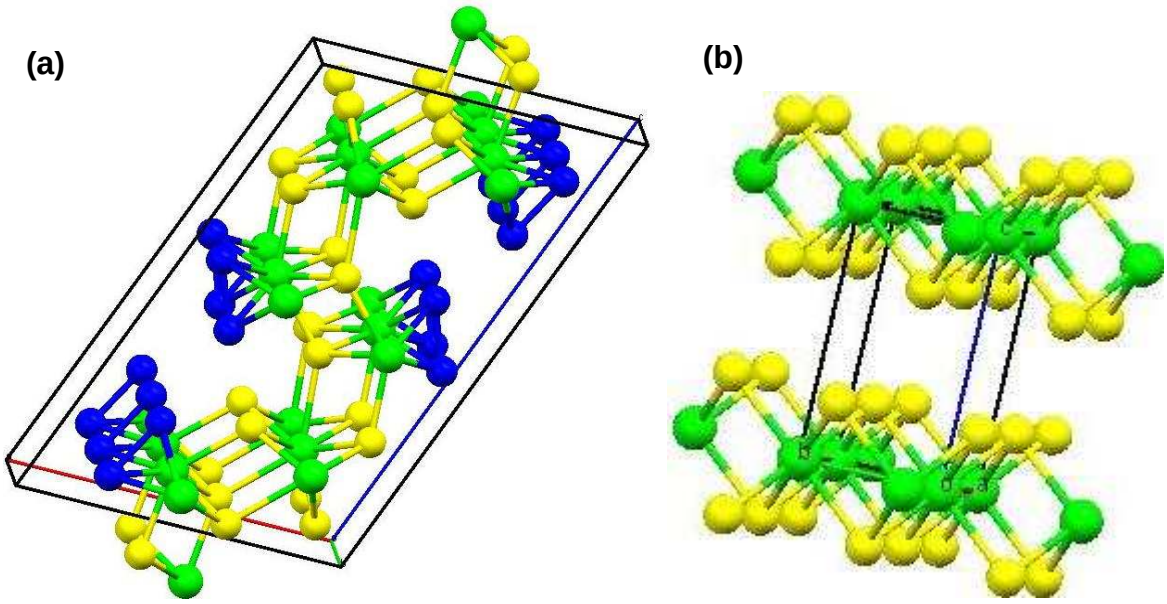

Figure 6.1. Structure of (a) *m*-TaS_3 [9] and (b) 1T-TaS_2 [13]. The yellow spheres represent S^{2-}, blue spheres represent S^{-} or $(S_2)^{2-}$ and the green spheres represent Ta^{4+}.

One dimensional solids are inherently unstable and undergo a Peierls distortion below a certain transition temperature [14]. In the cases of *o*-TaS_3 and *m*-TaS_3, the Peierls transition temperature, T_p, has been measured to be 210 K and 240 K, respectively [11]. The Peierls distortion is a periodic distortion of the crystalline lattice that gives rise to a

modulation of local electron density, commonly known as CDWs [14]. Figure 6.2 shows a graphical depiction of the Peierls distortion and its resultant CDW. As CDWs are a modulation of local electronic structure, they have been shown to be observable in XPS as changes in core-level electronic structure (for example 1T-TaS_2 and 1T-$TaSe_2$ [15-17]). Peierls distortions are changes in the lattice and are therefore observable with TEM, in particular with SAED (for example bulk TaS_3 [11], NbS_3 [18] and $MgTi_2O_4$ [19]). The SAED pattern is particularly sensitive to the Peierls distortion as the additional Peierls superlattice gives rise to extra diffraction spots.

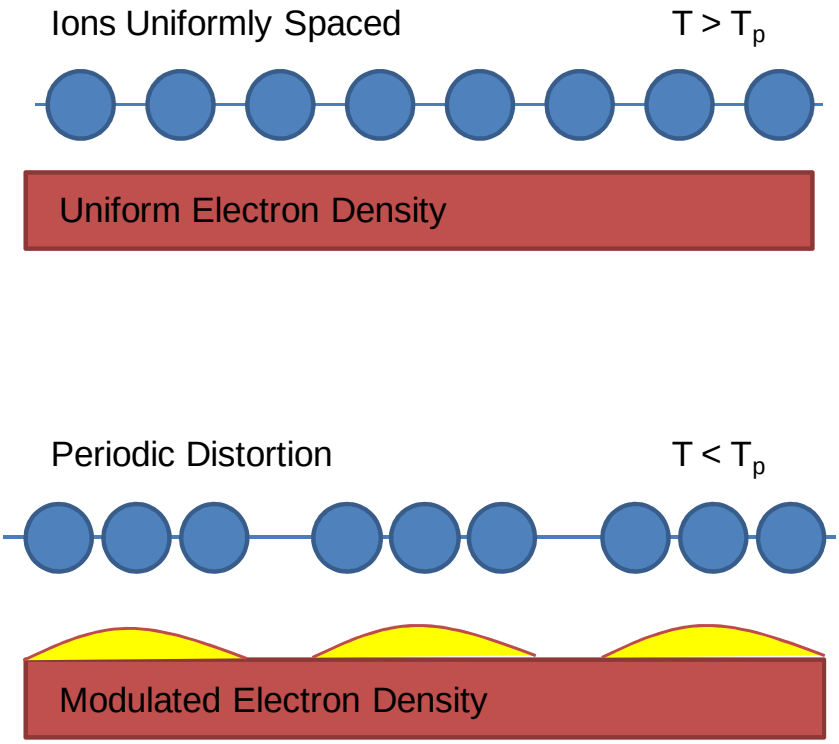

Figure 6.2. Schematic diagram illustrating the Peierls distortion and the resultant CDW. T_p is the Peierls transition temperature.

This chapter describes the characterisation of TaS_3 nanoribbons with electron microscopy and surface science experiments (XPS and UPS). The data show a striking dissimilarity between the structure and the thermal properties of the shell (2-20 nm) and the core (100-500 nm). Surprisingly, given the amorphous and heterogeneous nature of the nanoshell, our UPS data suggest that it has one dimensional electronic properties. Significantly, the chemical stability of the nanoshell is dependent on the nature of the supporting substrate.

6.2 Results

6.2.1 Synthesis

The synthesis of the TaS_3 nanoribbons was performed by Mr. Saleem Denholme in Prof. D. Gregory's inorganic materials group at the University of Glasgow [8,20,21]. The synthesis process will be described briefly here. Ta (99.9 % purity) and S (99.5 % purity) were ground together using a mortar and pestle, in a stoichiometric ratio of Ta : S = 1 : 3. The resultant mixture was loaded into a silica tube and sealed under a rough vacuum (~10^{-3} mbar). Once sealed, the ampoules were inserted horizontally into a furnace at 923 K for 60 hours. The products contained both powders and nanofibrous materials which were separated using tweezers. It should be noted that prior to introduction into UHV, it was observed that the nanoribbons were encased in a coating of globules of sulfur. A representative TEM image of the pre-UHV annealed nanoribbons is shown in figure 6.3 (a), with a TEM image of a nanoribbon that has been annealed to 400 K in UHV shown in figure 6.3 (b). The morphology of the pre-UHV nanoribbon is clearly different: it is rough and mottled compared to the smooth post-UHV ribbons. The EDS spectrum, labelled 1 in figure 6.3 (c) shows that the small globules are composed entirely from sulfur, a result of some sulfur not reacting. EDS also shows that the pre-UHV ribbons are sulfur rich, having a Ta : S ratio ~1 : 5, a result of the ribbon being encased in excess, unreacted sulfur. Therefore, to sublime any excess S, the ribbons were heated in a high vacuum (~10^{-7} mbar) at 400 K for 48 hours (i.e. a UHV bakeout).

6.2.2 Room Temperature Characterisation

6.2.2.1 Characterisation of TaS_3 Core

The physical structure of the core of the TaS_3 nanoribbons was determined with PXRD, SEM and TEM. Figure 6.4 shows the PXRD pattern obtained for the TaS_3 nanoribbons, overlaid with the accepted XRD pattern from *o*-TaS_3 [12], which is in reasonable agreement. The lines not accounted for by the TaS_3 reference pattern are elemental S, as the PXRD pattern was obtained before vacuum annealing of the TaS_3 nanoribbons, which was found to sublime excess S from the synthesis process. The PXRD pattern is also consistent with using SAED data shown in figure 6.5 (b), using refined lattice parameters of a = 3.694 ± 0.002 nm, b = 1.4182 ± 0.005 nm, c = 0.3349 ± 0.002 nm.

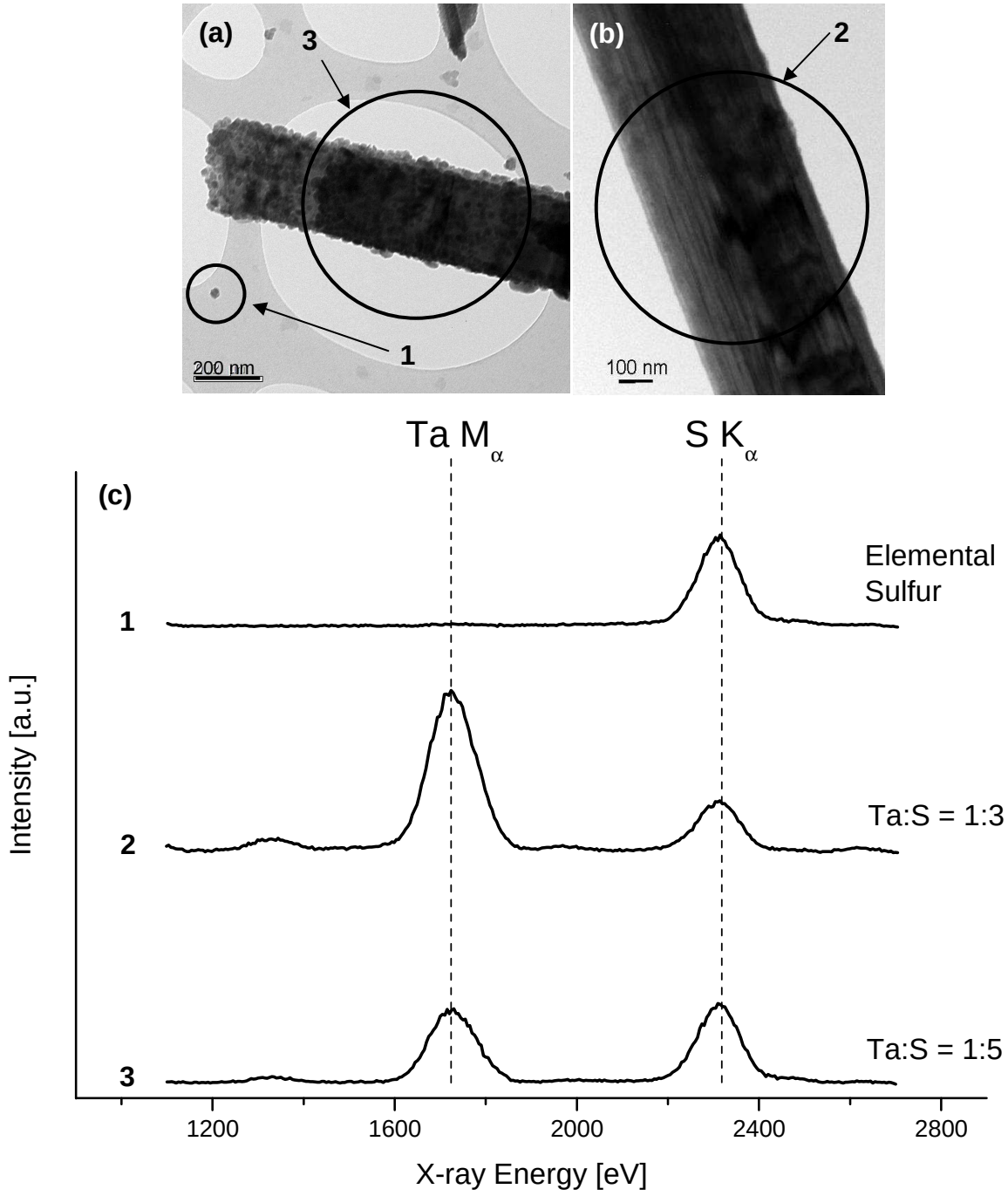

Figure 6.3. (a) TEM image of a TaS_3 nanoribbon immediately after synthesis and before vacuum processing. (b) TEM image of a TaS_3 nanoribbon after vacuum processing. (c) EDS spectra taken from areas indicated on the TEM images (see text for details on EDS quantification).

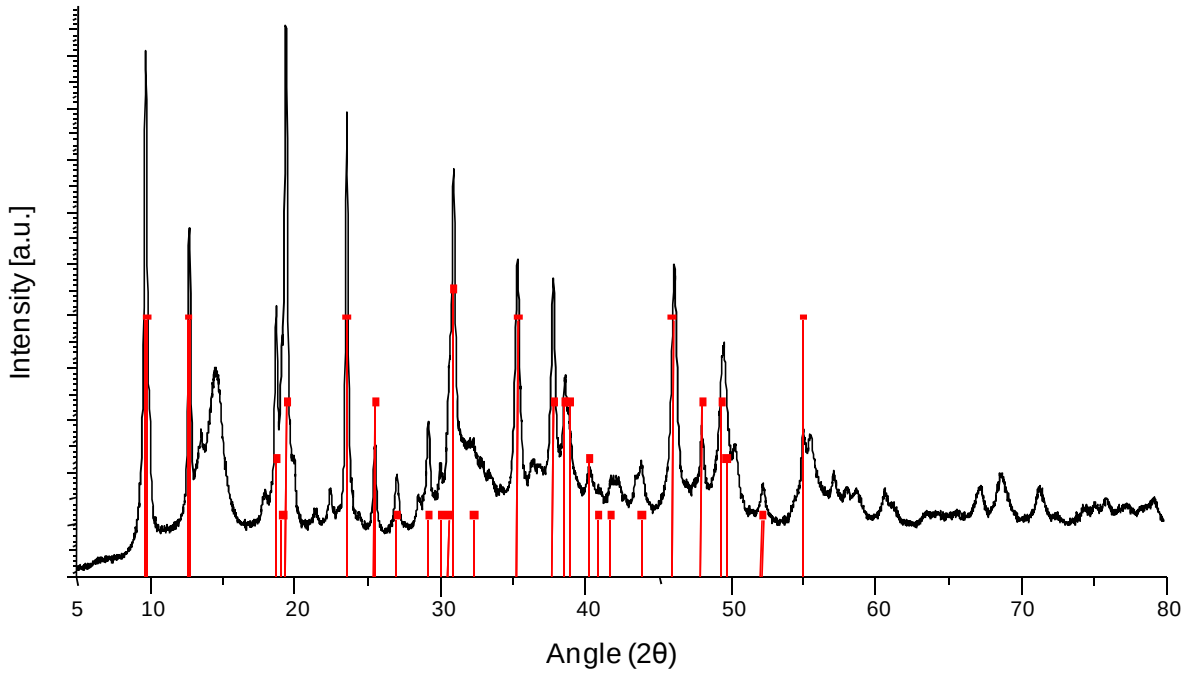

Figure 6.4. PXRD profile of TaS_3 nanoribbons immediately after synthesis and before vacuum treatment in UHV. The black line is the experimental spectrum. Red lines show the positions and relative intensities of the peaks from the standard PXRD pattern of *o*-TaS_3 [12]. The height of the red lines show the approximate relative intensity. The unaccounted lines (2θ ~15°, 22°) are attributed to unreacted sulfur.

A typical low magnification SEM image of the nanoribbons is shown in figure 6.5 (a). It reveals that the ribbons typically had rectangular cross sections with thicknesses of 20-100 nm, widths of 50-500 nm and lengths of several millimetres. These nanoribbons closely resemble those synthesized previously by Wu et al. [7] using a similar methodology. HRTEM images of a typical ribbon are shown in figures 6.5 (d) and 6.5 (e) and show good crystallinity within the bulk of ribbons: the lattice fringe spacing indicated in figure 6.5 (e) was measured to be 0.305 ± 0.008 nm and is indexed to the (12 0 0) reflection of *o*-TaS_3. This gives a lattice parameter of a = 3.65 ± 0.09 nm, which agrees within error with the PXRD data above. EDS data were quantitatively analysed using the Cliff-Lorimer technique, as described in section 2.4.5. The EDS spectra obtained from the ribbon displayed in figure 6.5 (c) is shown in figure 6.5 (f). It was collected from the centre of the ribbon and thereby dominated by its core material. The calculation was performed using equation 2.29. The Cliff-Lorimer k-factor was derived from an in house database [22]. The elemental ratio of Ta : S was calculated to be 1 : 2.98 ± 0.03, within error of TaS_3 composition.

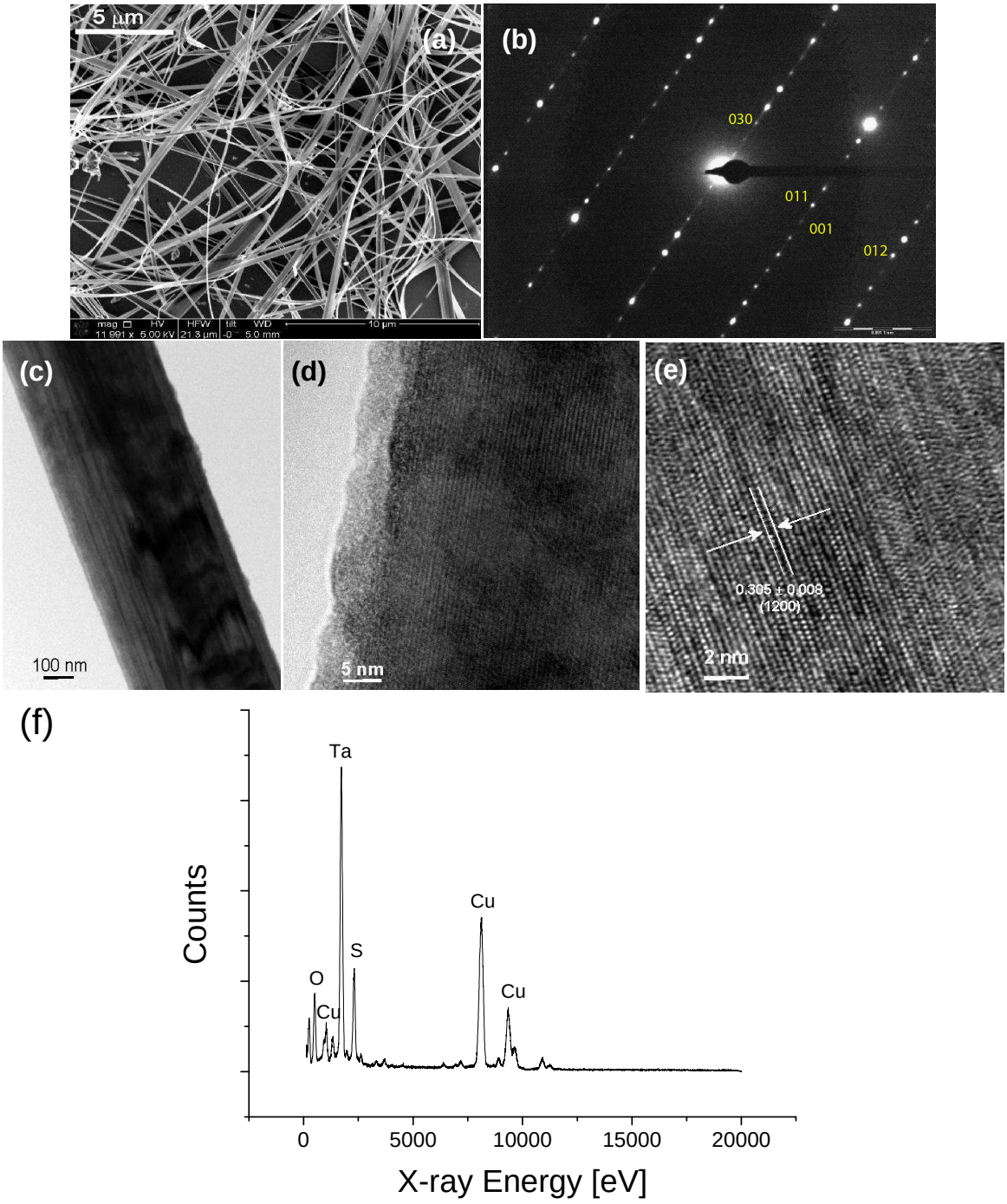

Figure 6.5. Electron microscopy analysis of nanoribbons showing: (a) an SEM image of nanoribbons; (b) electron diffraction and (c) bright-field image of separate ribbons; and HRTEM images of (d) the interfacial region between crystalline core and amorphous edge and (e) the nanoribbon core, showing a lattice fringe separation of 0.305 ± 0.008 nm, which corresponds to the (12,0,0) plane of *o*-TaS_3. (f) EDS spectrum from a typical TaS_3 nanoribbon, with a Ta : S ratio of 1 : 2.98 ± 0.03.

Cu is present in the EDS spectrum because the support grid consists of Cu; O is accounted for by a small amount of surface oxidation, ethanol and water adsorbed to the surface of the nanoribbon. The presence of O is in agreement with the XPS data, shown in figures 6.6 and 6.8. Figure 6.5 (d) clearly reveals a thin, amorphous shell encasing the ribbons, which had a thickness ranging from 2 to 20 nm from ribbon to ribbon and will therefore dominate the surface sensitive photoelectron spectroscopy data presented below.

6.2.2.2 Characterisation of TaS_3 Shell

The surface sensitivity of the XPS and UPS means that the data collected derive exclusively from the amorphous nanoshell of the material revealed by TEM, in figure 6.5 (d). Both XPS and UPS are spatially integrated measurements that probe a significant area of the surface (many mm^2). Figure 6.6 (a) is an XPS spectrum collected over the binding energy region for Ta 4d and S 2s photoelectrons and collected from nanoribbons that had been dispersed onto a Au surface. Identical spectra are obtained from nanoribbons that had been dispersed on the native oxide of Si. The spectrum has been decomposed into Ta $4d^{5/2}$ and $4d^{3/2}$ components and four separate S 2s components, with fitted peak parameters given in table 6.1. Each component was fitted to the sum of a Gaussian function and a Lorentzian function. The asymmetries (α) of the peaks in figure 6.6 were determined to be less than 0.01 and hence the DS function used in chapters 3-5 was replaced with a Lorentzian. The Ta $4d^{5/2}$ and $4d^{3/2}$ binding energies were set to accepted values for Ta^{4+} [23,24] while the four S 2s components could be assigned to $S^{(0)}$ (elemental), S^{2-}, S^- (i.e. $(S_2)^{2-}$) and SO_x^{n+} [25-27]. The SO_x^{n+} component, accounting for 15% of the S signal, is attributable to a small degree of surface oxidation, which is typical of TMCs after atmospheric exposure.

Other core level electronic states of Ta and S were probed with XPS. Figure 6.7 shows the XPS spectra obtained from Ta 4p and 4f core levels. The binding energy of the Ta $4p^{3/2}$ and $4p^{1/2}$ core levels was measured to be 426.7 eV and 404.5 eV respectively, which is in good agreement with Ta^{4+} [28]. The binding energy of the Ta $4f^{7/2}$ and $4f^{5/2}$ core levels were also in good agreement with Ta^{4+} [28] and measured 35.2 eV and 25.6 eV, respectively. The XPS spectra from the S 2p core levels had a low signal to noise ratio and contained spin orbit split peaks, therefore the acquisition of meaningful spectra was not possible for sensible acquisition times. In addition to Ta and S XPS data, O 1s spectra were obtained. Figure 6.8 shows the O 1s XPS data, which confirmed the presence of oxygen on the surface. The O 1s spectrum could be fitted to two peaks, at 533.9 eV and 531.5 eV.

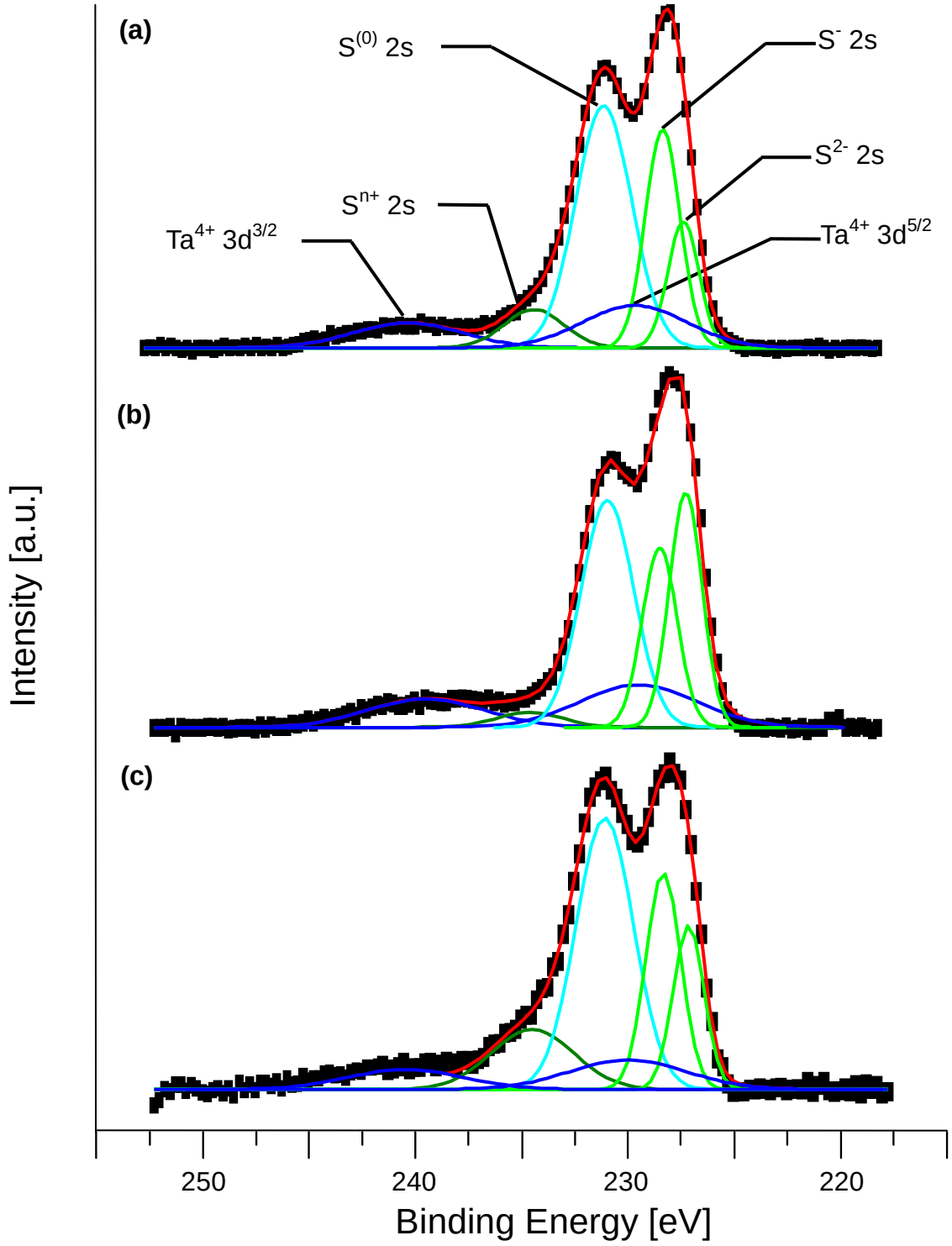

Figure 6.6. XPS spectra spanning the Ta 3d and S 2s core levels and their associated GL fits. (a) TaS_3 nanoribbons deposited on a Au sputtered silicon wafer, immediately after deposition on to the substrate. An identical spectrum is obtained when using Si substrates. (b) TaS_3 nanoribbons deposited upon a silicon substrate which had been flash annealed to 1173 K. (c) TaS_3 had been left for 3 days on Au. The component labels in spectrum (a) also relate to spectra (b) and (c).

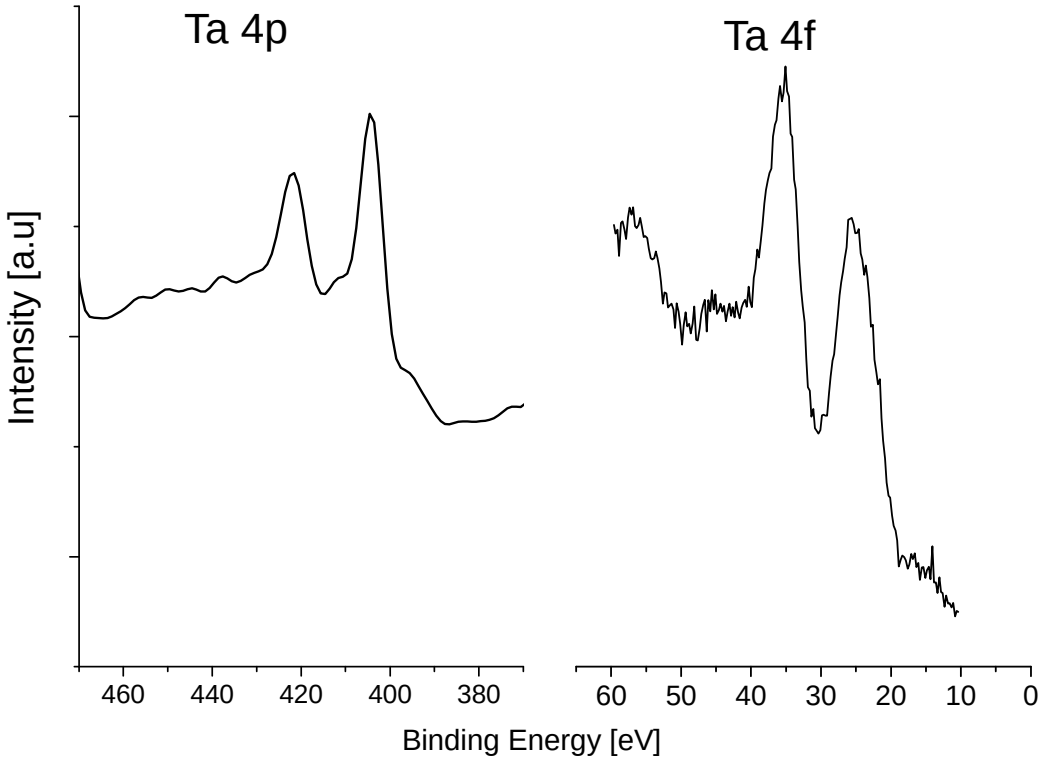

Figure 6.7. XPS spectra spanning the Ta 4p and Ta 4f core levels of TaS_3 nanoribbons on SiO_x.

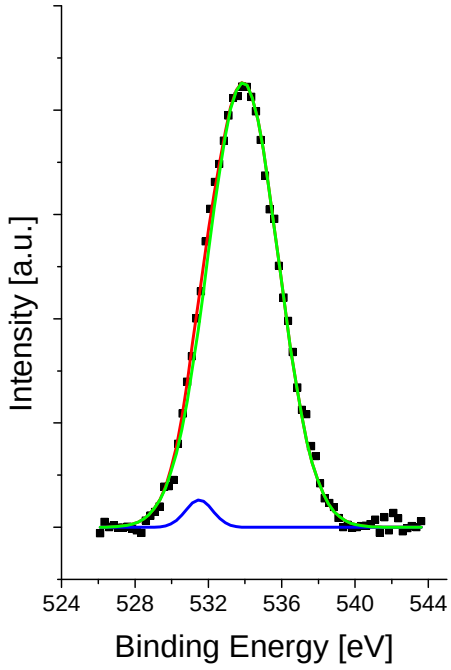

Figure 6.8. XPS spectra from the O 1s core level. The blue and green lines are fitted Gaussians. The green line represents molecular oxygen and is centred at 533.9 eV. The blue line represents ionic oxygen and is centred at 531.5 eV. The red line is the overall fit. The ratio of molecular to ionic oxygen is ~ 40:1.

	$Ta4d^{3/2}$	S 2s (SO_x^{n-})	S(0) 2s	$(S_2)^{2-}$ (S^-) 2s	S^{2-} 2s	$Ta\ 4d^{5/2}$
Binding Energy (eV)	241.7	234.5	230.9	228.4	227.2	230.1
FWHM (eV)	5.4	3.8	2.7	1.7	1.5	5.5
Rel. Intensity	1	2.2	6.8	4.1	2.4	1.5

Table 6.1. The parameters used to fit the Gaussians to the experimental XPS spectra shown in figure 6.2. The binding energies are initially set to values obtained from the literature, then allowed to vary by ± 0.2 eV. The FWHM is purely based on the measured peak shape.

The component at 533.9 eV is consistent with a molecular O species (such as in [29]) and most likely originates from the ethanol that the ribbons were dispersed in or contamination during the synthesis process. The component at 531.5 eV is ~40 times less intense than the molecular species and likely derives from slight surface oxidation of the ribbons.

In previous experimental chapters (chapters 4, 5 and 6), it was necessary to use equation 2.15 and sensitivity factors to quantify surface stoichiometry using XPS. The situation in this chapter is much simpler because the chemically shifted S 2s XPS peaks will have virtually identical photoionisation cross sections and hence virtually identical sensitivity factors. Consequently, the ratio of fitted peak intensities of S^-/S^2 is an accurate measure of TaS_3 stoichiometry. The fitting of the Ta 4d and S 2s region revealed several interesting aspects of the amorphous shell of the nanoribbon. The largest S 2s component is that of elemental S, contributing 43 % of the total S signal. Even though the ribbons were heated to sublime surface S deposits, large amounts of elemental S remains, indicating that it is strongly bound to the material. The ratio of the S^-/S^{2-} ($(S_2)^{2-}/S^{2-}$) components, at 1.7 ± 0.1 (0.85), is clearly smaller than the value of 2 (1) expected from the stoichiometry of TaS_3, implying a non-stoichiometric shell composition. The nature of the shell will be further examined in the discussion, section 6.3.

The blue line in figure 6.9 (a) shows the complementary UPS spectrum: it displays a single broad peak centred at ~7.0 eV upon a sloping secondary electron background. The spectrum is consistent with the valence region of an XPS spectrum collected by Endo et al. [30] from bulk TaS_3. The UPS spectrum obtained in the vicinity of E_F is shown in figure 6.9 (b) and is interesting because it shows a suppression of the Fermi edge, which is indicative of one dimensional behaviour. It is well established that the electronic properties of one dimensional conductors tend to follow the Luttinger Liquid model [14].

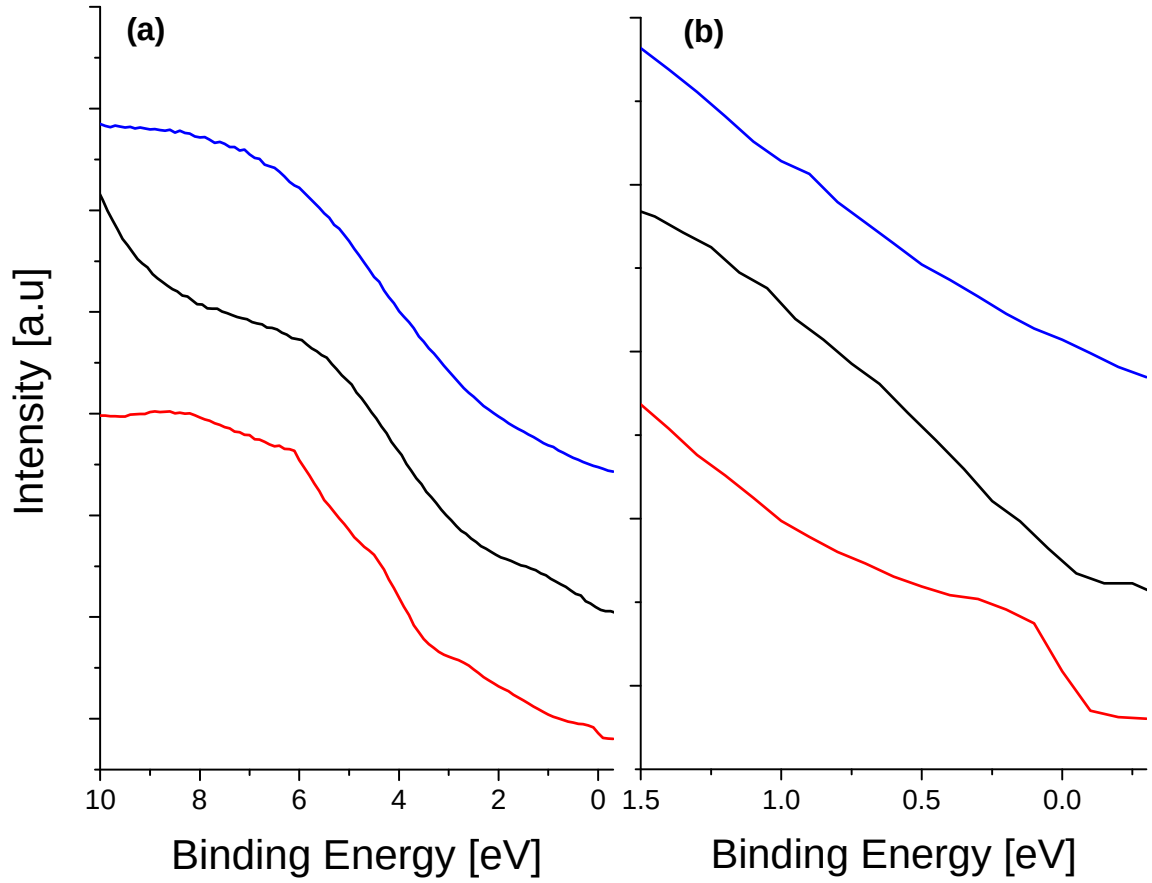

Figure 6.9. (a) UPS spectra collected under the same conditions as figure. 6.5. (b) is the magnification of the region around E_F. Blue is TaS_3 nanoribbons deposited on a Au-coated silicon substrate, immediately after deposition. An identical spectrum is obtained when using Si substrates. Black is TaS_3 nanoribbons deposited upon a silicon substrate which had been flash annealed to 1173 K. Red is TaS_3 nanoribbons that had been left on a gold substrate for 3 days.

The most prominent spectral feature of a one dimensional conductor is the lack of a discernible step at E_F, as observed here and in a number of other one dimensional systems (e.g. $BaVS_3$ [31], $Li_{0.9}Mo_6O_{17}$ [32], NaV_2O_4 [33] and a review [34]). Instead of a step, the spectral intensity, I, tails off across the Fermi edge and is well described by a power law relation [35]:

$$I = |E|^{\alpha}, \qquad (6.1)$$

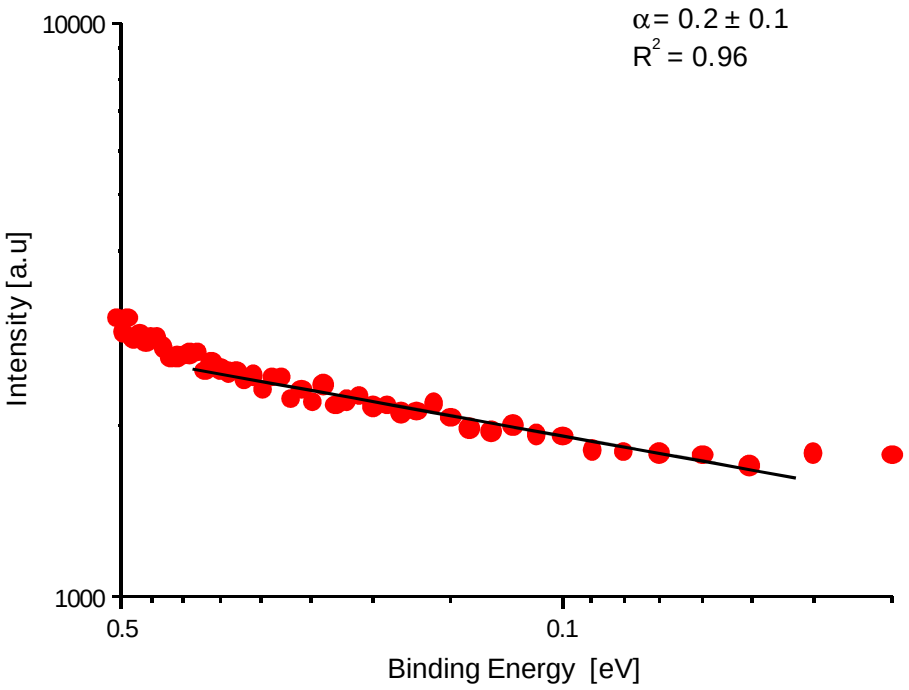

Figure 6.10. Log-Log plot of Intensity against binding energy. The red dots are the data points obtained and the black line is the fitted straight line. It has a gradient of α = 0.2 ± 0.1.

where E is the binding energy and α is a parameter characteristic of the one dimensional system. Taking logarithms of both sides of equation 6.1 gives:

$$\log I = \alpha \log|E|. \qquad (6.2)$$

Hence the gradient of a log-log plot will be α. High resolution UPS spectra (an energy increment of 10 meV) were obtained from the nanoribbons in the region up to 500 meV below E_F. Figure 6.10 shows a log-log plot of I against $|E|$. The data were fitted in the region 300-30 meV to a power law with α = 0.2 ± 0.1. Figure 6.10 shows that there is significant deviation from the power law behaviour at ~30 meV from E_F. This is a well established aspect of the model and has been accounted for in previous studies [33, 36-38] as being a result of external effects such as inter-chain hopping or thermal broadening. The region ~30 meV below E_F has therefore been intentionally discounted in measuring α. Theoretical models of one dimensional systems predict that α should not exceed 9/32 = 0.281 [39], although values above this limit have been observed in quasi

one dimensional systems and are attributed to interactions between conducting ‘‘chains’’. In our work, a value of α = 0.2 implies a lack of long range interactions compared to bulk one dimensional conductors, which is again consistent with the observed amorphous nature. Coupled with the XPS data, the UPS data therefore suggest that the composite layer contains sufficient Ta^{4+} ion chains to maintain one dimensional electronic states but that these chains must be short and randomly oriented if they are to be consistent with the TEM images of figure 6.5. The surrounding insulating sulfur matrix, along with an absence of long-range periodicity, would inhibit coupling between chains in the shell. This would be consistent with the observed value of α (0.2) that is lower than previous studies of quasi one dimensional bulk conductors and could also account for the absence of an observable Peierls transition, which will be described in section 6.2.3. Such a reduction in chain-chain coupling has also been observed to inhibit Peierls distortions in previous studies of bulk TMC crystals [40,41].

6.2.3 Thermal Processing

Cooling the nanoribbons to 150 K, a temperature below the Peierls transition (T_p = 210 K) for bulk *o*-TaS_3, had no discernible effect on the XPS and UPS obtained from the amorphous shell of TaS_3. The Peierls transition causes the formation of a CDW which modulates local electron density, as shown in figure 6.2. In terms of XPS spectra, a CDW is typically observed by the splitting or modulation of a particular core level peak, for example in TaS_2 and $TaSe_2$ [15-17]. Figure 6.11 shows XPS and UPS data obtained at room temperature (300 K) and at 150 K. Within error of the fit, no change was observed in the XPS when cooled. The UPS spectra showed a small change in the shape of the feature ~7.0 eV and no change in the vicinity of E_F. Hence the Peierls transition was not observable in the nanoshell, which is surprising as the suppression of a Fermi edge indicates that the material is one dimensional. However, the TEM and XPS data show that the nanoshell is amorphous so we conclude that there is insufficient ordering in the shell to observe the Peierls transition. The composition of nanoshell is further discussed in section 6.3.

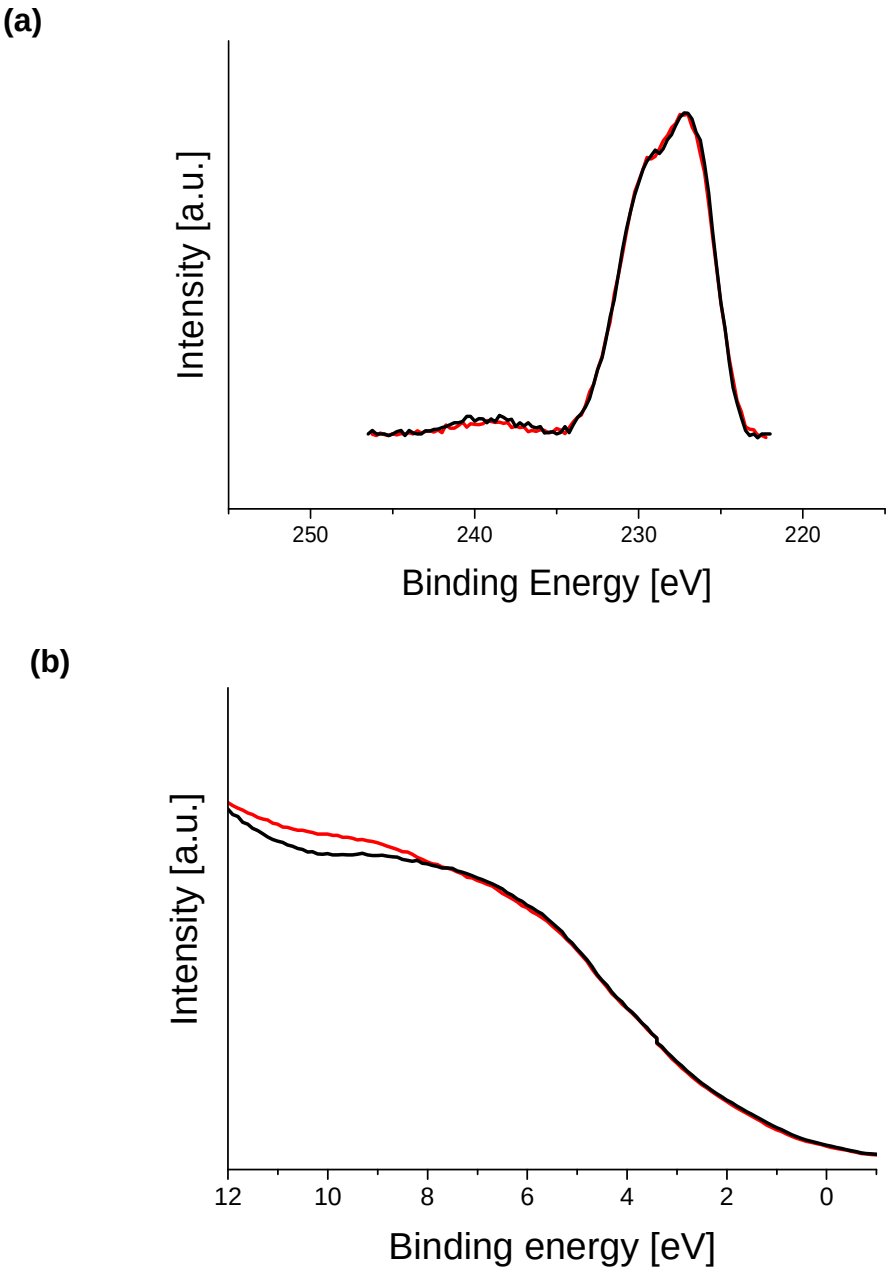

Figure 6.11. The effect of cooling on the photoemission spectra of TaS_3 nanoribbons. (a) XPS spectra spanning the Ta 4d and S 2s core levels and (b) UPS spectra. The spectra shown as a black line were obtained at 300 K and the red lines at 110 K.

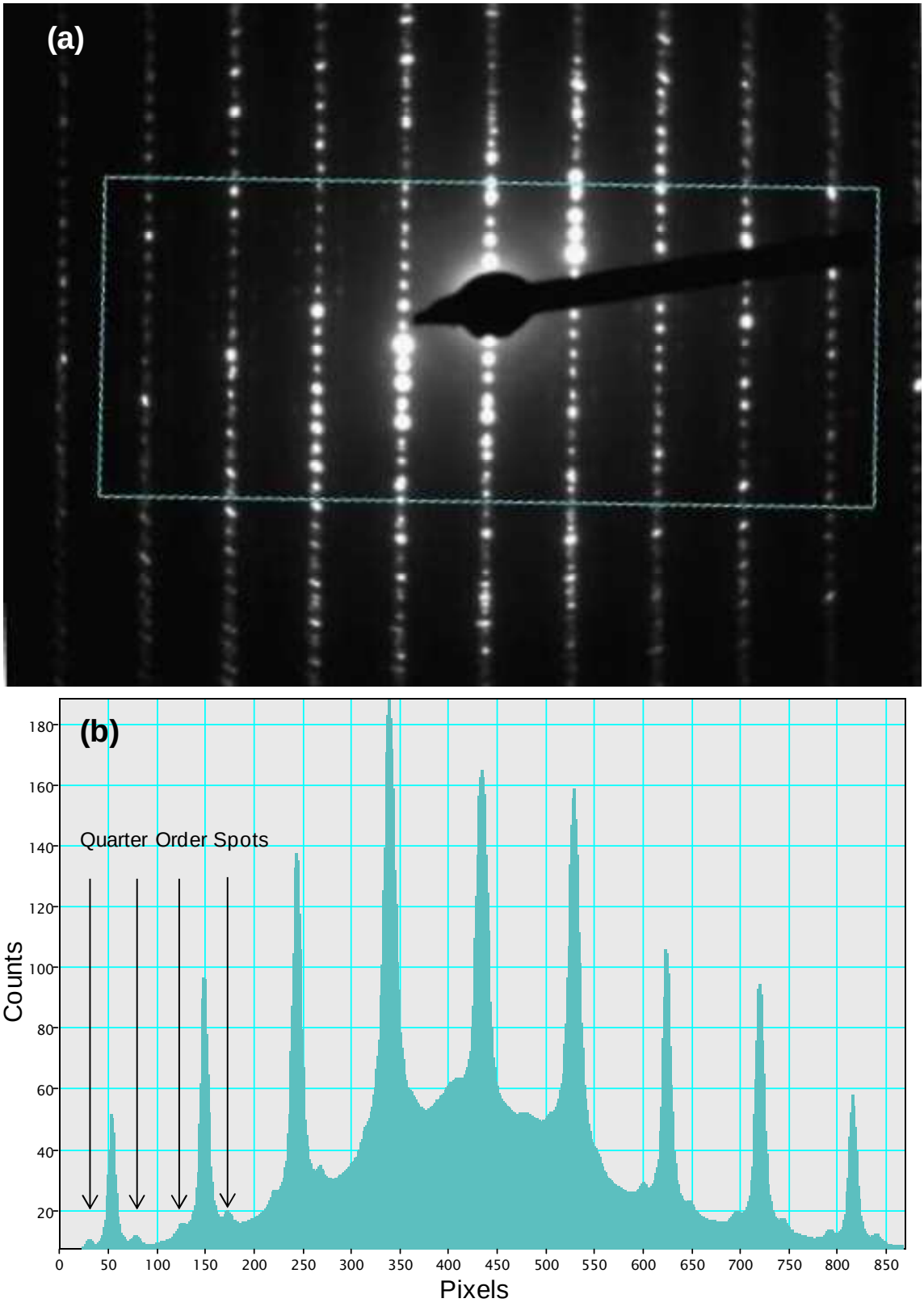

Figure 6.12. (a) SAED pattern from a typical TaS_3 nanoribbon that has been cooled to 110 K. (Peierls transition is at 250K). (b) integrated line profile from the box indicated on (a). Quarter order spots are indicated on the integrated line profile.

However, using TEM to explore the core of the material, data were collected that suggested the presence of a Peierls transition. Figure 6.12 (a) shows a SAED pattern of a typical nanoribbon that has been cooled to 130 K (i.e. below the Peierls transition temperature of 210 K). Compared to SAED obtained at room temperature, figure 6.5 (b), the pattern shows superlattice spots at (n + 0.25) $\boldsymbol{c}^*$ (i.e. quarter order along the c axis). Figure 6.12 is taken at a shorter camera length than figure 6.4 (b) because the intense (000) diffraction spot masks the lower intensity superlattice spots. These superlattice spots first appear ~220 K as streaks and condense into spots with decreasing temperature. To make this clearer, an integrated line profile is obtained from box on the 130 K, SAED pattern of figure 6.12 (a). The line profile is displayed in figure 6.12 (b) and clearly shows additional quarter order spots. This superlattice has been observed in previous study [11], and was interpreted to be a lattice distortion from the Peierls transition.

The thermal stability of TaS_3 ribbons dispersed on the silicon substrate was monitored by flash-annealing the samples to sequentially higher temperatures and collecting XPS spectra after cooling back to room temperature. The annealing process initially desorbed water and hydrocarbon species as shown by a reduction in intensity of the O 1s and C 1s XPS peaks in figure 6.13. The initial anneal to 573 K was the most effective in desorbing carbon species. Plots of the S^{2-}/Ta, S^{-}/Ta, $S^{(0)}$/Ta and S^{-}/S^{2-} ratios versus annealing temperature are shown in figure 6.14. Both the S^{-}/Ta and $S^{(0)}$/Ta ratios fall progressively upon annealing to 773 K and then show no measurable change. The S^{2-}/Ta ratio shows less pronounced changes, appearing to decrease slightly on annealing to 773 K and then increasing with further annealing up to 1173 K. The S^{-}/S^{2-} ratio illustrates the change in stoichiometry and decreases continually with annealing, but never reaches zero, indicative of incomplete conversion to TaS_2 within the amorphous shell. A representative XPS spectrum collected after annealing to 1173 K is shown in figure 6.6 (b). UPS spectra collected after annealing to 1173 K are shown in figure 6.9 (a) and display significant differences to the spectra obtained prior to annealing, with a broad peak upon the secondary electron background at ~6 eV and a significant increase in emission in the vicinity of E_F. This broad peak covers the same region in which calculations indicate significant density of occupied states for 2H-TaS_2 [42], albeit without the fine structure displayed by the calculations. The high resolution UPS spectrum of the annealed ribbons is shown in figure 6.9 (b). The spectrum shows that there is now a weak step at E_F, indicative of non one dimensional behaviour (i.e. Fermi Liquid behaviour) consistent with the shell becoming more TaS_2 like.

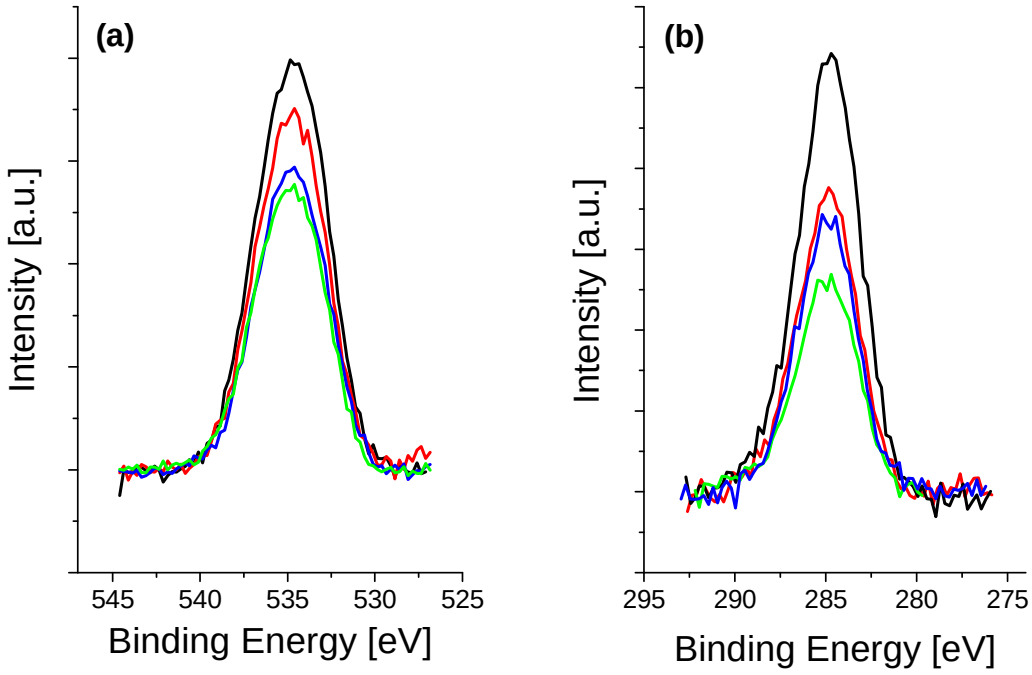

Figure 6.13. (a) O 1s and (b) C 1s XPS spectra, obtained after sequentially annealing the nanoribbons to higher temperatures. The black line indicates the spectra obtained after annealing 423 K. The red line indicates the spectra obtained after annealing to 573 K. The blue line indicates the spectra obtained annealing to 773 K. The green line indicates the spectra obtained after annealing to 1173 K.

After annealing, the nanoribbons were removed from the UHV chamber and studied using TEM, as illustrated in figure 6.15. The TEM experiments were conducted on nanoribbons that were subject to flash anneals to the maximum temperature of 1173 K. The nanoribbon is displayed in figure 6.15 (a) and shows that the morphology is unchanged (i.e. it is still a nanoribbon). However, the SAED pattern, shown in figure 6.15 (b), can only be indexed with lattice parameters from TaS_2, indicating that the core has been converted to TaS_2. SAED indicates that the transformation from TaS_3 to TaS_2 occurs more completely in the nanoribbon core than is suggested by XPS for the near surface region of the nanoshell. From the diffraction pattern a lattice parameter of a = 0.331 ± 0.04 nm was obtained. It is not possible to distinguish between the 1T, 2H and 3R polytypes of TaS_2 without further diffraction data, as the value of a is similar in all 3 polytypes. However, weaker half order spots [e.g. (1 ½ 0)] were also observed: these spots could be consistent with the superlattice arising from the formation of a CDW state.

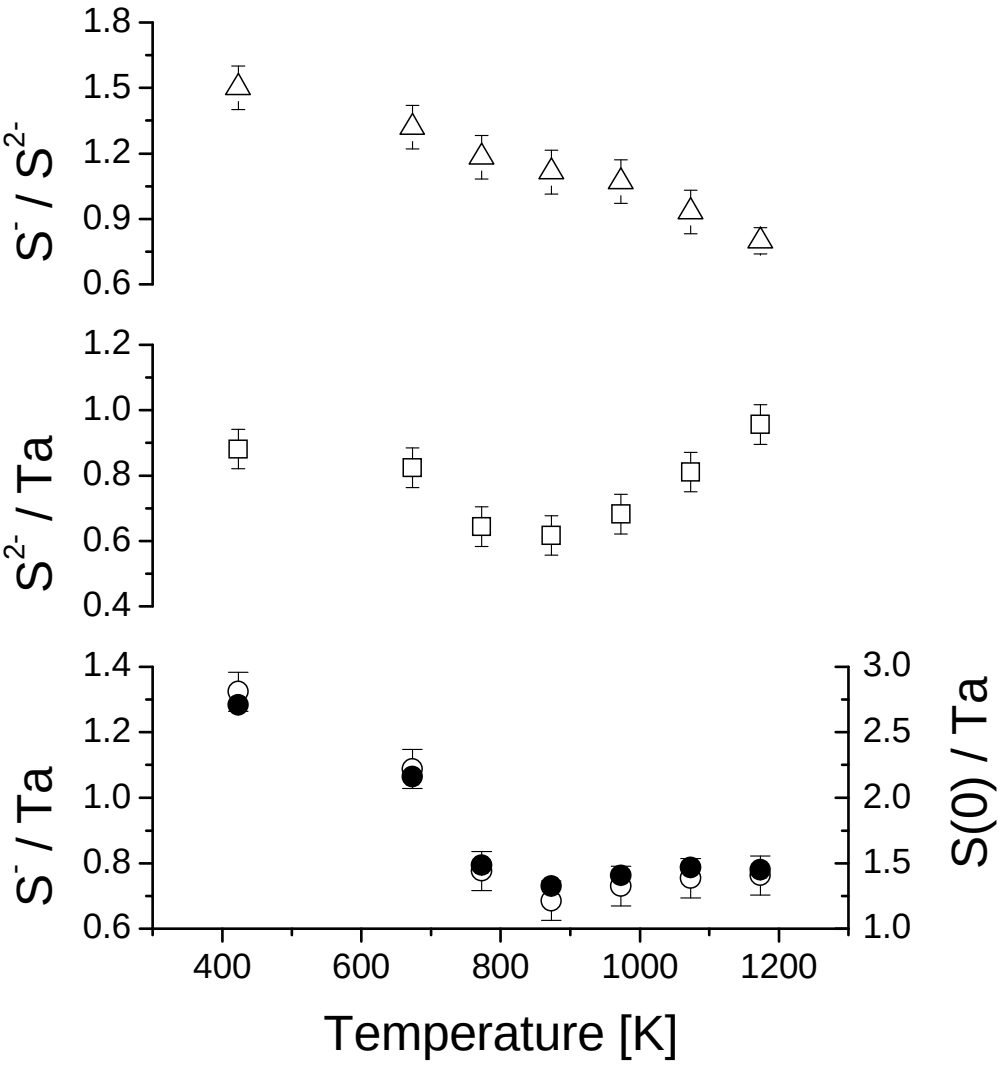

Figure 6.14. Ratios of integrated XPS peak intensities for spectra collected from TaS_3 /Si after flash annealing to sequentially higher temperatures. Plotted are $S^{(0)}$ /Ta (open circles), $(S_2)^{2-}$ /Ta (filled circles), S^{2-} /Ta (open squares) and $(S_2)^{2-}$ /S^{2-} (open triangles) ratios.

The periodicity previously observed at room temperature in the 1T polytype, is (√13 x √13) [43], which is inconsistent with half order spots, but may be consistent with a CDW state of 2H-TaS_2. Alternatively, the superlattice may originate from the intercalation of S, produced by decomposition, into the bulk of the TaS_2 nanoribbon. Superlattice spots similar to those observed here are found when Li and other species are intercalated in MoS_2 another layered TMC [44].

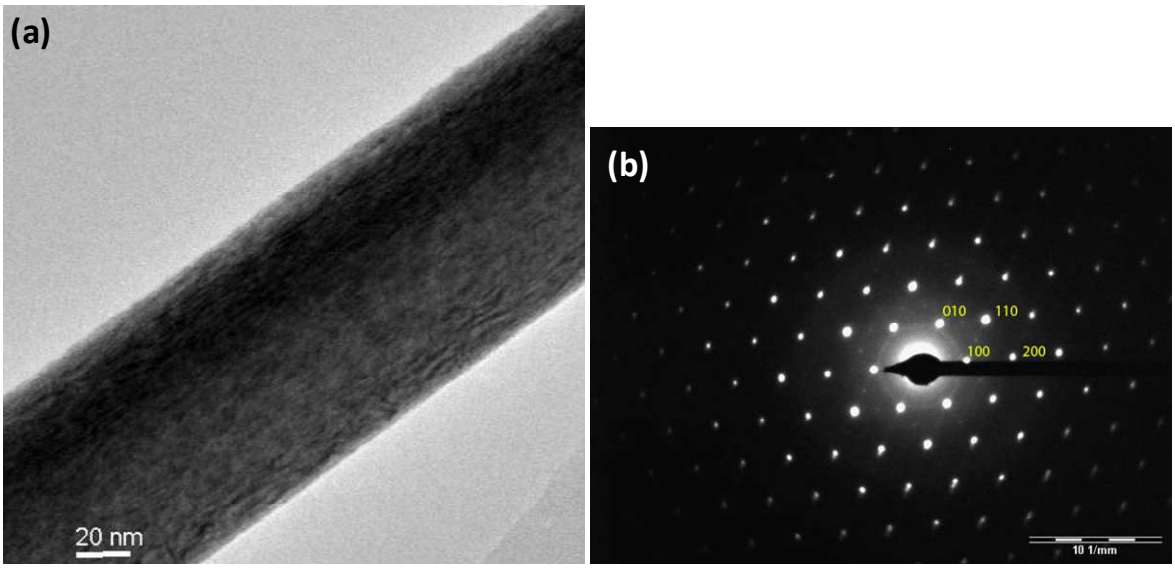

Figure 6.15. Electron microscopy of TaS_3 nanoribbons after annealing to 1173 K. (a) BF image of a typical ribbon. (b) SAED pattern from (a) with indexed spots corresponding to the TaS_2 structure.

6.2.4 Effects of the Substrate on Stability of TaS_3

In contrast to the above results, TaS_3 nanoribbons dispersed on a Au substrate were chemically unstable. The Au substrate was prepared by sputter coating a ~200 nm film of Au onto a SiO_x substrate. XPS and UPS spectra collected immediately after the introduction of TaS_3 nanoribbons to UHV were identical to those obtained for the silicon substrate, shown in figures 6.6 (a) and 6.9 (a), respectively. However, spectra recorded after 3 days (but subjected to no other processing) display significant changes, as illustrated in the XPS spectrum of figure 6.6 (c) and the UPS spectrum of 6.9 (c). XPS indicates significant reductions in the relative intensities of the $S^{(0)}$ and $(S_2)^{2-}$ components and the S^{-}/S^{2-} ($(S_2)^{2-}/S^{2-}$) ratio is reduced from 1.7 (0.85) to 1.2 (0.6). The UPS spectrum displays a broad band, centred at ~6.0 eV, like that observed for TaS_2 nanoribbons formed by annealing the TaS_3 nanoribbons to 1173 K. However, and in contrast to the spectra from TaS_2, some fine structure is discernible, with features at 4.5, 6.1 and 8.5 eV. The spectrum also shows a small feature at ~2.8 eV, which was not seen previously. These features are in reasonable agreement with sharp structure observed in the calculated DOS of 2H-TaS_2 and are associated with the S 3p and Ta d_z orbitals [42]. Another significant difference is that a step is now observed at the Fermi Energy, which is indicative of non one dimensional (i.e. Fermi Liquid) behaviour [14]. The data show the $(S_2)^{2-}/S^{2-}$ ratio to decrease to a value closer to that for TaS_2 when nanoribbons are left to

stand on Au. The UPS data are also consistent with the nanoshell becoming more like TaS_2. In particular, a step is now observable at E_F, signifying a transformation from the one dimensional behaviour expected for TaS_3 to that expected for a two dimensional conductor like TaS_2. We also note that the materials depleted in $(S_2)^{2-}$ and $S^{(0)}$ by prolonged exposure to the Au surface could be regenerated to their initial state, as evidenced by UPS and XPS, by annealing at 423 K for 10 min. These depletion and regeneration cycles were performed multiple times. No higher temperature thermal processing was performed because the Au film was observed to delaminate above 623 K.

6.3 Discussion

Our surface spectroscopic data provide new insight into the core-shell architecture of trisulfide nanoribbons and the chemical and electronic properties of the amorphous nanoshell. The XPS data show that the amorphous outer shell is not simply a surface oxide: although SO_x^{n+} species are present, XPS indicates them to be a minor component, even in the amorphous region. The observed S^{-}/S^{2-} ($(S_2)^{2-}/S^{2-}$) ratio of 1.7 (0.85) suggests the nanoshell is either a mixture of TaS_3 and TaS_2 or is a material with a non-integer stoichiometry such as "$TaS_{2.5}$". The UPS data are consistent with the latter model because, based on the spectra collected after annealing to 1173 K, one would expect materials containing appreciable amounts of TaS_2 to have a significant higher DOS in the vicinity of E_F than is observed in our experimental spectra.

We now turn to a discussion of the observation by XPS of significant elemental sulfur. This cannot be due solely to a thin surface film of remnant unreacted sulfur, since such a film would attenuate photoemission and prevent the detection of the underlying material. Similarly, TEM provides no evidence for the presence of isolated, unreacted islands or globules of elemental sulfur that would only partially cover the ribbons. It is also apparent from the XPS data that elemental sulfur is present even after prolonged (weeks) exposure to UHV (~10^{-10} mbar) and that annealing to temperatures between 773 K and 1173 K does not reduce the quantity. Neither of these observations is consistent with the elemental sulfur arising from surface deposits. The TEM and EDS data further illustrate that the elemental S observed with XPS is not a result of excess sulfur in the form of sulfur deposits, as these deposits have clearly sublimed upon heating in UHV. Furthermore, heating between 773 K and 1173 K should enhance sublimation, reducing the amount of elemental sulfur, rather than having no measurable effect.

One way to rationalise all of the above data is as follows. It is hypothesized that the amorphous layer is a composite of tantalum sulfide islands surrounded by a melted glassy

S matrix. During vacuum processing crystalline nanoribbons are surrounded by a coating of liquid sulfur, most of which subsequently desorbs but some of which reacts or intercalates with the nanoribbons. Delamination of the nanoribbons at this liquid-solid interface could then account for the apparent amorphisation observed by TEM whilst a glassy structure in the residual material would explain why residual sulfur does not sublime. TMCs readily intercalate elemental and molecular species and significant intercalation is known to cause delamination in related systems [45,46].

In contrast to the heterogeneity of the amorphous shell enclosing the nanoribbons, the core of the ribbons are crystalline as indicated by HRTEM, EDS and SAED in figure 6.5. The SAED pattern (figure 6.5 (b)) displays a phase transition that is consistent with the Peierls distortion (figure 6.12). When annealed to 973 K and above, the data suggest that the core of the TaS_3 nanoribbons undergo a pseudomorphic decomposition to TaS_2 via the following reaction:

$$TaS_{3\ (s)} \rightarrow TaS_{2\ (s)} + S. \qquad (6.3)$$

The observation of substrate-dependent stability is intriguing and consistent with a migration of sulfur from the TMC to the support, analogous to the ‘‘spillover’’ process observed in supported metal catalysts [47]. A requirement for spillover is that there is significant mass transport, in our case mobility of $S^{(0)}$ and $(S_2)^{2-}$ within the nanoshell. The $S^{(0)}$ is likely to have a level of mobility in the glassy matrix required for the spillover process. The apparent mobility of the $(S_2)^{2-}$ species is more surprising but could also be mediated by the amorphous sulfur matrix. Ultimately, the driving force for any spillover process must be the strength of the interaction between sulfur species and the substrate. Sulfur species have a very high affinity for Au surfaces; indeed this is exploited to produce well-ordered, self-assembled, monolayer structures of thiols [48]. In contrast, the SiO_2 surface of the silicon substrate has significantly less affinity for sulfur. The regeneration of the Au-supported amorphous nanoshell is not attributed to the result of a chemical reaction that forms new $(S_2)^{2-}$ to replace that which was lost. Rather, it is suggested that the regeneration is due to thermally activated diffusion of sulfur species into this depleted region, from outside the region probed by XPS, as this would be consistent with the proposed mass transport in the nanoshell.

6.4 Conclusions

The combination of surface sensitive spectroscopic techniques and electron microscopy has provided new insight into the chemical composition and properties of the core-shell

architecture of a TMC nanomaterial. The reduced dimensionality of a nanomaterial means that the surface plays an increasing role in determining the electronic and thermal properties. Hence, developing a good understanding of the structure of the surface is important. Typically, nanomaterials would be characterised only with electron microscopy and PXRD, which would have perhaps overlooked the core-shell asymmetry. The surface sensitivity of XPS and UPS mean that detailed information on the composition of the surface can be obtained. This chapter further highlighted the flexibility of XPS and UPS - that the surface composition of an amorphous material could be readily obtained. In contrast, surface sensitive electron diffraction (LEED) gave no information due to the random orientations of the nanoribbons on the surface. TEM experiments were essential in characterising the core of the material and confirming the disordered shell. The combination of PXRD, TEM, XPS and UPS gave a much more complete description of the structure and processes occurring in the shell and the core, rather than using the techniques individually.

The core of the ribbon is well matched to the structure of *o*-TaS_3 which is adequately ordered to undergo a Peierls transition below 250 K. The nanoshell of ribbon is amorphous and we have suggested that the nanoshell is a composite material, with islands of a Ta sulfide ("$TaS_{2.5}$") surrounded by a matrix of amorphous sulfur. The Ta sulfide islands display one dimensional electronic properties, as evidenced by UPS. However, the shell is sufficiently disordered not to show the Peierls transition. It is suggested that the nanoshell is formed by the interaction of a liquid sulfur layer, present during synthesis and processing, with the surface region of the TaS_3 nanoribbon. It was observed that the shell was unstable on a Au substrate with the shell persistently losing S to the substrate. This illustrates that if TaS_3 (or other transition metal sulfide) nanomaterials were integrated into a device; care would have to be taken over the correct choice of contact material to provide stable and efficient electrical contacts. It was also observed that the thermal decomposition of TaS_3 to TaS_2 was incomplete in the shell as the quantity of $(S_2)^{2-}$ never fully reached zero. In contrast, decomposition of TaS_3 to TaS_2 in the core was complete after annealing to 1173 K. We suggest that the disordered islands of Ta sulfide and amorphous sulfur inhibit this decomposition reaction.

6.5 References

[1] C.E. Housecroft, A.G. Sharpe, *Inorganic Chemistry*, 2nd edition (Prentice Hall) 2005.

[2] J.A. Wilson, A. D. Yoffe, *Adv. Phys* **18** (1969) 193.

[3] M.V. Nikitin, S.G. Zybtsev, V.Y. Pokrovskii, *Phys. Rev. B* **86** (2012) 045104.

[4] C.N.R. Rao, F. Deepak, G. Gundiah, A. Govindaraj, *Prog. Sol. Stat. Chem*. **31** (2003) 5.

[5] R. Tenne, L. Margulis, M. Genut G. Hodes, *Nature* **360** (1992) 444.

[6] M. Remskar*, Adv. Mater*. **16** (2004) 1497.

[7] X. Wu, Y. Tao, Y. Hu, Y. Song, Z. Hu, J. Zhu, L. Dong, *Nanotechnology* **17** (2006) 201.

[8] W. Shi, R.W. Hughes, S.J. Denholme, D.H. Gregory, *Cryst. Eng. Comm.* **12** (2010) 641.

[9] A. Meerschaut, L Guemas, J. Rouxel, *J. Sol. Stat. Chem.* **36** (1981) 118.

[10] S. Kikkawa, N. Ogawa, M. Koizumi, Y. Onuki, *J. Sol. Stat. Chem.* **41** (1982) 315.

[11] C. Roucau, R. Ayroles, P. Monceau, L. Guemas, A. Meerschaut, J. Rouxel, *Phys. Status Solidi (a)* **68** (1980) 483.

[12] E. Bjerkelund, A. Kjeksws, *Z. Anorg. Allg. Chem*. **328** (1964) 235.

[13] J. F. Revelli, W. A. Phillips, *J. Solid. State. Chem*, **9** (1974) 176.

[14] T. Giamarchi, *Quantum Physics in One Dimension* (Oxford:Clarendon) 2003.

[15] H.P. Hughes, J.A. Scarfe, *J. Phys.: Condens. Mater.* **8** (1996) 1439.

[16] H.P. Hughes, R.A. Pollak, *Phil. Mag.* **34** (1976) 1025.

[17] H.J. Crawack, C. Pettenkofer, *Sol. Stat. Comm.* **118** (2001) 325.

[18] S.G. Zybtsev. V.Ya. Pokrovskii, V.F. Nasretdinova, S.V. Zaitsev-Zotov, *Physica B* **407** (2012) 1696.

[19] H.X. Yang, B.P. Zhu, L.J. Zeng, H.F. Tian, C. Ma, J. Shi, J.Q. Li, *J. Phys.: Condens. Mater.* **20** (2008) 275230.

[20] C.W. Dunnill, Ph.D. thesis, *University of Glasgow*, 2007.

[21] C.W. Dunnill. H.K. Edwards, P.D. Brown, I. MacLaren, D.H. Gregory, *in preparation*.

[22] *FEI Tecnai on-line help manual* - TIA, Version 2, FEI.

[23] G.E. McGuire, G.K. Schweitzer, T.A. Carlson, *Inorg. Chem.* **12** (1973) 2451.

[24] L. Hernan, J. Morales, L. Sanches, J.L. Tirado, J.P. Espinos, A.R. Gonzalez-Elipe, C*hem. Mater.* **7** (1995) 1576.

[25] D. Gonbeau, C. Guimon, G. Pfisterguilluzo, A. Levasseur, G. Meunier and R. Dormoy, *Surf. Sci*. **254** (1991) 81.

[26] F. Jellinek, R. A. Pollak and M. W. Shafer, *Mater. Res. Bull.* **9** (1974) 845.

[27] M. E. Fleet, S.L. Harmer, X. Liu and H.W. Hesbitt, *Surf. Sci*. **584** (2005) 133.

[28] D.D. Sarma, C.N.R. Rao, *J. Electron Spectrosc. Relat. Phenom.* **20** (1980) 25.

[29] A. Schmidt, T.J. Schuerlein, G.E. Collins, N.R. Armstrong, *J. Phys.Chem.* **99** (1995) 11770.

[30] K. Endo, H. Ikara, K. Watanabe and S. I. Gonda, *J. Solid State Chem.* **39** (1981) 215.

[31] M. Nakamura, A. Sekiyama, H. Namatame, A. Fujimori, H. Yoshihara, T. Ohtani, A. Misu, M. Takano, *Phys. Rev. B* **49** (1994) 16191.

[32] Feng Wang, J.V. Alvarez, S.-K. Mo, J.W. Allen, G.-H. Gweon, J. He, R. Jin, D. Mandruse, H. Hochst, *Physica B* **403** (2008) 1490.

[33] T. Qian, K. Nakayama, Y. Sun, T. Arakane, T. Sato, T. Takahashi, K. Yamaura, E. Takayama-Muromachi, *J. Phys. Soc. Jpn.* **78** (2009) 024709-1.

[34] M. Grioni, S. Pons, E. Frantzeskakis, *J. Phys.: Condens. Matter* **21** (2009) 023201.

[35] B. Dardel, D. Malterre, M. Grioni, P. Weibel, Y. Baer, F. Levy, *Phys. Rev. Lett*. **67** (1991) 3144.

[36] G.H. Gweon, J.D. Denlinger, J.W. Allen, R. Claessen, C.G. Olson, H. Hochst, J. Marcus, C. Schlenker, and L. F. Schneemeyer, *J. Electron. Spectrosc*. **117-118** (2001) 481.

[37] H. Rauf, T. Pichler, M. Knupfer, J. Fink, and H. Kataura, *Phys. Rev. Lett.* **93** (2004) 096805.

[38] H. Ishii, H. Kataura, H. Shiozawa, H. Yoshioka, H. Otsubo, Y. Takayama, T. Miyahara, S. Suzuki, Y. Achiba, M. Nakatake, T. Narimura, M. Higashiguchi, K. Shimada, H. Namatame, and M. Taniguchi, *Nature* **426** (2003) 540.

[39] N. Kawakami, *Phys. Rev. B* **46** (1991) 3191.

[40] K.E. Wagner, E. Morosan, Y.S. Hor, J. Tao, Y. Zhu, T. Sanders, T.M. McQueen, H.W. Zandbergen, A.J. Williams, D.V. West, R. J. Cava, *Phys. Rev. B* **78** (2008) 104520.

[41] L. Fang, Y. Wang, P.Y. Zou, L. Tang, Z. Xu, H. Chen, C. Dong, L. Shan and H.H. Wen, *Phys. Rev. B* **72** (2005) 014534.

[42] G.Y. Guo, W.Y. Liang, *J. Phys. C: Solid State Phys.* **20** (1987) 4315.

[43] J.A. Wilson, *J. Phys.: Condens. Matter* **2** (1990) 1683.

[44] K. Chrissafis, M. Zamani, K. Kambas, J. Stoemenos, N.A. Economou, I. Samaras, C. Julien, *Mater. Sci. Eng. B* **3** (1989) 145.

[45] F.J. Di Salvo, G.W. Hull Jr, L.H. Schwartz, J.M. Voorhoeve, J. V. Waszczak, *J. Chem. Phys*. **59** (1973) 1922.

[46] J.F. Lomax, B.N. Diel and T.J. Marks, *Mol. Cryst. Liq. Cryst*. **121** (1985) 145.

[47] W.C. Conner, J.L. Falconer *Chem. Rev*. **95** (1995) 759.

[48] F. Schreiber, *Prog. Surf. Sci*. **65** (2000) 151.

7. Conclusions and Future Work

This thesis has presented a series of experiments focussing on the characterisation of several technologically important transition metal chalcogenide (TMC) systems. The systems studied ranged from model, single crystals to more realistic polycrystalline and nanoribbon systems. The structures formed were extensively characterised using a combination of surface sensitive probes (XPS, UPS, LEED, STM) and electron microscopy techniques (SEM, TEM, SAED, CBED, EDS, EELS, EFTEM). The data presented in this thesis has shown that the combination of both sets of techniques enhances the explanation of the physical model of the systems in question. For example, TEM data displayed in chapter 4 concerning the diffusion of Cu into CdTe showed that Cu_2Te crystallites form in the CdTe film. However, the TEM data cannot rival the surface sensitivity of photoemission which gave quantitative information about Cu content at the surface of the CdTe film. Hence, the use of both techniques gave a comprehensive picture of a particular material. This chapter will give a brief review into the results presented in this thesis and a discussion of possible future experiments.

Chapter 3 described the growth of Te thin films on Cu(111) and Cu_{poly}, a system of importance because of the use of Cu-Te back contacts in thin film CdTe photovoltaic devices. We showed that Cu and Te alloy above 275 K, readily forming ordered structures, the nature of which was dependent on Te coverage. Below 275 K, alloying was kinetically limited and rough Te films grew on the Cu(111) surface. For θ_{Te} < 0.33 ML, a Cu-Te SSA forms with either (2√3 x 2√3) R30°, (2 √3 x √3) R30° or (√3 x √3) R30° symmetry, depending on coverage. For θ_{Te} > 0.66 ML, a Cu_3Te_2-like alloy is formed, terminated in the (111) direction. For 0.33 ML < θ_{Te} < 0.66 ML, a mixture of the two aforementioned alloys (SSA and Cu_3Te_2) co-exists. If more than 0.66 ML Te was deposited on Cu(111) while the substrate was held at 673 K, then the resultant alloy displayed a phase change below 250 K. The precise nature of the phase change was undermined but it was speculated that it may be due to a surface corrugation. The nature of thick Te films (θ_{Te} > 10 ML) deposited on Cu_{poly} at 300 K were shown to form polycrystalline Cu_2Te, in contrast to Te/Cu(111). Further experiments on this system would be to identify the cause of the disagreement between the observed LEED IV curves and DFT calculations. For example, medium energy ion scattering (MEIS) could to used to identify if there were stacking faults in the Te/Cu(111) alloyed surface. Also, the reversible, low temperature phase change observed by LEED warrants further study to elucidate the precise nature of this observed change in surface structure.

The study CdTe of photovoltaics was extended in chapter 4 to the deposition of CdTe onto a variety of Cu and Cu_xTe surfaces. Chapter 4 can be broadly divided into two sections. The first of which was a surface science study of the growth of CdTe films on Cu(111) and Te/Cu(111) (i.e. Cu_3Te_2). The second part of the chapter studied thick CdTe films (θ_{CdTe} ~50 ML) on polycrystalline Cu surfaces using a combination of surface science techniques and TEM. The experimental results for the CdTe/Cu(111) and CdTe/Cu_3Te_2 systems were interpreted as follows. CdTe grew in a three dimensional or polycrystalline fashion on both Cu(111) and Cu_3Te_2. The low coverage growth of CdTe on Cu(111) indicated that the Te atoms interfaced with the Cu(111) surface, forming a Cu-Te SSA, as described in chapter 3. The data also show that bulk alloy formation of Cu_xTe does not occur, implying that CdTe does not dissociate on the Cu(111) surface. The second part of chapter 4 shows that the deposition of thick CdTe films results in the formation of Cu_2Te crystallites in the CdTe film, through Cu diffusion from the Cu substrate. These crystallites have a tendency to segregate at the surface. Cu diffusion results in the following redox reaction:

$$2\ Cu + CdTe \rightarrow Cu_2Te + Cd \qquad (4.2)$$

There is also evidence of a slight expansion of the CdTe lattice parameter, which suggests that Cu may also occupy interstitial sites, however, this appears to be a minor process. The extent Cu diffusion into the CdTe film was found to be substrate dependent, with Cu_3Te_2 being the most effective.

Photovoltaic materials can be considered some of the most widely studied materials due to their ability to generate clean and renewable energy, with an extensive body of work already existing. Nevertheless, this thesis has provided some new insight into the CdTe system with particular emphasis on the back contact interface. Potential further experiments will now be discussed. Part of this thesis has investigated the structural and thermal properties of the growth of some components of a CdTe photovoltaic cell. An interesting extension to the fundamental studies described here, would be to more applied studies. For example, chapter 4 described the growth of CdTe on Cu containing substrates and showed that the magnitude of Cu diffusion was dependent on the substrate that the CdTe film was deposited on. It would be interesting to fabricate a series complete working photovoltaic devices using these different Cu substrates and examine how the different substrates affect the operational parameters of the photovoltaic cell, such as efficiency and stability. A further experimental avenue to explore could be the study of other components of the CdTe photovoltaic cell, using a combination of surface science and electron microscopy. For example, the CdTe-CdS and the CdTe-ITO interfaces. A natural extension to the back contact work, described in chapter 3, is to new,

somewhat more exotic materials currently being proposed to enhance the properties of the back contact interface of CdTe photovoltaics. For example, ZnTe, Sb_2Te_3/Mo, As_2Te_3, Ni/P which have all be recently proposed as a potential back contact. The deposition of these materials onto CdTe or Cu, for example, would simulate the integration of these materials into the photovoltaic module. Therefore, there is a lot of scope and importance for studying the fundamental growth process of these materials to aid the selection of the optimum material for the back contact interface.

Chapter 5 described the first study of Te onto Cu(643)^R, a stepped substrate in contrast to the flat Cu(111) surface. The experimental data showed that there are two chiral sub-monolayer CuTe structures formed on this surface, dependent on Te coverage. The first of which exists in range of θ_{Te} = 0.18-0.45 ML and forms an oblique (chiral) unit cell. The unit cell has parameters of a_1 = 0.51 ± 0.01 nm, b_1= 0.71 ± 0.01 nm and α_1 = 57 ± 2°. The second structure exists in the range of θ_{Te} = 0.45-1.1 ML and forms a rectangular unit cell. The unit cell has parameters of a_2 = 0.48 ± 0.01 nm, b_2= 2.25 ± 0.05 nm and α_2= 87 ± 4°. However, the observed atomic arrangement on the terraces suggested that chirality is retained in structure 2. Interestingly, from a homochiral Cu(643)^R substrate, both handedness of enantiomers of the CuTe alloy exist on the surface for the 0.28 ML coverage. We proposed that the formation of a unique chiral CuTe surface alloys relies on the kink sites of the Cu(643)^R sites. These sites act as points of nucleation for the growth of the CuTe alloy. Cu_2Te is also formed at all coverages, forming a minor component of the surface at low coverage but dominating the overlayer at thicker coverages. The Cu_2Te alloy grows in a rough or polycrystalline fashion. Further experiments here are required to gain full insight into the atomic structure of these complicated alloy phases. For example, a combined LEED IV and DFT study could give good insight into the atomic structure of these surface alloys. An interesting development of the work described in chapter 5, the deposition of Te on Cu(643)^R, would be to systems, such as topological insulators, where the physical phenomena explicitly depend on the chirality of the surface. The work presented in chapter 5 showed that intrinsically chiral surfaces can template the growth of chiral surface alloy phases. For example, an interesting experiment would be to deposit Te onto a chiral miscut of the Bi and see if any chiral alloy phases formed and then assess how this affects its topological insulation.

The nature of the Cu-Te alloying was found to be strongly dependent on (a) coverage, (b) substrate temperature and (c) substrate termination. For example, (a) is demonstrated by the deposition of Te onto Cu(111). At low Te coverages on Cu(111) (θ_{Te} < 0.33 ML), a SSA was formed, while at higher coverages (θ_{Te} > 0.66 ML), Cu_3Te_2 was formed. (b) is

demonstrated by the kinetic inhibition of Cu-Te alloying. In that, depositing Te with the substrate temperature fixed below 275 K on Cu(111) and 225 K on $Cu(643)^R$, resulted in no alloy forming, instead, a disordered Te overlayer was observed. Most interestingly, the surface termination strongly dictated the structure of alloy growth, (c). The good lattice match between the (111) termination of Cu_3Te_2 and the Cu(111) surface was ascribed to be the reason why this unusual alloy phase was stable. The formation of a distorted form of the CuTe alloy (Vulcanite) was attributed to the kink sites on the $Cu(643)^R$ surface acting as nucleation points for the growth of the alloy. The open, rough and polycrystalline nature of the Cu_{poly} substrate were the reasons attributed to why the Cu-Te alloy formed was polycrystalline Cu_2Te. These observations illustrate how sensitive the alloying of Cu-Te is to the experimental conditions.

The experiments described in chapters 3-5 are well suited to study with surface science techniques (XPS, UPS, LEED, STM). Chapter 6 described a study of the physical and electronic structure of nanoribbons of TaS_3, which would naturally lend its self well to being studied with techniques based on electron microscopy rather than surface science. The nanoribbons were identified as having a rectangular cross section with thickness of 20-100 nm, widths of 50-500 nm and lengths of up to several millimetres. A core-shell type structure was identified in TaS_3. The core of the TaS_3 nanoribbon was observed to be crystalline, with the shell being amorphous. The surface sensitive techniques showed that the shell was deficient in $(S_2)^{2-}$. TaS_3 is a one dimensional conductor and thus has been shown to exhibit a Peierls transition. However, we found no evidence of the Peierls transition in the shell but SAED data suggested that a Peierls transition occurred in the crystalline core of the material. When dispersed on a Au substrate, the TaS_3 ribbons showed dynamic effects, with the shell consistently losing S, due to the strong interaction between S and the Au substrate. The S content of the shell was found to be replenished through annealing, which was ascribed to increased S diffusion from the inner of the material. The applicability of the TaS_3 nanoribbons, described in chapter 6, to device integration could be further tested through conductivity measurements, with particular interest into the effect that the amorphous shell has on the electronic transport properties of the material. Nanomaterials are a large and increasing field, so it would be therefore interesting to apply the techniques described in this thesis to newly synthesised nanomaterials to compare the structure of the bulk and the surface.

This thesis has shown the power and limitations of surface science as a method of identifying the physical and electronic structure of solids. Supplemented by bulk techniques such as PXRD and TEM, this thesis has shown that surface science is applicable to wide range of different of systems of current scientific interest.